Photocatalytic CO$_2$ reduction by porphyrin rhenium dyads

Christopher David Windle

PhD

The University of York

Chemistry

May 2013

Abstract

The storage of solar energy in chemical fuel is currently under intense investigation, but many of the challenges associated with this goal remain unsurmounted. The investigation of supramolecular assemblies, in which one unit harvests visible light and transfers energy or electrons to another catalytic unit capable of energetically uphill chemical transformations, is of importance. This thesis describes the synthesis, electrochemistry, photochemistry and visible light CO_2 photoreduction ability of several rhenium tricarbonyl appended zinc porphyrins. The basic structure comprises a zinc tetraphenyl porphyrin in which one phenyl possesses a NHCO group bound to bipyridine. The bipyridine is complexed to a $Re(CO)_3X$ unit.

Introduction of a methoxybenzamide spacer produced **[Dyad 2 Pic][OTf]** and its bromide analogue. Synthetic methodology was developed for the introduction of a methylene spacer to produce **[Dyad 3 Pic][OTf]** and its bromide analogue. Further synthetic efforts produced routes to novel porphyrin and rhenium complexes possessing phosphonic acid groups for anchoring to metal oxide surfaces. In the ground states of the two dyads there is little interaction between the metalloporphyrin and rhenium units. However, emission quenching of the porphyrin by the rhenium was demonstrated. Remote site photosubstitution was observed in **[Dyad 2 Pic][OTf]**. Electrochemical and steady state emission studies indicate that electron transfer is energetically favourable in all systems except **Dyad 3 Br**. All the catalysts developed produced catalytic quantities of CO under visible light in CO_2 saturated DMF/TEOA 5/1. Activity increases in the order **Dyad 1 < Dyad 2 < particle system < two components < Dyad 3**, reaching a turnover number of 360 for **[Dyad 3 Pic][OTf]**. TRIR experiments demonstrated that the lifetime of charge separation in the dyads increases in the order **[Dyad 1 Pic][OTf]** < [Dyad 2 Pic][OTf] < [Dyad 3 Pic][OTf] and is 335 ps for **[Dyad 3 Pic][OTf]**, consistent with catalytic activity.

Reaction mixture analysis by UV-Vis and NMR spectroscopy and ESI mass spectrometry indicated hydrogenation of the porphyrin, the product of which is also active for CO_2 photoreduction. ESI-MS studies showed that substitution of the picoline ligand by TEOA and DMF occurred.

The Re and porphyrin units were successfully immobilised on TiO_2 nanoparticles. The Re catalyst anchored on TiO_2 is active for CO_2 photoreduction under visible light. Addition of the porphyrin, and its selective excitation, produced catalytic quantities of CO (TON = 32). This confirmed sensitisation of the Re complex around the TiO_2 particle. Electrochemical and steady state emission studies indicate a porphyrin to TiO_2 then TiO_2 to Re electron transfer mechanism is favourable.

Contents

CHAPTER 3.   ELECTROCHEMISTRY AND PHOTOCHEMISTRY ..118

Table of figures

XVI

Table of tables

Acknowledgements

This thesis and the last three and a half years work towards it could not have been possible without several people. I would first like to thank my supervisor, Professor Robin Perutz, for giving me this opportunity and providing guidance, patience, belief, support and willingness to help. I would also like to thank the students, postdocs and technicians I have worked with during this time (in no particular order): Naser, Jess, Dan, Barby, Magnus, Vargini, George, Ollie, Simon, Sarah, Ruqia, Olga and Katie. I would like to add a special thank you to Dan for proof reading. I would also like to thank Richard Lidster for the time he gave to get me up to speed with GC maintenance. My thanks go to Robert Mitchell for help with use of the DRUVS kit and Robert Smith for time spent working with HPLC. I would like to thank Karl for the mass spectrometry service, Heather for the NMR service and Steve and Mike in the stores. Thanks to Adrian and Natalie for help with crystal structure determination.

I would like to extend a special thank you to those students and post docs who worked on the same project as me; Jake, Alvaro, Marius and Ollie.

I can't complete my acknowledgements without a paragraph for Jake Schneider. Thank you for your support and encouragement from day one, for taking the time to answer all my questions and teach me the techniques I would need for much of the PhD. Thank you for the chats, the jokes and the sharing of music.

I would like to thank Erwin Reisner for the opportunity to work in his laboratory for six months of the PhD and for his support during that time. I would also like to thank members of the Reisner group who were so welcoming when I started and supportive during my time there. In no particular order: Fezile, Claire, Nicoleta, Masaru, Dirk, Nick, Moritz, Chia-Yu, Yi-Hsuan, Tsubasa, Manuela, Ahu and Christine. I would also like to thank David Reid for the MAS-NMR experiments.

Declaration

The following results were obtained by or with the assistance of other researchers:

1. CO_2 photoreduction by zinc tetraphenyldihydroporphyrin and **[ReBpy(CO)$_3$Pic][PF$_6$]** by Marius Câmpian.
2. Cyclic voltammetry of **[Dyad 1 Pic][PF$_6$]**, **[Dyad 2 Pic][OTf]** and **6c** with the assistance of Alvaro Martinez.
3. Time resolved infrared spectroscopy with the assistance of Dr Sun Xue-Zhong and Mr Peter Summers in the University of Nottingham.
4. The MAS-NMR data was obtained by David Reid in the University of Cambridge.
5. X-ray diffraction data collection and structure solution was performed by Adrian Whitwood.

All other work was performed by the author. This thesis has not been submitted for examination at the University of York or any other institution for another award.

The work of chapter 5 was performed in collaboration with Erwin Reisner.

Portions of the thesis have been published and are referenced below.

C. D. Windle, R. N. Perutz, *Coord. Chem. Rev.,* 2012, **256**, 2562-2570

C.D. Windle, M. V. Câmpian, A. Duhme-Klair, E. A. Gibson, R. N. Perutz, J. Schneider, *Chem. Commun.,* 2012, **48**, 8189-8191

Compound Key

Chapter 1.   Introduction

Current civilisation is fuel hungry and fed almost entirely with crude oil from non-renewable fossil fuel reserves. The processes involved are unsustainable and lead to climate change.[1, 2] One alternative is nuclear power but considering disasters such as the one at Fukushima[3], coupled with long-lived radioactive waste, nuclear power has severe health and safety risks. It is also typically utilised for electric current and not fuel. Fuels are important because energy must be stored efficiently in very energy-dense media.

There are various alternative sources of energy and solar power is the most promising. This is because the sun is sustainable, clean and can theoretically provide sufficient energy for the world both now and in the future.[4, 5] Existing solar technology is based on photovoltaics, these include cells designed around crystalline silicon and molecular dyes on TiO_2. Photovoltaic technology produces electrical energy, which is difficult to store. The major technology for storage of electrical energy is batteries and they currently exhibit low energy densities and are slow to charge. The main other global energy carrier is liquid fuel composed of hydrocarbons, these have a relatively high energy density, are compatible with our current infrastructure and a car can be fuelled in minutes. The field of 'solar fuels', whereby photochemistry allows solar energy to be stored as fuel, is of ever increasing importance. The two feedstocks of major interest for such processes are water and carbon dioxide. The direct photochemical reduction of CO_2 would in principle allow the storage of solar energy in carbonaceous fuels; compounds with high energy density and an established infrastructure. Hydrogen is an alternative solar fuel but this exhibits a lower energy density than hydrocarbons and is not compatible with our current infrastructure. Aside from fuels, carbonaceous materials could feed into industry that currently relies on starting materials derived from crude oil.

The fixation of CO_2 using the energy of sunlight also describes photosynthesis. Natural photosynthetic systems utilise antennae composed of chromophores for

visible light harvesting. The energy is funnelled down to reaction centres I and II where charge separation is exploited through the Z-Scheme[6] to split water into oxygen and NADPH and produce ATP. NADPH and ATP feed the enzyme RuBisCo which is the first step in fixing CO_2 into carbohydrates.

The artificial fixation of CO_2 via photocatalysis by transition metal complexes began with the work of Lehn and co-workers in the 1980's. Initially $[Ru(Bpy)_3]^{2+}$ was combined with $CoCl_2$ in an $CH_3CN/H_2O/Et_3N$ mixture under $\lambda > 400$ nm to produce a mixture of H_2 and CO at a combined turnover number of 9 with respect to $CoCl_2$.[7] In this system the $[Ru(Bpy)_3]^{2+}$ was light harvester and the $CoCl_2$ was pre-catalyst. Soon after, the same laboratory reported $Re(Bpy)(CO)_3X$ as a highly selective CO_2 reduction photocatalyst, producing only CO, with TEOA as sacrificial electron donor.[8] The rhenium complexes act as both photosensitizer and catalyst and show high efficiency, reaching turnovers of 48 in the presence of excess Cl^- (when X = Cl). Catalysis was tested with 90.5% enriched $^{13}CO_2$ and only ^{13}CO (88% enriched) was produced as observed with ^{13}C NMR spectroscopy and GC-MS.

Rhenium compounds do not represent a solar fuels solution for several reasons, one of which is that they do not absorb visible light efficiently. Compounds of the type $Re(Bpy)(CO)_3X$ typically posses a peak absorption at approximately 380 nm which tails, with low intensity, into the visible and is lost around 450 nm.

Since the same motif of rhenium complexes will perform electrocatalytic carbon dioxide reduction, two pathways are open for increasing the efficiency of visible light induced CO_2 reduction. Solar cells maybe used to provide current for driving electrocatalysis and alternatively sensitisers may be used to harvest visible light and transfer energy or electrons to the catalyst. Furthermore, the distinction between photo- and electro- catalyst becomes blurred when discussing photoelectrodes and photoelectrocatalysts. The work herein is primarily concerned with photosensitising rhenium catalysts to visible light.

However, electron transfer between sensitiser and catalyst is an important step in the function of such systems and therefore electrochemistry and electrocatalysis will be covered.

1.1 *Electrocatalytic CO$_2$ reduction*

The standard electrode potential (E$^\circ$) specifies the equilibrium potential and free energy required for a reaction. Often a greater potential is necessary in order to achieve a significant rate of reaction. This overpotential may be considered as an activation energy for the reaction. Electrocatalysts reduce the overpotential required for an electrochemical process opening up routes for less energetically demanding reactions. In the case of CO$_2$ reduction an electrocatalyst may facilitate a proton-coupled multi-electron process, which requires a lower potential than the single-electron reaction. The potentials for various routes to CO$_2$ reduction (Table 1) show that the potential required for reactions involving multiple electrons and protons is much lower than for the single-electron process.

Reaction	E° (V)
$CO_2 + e^- \longrightarrow CO_2^{\cdot-}$	-1.90
$CO_2 + 2H^+ + 2e^- \longrightarrow HCO_2H$	-0.61
$CO_2 + 2H^+ + 2e^- \longrightarrow CO + H_2O$	-0.53
$2CO_2 + 2H^+ + 2e^- \longrightarrow H_2C_2O_4$	-0.49
$CO_2 + 4H^+ + 4e^- \longrightarrow HCHO + H_2O$	-0.48
$CO_2 + 6H^+ + 6e^- \longrightarrow CH_3OH + H_2O$	-0.38
$CO_2 + 8H^+ + 8e^- \longrightarrow CH_4 + 2H_2O$	-0.24
$CO_2 + 4H^+ + 4e^- \longrightarrow C + 2H_2O$	-0.20

Table 1 CO_2 reduction potentials vs SHE[9]

Some of the more notable CO_2 reduction electrocatalysts [10] include Savéant's iron porphyrins[11, 12], Eisenberg's tetraazomacrocyclic complexes [13] and the palladium phosphines of DuBois (Fig. 1).[14]
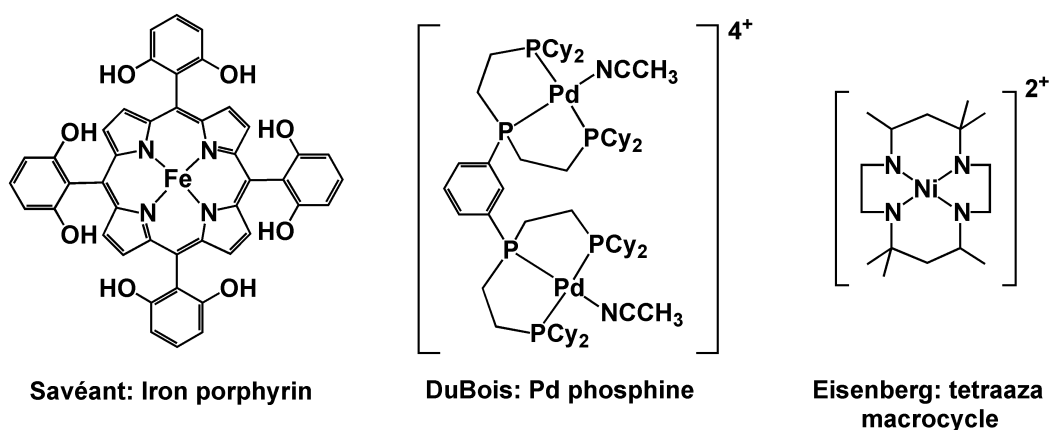
Fig. 1 Structures of notable electrocatalysts for CO_2 reduction.[12-14]

In 2010 Bouwman reported a dinuclear copper system that binds CO_2 selectively from the air and couples it to generate a tetranuclear oxalate complex (Fig. 2 $[2]^{4+}$).[15] On addition of $Cu(acac)_2$ to the ligand ([N-(2-mercaptopropyl)-N,N-bis(2-pyridylmethyl)amine]) in acetonitrile with HBF_4, a dinuclear copper complex (Fig. 2, $[1]^{2+}$) is formed. On exposure to air, the solution changes color, yielding crystals of an oxalate-bridged tetramer ($[2]^{4+}$). The same product may be formed more rapidly by purging carbon dioxide through a solution of $[1]^{2+}$. The source of oxalate was confirmed to be carbon dioxide with $^{13}CO_2$ labeling studies. $[1]^{2+}$ could be generated electrochemically from $[4]^{4+}$ and converted to $[2]^{4+}$ by bubbling CO_2 through the solution. When lithium perchlorate is used as electrolyte, lithium oxalate is precipitated in near quantitative yield and $[4]^{4+}$ (acetonitrile complex) is re-formed. Purging with argon and reducing again showed that $[1]^{2+}$ could be regenerated. The electrocatalytic reduction of CO_2 succeeded at -0.03 V vs SHE with continuous purging of CO_2. The potential for formation of oxalate under standard conditions is -0.49 V, but additional stabilization will accrue from complexation to copper or precipitation as the lithium salt.

5
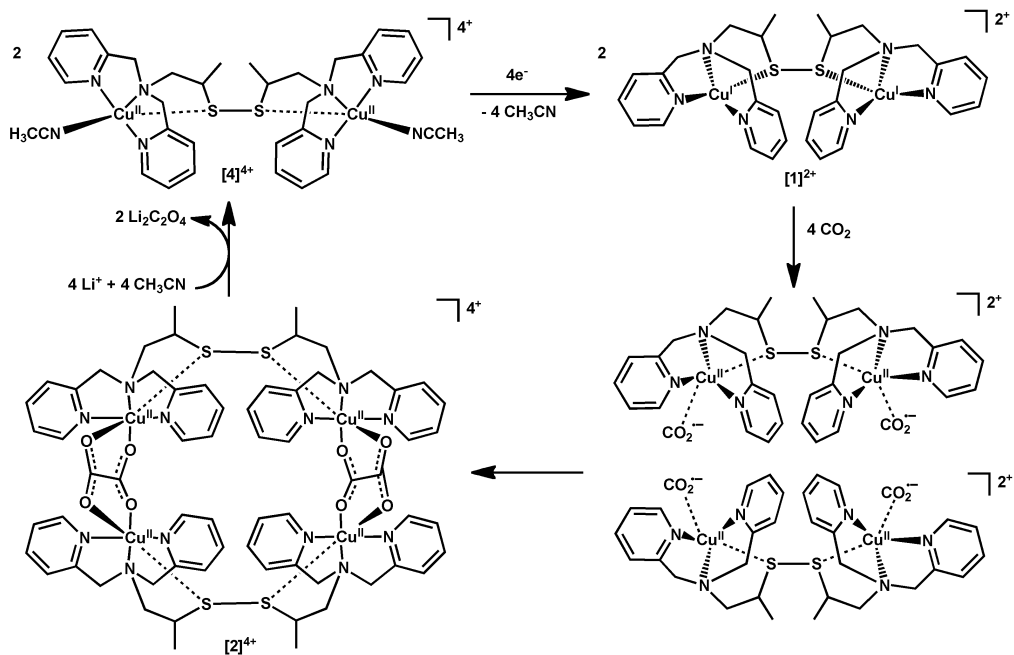
Fig. 2 Bouwman's proposed electrocatalytic cycle for conversion of CO_2 to lithium oxalate.[15]

The use of $Re(Bpy)(CO)_3Cl$ as an electrocatalyst for CO_2 reduction goes back to the early work of Lehn.[16] Recently Kubiak and co-workers [17] have reported improved electrocatalysis by altering the substituents at the 4 and 4' positions of the bipyridine ligand. The complex with 4,4'-tBu$_2$Bpy significantly out-performs the original electrocatalyst as is shown by a catalytic reduction wave in the presence of CO_2, that is 3.5 times greater in current than that observed with the simple bipyridine complex. In terms of CO production the 4,4'-tBu$_2$Bpy complex is reported to give ca. twice as much CO as the simple bipyridine complex during the first 15 minutes of controlled potential electrolysis (held at -1606 mV vs SHE), it has a second order rate constant of 1000 M^{-1} s^{-1} (similar to the Pd phosphines of DuBois) and does not lose activity as rapidly.

In the same year Kubiak also reported the use of the optimized electrocatalyst with a p-type hydrogenated silicon electrode. Under illumination ($\lambda = 661$ nm) with a p-H-Si photoelectrode, a full cyclic voltammogram of the rhenium catalyst can be recorded displaying both the expected reduction waves.[18]

Furthermore, both waves occur at reduction potentials at least 600 mV lower in magnitude than those required when using a platinum electrode (Fig. 3). The system reduces CO_2 electrocatalytically under illumination with a Faradaic efficiency of $97 \pm 3\%$. The photocurrent density increases with light intensity. Bulk electrolysis was conducted for 3 hours after which both catalyst and electrode remained fully functional.
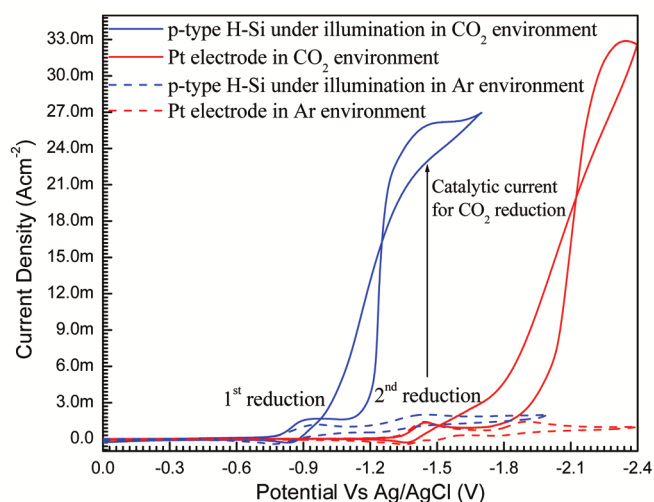
Fig. 3 Photo-electrocatalytic CO_2 reduction with $Re(4,4'-tBu_2bpy)(CO)_3Cl$ on p-type hydrogenated silicon (sweep direction left to right).[18]

Kubiak combined the *t*BuBpy rhenium catalyst with an H_2 evolving photoelectrode to produce H_2 and CO (or syngas) from aqueous acetonitrile under CO_2.[19] In the presence of water but under Ar, only H_2 was produced either with, or without, the Re catalyst. The authors conclude that the H^+ reduction is therefore heterogeneous (it requires the electrode). The H_2:CO production ratio can be tuned to the desired value of 2:1 H_2:CO. An increase in Re catalyst gave more CO and increased water content gave more H_2. The optimum system used 0.5 mM catalyst at a potential of -1260 mV vs SHE to give H_2:CO of 2:1 and a Faradaic efficiency (for both H_2 and CO) of $102 \pm 5\%$ (in acetonitrile/water mix, $\lambda = 661$ nm).

The rhenium catalysts cause concern because rhenium is not an abundant element, so investigation of manganese analogues is desirable. Manganese is 1.3 million times more abundant in the Earth's crust than rhenium.[20] Deronzier et al. recently reported the electrocatalytic activity of manganese complexes of the type $Mn(Bpy)(CO)_3Br$.[21] Electrolysis in acetonitrile in the absence of CO_2 leads to the formation of manganese-bonded dimers that undergo a two-electron oxidation giving $[Mn(Bpy)(CO)_3(MeCN)]^+$. In solution saturated with CO_2, there is no voltammetric difference but on addition of 5% water a significant increase in the cathodic current for the second reduction is observed. The authors conclude that the dimer is the active species in the electrocatalytic process. They also suggest that the need for H_2O is analogous to the H_2O requirement of similar rhenium electrocatalysts. The manganese catalyst gave a turnover number of 13 (over 4 hours) and a quantitative Faradic efficiency for CO production. The catalyst remained stable after 4 hours of electrolysis but if left longer, there was a decrease in current and the selectivity was lost. The complex with Me_2Bpy remained selective for longer electrolysis times, lasting up to 18 h and giving a turnover number of 34. The authors also conclude that this second catalyst can perform CO_2 reduction via two different pathways that are one- and two-electron in nature, respectively. All catalysis was performed at -1470 mV vs SHE, a potential 40 mV more positive than that required for rhenium analogues.

In 2013 Kubiak and colleagues continued the manganese work by applying investigative techniques and structural optimizations they had developed for Re analogues.[20] The requirement of water by Mn catalysts was extended to the broader need for Brønstead acids.[20] The Bpy-*t*Bu complex was 300 times more active than the simple Bpy in terms of TOF (CH_3CN with 5% H_2O) and 7 times less active than $ReBpy(CO)_3Cl$ (DMF with 2 M H_2O). The Mn catalysts showed high selectivity, efficiency and stability for CO_2 reduction to CO in the presence of H_2O, CH_3OH and 2,2,2-trifluoroethanol. The anion was isolated and XRD indicated bond lengths consistent with significant electron density on the Bpy. DFT calculations suggested the HOMO contained substantial Bpy π^* character along with Mn. The Bpy acts as a reservoir for electron density as found for the

Re analogues. IR spectroelectrochemical studies indicated that three species were present; the starting complex, dimer and the anion. Infrared spectroscopy also shows a significant increase in CO backbonding compared with the rhenium complexes. The authors suggest the need for protons is for solvolysis of the Mn-Br bond to give the solvent complex and to protonate the $Mn-CO_2$ adduct. Stronger Brønstead acids give higher current densities.
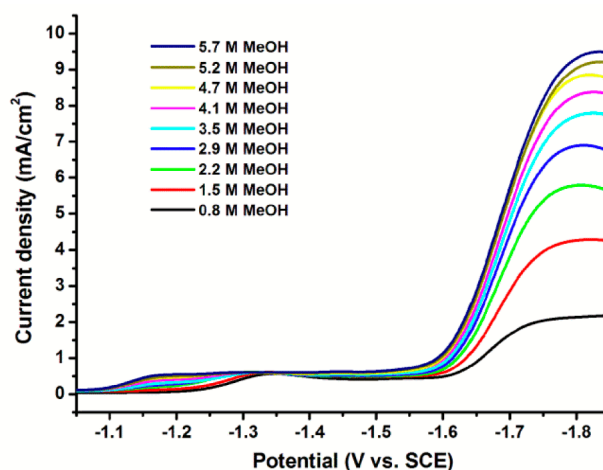
Fig. 4 Linear sweep voltammograms of 1 mM Mn(Bpy-*t*Bu)(CO)$_3$Br in CO_2 saturated CH_3CN and increasing concentrations of CH_3OH.[20]

Meyer et al. investigated the electrocatalytic activity of two Ru terpyridine complexes (Fig. 5).[22] Cyclic voltammetry under CO_2 showed sequential one-electron reductions first at the terpyridine, then at the bipyridine/carbene. The bipyridine and carbene complexes gave Faradaic efficiencies of 76% and 85%, respectively (for ca. 5 turnovers). For both catalysts only CO could be seen in the gas chromatographs and small amounts (< 20%) of CO_3^{2-} and $HCOO^-$ were seen by ^{13}C and ^1H NMR spectroscopy. Kinetic studies were conducted that showed the rate limiting step to be the dissociative loss of acetonitrile from the doubly reduced complex. The catalytic rate constants were determined to be 5.5 and 19 s^{-1} for the bipyridine and carbene complexes, respectively, correlating well with the difference in activity. They postulate that coordinated acetonitrile is substituted for CO_2, which acquires a double negative charge while the

9

polypyridine ligands return to neutral. A further two electrons reduce both polypyridine ligands again and then with the aid of another molecule of CO_2, CO and CO_3^{2-} are produced and the solvent complex reformed.
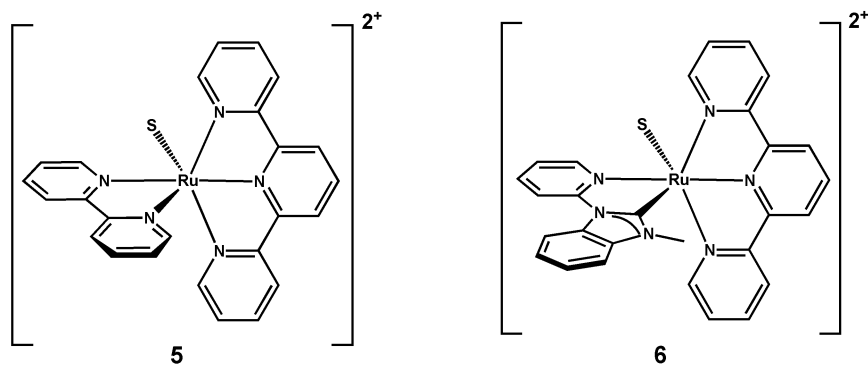
Fig. 5 Ruthenium terpyridine bipyridine (**5**) and carbene (**6**), S = solvent.[22]

Sato and Arai and co workers report the photoelectrochemical reduction of CO_2 to formate using a polymer based on ruthenium complexes linked to polypyrrole and anchored to various semiconductors.[23] The system is designed to mimic the Z-scheme of photosynthesis with two photoelectrodes, a Ru-linked InP electrode for CO_2 reduction and a TiO_2/Pt electrode for H_2O oxidation. The most active system used an InP photoelectrode with a glassy carbon counter-electrode and Ru catalysts labeled **7** + **8** (Fig. 6 right). It gave 4.71 μmol $HCOO^-$ cm^{-2} with an efficiency for formate of 78% at -170 mV vs SHE (in H_2O under $\lambda > 400$ nm). In order to couple water oxidation with CO_2 reduction, the anode was replaced by platinum on titanium dioxide (Fig. 6 left) with 10 mM $NaHCO_3$ electrolyte. The system gave a turnover number ($HCOO^-$) of > 17 after 24 h irradiation. Negligibly small amounts of H_2, CO and $HCOO^-$ were produced in the TiO_2/Pt compartment and this suggests the electrons from H_2O were transferred through the external circuit. Isotope tracer analysis showed the carbon and proton sources for the formate were CO_2 and H_2O, respectively, and the oxygen from water oxidation was traced with $H_2^{18}O$.
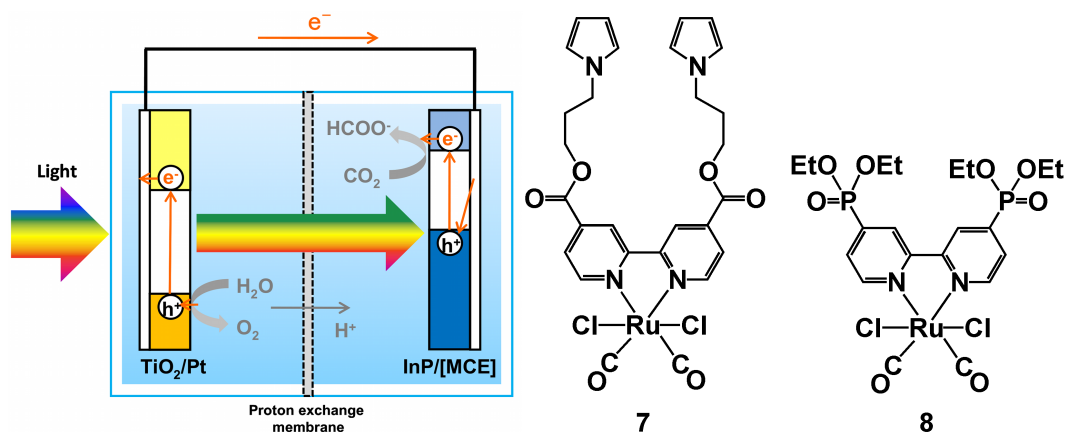
Fig. 6 Right: ruthenium complexes that were incorporated into polypyrrole for CO_2 reduction, Left: photochemical cell for tandem CO_2 reduction - H_2O oxidation.[23]

Arai continues this work by loading the ruthenium polymer onto Cu_2ZnSnS_4 (CZTS) [24], which has a narrow band gap and a large absorption coefficient. Irradiation of the CZTS + Ru as photocathode with a Ag/AgCl anode allows CO_2 reduction to formate to occur at -170 mV vs SHE (in H_2O). In the absence of light or Ru catalyst, no formate is produced. With mixed Ru catalysts (Fig. 6) under $400 < \lambda < 800$ nm, 0.34 C of charge was passed and 0.29 mM formate was produced. The current efficiency for formate was 80% and the turnover number was greater than 5. Another form of CZTS with added selenium was investigated (CZTSe), resulting in a higher photocurrent and reaction rate, probably due to improved hole mobility in the new material.

Some years ago Bocarsly and co-workers demonstrated that the pyridinium ion acts as an electrocatalyst for the six electron reduction of carbon dioxide to methanol.[25, 26] The most recent work investigates the mechanism for the observed reaction on a Pt electrode.[27] The pyridinium ion reduces carbon dioxide to methanol stepwise by providing the six electrons sequentially. The reaction is split into three two-electron steps each with defined products that have been observed in the reaction solution (Fig. 7).
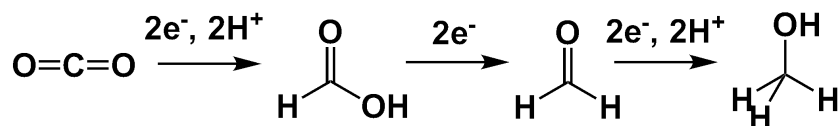
Fig. 7 Sequential reduction of CO_2 by pyridinium.[27]

The first electron transfer from pyridine to CO_2 is inner sphere. A separate investigation using gas phase photoelectron spectroscopy reported the pyridine-CO_2 adduct to be a stable species. Analysis of rate constants by application of the Marcus cross-relation also points to an inner sphere mechanism. The authors conclude that a small amount of CO_2 adduct is present prior to reduction but that the dominant mechanism is the reaction of the pyridinium radical (Fig. 8). The proposed mechanisms of steps two and three are given in Fig. 9.
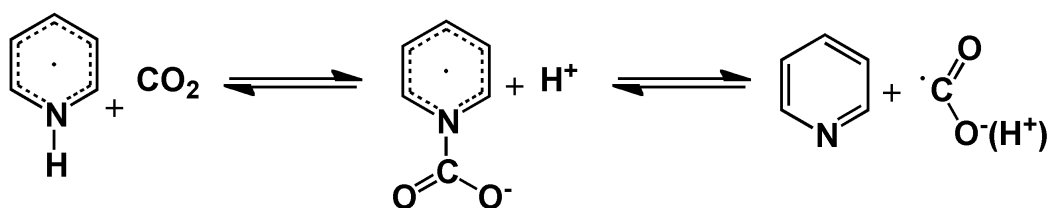
Fig. 8 Initial electron transfer by pyridinium to CO_2.[27]
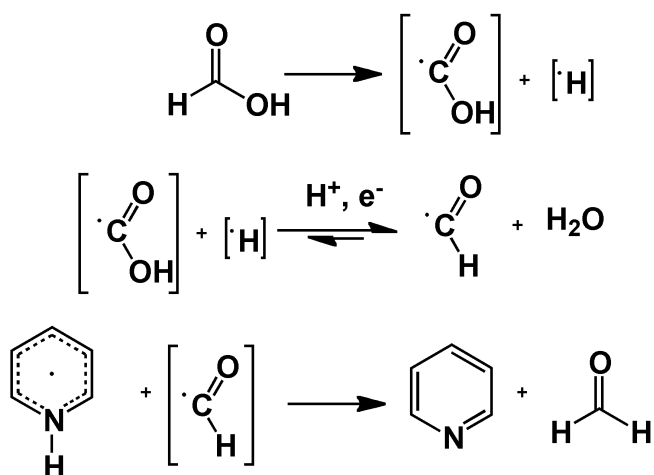
Fig. 9 Proposed mechanism for second (left) and third (right) two-electron steps.[27]

The system operates with a hydrogenated Pd electrode, at pH 5.4, at an overpotential of 200 mV (CO_2 reduction onset at -306 mV vs SHE) and gives Faradaic efficiencies of 30%. Bocarsly and co-workers have also developed the system to operate in conjunction with a photoelectrode.[26] It reduces CO_2 to methanol at an underpotential (i.e. below the thermodynamic potential) of 300 mV (at +44 mV vs SHE) and has a Faradaic efficiency of 100% when using $\lambda = 365$ nm.

Masel et al. conducted electrochemistry on CO_2 in an ionic liquid electrolyte (1-ethyl-3-methylimidazolium tetrafluoroborate) with a silver cathode and a platinum anode.[28] CO could be formed with an overpotential of 170 mV which is 600 mV less than without the ionic liquid. The authors quote a cell reaction as $CO_2 \rightarrow CO + \frac{1}{2} O_2$, but quote no half-reactions or electrode potentials for their ionic liquid, so it is unclear whether this is a proton-coupled reaction and unclear how the potentials compare with an aqueous solution. The authors postulate that the ionic liquid can form a complex with CO_2^-, the product of the first step of the reaction mechanism. Stabilization of this anion could therefore reduce the potential required for conversion. They also state that in this particular ionic liquid binding of CO_2 is weakest and so the necessary balance in binding strength is achieved (if it bound too strongly, the CO_2 could be rendered unreactive). The Faradaic efficiency is 96%, with 3% due to H_2 production from electrolysis of water.

In 2012 Savéant reported the optimization of iron porphyrins for CO_2 reduction to CO.[12] Fe(III) porphyrin is reduced in three sequential steps to the active Fe(0) species. Protons are required to reduce CO_2 to CO and so the authors modified the simple FeTPP by installing OH groups at all eight ortho positions (Fig. 1). The close proximity of a proton source is used to explain the high activity. The catalyst is capable of 50 million turnovers in 4 h of electrolysis ($_{\log}TOF = 2.3$-4.2 s^{-1}). The catalyst operates with an overpotential (η) of 0.41-0.56 V which compares well with Re(Bpy)(CO)$_3$Cl ($\eta = 0.57$ V, $_{\log}TOF = 3.3$), Mn(Bpy)(CO)$_3$Br ($\eta = 0.51$ V, $_{\log}TOF = -0.05$), {m-(triphos)$_2$-[Pd(CH$_3$CN)]$_2$} (η

= 0.80 V, $_{\log}TOF$ = 0.67) and Ni(cyclam) (η = 0.55 V, $_{\log}TOF$ = 2.2). A deeper look into the purification and characterization of the catalyst raises an issue. The final catalyst was purified on silica with CH_3OH/Ethyl acetate 1:1 with no further purification steps and only mass spectrometry for characterization, which is an ambiguous indicator of purity. Use of any more than 5% CH_3OH as column eluent will begin to dissolve significant quantities of silica. When the crux of an investigation is the availability of OH functionalities then absorption onto a small amount of silica could have a significant impact. Elemental analysis or a silicon NMR spectrum of the catalyst would help remove this uncertainty. Otherwise, a comparison of the electrocatalytic activity of FeTPP with FeTPP absorbed onto 5% silica would suffice.

1.2 Photocatalytic CO_2 reduction

1.2.1   Development of Re(Bpy)(CO)₃X type catalysts

Lehn conducted some of the first work on photocatalytic CO_2 reduction in the early 1980s.[7, 16] Ishitani took up the rhenium baton in the early 1990s through the use of triethylphosphite as the X ligand.[29, 30] The lifetime of the excited state of the complex was five times longer than with X = Cl (250 ns vs 50 ns respectively). The complex was irradiated at 365 nm in TEOA/DMF under a CO_2 atmosphere and produced a maximum turnover number of CO of 7.5 in 16 h.[31]

To increase the efficiency of visible light utilisation Ishitani combined rhenium catalysts with $[Ru(Bpy)_3]^{2+}$ as sensitiser.[32] The two separate components and a wide range of dyads were tested. The dyads differed by their bridging group between the two metal centres, by the ratio of Re to Ru and by the groups on the bipyridine ligands of the $[Ru(Bpy)_3]^{2+}$ (Fig. 10).
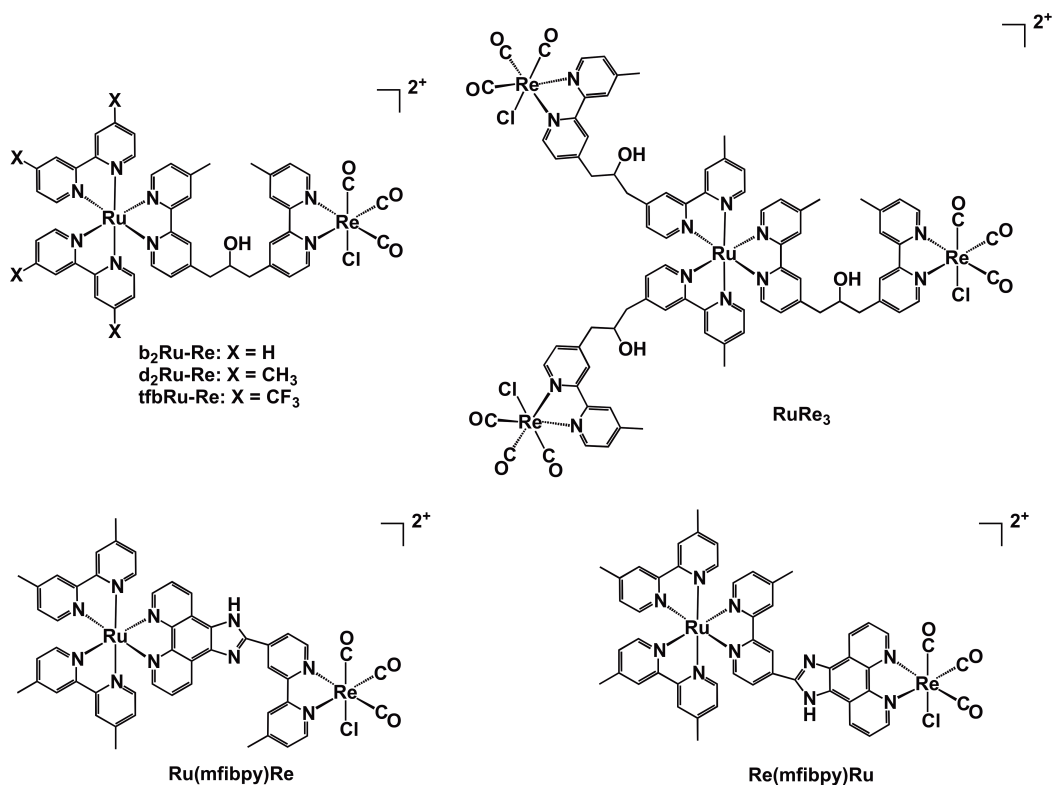
Fig. 10 Ru and Re dyads developed by Ishitani.[32]

The catalysts were employed in DMF/TEOA (triethanolamine) 5/1 v/v solution containing 0.1 M BNAH (1-benzyl-1,4-dihydronicotinamide) as e⁻ donor and irradiated with $\lambda \geq 500$ nm. The greatest activity in terms of turnover number for CO (TN_{CO}) was achieved with complex RuRe$_3$ at 240, calculated on a per molecule basis. However, RuRe$_3$ contains three potentially catalytic centres and on a per ReBpy(CO)$_3$Cl basis d$_2$Ru-Re exhibits the highest TN_{CO} with 170. Furthermore, of those tested, d$_2$Ru-Re gave the highest quantum yield for CO production (Φ_{CO}). A simple mixture of the two components gave $TN_{CO} = 101$. Changing the electronics of the Bpy on the $[Ru(Bpy)_3]^{2+}$ unit had a dramatic effect with b$_2$Ru-Re and tfbRu-Re achieving TN_{CO} of 50 and 3 respectively, apparently due to a rise in the oxidation potential of the $[Ru(Bpy)_3]^{2+}$. The complexes with phenanthroline-imidazole type ligands broadly followed the trend in TN_{CO} and oxidation potential. However, the $[Ru(Bpy)_3]^{2+}$ of Re(mfibpy)Ru is easier to oxidise than that of b$_2$Ru-Re yet shows half the TN_{CO},

this is likely due to increased charge recombination. The bridging ligand can exhibit a totally conjugated conformation that would allow rapid back electron transfer.

Complex	TN_{CO}	$E_{1/2}^{ox}$
d_2Ru-Re	170	+0.75
b_2Ru-Re	50	+0.85
tfbRu-Re	3	+0.94
Ru(mfbpy)Re	14	+0.89
Re(mfbpy)Ru	28	+0.81

Table 2 Ishitani dyads TN_{CO} and first oxidation potential.

In 2007 the results on the dyads and those on the rhenium complexes with the triethylphosphite ligand were brought to bear when the two were combined.[33] The best dyad from above, with the C_3OH bridge and CH_3 groups on the Ru(Bpy)$_3$, was synthesised with a triethylphosphite ligand instead of chloride. A dyad with pyridine in place of chloride was also investigated. The triethylphosphite and pyridine complexes achieved TN_{CO} of 232 and 97 respectively. ESI-MS analysis showed the X ligand was substituted by DMF or TEOA to yield what the authors conclude to be the real catalyst. The P(OEt)$_3$ and pyridine complexes underwent complete substitution in the early stages of the reaction whereas some Cl$^-$ was still bound after 3 h irradiation. The P(OEt)$_3$ and pyridine complexes are more effective precursors to the active catalyst due to rapid substitution. However, the pyridine complex decomposed much more rapidly than the P(OEt)$_3$ complex via loss of the rhenium (Fig. 11). Furthermore,

on addition of pyridine to the P(OEt)$_3$ catalyst solution, CO formation was inhibited and the TN$_{CO}$ was halved.
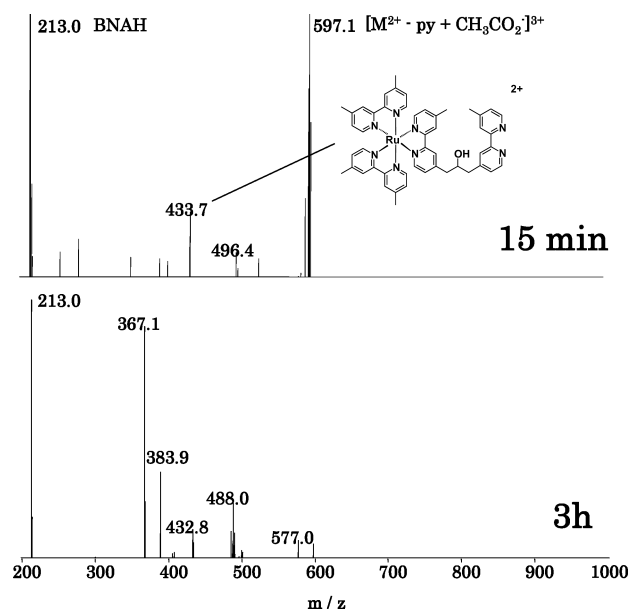
Fig. 11 HPLC-MS of [d$_2$Ru-Re]$^{2+}$ dyad with pyridine ligand during photocatalysis.[33] CH$_3$CO$_2^-$ present due to use as eluent.

A year later a tripodal system was reported by the same laboratory. Development of the tripodal tris bipyridine ligand allowed for two different ratios of rhenium to ruthenium; 2:1 and 1:2 (Fig. 12). Catalyst RuRe$_2$ and Ru$_2$Re exhibited TN$_{CO}$ = 190 and 110 respectively. The authors invoke theories on the mononuclear Re CO$_2$ reduction mechanism in order to rationalise the results. Mononuclear Re complexes are thought to form CO$_2$ bridged dimers in order to provide the two electrons required for CO$_2$ reduction.[34] The structure of RuRe$_2$ could allow the Re to dimerise via an intramolecular mechanism as well as intermolecular, this is a plausible explanation but the turnovers are calculated on the basis of the entire complex concentration and not the concentration of Re centres. The extra activity may be due to the presence of twice as many catalytically active sites.

17
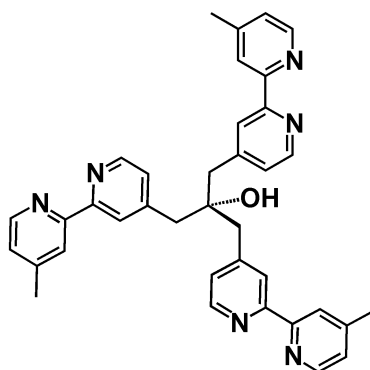
Fig. 12 Tripodal ligand that was coordinated to different ratios of $Ru(Me_2Bpy)_2$ and $Re(CO)_3Cl$.

1.2.2   Recent CO_2 reduction photocatalysis

$Re(Bpy)(CO)_3Cl$ compounds are selective and efficient photocatalysts for CO_2 reduction. The main drawbacks of this system are (a) that these complexes absorb in the UV and not the visible part of the solar spectrum, (b) that rhenium exists in low abundance, (c) that the catalyst has rather low turnover numbers and (d) that a tertiary amine sacrificial electron donor is required (typically triethanolamine, TEOA). Nevertheless, it has served as an inspiration for further development.

Deronzier and co-workers report the photocatalytic reduction of CO_2 by Os(II) complexes $Os(Bpy)(CO)_2Cl_2$ and $Os(4,4'-Me_2Bpy)(CO)_2Cl_2$.[35] In the absence of CO_2, photo-reduction leads to the formation of Os-Os bonded polymers. In the presence of CO_2 ($\lambda = 400$ nm in $DMF/[Bu_4N][PF_6]$ + TEOA), catalytic quantities of CO were produced and only traces of H_2, displaying activity comparable to that of $Re(Bpy)(CO)_3Cl$ catalysts. The activities of the complexes followed the order $Os(Bpy)(CO)_2Cl_2 < Os(4,4'-Me_2Bpy)(CO)_2Cl_2 < Re(Bpy)(CO)_3Cl$. However, the Os catalysts exhibit a far slower reduction in turnover during the 4 h irradiation period than the Re complex.

One major strategy for using visible light for catalytic CO_2 photoreduction is to attach sensitizers to known electro- or photo-catalysts. The last decade has seen

the majority of work in this area and the most recent developments are concerned with the linkage or bridge between photosensitizer and catalyst. In order to sensitize CO_2 reduction at a site remote from the chromophore, charge separation is necessary, as identified in natural photosynthetic reaction centers. The subsequent charge-separated state needs to have a lifetime long enough for CO_2 reduction to occur before it is lost through charge recombination. The nature of the bridge between catalyst and sensitizer is thought to have great bearing on these important mechanistic requirements. Bian and co-workers report the synthesis and interrogation of two systems that are identical except that one has a conjugated bridge (Ru=Re) and the other has a saturated bridge (Ru-Re, Fig. 13).[36]
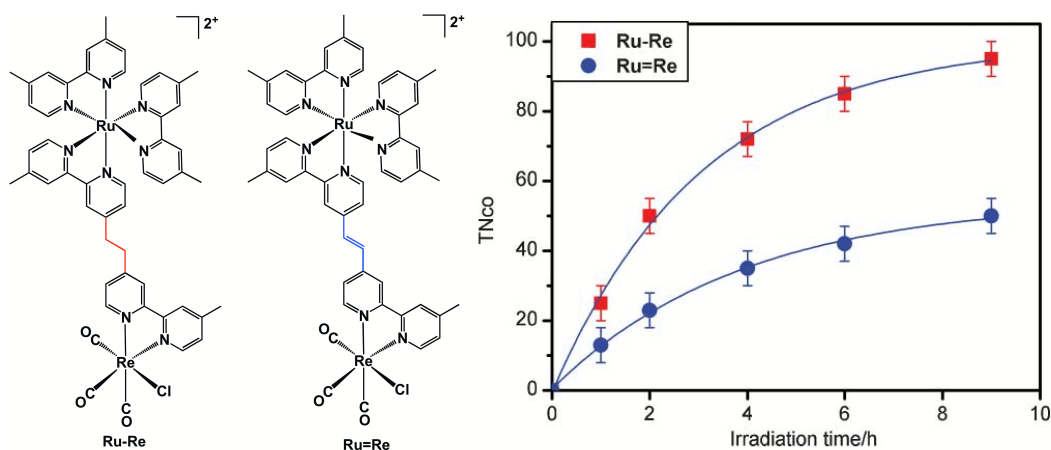
Fig. 13 Structure and activity of conjugated and non-conjugated bridged systems.[36]

Electronic absorption spectra show the Ru-Re system to be identical to the sum of its components, suggesting that the two units are not coupled in the ground state. In the Ru=Re system, the maxima of the MLCT bands extend to 490 nm, 30 nm beyond that seen in the Ru-Re system and a shoulder is observed at 300 nm attributed to an intraligand transition involving the ethene link. This assignment is backed up by DFT calculations showing that in the Ru-Re system the highest occupied orbitals are localized on Ru. In the Ru=Re system, there is a contribution from intraligand as well as MLCT transitions to the absorption band

at 490 nm. The highest occupied orbitals are located on the double bond of the bridge as well as on the Ru^{II} center. Unoccupied orbitals were found mainly on the bridge. This analysis suggests that an excited electron, originating in the RuBpy unit, would be delocalized across the bridge. It is clear from Fig. 13 that Ru-Re shows significantly greater CO_2 reduction ability under visible light irradiation ($\lambda \geq 500$ nm, DMF/TEOA/BNAH) than Ru=Re. The authors conclude that the incorporation of a delocalized π system between sensitizer and catalyst is detrimental, whereas weak interaction between Ru^{II} and Re^{I} increases photocatalytic ability. They do not discuss the increased flexibility of the non-conjugated link that may favour charge-transfer mechanisms by altering the conformer distribution.

In a study of complexes closely related to the previous system, Ishitani and co-workers investigated the effect of the length of the alkyl chain between Ru(Bpy)$_3$ and Re(Bpy)(CO)$_3$.[37] Three different supramolecular catalysts were synthesized for the study (Fig. 14) with a two-carbon spacer (C$_2$), a four-carbon spacer (C$_4$), a six-carbon spacer (C$_6$) and a three-carbon spacer with an OH on the second carbon (C$_3$-OH).
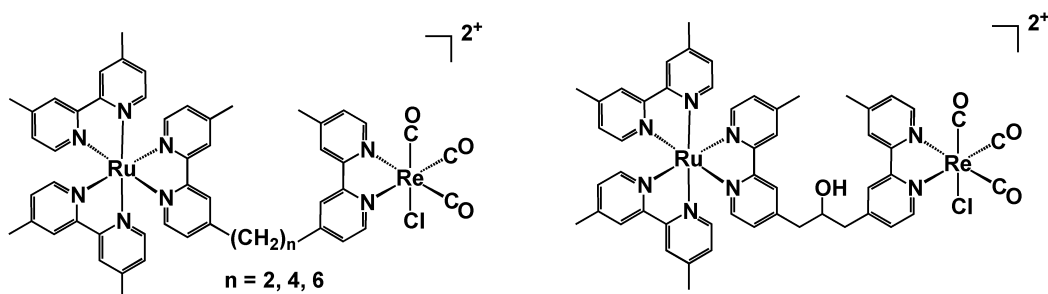
Fig. 14 Supramolecular catalysts synthesized for their varying spacer length.[37]

The absorption and emission spectra and the cyclic voltammograms provided no evidence for ground state communication between the Ru and Re components except for the complex with a C$_2$ spacer. The latter shows a slight red shift in the emission spectrum and in the first oxidation and first reduction potentials. A very weak interaction between Ru and Re sites is postulated in the C$_2$ spacer complex

but not in the C_4 and C_6 spacer dyads. On testing for photocatalytic activity (DMF/TEOA + BNAH, $\lambda > 500$ nm), the C_2 spacer complex was most active exhibiting a turnover number for CO of 180 and a quantum yield of CO formation of 0.13. The C_4 and C_6 spacer catalysts gave a maximum turnover number of 115 and quantum yields of 0.11. The C_3-OH catalyst gave comparable results.

Ueno et al. report the immobilization of rhenium catalysts and ruthenium photosensitizers on the surface of nanotubes.[38] A triple-stranded β-helix fusion protein was assembled and then bioconjugated with maleimide and succinimidyl ester derivatives of the metal complexes (Fig. 15). The best performing system employed the Re and Ru complexes in a ratio of ca. 6:20 and gave a TOF_{co} of 1 h^{-1} (in DMF/MOPS buffer + BNAH, $\lambda > 500$ nm for 15 h). When the catalyst and sensitizer were switched to be in a ratio of 20:6, the TOF_{co} became 0.23 h^{-1}. If the helix was modified with Re and simply mixed with Ru, the TOF_{co} was 0.30 h^{-1}, indicating that attachment of Ru to the helix is necessary for enhanced performance.
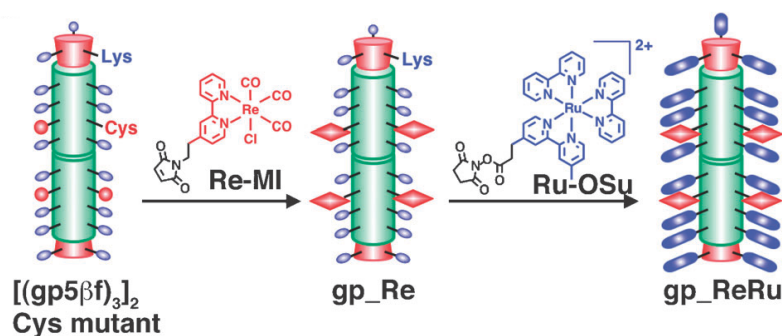
Fig. 15 Bioconjugation of rhenium and ruthenium complexes with a b-helix nanotube.[38]

Hirose et al. designed a series of Ru and Co complexes to be soluble in sc-CO$_2$ by employing bipyridine ligands with long fluoroalkyl chains (Fig. 16).[39] Those with $B[2,3-C_6H_3(CF_3)_2]_4^-$ as a counter-ion were significantly more soluble than those with PF_6^- and introducing an alkoxy functionality on the bipyridine

improved solubility, but aromatic structures decreased solubility. Ruthenium complexes were more soluble than those of cobalt. The complexes that were most soluble in sc-CO_2 were trialed for photocatalytic CO_2 reduction in pure sc-CO_2 (8 mL + 2 mL TEOA, λ = 400-750 nm for 48 h) and in DMF/sc-CO_2 mixtures (5 mL CO_2, 4 mL DMF + 1 mL TEOA). Solubility is a major determinant of activity: the F440Ph complexes gave low activity in pure CO_2 but the best activity of all systems when in CO_2/DMF (27 turnovers at 50 °C and 72 atm). All systems that produced CO also produced H_2, with the most selective being the F620 complex in DMF/CO_2.

F440Ph: Rf = -(CH_2)_4(CF_2)_4F   **F620: Rf = -(CH_2)_2(CF_2)_6F**
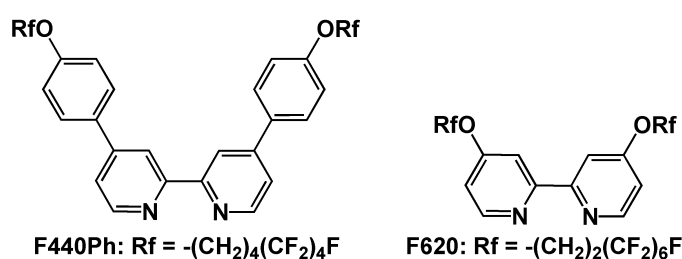
Fig. 16 Fluorinated bipyridines complexed with Ru and Co.[39]

Inoue and co-workers reported the covalent attachment of a zinc porphyrin to a rhenium bipyridine tricarbonyl complex with the aim of CO_2 reduction activity (Fig. 17).[40] The paper is principally concerned with the identification of electron transfer exclusively from the S_2 state of the porphyrin to the rhenium bipyridyl unit. In terms of CO_2 reduction (DMF/Et_3N 5/1, λ = 428 nm for dyad), the dyad has a quantum yield of CO formation of 0.64%, which the authors compare to that of the rhenium-amide fragment at 10.0% (excitation at 364 nm). The rate of charge recombination in the dyad was of the same order as the diffusion-limited rate of porphyrin reduction by Et_3N (1.1 x 10^{10} and 3 x 10^{10} s^{-1}, respectively) whereas the excited state of the rhenium-amide fragment is much longer lived. It is concluded that the fast charge recombination is the reason for the low quantum yield of CO formation in the dyad.
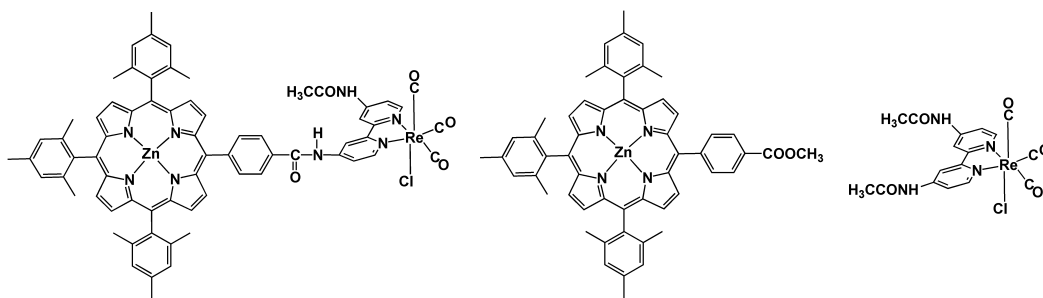
Fig. 17 Zinc porphyrin – rhenium dyad and mononuclear structures investigated by Inoue.[40]

Semiconducting metal oxide materials absorb light in the UV and sometimes in the visible region of the spectrum and have been used successfully in catalytic activation of small molecules. It is therefore unsurprising that there is much interest in the use of metal oxide particles in CO_2 photo-reduction. There are several ways to go about this type of photocatalysis: one is to find a metal oxide composition that itself absorbs light and catalyzes CO_2 reduction; another is to utilize the methodology developed in dye-sensitized solar cell research to anchor Ru and Re complexes to metal oxides. The metal oxide and the anchored complex can play a variety of roles in the overall photoreaction. We confine ourselves here to examples using visible light. Ishitani has made a critical assessment of CO_2 photoreduction with particles.[41]

Sato and co-workers report the use of N-doped Ta_2O_5 as a sensitizer for $[Ru(Bpy)_2(CO)_2]^{2+}$ catalysts (Fig. 18).[42] The investigation aims to act as a proof of concept for charge injection from metal oxide to catalyst with oxides capable of water oxidation. In effect, water should act as the sacrificial electron donor. However, this paper reports CO_2 reduction only in the presence of TEOA as sacrificial donor. The doping of Ta_2O_5 with nitrogen causes a red shift in the absorption spectrum so that wavelengths as high as 520 nm may be employed. On increasing the number of carboxylate groups on Bpy from 0 to 2 to 4, the free energy for electron transfer from Ta_2O_5 to Ru complex changes from -0.3 to -0.4 to -0.5 V, making it more energetically favorable to transfer electrons to

$[Ru(Bpy)_2(CO)_2]^{2+}$. No binding investigations were carried out, but one would expect a greater number of anchoring groups to enhance binding and therefore electron transfer. CO_2 reduction to formic acid was observed with all three catalysts in MeCN/TEOA 5:1 mixture and $410 \leq \lambda \leq 750$ nm. The greatest activity came from [Ru-dcbpy] (Fig. 18) yielding 75% selectivity for formic acid together with H_2 and CO. The authors demonstrate, using isotopic labeling studies, that TEOA is a proton donor as well as electron donor. The plot in Fig. 18 shows that turnover numbers increase with the number of anchoring groups. Should this trend transfer to complexes of other kinds, it serves as a useful investigation for the informed design of future metal oxide anchored systems.
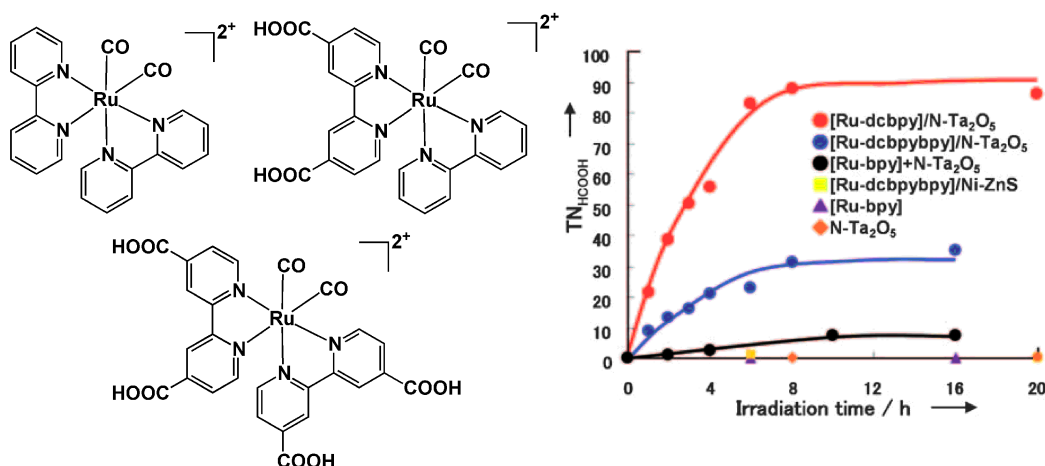
Fig. 18 Ru catalysts on Ta_2O_5 showing formation of HCO_2H on irradiation.[42]

The same group[43] continued to optimize their Ta_2O_5/Ru system by using phosphonate anchoring groups. Ligands with phosphonate groups and their complexes are often difficult to handle due to low solubility. A new strategy for assembly of the complexes on metal oxide particles is reported in which the ligand is adsorbed onto the particle first and then the Ru complex is formed. The system with phosphonate anchors was significantly more active and more photo-stable for CO_2 reduction to formic acid (Fig. 19). The electrochemistry was investigated and the phosphonate catalyst could reduce CO_2 at a less reducing potential than the carboxylate catalyst. The authors suggest that the phosphonate

24

anchors perform better because the free energy for electron transfer from N-Ta_2O_5 to Ru is greater and there is better coupling to Ta_2O_5 through the phosphonate.
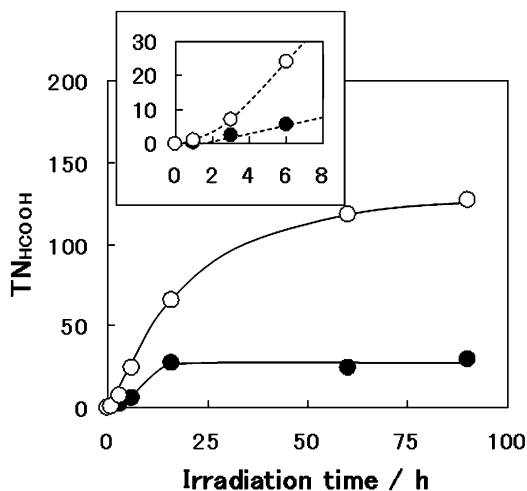
Fig. 19 Catalytic system with phosphonate (o) versus carboxylate (•) anchors. Inset: initial photocatalysis.[43]

Armstrong and co-workers report a photocatalytic and biochemical approach to CO_2 reduction[44, 45], making use of the CO_2 reducing enzyme carbon monoxide dehydrogenase (CODH I) from the anaerobic microbe *Carboxydothermus hydrogenoformans*. This enzyme has a $NiFe_4S_4$ active site in which CO_2 is thought to bridge between nickel and one of the iron atoms, as Ni-C(O)-O-Fe.[46] A $[Ru(Bpy)_3]^{2+}$ photosensitizer was attached to a TiO_2 nanoparticle, which in turn was attached to the enzyme (Fig. 20). The sacrificial electron donor in this case is 2-(N-morpholino)ethanesulfonic acid (MES) and the system absorbs light at 420 nm. In an enzyme system, the metal oxide needs to communicate electronically with the active site. The active site of CODH I is said to be wired to the protein surface by a chain of Fe_4S_4 clusters. Different metal oxides with different morphologies were trialed in more recent studies; binding of the enzyme and sensitizer to the particles was investigated along with variations in light source. The best catalytic system used TiO_2 in a mixture of anatase and rutile forms (3:1), giving a turnover frequency of 0.14 s^{-1} per mol enzyme and a

25

total yield of ca 5 μmol CO after 4 h irradiation. The preference for these materials is attributed to their strong binding with enzyme and photosensitizer and their electronic structure. The conduction band potentials are sufficiently oxidizing to take electrons from the photosensitizer, whilst also being sufficiently reducing to supply them to the enzyme for CO_2 reduction.
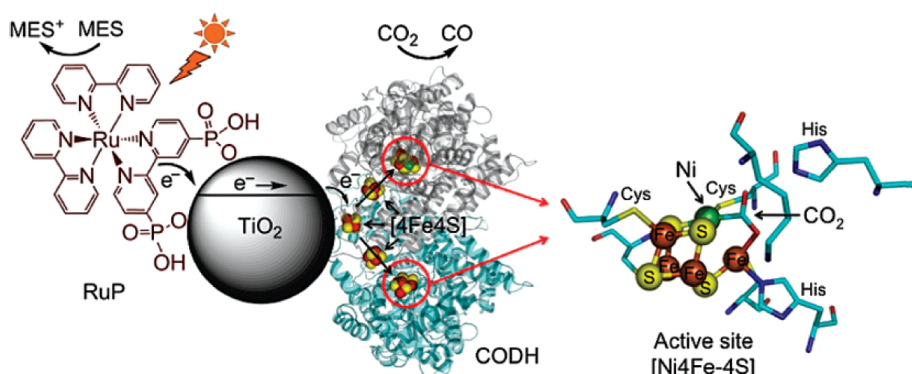
Fig. 20 Ru(Bpy)$_2$(BpyPO$_3$) sensitizes CODH via electron injection into TiO_2. The TiO_2 allows sensitizer and enzyme to be brought together whilst achieving charge separation.[44]

Armstrong et al. also report the attachment of CODH to CdS nano crystals.[47] Since CdS nano crystals can absorb visible light, a separate molecular sensitizer is not required. The best system, that using CdS nano rods, produced a turnover frequency of 1.23 s^{-1} per mol enzyme (in MES buffer, $\lambda > 420$ nm). Other donors and morphologies of CdS were investigated including quantum dots that gave turnover frequencies up to 0.25 s^{-1}. It is suggested that the trend in activity with respect to morphology results from changes in the rate of electron-hole recombination. The best turnover with this system is ca. 200 times greater than that for Ishitani's Ru/Re photo-catalysts on a per mol basis, but it is important to remember that the figures look very different on a per gram basis. In terms of turnover frequency Ishitani's Ru Re dyad [RuRe(P(OEt)$_3$)]$^{3+}$ operates at 0.0065 s^{-1} compared with Armstrong's Ru dye sensitized CODH at 0.14 s^{-1} and the above CODH on nano rods at 1.2 s^{-1}.

In 2013 Ishitani reported an Ir-based CO_2 reduction photocatalyst (CH_3CN/TEOA 5/1, $410 \leq \lambda \leq 750$ nm).[48] The structure is given at the top right of the mechanism in Fig. 21. The catalyst reduces CO_2 selectively to CO under irradiation at $\lambda = 480$ nm. Importantly, compared with rhenium complexes, this catalyst can operate efficiently under visible light irradiation without additional photosensitization and does not lose selectivity in the presence of water. The Ir complex is also an efficient electrocatalyst for CO_2 reduction operating at a relatively low overpotential. Ideal proton mediated CO_2 reduction is at about -0.76 V, ReBpy(CO)$_3$Cl operates at -1.40 V and the Ir catalyst at -1.05 V vs SCE. During photocatalysis, changes in the structure of the complex were observable by UV-Vis and ^{1}H NMR spectroscopy, leading the authors to propose a hydride-bearing intermediate as the active species. Mass spectrometry indicated that when the catalyst becomes inactive species of significantly larger mass are formed; probably Ir dimers. The proposed mechanism is depicted in Fig. 21. The ^{3}MLCT of the complex is reductively quenched by TEOA resulting in a one electron reduced species. Addition of a proton and an electron along with loss of the chloride ligand produces the hydride complex. This also absorbs light and is reductively quenched to produce a one electron reduced species that can react with CO_2. The CO_2 adduct receives an electron from another molecule of the one electron reduced hydride. CO is released and the hydride regenerated by addition of an electron and a proton. The TEOA is proposed as a proton source. More mechanistic work is underway. Addition of electron donating CH_3 groups to the phenylpyridine ligand and electron withdrawing CF_3 groups caused an increase and decrease in photocatalytic CO production respectively (Fig. 22).
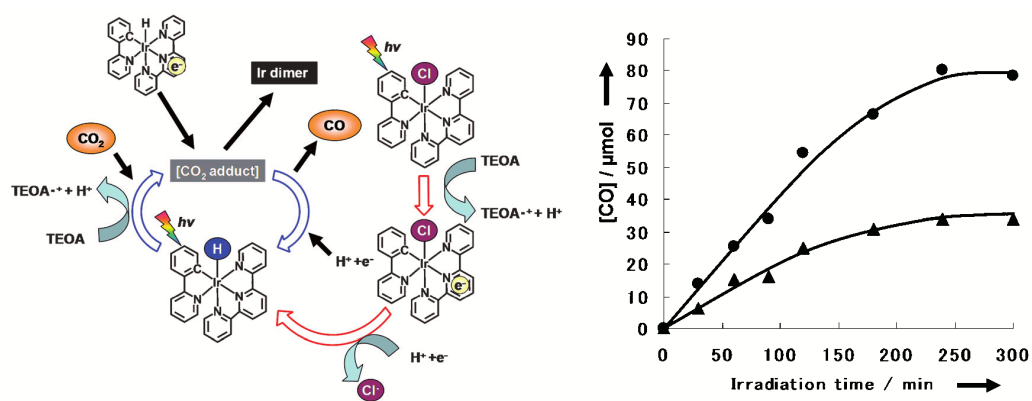
Fig. 21 Ishitani and co-worker's Ir photocatalyst for CO$_2$ reduction. Left: Proposed mechanism. Right: CO production for Ir catalyst in CH$_3$CN/TEOA 5/1 (circles) and ReBpy(CO)$_3$Cl DMF/TEOA 5/1 (triangles) both under 410≤ λ≤750 nm.[48]
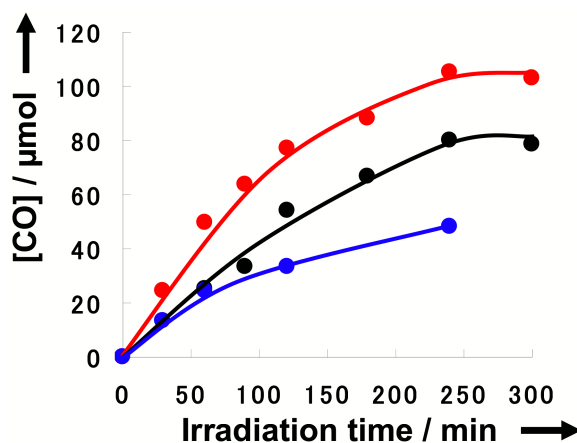
Fig. 22 CO production of the mononuclear Ir catalysts developed by Ishitani and co-workers. Red: Me on the phenylpyridine. Black: simple phenylpyridine. Blue CF$_3$ on the phenylpyridine.[48]

Ishitani published again in 2013 with a system capable of tandem CO$_2$ reduction to formic acid and methanol oxidation to formaldehyde.[49] A Ru-Ru dyad, one Ru centre for CO$_2$ reduction and one for light absorption, was anchored via phosphonic acid functionalities onto TaON particles loaded with Ag (Fig. 23). Irradiation of 24 nmol of complex on 8 mg of particles with λ > 400 nm in

methanol under an atmosphere of CO_2 gave 41 turnovers of HCOOH. Some CO and H_2 was produced along with formaldehyde. The moles of formaldehyde produced was similar to the total moles of HCOOH, H_2 and CO. $^{13}CO_2$ produced almost entirely $H^{13}COOH$. Use of $^{13}CH_3OH$ produced $H^{13}CHO$. Light is absorbed by the $[Ru(Bpy)_3]^{2+}$ unit, the TaON and the Ag. Analysis of the band potentials of the TaON along with cyclic voltammetry and emission spectra of the molecular dyad unit allowed the authors to conclude that electron transfer can proceed from the conduction band of the TaON to the sensitizer unit either in the photo-excited state or the one-electron oxidised state. This strongly suggests that photocatalytic CO_2 reduction requires excitation of both the sensitizer of the molecular dyad and the TaON. The proposed mechanism is depicted in Fig. 23. Light is absorbed by TaON and the holes generated in the valence band oxidise methanol. Absorption of light by the $[Ru(Bpy)_3]^{2+}$ unit either leads to charge separation, reducing the catalytic Ru centre and leaving the $[Ru(Bpy)_3]^{2+}$ oxidised, or the $[Ru(Bpy)_3]^{2+}$ remains excited. Either state can receive an electron from the TaON. If the excited state received the electron an intramolecular electron transfer occurs to produce the one-electron reduced Ru catalyst unit. CO_2 reduction to formic acid requires two electrons so the authors propose that stepwise two photon absorption occurs at the $[Ru(Bpy)_3]^{2+}$ unit. An induction period was observed for HCOOH formation but not for formaldehyde production. This is explained as the requirement for accumulation of electrons in the conduction band of TaON before excitation of the $[Ru(Bpy)_3]^{2+}$.
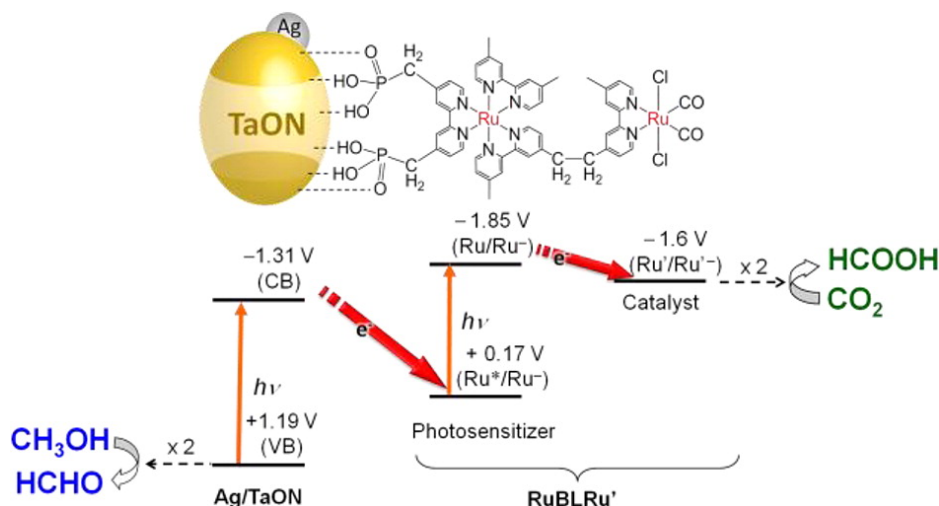
Fig. 23 Ishitani and colleagues' system that oxidizes methanol to provide electrons for tandem CO_2 reduction. Both particle and sensitiser $[Ru(Bpy)]^{2+}$ unit absorb light.

1.2.3 CO_2 reduction mechanism of $Re(Bpy)(CO)_3X$

Lehn put forward mechanistic detail in the original paper reporting the discovery of ReBpy(CO)$_3$X complexes as CO_2 reduction photocatalysts.[8] Visible light absorption generates a Re^I excited state, which is reductively quenched by TEOA. A Re^0 ground state is formed with a redox potential reducing enough to convert CO_2 to CO. A free co-ordination site is created by the loss of X allowing CO_2 to bind to the Re centre but the authors do not rule out loss of co-ordination of one N of the Bpy. There was no further explanation beyond this point except that scrambling of the carbonyls on the Re was evident from $^{13}CO_2$ studies and a ReBpy(CO)$_3$(O$_2$CH) species was isolated and characterised.

1986 saw Lehn follow up the previous mechanistic investigations.[16] Irradiation of ReBpy(CO)$_3$Cl with $\lambda > 400$ nm in the typical DMF/TEOA solution without CO_2 resulted in bleaching of the solution due to loss of the bipyridine (observed with ^{13}C NMR and UV spectroscopy). Bleaching does not occur in the presence of CO_2 and the authors conclude that irradiation generates a reduced complex, which reacts immediately with CO_2 and returns the original compound. The

chloride complex was more efficient than the bromide analogue. Additional Bpy did not improve stability and neither did the addition of Br⁻ to the bromide catalyst. However, Cl⁻ added to the chloride catalyst solution gave a significant improvement in efficiency and stability. The introduction of Br⁻ to the chloride catalyst (DMF/TEOA) resulted in a mixture of halide complexes under light but not in the dark. Cl⁻ added to the bromide catalyst gave a mixture of complexes both in light *and* in the dark further supporting the idea that the chloride catalyst has greater stability. Ligand exchange occurred more readily with light and TEOA and so the authors conclude that the reduced complex [Re(Bpy)(CO)$_3$X]⁻ is more reactive. The carbonyl ligands appeared quite stable as no free CO was present after irradiation without CO_2, also under an atmosphere of ^{13}CO with or without light saw no exchange (TEOA absent).

NMR experiments of the chloride complex under $^{13}CO_2$ in (D$_7$)DMF/TEOA with irradiation showed exchange of the CO, generation of a formate complex and that TEOA is oxidised to 2-hydroxyethanol and iminodiethanol. When excess Cl⁻ was added the formate complex was not observed. The formate complex was isolated and characterised as monodentate by X-ray crystallography and IR spectroscopy. An authentic sample of the formate complex was synthesised and tested for CO_2 photoreduction. The activity was half that of the chloride complex but comparable on the introduction of Cl⁻ to the solution; the authors conclude that the active species must be the same in both systems. Adding HCOO⁻ to either the chloride or formate complex solutions inhibited CO_2 production. For the formate complex to be an intermediate the formate ligand must be replaced by CO_2 to give CO, but only traces of CO were produced. The authors showed that Cl⁻ can substitute formate even in the dark and so additional Cl⁻ prevents build-up of formate complex, which is substantially less active for CO_2 photoreduction. The full cycle is given in Fig. 24.
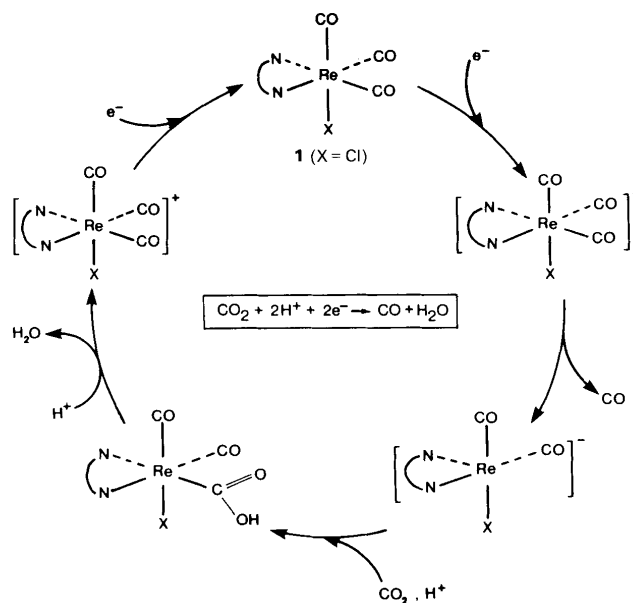
Fig. 24 Mechanism propsed by Lehn and co-workers 1986. Note there was no direct evidence for $[Re(Bpy)(CO)_3Cl]^+$.[16]

Ishitani reported a photophysical study combining flash photolysis with time resolved infrared spectroscopy on his $[ReBpy(CO)_3\{P(OEt)_3\}]^+$ catalyst.[29] Excitation ($\lambda = 308$ nm) causes the CO stretches to shift to higher wavenumber, indicative of oxidation of the Re via an MLCT transition. The lifetime of the excited state of the complex was five times longer than that with X = Cl (250 ns vs 50 ns respectively). The excited state of the rhenium was quenched by TEOA to produce a one electron-reduced complex with the electron localised on the Bpy. It was concluded that the first step in the photocatalytic process is electron transfer from TEOA to the ^{3}MLCT state. The one electron reduced (OER) phosphite complex was much more stable than that of the chloride complex and was accumulated in solution even under a CO_2 atmosphere. The OER would undergo a dark reaction with CO_2 but did not produce CO. Further irradiation was required and an induction period was observed prior to catalytic CO production.

In a spectroelectrochemical investigation into electrocatalytic CO_2 reduction Turner and co-workers discussed their results[50] in comparison with contemporary

findings by others[51, 52] and showed that the [ReBpy(CO)$_3$Cl]$^{\bullet-}$ does not react directly with CO_2 but that the chloride ligand is lost. The result, when working in CH$_3$CN, is [ReBpy(CO)$_3$(CH$_3$CN)] which can undergo a second reduction at a very similar potential to the first, to produce a mixture of [ReBpy(CO)$_3$\{CH$_3$CN\}]$^-$ and [ReBpy(CO)$_3$]$^-$. CO_2 attacks [ReBpy(CO)$_3$]$^-$ and is reduced via what is termed the two electron pathway. Intriguingly the Re(Me$_2$Bpy)(CO)$_3$Cl complex forms dimers in CH$_3$CN solution and cannot reach [Re(Me$_2$Bpy)(CO)$_3$]$^-$ without more negative potential. A two-electron pathway for the Me$_2$Bpy complex was ruled out but the origin of the second electron is not understood for the one electron pathway. The authors suggest that a CO_2 adduct could form and is reduced by a second electron and that the CO_2 adduct was not observed spectroscopically because the second reduction is very fast.

1997 saw Ishitani publish[53] an investigation into the spectroscopic properties and reactivities of the OER species of various rhenium complexes with different X ligands and substituents on the Bpy (Fig. 25). The first finding of note is that complexes **13$^+$**, **14$^+$** and **19$^+$** show no catalytic ability. All the complexes emitted from the ^{3}MLCT at room temperature and the emission was totally quenched in DMF/TEOA 5/1 solution. The OER of these complexes was readily observable by UV-Vis spectroscopy. Fig. 26 a) shows growth of the OER (**18**) during photolysis and Fig. 26 b) corroborates this assignment by displaying the UV-Vis spectrum during electrolysis. The OER produced via electrolysis was characterised by IR spectroscopy. Complexes **13-17** and **19** also produced an OER species in high yield. The remarkable observation that the quantum yield of formation of **18** was 2 was explained by the oxidation of TEOA producing TEOA$^{\bullet+}$, which is capable of reducing another molecule of **18$^+$**. Due to accumulation of the OER species in solution, formation of the OER must be much faster than the processes of its decomposition. The authors also conclude that differences in the ligand only have minor effects on the rate and yield of OER production.
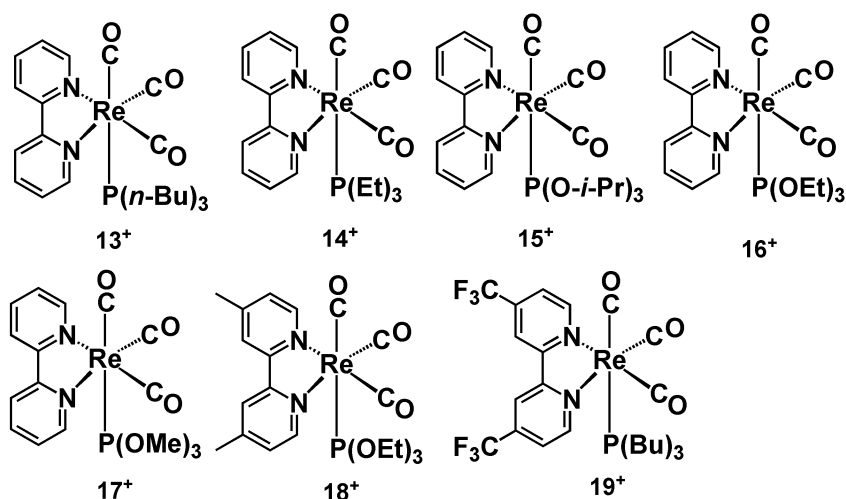
Fig. 25 Rhenium complexes with varying substituents on the Bpy and X ligand.
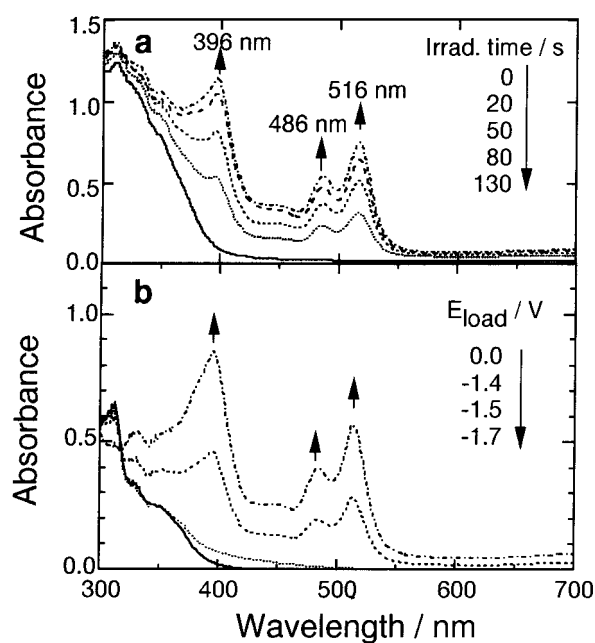
Fig. 26 UV-Vis spectra of a) 18^+ during irradiation in DMF/TEOA 5/1 (365 nm) under CO_2 b) 18^+ during electrolysis in CH_3CN.[53]

Once formed, the stability of the different OER complexes differed and correlated with activity; the OERs **13**,**14** and **19** were extremely stable (degassed solution, in the dark), whereas the others decomposed. The decay kinetics of these other complexes was second order and the rate of decay increased when

CO_2 was introduced. However, degassed or under CO_2 the second order rate constant was essentially the same. The authors conclude that the reaction under CO_2 in the dark has two processes, (1) of the OER with CO_2 and (2) between two OER species, which does not include CO_2. Two different reactions were proposed (Fig. 27). The authors assumed that each produces CO quantitatively and then calculated the yield of CO with respect to time by analysing the growth and decay of the OER, which was fitted with the observed yields of CO. No correlation was seen between process 2 and the observed yields but the calculation for process 1 gave approximately double the real yield of CO. The authors conclude that the OER reacts with CO_2 and a disproportionation pathway between two intermediate Re species gives one molecule of CO. Through consideration of the change in the electronics of the Re centre on alteration of the X ligand and considering the results of others it is also concluded that the reaction with CO_2 proceeds via a dissociative mechanism i.e. the ligand is lost and the coordinatively unsaturated complex reacts with CO_2.

(1) $[Re(Me_2Bpy^{-\bullet})(CO)_3\{P(OEt)_3\}] + CO_2$ $\xrightarrow[\text{dark}]{K_1}$ $\xrightarrow{\quad}$ CO

(2) $2[Re(Me_2Bpy^{-\bullet})(CO)_3\{P(OEt)_3\}]$ $\xrightarrow[\text{dark}]{K_2}$ $\xrightarrow{\quad}$ CO
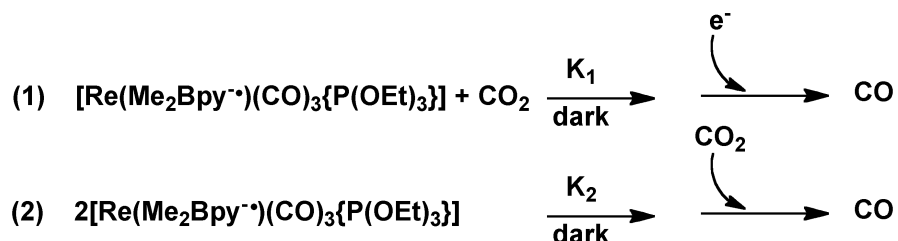
Fig. 27 Proposed reaction pathways between OER and CO_2.[53]

A decade on Ishitani[54] provided more evidence of a dissociative mechanism. Rhenium complexes with a Cl^- or SCN^- ligand are active for CO_2 reduction whereas those with CN^- are not, yet all are very similar with respect to OER formation. CN^- cannot photo-dissociate from Re. Furthermore, adding excess SCN^- to the reaction solution of $[ReBpy(CO)_3SCN]$ significantly increases the quantity of the OER $[ReBpy(CO)_3SCN]^{-\bullet}$ but does not cause an increase in the yield of CO. By invoking investigations by Fujita[55, 56] where $[ReBpy(CO)_3]^{-\bullet}$ is shown to rapidly produce the solvento complex (in THF, CH_3CN), the authors

conclude it is $[ReBpy(CO)_3S]^{\bullet-}$ (S = DMF or TEOA) that reacts with CO_2. The solvento complex itself is not active for CO_2 photoreduction as the excited state lifetime is too short lived to be photochemically reduced by TEOA therefore the parent Cl^- or SCN^- complex must be regenerated. The ability of the ligand to both dissociate and re-coordinate is important; the SCN^- complex is more active than the Cl^- complex and the authors showed the coordination ability of Cl^- is lower than SCN^-.

A rhenium dimer bridged by CO_2 and $[ReBpy(CO)_3(COOH)]$ have been put forward as intermediates immediately prior to CO formation.[34] NMR studies under $^{13}CO_2$ showed that all the carbonyl ligands became ^{13}CO and so the CO of the bridging CO_2 or COOH is not simply ejected. The SCN^- complex is much more active for CO_2 reduction than the Cl^- complex. SCN^- does not dissociate as readily as Cl^- and much more of the OER of SCN^- accumulates in solution, therefore accumulation of the OER $[ReBpy(CO)_3SCN]^{\bullet-}$ must be adventitious even though $[ReBpy(CO)_3]^{\bullet-}$ is thought to be the species that eventually reacts with CO_2. The six coordinate OER acts as electron donor to the as yet unobserved CO_2 adduct thus providing CO_2 with the second electron required to produce CO (Fig. 28).
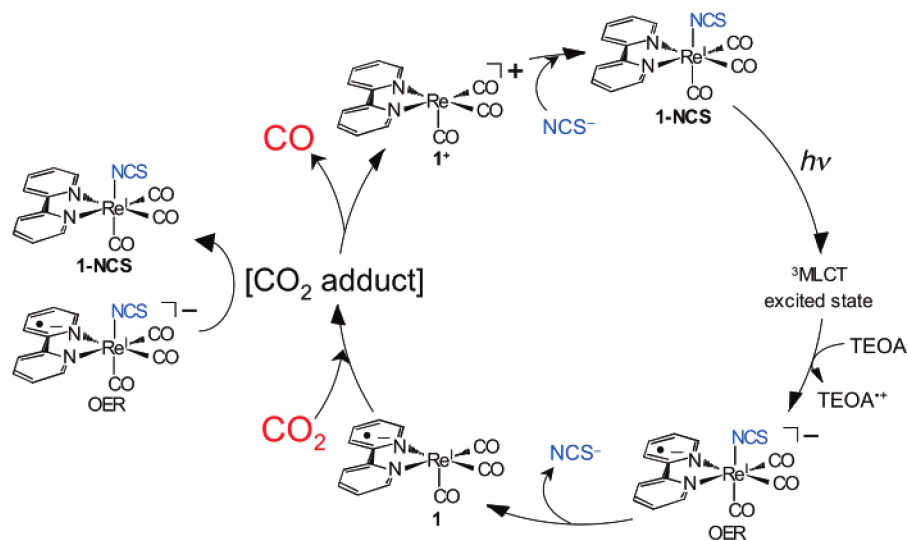
Fig. 28 CO$_2$ photoreduction mechanism for ReBpy(CO)$_3$X type complexes by Ishitani in 2007.[54]

Observing species in the photoreaction mixture is difficult due to the large excess of TEOA and TEOA oxidation products. Fujita and co workers combined DFT calculations with experimental observations using a simplified system.[34, 55] A Re–Re dimer was photocleaved to produce the coordinatively unsaturated OER [Re(Me$_2$Bpy)(CO)$_3$]$^{\bullet}$ so that the only species present at the start are the OER, CO$_2$ and solvent (Fig. 29). Several species were observed in CO$_2$ saturated DMF; CO, [Re(Me$_2$Bpy)(CO)$_3$]$_2$(OCO$_2$), Re(Me$_2$Bpy)(CO)$_3$(OCO$_2$H) and [Re(Me$_2$Bpy)(CO)$_3$]$_2$(C(O)O). The latter, a long-lived intermediate, decomposed to produce CO.
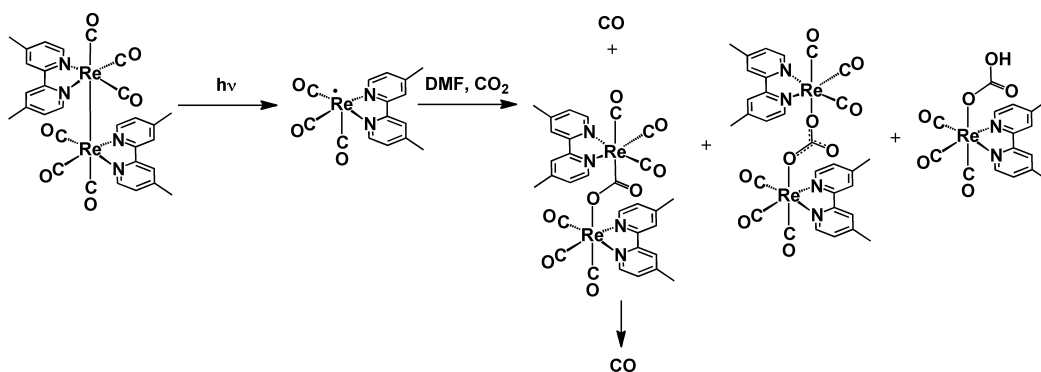
Fig. 29 A simplified system: photocleavage of Re-Re dimer and introduction of DMF and CO_2.[34]

In the subsequent publication utilising DFT (Fig. 30) the dimer species **22** forms via combination of two molecules of the OER and one of CO_2; entropically unfavourable but exothermic. A second molecule of CO_2 may insert into the oxygen-rhenium bond of **22** to give **TS25**, the activation barrier to this process is lower than the alternative, isomerisation via **TS23** to **24**. **TS25** leads into **26**, which is a local minimum. From **26** a rhenium centre migrates from the carbon of the first CO_2 to the oxygen of the second CO_2, thus breaking a carbon-oxygen bond and yielding CO. The dimer **28**, bridged by carbonate, remains. The entire process from **22** through to **28** is endothermic by 5.9 kcal mol^{-1}. In the corresponding experimental work[55] (here diimine ligand Me$_2$Bpy) a long lived CO_2 bridged intermediate is observed, analogous to **22**. Insertion of the second CO_2 has a high barrier, backed up by observation of a slow reaction rate 0.003 s^{-1}. Decay of the CO_2 bridged dimer was first order with respect to CO_2, agreeing with the proposed insertion of a second molecule of CO_2. Experiment showed that only ^{13}CO was produced, this also discounts the isomerisation pathway, which would allow for dissociation of unlabelled ^{12}CO. The DFT investigation is a valuable step forward but it does not deal with regeneration of the original catalyst (a necessary artefact of starting by photocleavage of dimer) and, by stopping at **28**, does not account for previous observations that all carbonyl ligands become labelled when using $^{13}CO_2$.[8] An additional drawback of this work is the comparison against experimental observation with the Me$_2$Bpy

complex. In other circumstances this may be considered a reasonable model but previous investigations suggest Me$_2$Bpy complexes can operate by a quite different mechanism to that of the Bpy complexes.[50] In the context of [Ru(Bpy)$_3$]$^{2+}$ and porphyrin sensitized rhenium systems[32, 57], in which the catalyst is present at 0.05 mM, the theory that two rhenium centres bridge is bold.
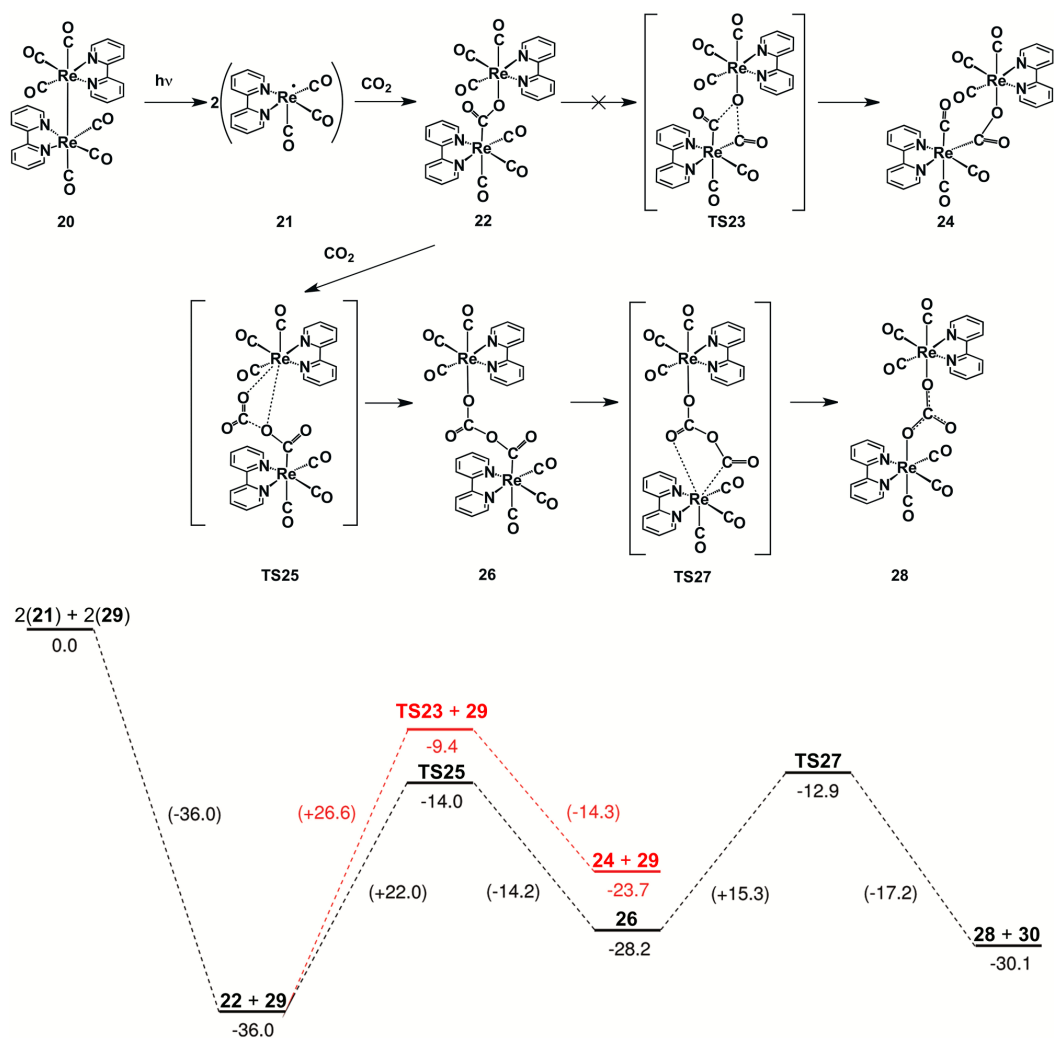
Fig. 30 Proposed mechanistic scheme (above) and standard enthalpy profile (below). Energies in kcal mol^{-1}.[34]

Kubiak and co-workers address the latter stages of the catalytic mechanism with an investigation into tetracarbonyl complexes.[58] A mechanism was proposed in

which CO_2 binding and successive proton and electron transfers results in a $ReBpy(CO)_4^+$ complex. Two successive reductions stimulate CO loss, regenerating the five-coordinate anion ready for another catalytic cycle. The tetracarbonyl complex was synthesized and cyclic voltammetry under N_2 in the reductive direction showed a small irreversible wave followed by two larger quasi-reversible waves. Under CO_2 the most negative wave lost reversibility and exhibited a current increase; both changes consistent with catalysis. Infrared spectroelectrochemistry indicated that $ReBpy(CO)_3CH_3CN^+$ is formed, not via stoichiometric reduction but by a reduction catalyzed process. This was also achieved by chemical reduction demonstrating that the process is inherent to the molecule and does not require the electrode. Further reduction produced species assigned to $[ReBpy(CO)_3CH_3CN]^0$ and $[ReBpy(CO)_3CH_3CN]^{-1}$.
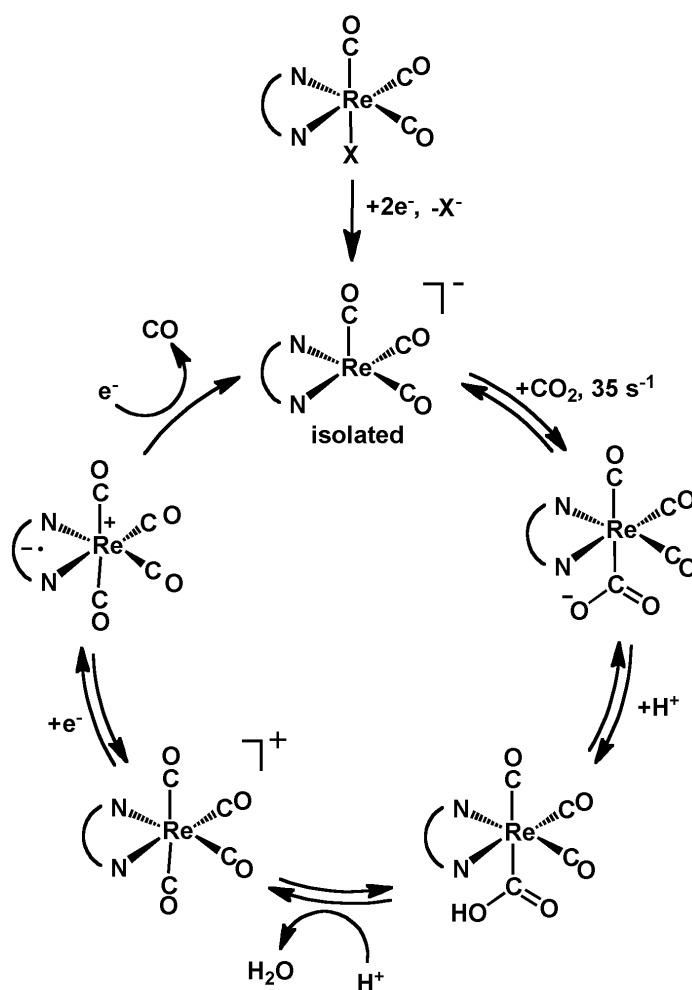
Fig. 31 Overall electrocatalytic cyclic from data by Kubiak and co-workers.[58] The mechanism could be relevant to electron supply by metalloporphyrins if it is analogous to electron supply by an electrode.

In 2013 Kubiak published an in depth investigation into the structural and electronic relationship between rhenium catalysts and activity.[59] Particular attention was a paid to the anions $[ReBpy(CO)_3]^-$ as these react 35 times faster with CO_2 and are considered to be the active species that engages CO_2. This is counter to the photocatalytic mechanisms put forward so far. A range of rhenium complexes was investigated, some with Bpy and some without. IR spectroscopy showed that the two electron reduction of a Re complex containing Bpy had a much smaller effect on the electron density at the Re than a complex without

Bpy. This indicates that the Bpy stores a significant amount of electron density. X-ray absorption spectroscopy showed the metal centre in one electron reduced rhenium species has very similar electronic states to that of two electron reduced species. A very similar amount of electron density sits on the Re in one- and two-electron reduced complexes. DFT calculations agreed with this and indicated that the HOMO of the anion is delocalized across both the Re centre and the Bpy. As a simplification it is best to view the ground states of the doubly reduced anion as $Re^0(Bpy^-)$. The authors use this to explain the selectivity for rhenium catalysts towards CO_2 reduction over the more energetically favourable H^+ reduction. The $Re^0(Bpy^-)$ formalisation puts an electron in the Re dz^2 and one in the Bpy π^*, reduction of CO_2 gives both σ and π interactions whereas H^+ can only give σ. The d_z^2 orbital can form a σ bond to the carbon atom of CO_2 (HOMO). The interaction with CO_2 is further stabilized by a π interaction of the metal d_{xz} and d_{yz} orbitals with p orbitals on the CO_2 oxygen atoms.[60] This stabilizing interaction is not available for H^+. The authors also suggest that this provides a lower reorganization energy for transferring two electronic charges. Much of this work was based on the assumption that the anions are five coordinate in solution, as identified by XRD in the solid state.[61] EXAFS was used to indicate that the anions remain five co-ordinate in solution and neither coordinate solvent (THF) nor form dimers.

1.3   Excited state redox potentials

It is possible to calculate an estimate of the free energy change of a photo-redox reaction if one knows the ground state oxidation potential of the electron donor, the ground state reduction potential of the electron acceptor and the highest energy emission maximum of the photoexcited species. In 1970 Rehm and Weller developed an expression for the free energy change ΔG based on these terms (Equation 1). The assumption is made that structural changes occurring with electron transfer are negligible and entropy changes are neglected in the calculation of overall free energy changes.

$$\Delta G = E_{ox} - E_{red} - E_{00}$$

Equation 1 The relationship between the free energy change of electron transfer (ΔG) and the ground state oxidation and reduction potentials of donor and acceptor (E$_{ox/red}$) and the highest energy emission maximum of the absorbing species (E$_{00}$).

Equation 1 was used to calculate the free energy change of electron transfer from the photoexcited metalloporphyrin species to the rhenium complexes investigated herein. The emission spectra were taken of the porphyrin and cyclic voltammetry was used to obtain the redox potentials for both complexes. This was performed for both the two component systems and the dyads. Calculations were also performed for the driving force of electron transfer from zinc tetraphenyldihydroporphyrin to the rhenium complexes.

1.4   Photocatalysis and electron transfer

1.4.1   Photocatalysis

The term 'photocatalysis' is quite broad and encompasses reactions that require both light and a catalyst. The catalyst is active in a thermal sense but may also affect the free energy balance of a process due to the involvement of electronically excited species.[62] The photon may be absorbed either by the catalyst or the substrate (catalysed photoreactions). A reaction can be defined as photocatalytic if it follows the inequality in Equation 2.[62] Here ΦS is the quantum yield of substrate consumption and ΦU is the quantum yield of the photoreaction in the absence of catalyst.

$$\phi S > \phi U$$

Equation 2 Definition for a reaction to be considered photocatalytic. ΦS is the quantum yield of substrate consumption and ΦU is the quantum yield of the photoreaction in the absence of catalyst.[62]

In a less general sense the photocatalysis of CO_2 reduction typically occurs via light absorption by the catalyst. In this case the catalyst can bring the light energy together with the reactants because it becomes simultaneously a stronger reductant and a stronger oxidant. Therefore the light energy allows the catalyst to oxidise one substrate and reduce another (Fig. 32). More specifically, two TEOA molecules are oxidised and one CO_2 molecule is reduced.
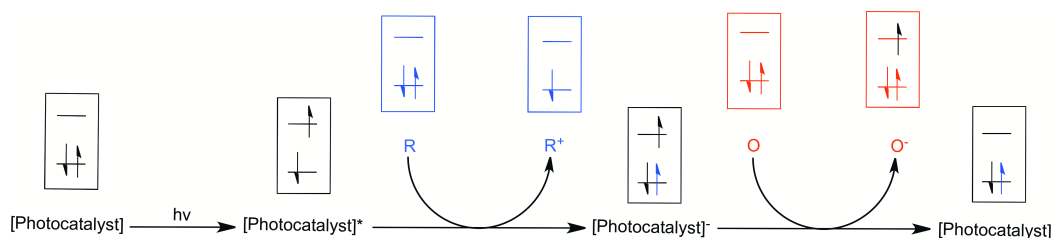
Fig. 32 The photocatalyst absorbs light, receives an electron and then donates an electron. Oxidation may happen prior to reduction.

If it is desirable to promote a reaction with light that a catalyst cannot absorb then a sensitiser may be utilised. In this case the sensitiser absorbs the light and transfers the energy or an electron to the catalyst. If an electron is transferred then the sensitizer must be involved in the electron transfer chain. In the context of CO_2 reduction sensitised catalysis the sensitiser now oxidises TEOA (sometimes BNAH) and the catalyst reduces CO_2.

1.4.2   Electron transfer

Marcus theory of electron transfer is concerned with outer-sphere reactions, in which the interaction of the electronic orbitals is weak, as this is generally

simpler. The reactants must come together and so the various co-ordinates of the molecules are crucial. These include vibrational coordinates of the reactants and orientational co-ordinates of the solvent. The potential energy of the reactants and solvent molecules is a function of these thousands of nuclear co-ordinates, generating a many-dimensional potential energy surface. Typically a one-dimensional profile is used to illustrate the theory (Fig. 33).
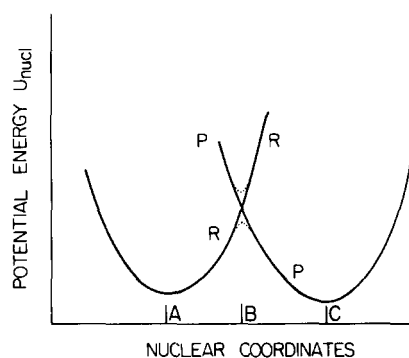
Fig. 33 One dimensional potential energy surface for reactant and product. R= reactants, P = products.[63] Dotted lines show splitting due to electronic interaction of reactants. A and C are nuclear coordinates at equilibrium for R and P respectively and B is the nuclear configuration at the intersection of the surfaces.

The mass of an electron is very low compared with the mass of the nucleons and so the Franck-Condon principle is applied. As a result, electron transfer will only occur when the nuclear configuration of the reactants and surrounding medium is the same as that of the products and surrounding medium. This is represented by the intersection of the two curves in Fig. 33. Thermal fluctuations of the co-ordinates from the minimum of R are required to access the crossing point. It is also necessary to consider the fluctuations in vibrational coordinates if the reactant has different equilibrium bond lengths or angles to the product. If the solvent is polar, the orientational coordinates must also be accounted for.

Once the nuclear coordinates of the intersection have been achieved, the probability of going from R to P depends on several factors including the

coupling of the orbitals of the reactants which itself depends on the separation of the reactants (r). Electronic motion must also be considered and is illustrated in relation to the nuclear coordinates in Fig. 34. Figure a) represents the electrons in the two reactants (1 and 2) at their equilibrium energy levels. Thermal fluctuations occur in the coordinates of the nuclei and in b) positions of the electronic-energy levels are the same, this corresponds to the intersection of the nuclear potential energy curves. Figure c) illustrates the result after further fluctuations resulting in the energy levels being at equilibrium for the products.
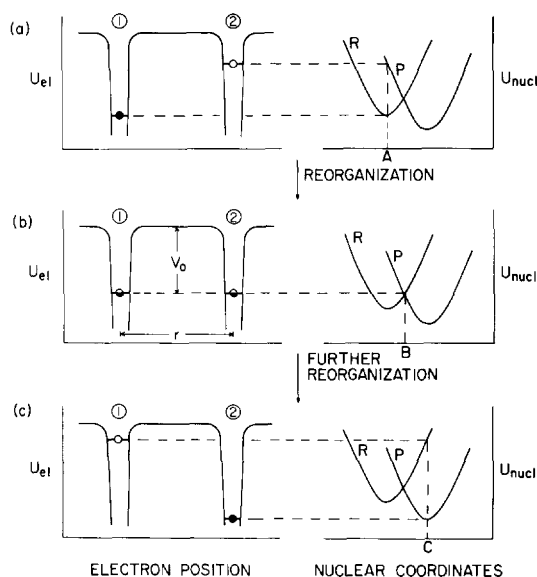
Fig. 34 Electronic potential energy curves (left) and corresponding nuclear potential energy curves (right).[63]

The averaged transition probability for electron transfer through the intersection region is termed the transmission coefficient and is denoted by $\kappa(r)$. Where r is a fixed separation distance of the two reactants. For a system where there is substantial electronic coupling between reactants (adiabatic) κ is unity.

In order to calculate the rate constant for an electron-transfer reaction occurring, one must calculate the probability of reaching the intersection multiplied by the frequency for crossing the intersection and by the probability of the transition

from R to P. The result is Equation 3 where k is the rate constant for a bimolecular electron transfer reaction.

$$k = \kappa A \sigma^2 \exp(-\Delta G^*/RT)$$

Equation 3 $A\sigma^2$ is the collision frequency, σ is the average centre-to-centre distance of the reacting pair during electron transfer and ΔG^* is the free energy of activation.

Marcus took this one step further by producing Equation 4 for the calculation of ΔG^{*}.[64] For a reaction to be thermodynamically allowed it is necessary for the reorganisation energy, λ, to be greater than zero and the standard reaction energy, $|\Delta_r G^\theta|$, to be less than zero; λ > 0 and $\Delta_r G^\theta$ < 0. Therefore, using Equation 4 and provided $|\Delta_r G^\theta| << |\lambda|$, then the rate constant increases exponentially as $\Delta_r G^\theta$ becomes increasingly favourable (i.e. more negative). However, if $|\Delta_r G^\theta|$ is comparable to $|\lambda|$ the equation begins to break down and the reaction rate peaks before declining as $|\Delta_r G^\theta| > |\lambda|$. When $\Delta_r G^\theta = -\lambda$, $\Delta G^* = 0$ and the reaction is activationless. At subsequently more negative values of $\Delta_r G^\theta$ the activation energy increases; in this case the rate of the reaction falls as it becomes more exergonic. This is termed the 'inverted region'. A plot of the $\log_{10}$ of the reaction rate vs $\Delta_r G^\theta$ for a theoretical redox reaction with λ = 1.0 eV produces a curve illustrating the growth, peak and decline in reaction rate as the standard reaction energy becomes more negative (Fig. 35).

$$\Delta G^* = \frac{1}{4}\lambda\left(1 + \frac{\Delta_r G^\theta}{\lambda}\right)^2$$

Equation 4 The Marcus equation for calculating the free energy of activation for outer sphere electron transfer. ΔG^* is the free energy of activation, λ is the re-organisation energy and $\Delta_r G^\theta$ is the standard reaction Gibbs energy.[64]
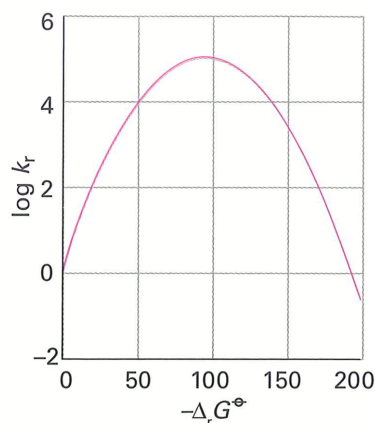
Fig. 35 Log_{10} of the reaction rate vs the standard reaction energy ($\Delta_r G^\theta$) in kJ mol^{-1} for a theoretical redox reaction with a re-organisation energy (λ) of 1.0 eV.[64]

1.4.3 Examples of photoinduced electron transfer

Sauvage and co-workers synthesised a series of Ru-Rh dyads with a variable number of *p*-phenylene spacers (Fig. 36).[65] The Ru unit is the electron donor and the Rh unit is the electron acceptor. In these systems energy transfer is energetically forbidden whereas electron transfer is thermodynamically allowed. Ru(II) terpyridine complexes exhibit sub-nanosecond excited state lifetimes. A model complex of the Ru unit, with two identical terpyridine ligands possessing a tolyl group on the central pyridine, exhibited an emission lifetime of 860 ps. The dyad emission lifetimes were 17 ns, 240 ps and 1.9 ns for n= 0, 1 and 2 respectively. Discussion of dyad n=0 is separated from n = 1 and 2 due to a significant difference in intercomponent coupling. The difference between n=1 and 2 was attributed to a decrease in electron transfer rate due to the increased distance between donor and acceptor. For n=2 electron transfer cannot compete with deactivation of the MLCT excited state. Interestingly the authors compare these results with a Ru-Rh dyad with an ethylene bridge, where the distance between donor and acceptor is smaller than for the n=1 dyad but electron transfer rates are lower; the nature of the bridge bears great importance. For the dyad n=0 there is a much stronger metal-metal electronic coupling as signalled by a red

shift of the Ru unit absorbance and emission compared with the mononuclear model. As such, and along with the drastically different emission lifetimes, the Ru model was deemed unsuitable and the n=0 dyad was compared instead with a Ru-Ru dyad. It was concluded that the Ru-Rh emission lifetime for n=0 was long because of the presence of overlapping emissions from two types of excited states in fast thermal equilibrium.
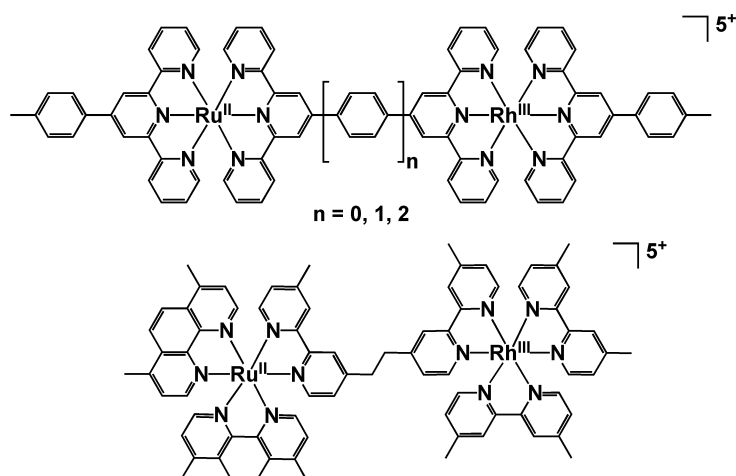
Fig. 36 Ru-Rh electron transfer systems studied by Sauvage and co-workers. Dyad n=1 exhibits a faster electron transfer rate (3.0×10^9 s^{-1}) than the ethylene spacer dyad below (1.7×10^8 s^{-1}).[65]

Sauvage, Harriman and co-workers investigated Zn porphyrin – Au porphyrin dyads for electron transfer (Fig. 37).[66] The Zn porphyrin fluorescence is quenched by 97% in the presence of the Au porphyrin. Selective excitation of the Zn porphyrin lead to the excited singlet state, which decayed rapidly to give a charge separated state with a lifetime of 600 ±40 ps. The authors prefer to call this a 'charge shift' as the cationic Au centre becomes neutral and the Zn centre goes from neutral to cationic. Excitation at 532 nm where absorbance is dominated by the Au porphyrin led to the Au porphyrin triplet excited state. This decayed with a lifetime of 120 ±10 ps to give two products. The shorter lived product is the charge separated state, which decays in 570 ± 30 ps due to charge recombination. The longer-lived product is the Zn porphyrin triplet state formed

by energy transfer. The authors conclude that both singlet and triplet excited states of the Zn porphyrin are electron donors. The Au porphyrin undergoes quantitative intersystem crossing to the triplet state and this is the electron donor. The consequence is that virtually every photon absorbed by the bisporphyrin results in charge transfer.

$$M_1 = Au; \quad M_2 = Zn$$
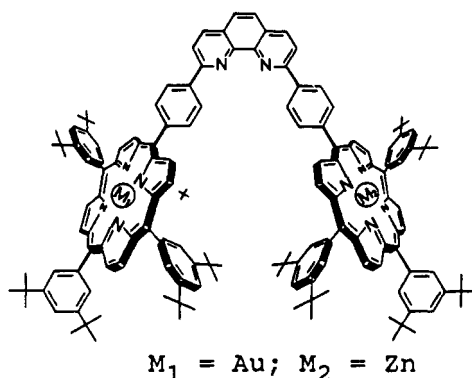
Fig. 37 Bisporphyrin studied by Sauvage and co-workers. Excitation of either porphyrin leads to electron transfer from the Zn porphyrin to the cationic Au porphyrin.[66]

Odobel and colleagues investigated a series of porphyrin - Pt acetylide dyads for photoinduced electron transfer (Fig. 38).[67] In all cases the porphyrin emission is quenched relative to porphyrin monomers. The emission lifetime of the S_1 state is much shorter in the dyads than in the model porphyrins (without the Pt terpyridine unit, but with the *p*-phenylene bisacetyline). Transient absorption spectra for compounds **29** to **34** were measured. The compounds with the electron withdrawing phosphonate group (**29** and **32**) decayed fastest and those with the electron donating OC_7H_{15} (**31** and **34**) decayed most slowly. It was possible to observe regeneration of the ground state with the same kinetics as the S_1 decay ruling out significant intersystem crossing to the triplet. Energy transfer was ruled out on the basis of unfavourable energetics and no products of an energy transfer process were observed. Deactivation due to aggregation was also ruled out as changes in concentration had no effect. Photoinduced electron transfer was calculated to be exergonic in all cases. The variation in rate constant

for the decay of the porphyrin S_1 excited state with respect to the driving force for electron transfer agrees with the Marcus relation of the free energy dependence of the electron transfer rate constant. From this data the authors conclude that photoinduced charge separation is occurring despite having never detected a charge transfer intermediate. The dyad porphyrin S_1 excited state is quenched more quickly than the instrument response (in less than 40 ps compared with the model porphyrins at several nanoseconds). Charge recombination that is faster than the initial electron transfer is in agreement with previous studies of Zn porphyrin dyads linked by the same type of bridge.

29: $R_1 = PO_3Et_2$, M = Zn^{II} 32: $R_1 = PO_3Et_2$, M = Mg^{II}
30: $R_1 = H$, M = Zn^{II} 33: $R_1 = H$, M = Mg^{II}
31: $R_1 = OC_7H_{15}$, M = Zn^{II} 34: $R_1 = OC_7H_{15}$, M = Mg^{II}
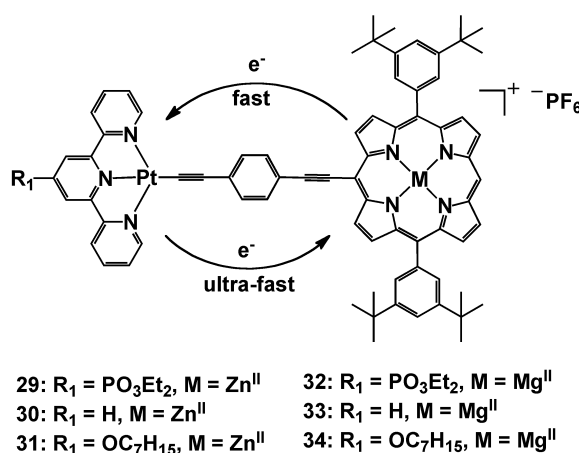
Fig. 38 Metalloporphyrin – Pt acetylide dyads investigated by Odobel and colleagues.[67]

1.4.4   Examples of proton-coupled electron transfer

The term proton-coupled electron transfer (PCET) was coined in 1981 to describe an elementary step in which electrons and protons transfer together.[68] PCET can help reduce charge build-up as consecutive electron transfers occur. This is illustrated by the well known water oxidation catalyst the 'blue dimer' *cis,cis*-[(Bpy)$_2$(H$_2$O)Ru^{III}ORu^{III}(H$_2$O)(Bpy)$_2$]$^{4+}$ where successive oxidations coupled with proton loss are required to form two Ru^V centres.[68, 69]

In 2012 Nocera and colleagues investigated bidirectional PCET in rhenium diimine tricarbonyl systems coordinated to amino acid residues (Fig. 39).[70] One complex had phenylalanine and the other, tyrosine. Crucially the tyrosine residue possesses an OH group (**35**) that phenylalanine does not. Addition of a base (pyridine or imidazole) forms a PCET network via hydrogen bonding to the OH group in **35**, whereas **36** is a control system in which this is not possible. **36** is also redox inactive and so the authors can attribute differences in excited state lifetimes to reactivity at the tyrosine phenol. The ground state absorption and steady state emission spectra of **35** and **36** are nearly identical and are dominated by the electronics at the rhenium. **35** is emissive from the ^{3}MLCT excited state and this is quenched on addition of base (pyridine or imidazole). The rhenium excited state is highly oxidising, abstracting an electron from the amino acid. The tyrosine should be photo oxidised but a signal for this intermediate cannot be observed due to fast back electron transfer. For **35** the emission quenching is greater on addition of base. The Stern Volmer plots for **36** are linear with respect to base whereas for **35** they are curved in agreement with previously derived relationships for PCET quenching mechanisms.
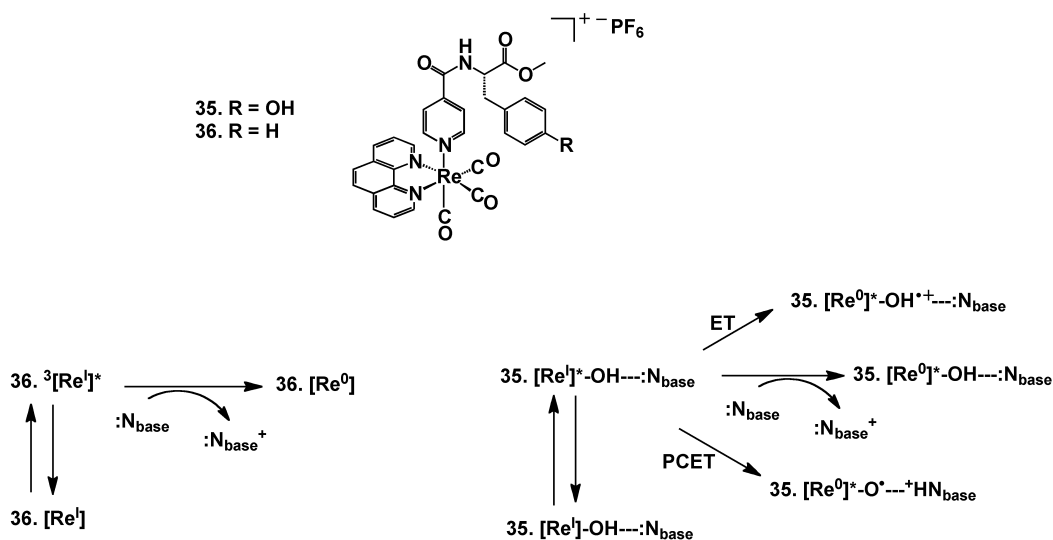
Fig. 39 PCET in a Re^I amino-acid assembley. When an OH group is present (**35**) PCET is enabled in the presence of base.[70]

1.5 Previous work at York

The Perutz group has been investigating dyads of porphyrins and metal carbonyls for over a decade. The first structures investigated were those of zinc porphyrin appended to $Re(CO)_3Br$ (**Dyad 1 Br**) in 1999.[71] The dyad showed quenching of the porphyrin emission when the rhenium unit was bound but no emission could be observed from the rhenium. Transient absorption spectroscopy indicated formation of the porphyrin $^3(\pi\pi^*)$ excited state, which had essentially the same lifetime whether the rhenium was present or not.

In 2002 Aspley[72] published work on zinc and free-base porphyrins appended to $W(CO)_5$ via a pendant pyridine group. Two variations were made with the pyridine amide-bound to the porphyrin at either the 3 or 4 position (Fig. 40). For the 3-position dyads irradiation of the Soret band caused substitution at the W, suggestive of energy transfer. The free-base dyads did not show emission quenching in the presence $W(CO)_5$. For the zinc porphyrin dyads prolonged excitation resulted in a new emission band that was tentatively assigned to photoinduced electron transfer. This additional band could also be seen in time-resolved emission measurements of the 3 position bound zinc dyad but not in the free base analogue. Time-resolved absorption spectra were unaffected by $W(CO)_5$.
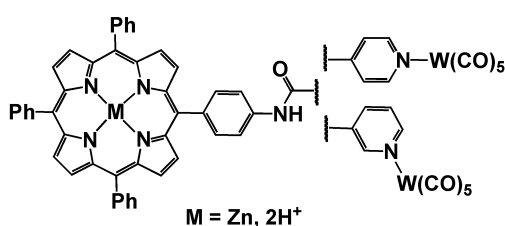
Fig. 40 Porphyrin-$W(CO)_5$ structure investigated by Aspley et al.[72]

In 2005 Gabrielsson performed an in-depth photophysical investigation into **[Dyad 1 Pic][OTf]** and the Mg porphyrin analogue.[73] The porphyrin emission was quenched when the rhenium was present and the degree of quenching was

solvent dependent. Time-resolved infrared spectroscopy indicated the formation of a charge-separated state due to electron transfer from porphyrin to rhenium in the presence of electron donor (Et_3N). The charge separation lifetime in **[Dyad 1 Pic][OTf]** was ca. 55 ps. Later investigations including a Pd porphyrin dyad[74] suggest the Zn and Mg dyads pre-coordinate triethylamine resulting in inner-sphere electron transfer. The Pd dyad reacted via outer-sphere reductive quenching of the porphyrin excited state. In all cases substitution reactions could be induced at the rhenium centre via selective excitation of the porphyrin.

In 2011 Schneider further investigated the photochemistry of the Pd dyad (Fig. 41), including CO_2 reduction experiments (DMF/Et_3N 5/1). The dyad showed charge separation lifetimes of 20-50 ps. Irradiation of the dyad with $\lambda > 420$ nm produced 2 turnovers of CO and the two components produced 3. Formation of a hydrogenated porphyrin intermediate was identified and a two component system of PdTPDHP (tetraphenyl dihydroporphyrin) and [ReBpy$(CO)_3$Pic][PF_6] produced 9 turnovers of CO. The values of $\Delta G_{ox}*$ for intermolecular electron transfer from sensitizer to rhenium unit were calculated for PdTPP and PdTPDHP and were +0.02 and −0.17 eV respectively. This result shows that the driving force is much greater for electron transfer from the dihydroporphyrin to rhenium than from the porphyrin and suggests that the induction period may be the time required for dihydroporphyrin to form.
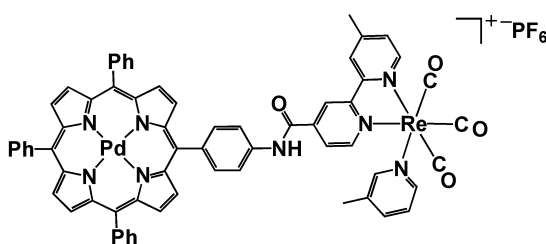
Fig. 41 Palladium-rhenium dyad investigated by Schneider et al.[75]

1.6 Dyads versus monomers

The chemical structures of a range of dyads and monomers utilised for photocatalysis are shown in Fig. 42. Beneath each catalytic system is the turnover number for the reaction catalysed and the type of reaction is stated to the right. For six of the seven systems shown, the dyad outperforms the monomers. The system in which the two components are more active is the only one using an amide linkage. It is not easy to suggest an optimal spacer as dyads outperform monomers whether the spacer is free to rotate, free to bend or is completely rigid and provides little separation. Between dyads, comparisons are not clear as many factors differ but, in turnover number, none are more than one order of magnitude apart. Ruthenium dominates as the metal of choice for both sensitiser and catalyst. There is only one other example of zinc porphyrin used as a sensitiser.
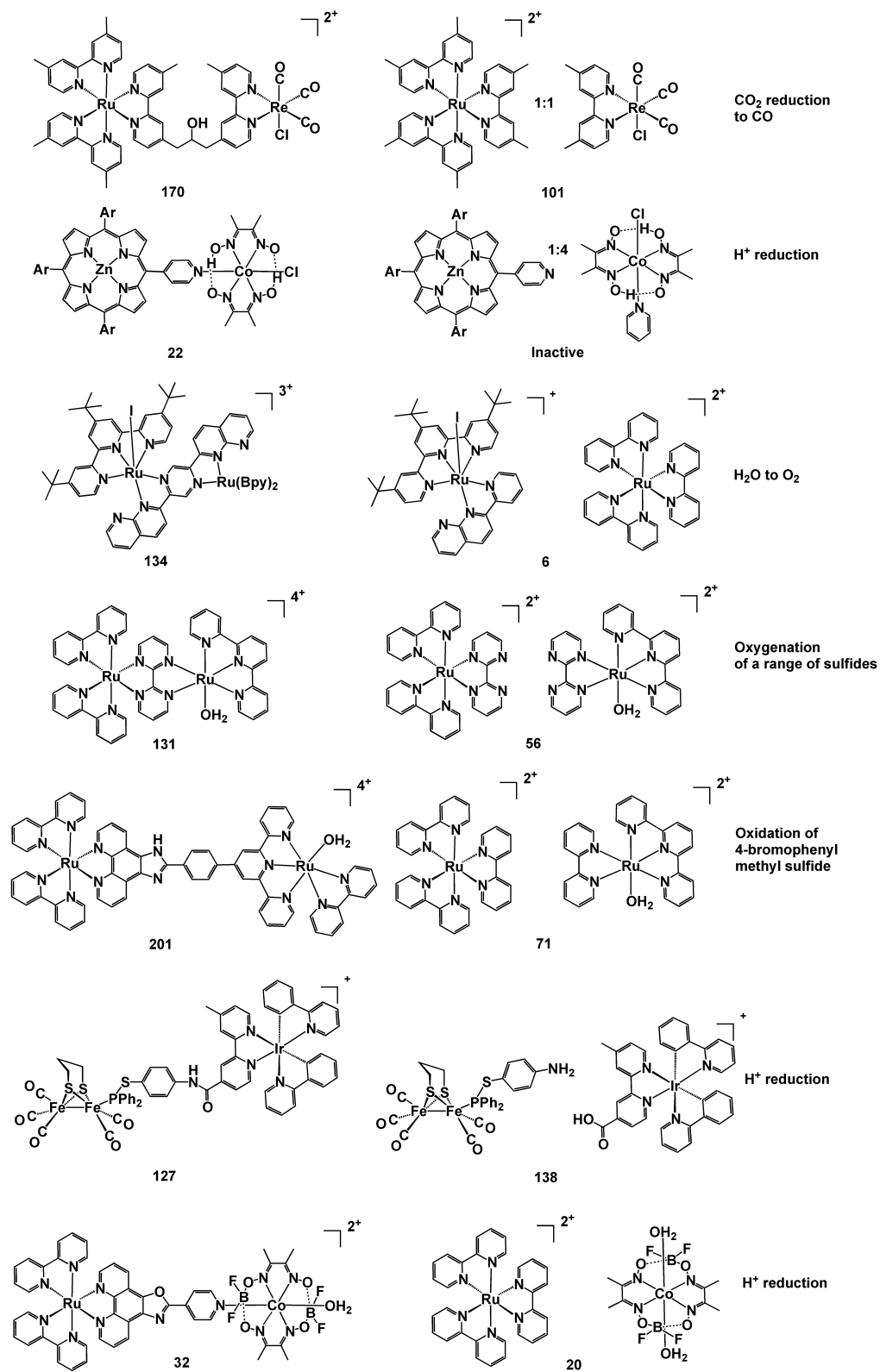
Fig. 42 Comparison of the turnover number for a range of photocatalytic dyads and their monomeric counterparts.[32, 76-81]

1.7   Aims and thesis outline

The aim of this work was to explore structural changes in the chemical spacer unit between metalloporphyrins and rhenium bipyridine tricarbonyl complexes. This was based around elaboration of the original dyad structure investigated by Aspley and Gabrielsson. Initial efforts will build on synthetic strategies developed by Gibson. During the course of the project, other spacer units will be considered and investigated. The original dyad and the novel ones created during this work were to be tested for visible light CO_2 reduction capability. The differences in activity between the systems were to be rationalised by investigation of the electrochemical and photochemical behaviour of the complexes. Cyclic voltammetry and steady state emission spectroscopy allow for the estimation of the driving force for electron transfer between metalloporphyrin and rhenium complex. Remote site photoactivity will also be probed. Time resolved infrared spectroscopic studies could provide unequivocal identification of a charge separated state and measurement of the lifetime of charge separation.

Should catalytic activity be established then efforts were to be made to elucidate the mechanism. A photolysis cell was developed such that the solution could be analysed by UV-Vis spectroscopy during the photoreaction. The mixture may also be analysed by mass spectrometry and NMR and IR spectroscopy, along with any other techniques that may be brought to bear. Comparisons can then be made between systems and strategies for the optimisation of catalysts for CO_2 photoreduction may be considered. In Chapter 2 the synthetic strategies towards the dyads and the phosphonate functionalised components are discussed along with their characterisation data. Chapter 3 covers the electrochemical and photochemical properties of the complexes followed by chapter 4 in which the CO_2 photoreduction capability is tested. Chapter 5 is focused on a slight side-step from the molecular approach in which the porphyrin and rhenium components are immobilised on TiO_2 particles as an alternative strategy for long-lived charge separation.

Chapter 2.   Synthesis and Characterisation

2.1 General procedures

2.1.1   Mono-amino porphyrin

Mono-amino porphyrin was a critical building block throughout this work and served as a starting point for the dyads and for introducing other functionalities. Porphyrins are typically synthesised via condensation of pyrrole with the corresponding aldehyde.[82] This method works well for highly symmetric porphyrins but less so for those with low or no symmetry. For the latter, a greater number of products is possible and statistics dictate a reduction in yield and an increase in by-products that often hamper purification.

An alternative method for preparing a functionalised tetraphenylporphyrin is to react directly the ready-formed porphyrin. In a method developed by Luguya et al[83] nitration of the phenyl groups occurs readily to give yields of the mono-nitrated product in excess of 80-90% (Fig. 43). Here, the relatively mild conditions of $NaNO_2$ in trifluoroacetic acid were responsible for higher yields and minimum macrocyclic degradation compared with methods using fuming HNO_3 or a HNO_3/H_2SO_4 mixture[84, 85] (46-56% and 74% yields respectively). Continuing the method of Luguya, the mono-nitrated product was not isolated and the crude mixture was subsequently reduced by the well established conditions of $SnCl_2$ in HCl.[86] Purification was by column chromatography on silica.
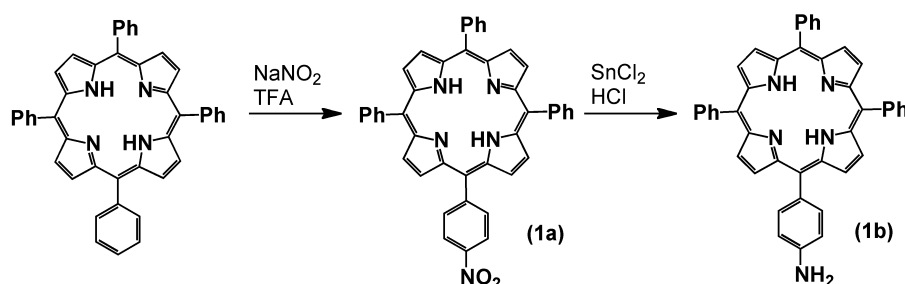
Fig. 43 Preparation of mono amino porphyrin.

2.1.2 Metallation of porphyrins

An established route using $Zn(OAc)_2$ in a $CH_3OH/CHCl_3$ mixture was used.[73] Excess zinc and acetate was removed by multiple washes with EDTA solution and water.

2.1.3 Coordination of rhenium bromide

A procedure established within the Perutz group was utilised.[87] The bipyridine was combined in a 1:1 molar ratio with $Re(CO)_5Br$ in benzene and heated to reflux. Progress was monitored by IR spectroscopy and on completion the mixture was allowed to cool and filtered, yielding a pure solid. The filtration step was essential to obtaining very pure material.

2.1.4 Substitution of bromide by 3-picoline

AgOTf was used to abstract the bromide. To AgOTf was added dry THF followed by excess 3-picoline and finally the bromide precursor. The order of addition is essential as AgOTf can often contain traces of trifluoromethanesulfonic acid and so addition of picoline can first neutralise this before introduction of the precious bromide complex. Completion of the reaction could be identified by IR spectroscopy after which a filtration removed AgBr. The main impurity was excess 3-picoline, which could mostly be washed out with hexane. However, there always remained between 1 and 2 equivalents probably due to coordination to the zinc in the case of the dyads. Column chromatography in CH_2Cl_2/THF on silica has been used previously in the Perutz group to purify Zn-RePic dyads.[73] These conditions were unsuccessful in this case and it has been found that separate zinc porphyrins and $ReBpy(CO)_3Pic$ complexes decompose rapidly on silica in chlorinated solvents. Size exclusion chromatography (Sephadex) in THF was found to be very successful in purifying the product. Often the product would elute with small amounts of additional aliphatics, possibly due to polymers in the THF, which were easily removed by washing the product with an ethanol/petrol 20/80 solution.

2.2   Preparation of methoxybenzamide dyad

2.2.1   Amide coupling with 2-methoxy-4-nitrobenzoic acid

Methodology for the introduction of the methoxybenzamide unit to amino porphyrin had been developed previously in the Perutz group.[88] 2-methoxy-4-nitro benzoic acid was activated for amide coupling by formation of the anhydride using DCC (Fig. 44). The coupled product **2d** was obtained in good yield (86%).
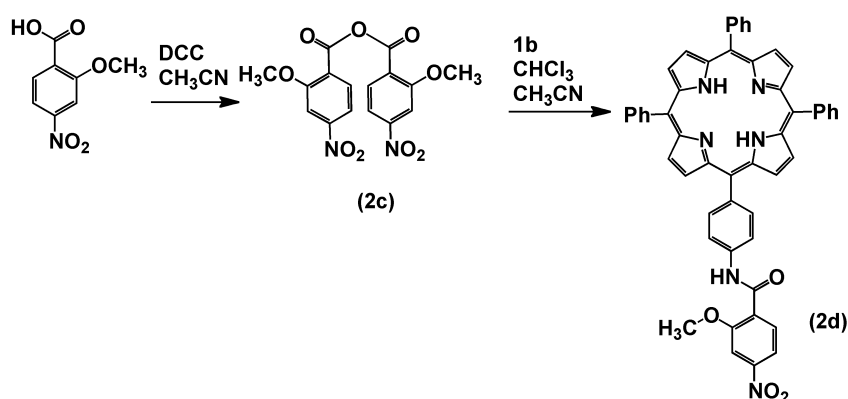
Fig. 44 Amide coupling of amino porphyrin with 2-methoxy-4-nitro benzoic acid.

2.2.2   Reduction of methoxybenzamide nitro group

The next step was to reduce the nitro group to an amine. This required conditions to which the other functional groups were tolerant and methodology for this step was established in the Perutz group.[88] Compound **2d** was dissolved in a mixture of ethanol and saturated ammonium chloride solution. Indium powder was added and the mixture heated at reflux for 72 h. Once the reaction had reached completion a Soxhlet extraction was required followed by treatment with acid to remove indium coordinated to the tetrapyrrole. Yields were poor (33%) resulting in a very difficult purification step on silica due to large amounts of starting material, which eluted very close to the desired product. Attempts were made to improve on this methodology in order to: (i) reduce reaction time (ii) remove the need for Soxhlet extraction (iii) remove the need to demetallate the porphyrin (iii) increase the yield (iv) improve purification. A procedure using elemental

60

sulphur with $NaHCO_3$ in DMF at 130 °C was tried.[89] Using TLC, by 68 h it was evident that no product had formed. Starting material was recovered at 46% along with material that could not be moved from the silica column. A procedure using $SnCl_2$ in HCl/ethanol was tried[90], only to yield 4% desired product and return 86% starting material. Next, a procedure using elemental zinc nano powder in an acetone/NH_4Cl solution/H_2O mixture was tested.[91] This produced some of compound **2e** by TLC but also significant quantities of the product with the methoxy converted to hydroxyl and the NO_2 intact. Finally a procedure using $Pd(OAc)_2$, polymethylhydrosiloxane (PMHS) and KF in a THF/H_2O mixture was tried[92] and gave complete conversion by TLC (Fig. 45). After work up the compound appeared pure by ^1H NMR but the yield was > 100%. The product was applied to a silica column resulting in 90% yield.
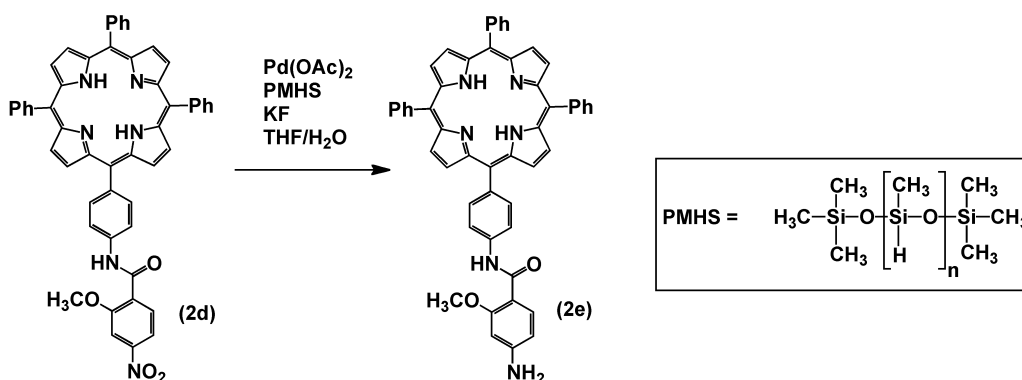
Fig. 45 Selective reduction of nitro functionality to amine.

The active catalyst in the reduction is composed of Pd nanoparticles and the PMHS acts as a hydride source.[92-94] The authors suggest that fluoride aids the formation of polycoordinate siloxane intermediates, allowing for facile transfer of the hydride. KF can be used as a nucleophilic activator of silanes, providing a hypervalent silicate species that acts as a powerful hydride donor.[95] Nitro reductions can still be performed in the absence of fluoride but the reaction times are longer and yields are reduced.

2.2.3 Amide coupling with bipyridine acid

The next stage was to perform an amide coupling between compound **2e** and the bipyridine acid (**2f**). A procedure previously used to couple palladium amino porphyrin with bipyridine acid **2f** was used[73] (Fig. 46). The acid was heated at reflux in thionyl chloride and then evaporated to dryness. A CH_2Cl_2 solution of porphyrin **2e** was added followed by pyridine and the mixture was heated at reflux for 1 h then stirred overnight. The desired product **2g** was obtained in 53% yield. Purification of the product was difficult because the basicity of **2g** gave strong interaction with silica. The silica was deactivated by use of Et_3N in a gradient elution with CH_2Cl_2 and CH_3OH. It was later found that previously in the Perutz group compound **1b** had been coupled with **2f** using Et_3N in place of pyridine.[73] In an effort to avoid pyridine, Et_3N was tried but the reaction did not proceed. In efforts to increase the yield the coupling reagents N-(3-dimethylaminopropyl)-N'-ethylcarbodiimide (EDC)[96], 1-propanephosphonic anhydride (T3P) and methylpyridinium iodide[97] were tested but showed no improvement.
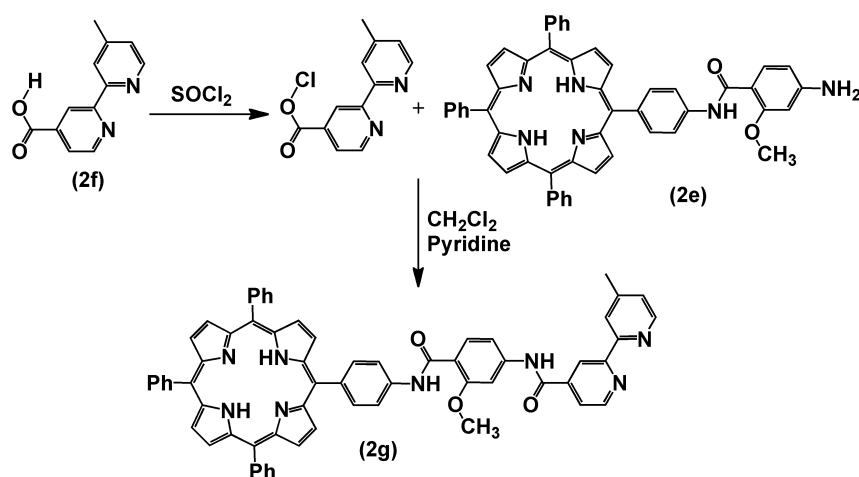
Fig. 46 Amide coupling of **2e** with bipyridine acid (**2f**).

2.2.4 Coordination of zinc, rhenium and picoline

After introduction of the bipyridine, the porphyrin ring was metallated with zinc. Then rhenium was introduced by reaction with $Re(CO)_5Br$ and subsequently the bromide ligand was substituted for 3-picoline. Purification was performed with

size exclusion chromatography. The desired product, **[Dyad 2 Pic][OTf]** (Fig. 47), was obtained in moderate yield (54%).
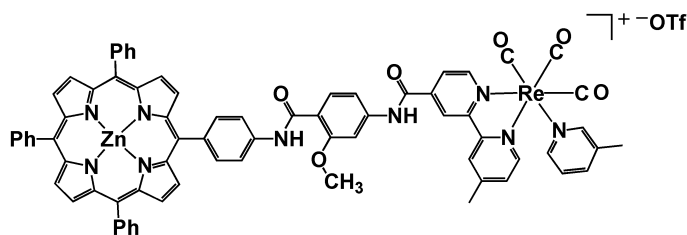
Fig. 47 Dyad with methoxybenzamide spacer, **[Dyad 2 Pic][OTf]**.

2.3 *Preparation of methylene spacer dyad*

2.3.1 **Preparation of 4-acetic acid-4'-methyl-2,2'-bipyridine**

The methylene unit was introduced between the bipyridine and the carbonyl group. Two different methods were tried to prepare the bipyridine acid with the additional CH_2. The first involved treating 4,4'-dimethyl-2,2'-bipyridine with LDA in THF followed by CO_2[98]. A lengthy work up procedure followed, culminating in evaporation of water without using heat as the product is liable to decarboxylate at elevated temperatures. The procedure was developed for large-scale synthesis (50 g) and for this scaled-down attempt (3 g) the yield was poor at 16%. The second procedure[99] treated 4,4'-dimethyl-2,2'-bipyridine with LDA but trapped with methyl chloroformate yielding the methyl ester (**3b**) in 17% yield. The starting material was returned at 48% and a significant amount of bpy with two ester groups on the methyl position was produced. These were all separated by column chromatography on silica. **3b** was subsequently hydrolysed by KOH[100] and used without further purification.
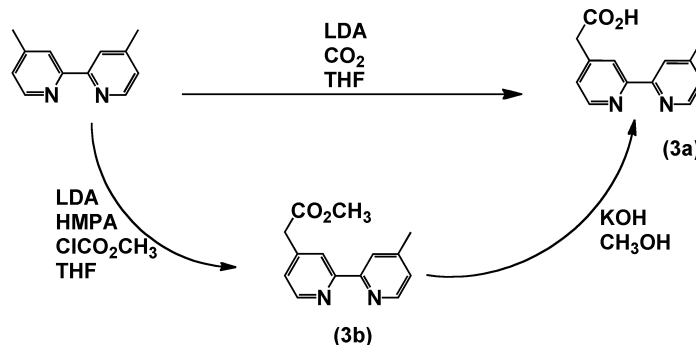
Fig. 48 Preparation of 4-acetic acid-4'-methyl-2,2'-bipyridine (**3a**).

2.3.2   Amide coupling with acetic acid bipyridine

Amino porphyrin **1b** was then coupled to bipyridine acid **3a**. Several coupling conditions were attempted including anhydride formation by DCC, thionyl chloride followed by pyridine in CH_2Cl_2 and oxalyl chloride in DMF, all of which failed to produce any coupled product. Finally 2-chloromethylpyridinium iodide in CH_2Cl_2 was tested and gave the desired product **3d** in 94% yield.
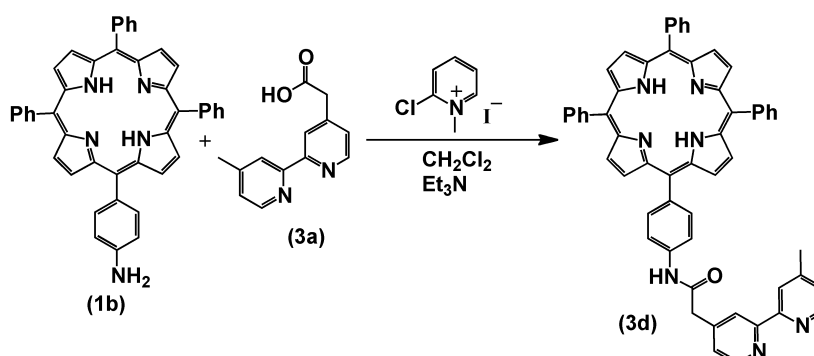
Fig. 49 Amide coupling of amino porphyrin with acetic acid bipyridine.

The 1-methyl-2-chloropyridinium reacts with the acid to give an intermediate in which the acid is bound to the pyridinium in place of the chloride. This reacts with the amine to produce the amide and N-methylpyridone. HCl is formed and subsequently scavenged by the Et_3N.

64
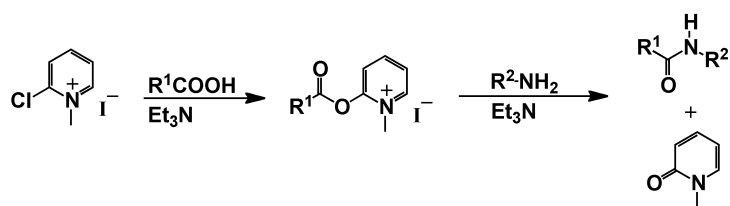
Fig. 50 Mechanism of amide bond formation by 1-methyl-2-halopyridinium reagents.[97]

2.3.3   Coordination of zinc, rhenium and picoline

Following the amide coupling, zinc, rhenium and picoline were coordinated and the final dyad purified as described under the general procedures.

2.4   *Preparation of zinc tetraphenyldihydroporphyrin*

Tetraphenyldihydroporphyrin was metallated with zinc via a modified literature procedure.[101] The free base compound was combined with $Zn(acac)_2$ in dry benzene and heated to reflux for 11 h, following by UV-Vis spectroscopy. Handling was difficult as the dihydroporphyrin decomposed rapidly in light. Even after filtration with a microfiber filter paper a white solid was still present which was probably $Zn(acac)_2$. A silica column was attempted and the impurity was removed but the dihydroporphyrin is oxidised on silica to porphyrin. The reaction was repeated and the product purified by performing five washes with water and then drying under high vacuum for 72 h.
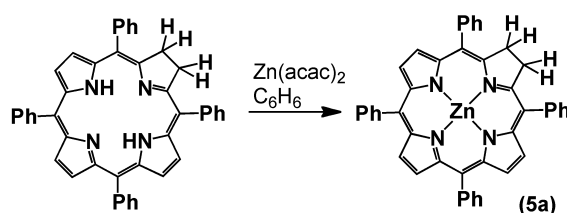
Fig. 51 Metallation of tetraphenyldihydroporphyrin.

2.5 Preparation of Re(4,4'-bis phosphonic acid-2,2'-bipyridine)(CO)$_3$(3-picoline)

Preparation of 4,4'-bis diethyl phosphate-2,2'-bipyridine was completed via a literature method[102] and coordination with Re(CO)$_5$Br was performed as detailed in the general procedures. The picoline was coordinated as detailed before but the purification procedure was altered. The product was precipitated out of CH$_2$Cl$_2$ with hexane and washed exhaustively with more hexane but one equivalent of free picoline remained. The product was applied to a silica column eluting with EtOAc until picoline could no longer be detected in the elute, then 5% CH$_3$OH in CH$_2$Cl$_2$ caused the desired product to elute. Some yellow material remained on the top of the column indicating decomposition of the rhenium but a good yield was obtained nonetheless.
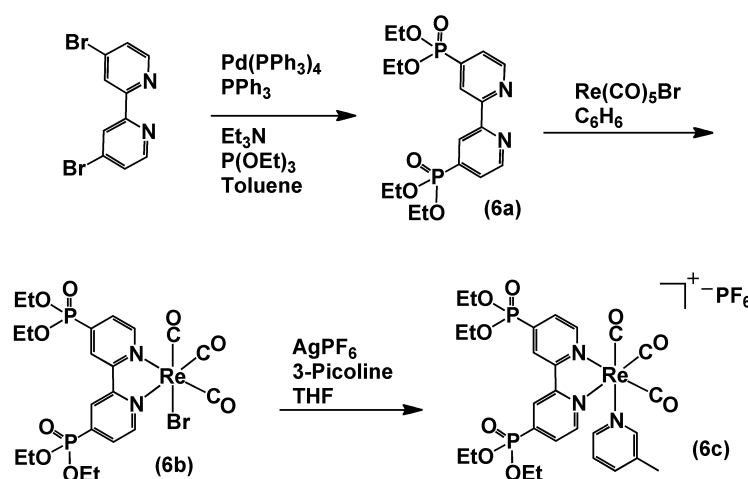
Fig. 52 Preparation of Re(CO)$_3$(4,4'-bis diethyl phosphonate-2,2'-bipyridine) bromide and picoline complexes.

The final stage was to saponify the phosphonate esters to produce the free acid. Known selective reagents for this transformation are halogenotrimethylsilanes. These reagents will break the oxygen-carbon bond to produce a trimethylsilylester which readily hydrolyses in CH$_3$OH to produce the acid. BrSi(CH$_3$)$_3$ was tried but at low temperatures it could not break all of the ester groups and at high temperature the picoline was substituted with bromide. The more reactive ISi(CH$_3$)$_3$ was tried at 0 °C and all the ethyl groups were removed, yielding **6d**. A small bipyridine impurity was produced but was mostly removed

with recrystallisation from CH_3OH with diethyl ether. In the first instance **6c** was made as the triflate salt and on treatment with $ISi(CH_3)_3$ a white rubbery material was formed along with the desired product. One explanation for the by-product is that silyl triflates are known precursors to silicone polymers.[103] The hexafluorophosphate salt did not produce any by-product.
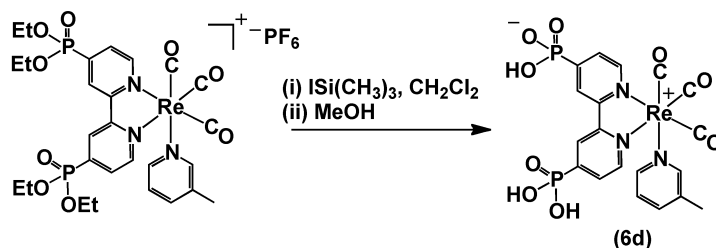
Fig. 53 Hydrolysis of phosphonate esters to yield **6d**.

2.5.1   Preparation of phosphonic acid porphyrin

In order to introduce a phosphonic acid group to one side of the porphyrin it was simplest to work from the amino porphyrin and use the amide coupling methodology. Diethylphosphonoacetic acid could be purchased and was coupled to amino porphyrin in high yield using the chloromethylpyridinium iodide reagent. The porphyrin was metallated with zinc as detailed in the general procedures. The diethylphosphonate then needed to be cleaved to produce the free acid in the presence of base as Brønstéd acids will demetallate porphyrins. After trialling several sets of conditions success was achieved with $BrSi(CH_3)_3$ in $CHCl_3/Et_3N$ at reflux yielding the product as the triethylammonium salt **7c**. Efforts to replace the HN^+Et_3 with Na^+ or Li^+ were unsuccessful or produced a salt that was difficult to handle due to low solubility in common solvents.
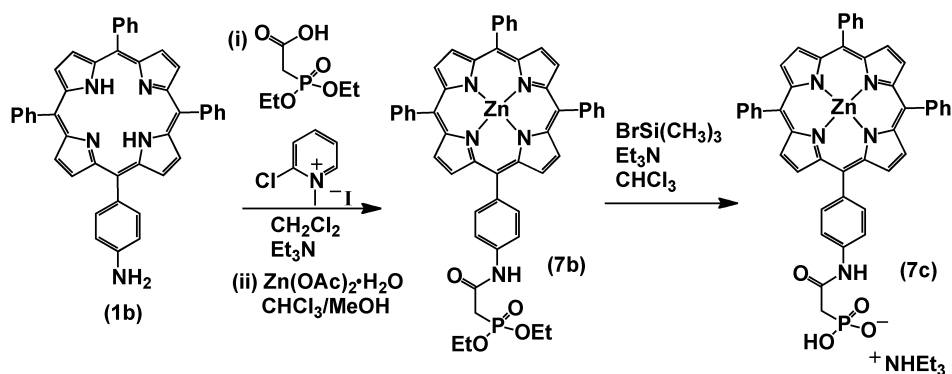
Fig. 54 Preparation of phosphonic acid porphyrin **7c**.

2.6 Characterisation

Compounds that had been synthesised previously were identified by ^{1}H and ^{31}P NMR spectroscopy and EI- and ESI-mass spectrometry. Comparison with the established data showed good agreement. Novel compounds that were synthesised en route to the final catalysts were characterised by ^{1}H NMR spectroscopy and, when possible, with high-resolution ESI-mass spectrometry. UV-vis spectroscopy was also utilised along with IR spectroscopy for compounds containing rhenium carbonyl species. The final photocatalysts were also characterised by ^{13}C NMR spectroscopy followed by complete assignment with the aid of COSY, NOE, HMQC and HMBC NMR spectroscopy. For compounds containing phosphorus and fluorine nuclei, ^{31}P and ^{19}F NMR spectroscopy was also employed.

2.6.1   NMR spectroscopy of methoxybenzamide bipyridine appended porphyrins
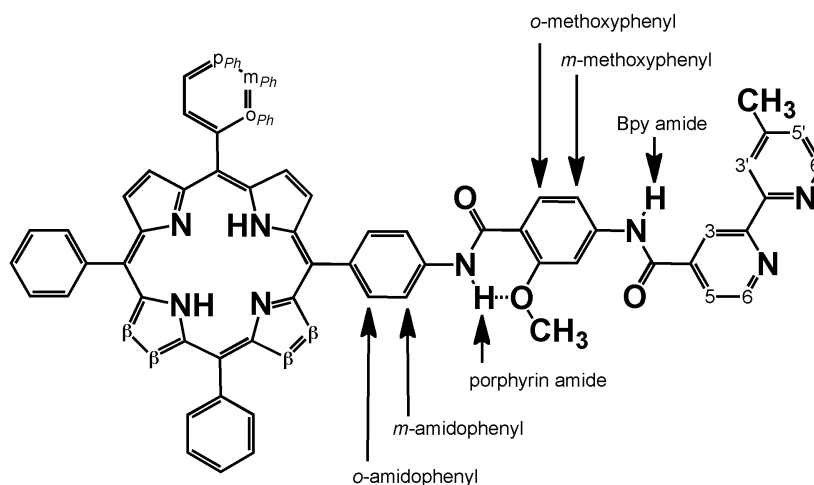
Fig. 55 Proton labels for the methoxy benzamide bipyridine appended porphyrins.

2.6.2   NMR spectroscopy of 2g

There are several characteristic features to the NMR spectra of the methoxybenzamide functionalised porphyrins (Fig. 56). Initially, as with all free base porphyrins, the two protons on the nitrogen atoms of two of the pyrroles, have a unique and isolated chemical shift. Due to the aromatic ring current of the porphyrin these protons are found at δ = -2.8. The methyl group on the bipyridine can be found alone at δ = 2.5. The methoxy signal is at δ = 4.3 due to the electron withdrawing oxygen atom deshielding the hydrogen nuclei. There are two amide protons in the molecule. The one adjacent to the bipyridine is found near δ = 8.3 which does not form hydrogen bonds as the spectra are taken in CDCl$_3$. The amide proton nearest the porphyrin is hydrogen bonded to the oxygen of the methoxy group and the signal for this proton can be found at δ = 10.2. Electron density is shared with the oxygen atom and so the proton is deshielded. Six of the β-pyrrole protons are found as a multiplet at δ = 8.85 with the two adjacent to the functionalised meso position coming at slightly higher field. The *o*-phenyl protons of the porphyrin are almost equivalent and are found as a multiplet at δ = 8.25. The two protons denoted as *o*-amidophenyl are similar in chemical shift and can be found also within the multiplet at δ = 8.25 indicated

69

by an integration ratio of 8. The *m-* and *p-* protons of the porphyrin phenyl groups are present as a large multiplet at δ = 7.75. The *m*-amidophenyl protons are further upfield at δ = 8.08 and present as a doublet due to coupling with the *o*-amidophenyl protons. The two *m*-methoxyphenyl protons appear very close together at δ = 8.08 and 8.10. The bipyridine signals are expected to be those at δ = 8.89, 8.58, 8.46, 8.43, 8.33, 7.90 and 7.19 by comparison with previous work on bipyridine-appended porphyrins.[104] This leaves the *o*-methoxyphenyl proton at δ = 7.22.
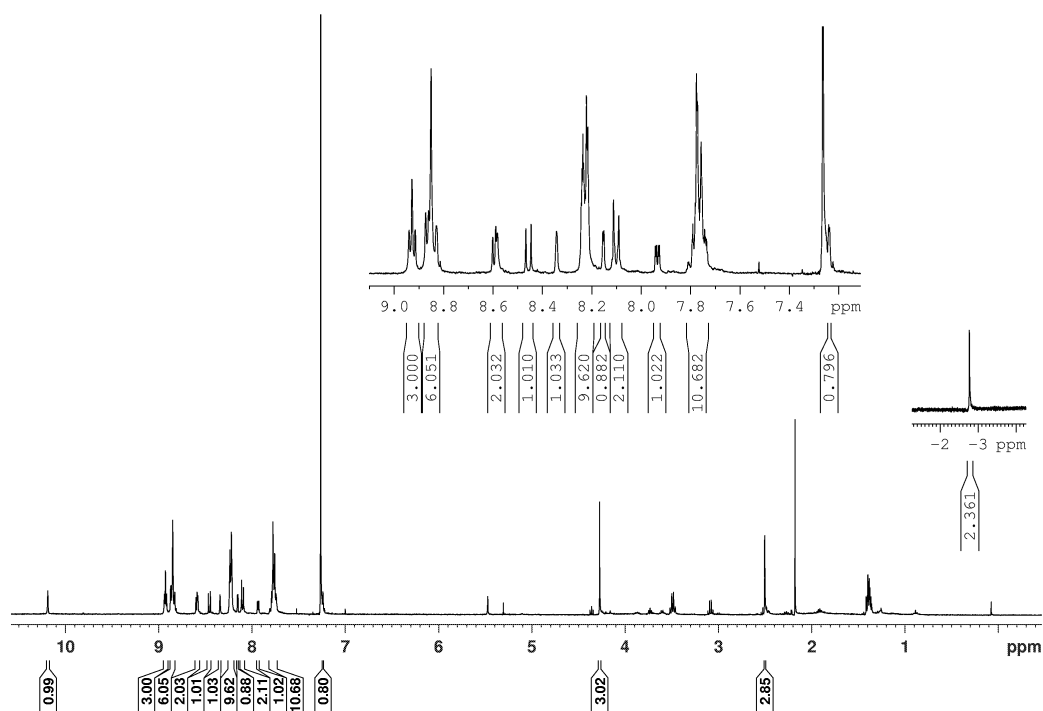
Fig. 56 ^{1}H NMR spectrum of **2g** (CDCl$_3$ 400 MHz).

2.6.3   NMR spectroscopy of 2h

Zinc was coordinated to the porphyrin core to yield **2h** and the ^{1}H NMR spectrum is shown in Fig. 57. The assignments for **2h** were confirmed with the aid of NOE and COSY NMR spectroscopic experiments. The region of the spectrum at δ = -3.0 now shows no signal as the free base porphyrin protons have been replaced with Zn. The signals for the bipyridine methyl group and the methoxy group have not changed and the hydrogen bonded amide proton

70

remains at δ = 10.2. The β protons shifted downfield by 0.12 but the *o-, m-* and *p-* phenyl protons did not change chemical shift.
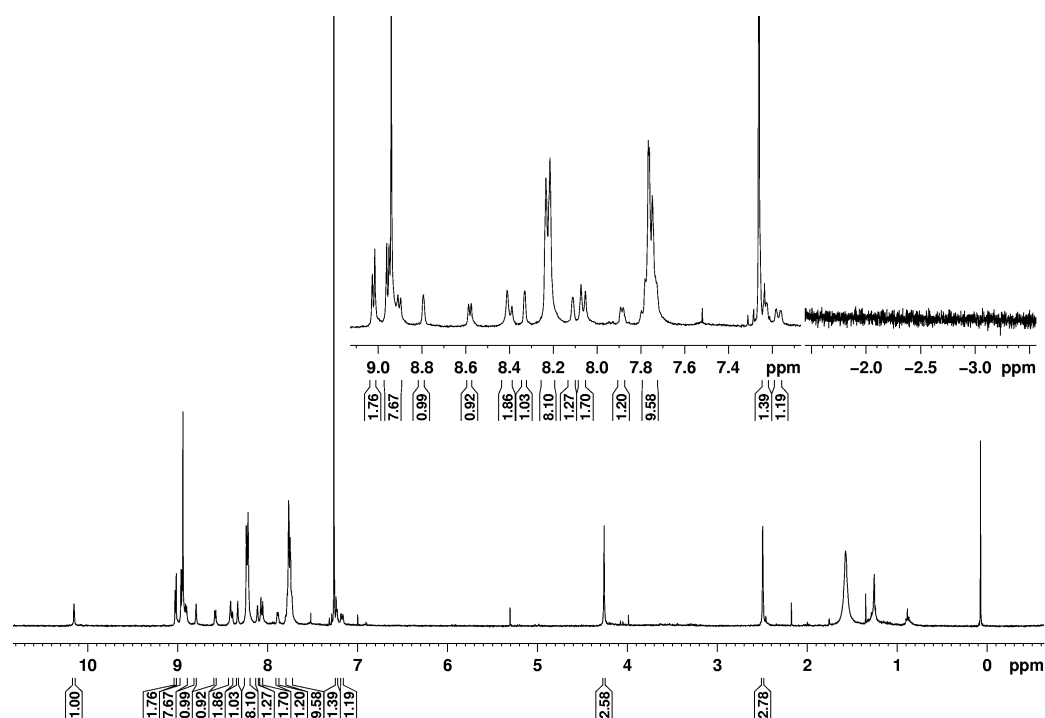
Fig. 57 ^{1}H NMR spectrum of **2h** (CDCl$_3$ 400 MHz).

2.6.4   NMR spectroscopy of compound Dyad 2 Br

Rhenium tricarbonyl bromide was coordinated to the bipyridine and the ^{1}H NMR spectrum (Fig. 58) has been assigned with the aid of COSY and NOE NMR spectroscopic experiments. Although there are numerous different aromatic protons in the compound, the signals are all well resolved in THF-*d$_8$*. The THF is capable of hydrogen bonding and so both amide protons can be found between δ = 10.22 and 10.35 (**a** and **b**). The methyl and methoxy groups are characteristic as singlets at δ = 2.5 and 4.25 respectively (**p** and **o**). The multiplets at δ = 8.9, 8.25 and 7.8 are the β, *o-* phenyl and *m-, p-* phenyl protons respectively.
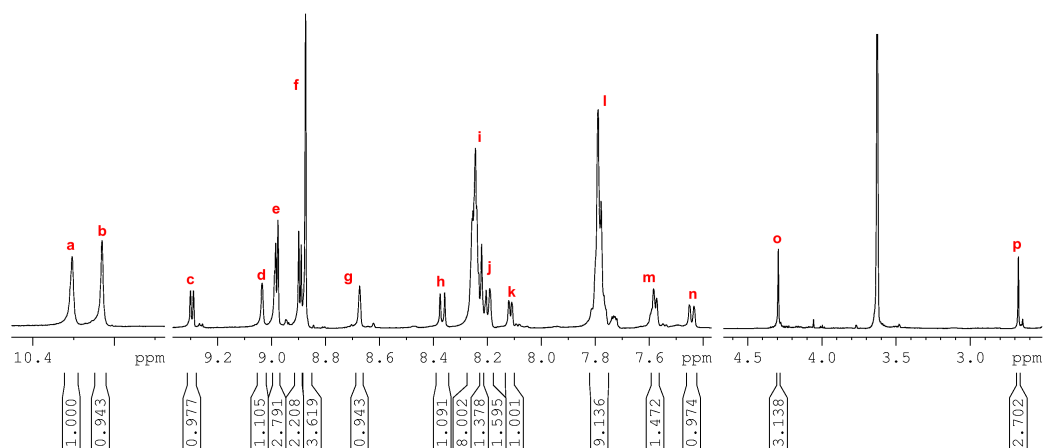
Fig. 58 ^{1}H NMR spectrum of **Dyad 2 Br** (THF-d_8 400 MHz).
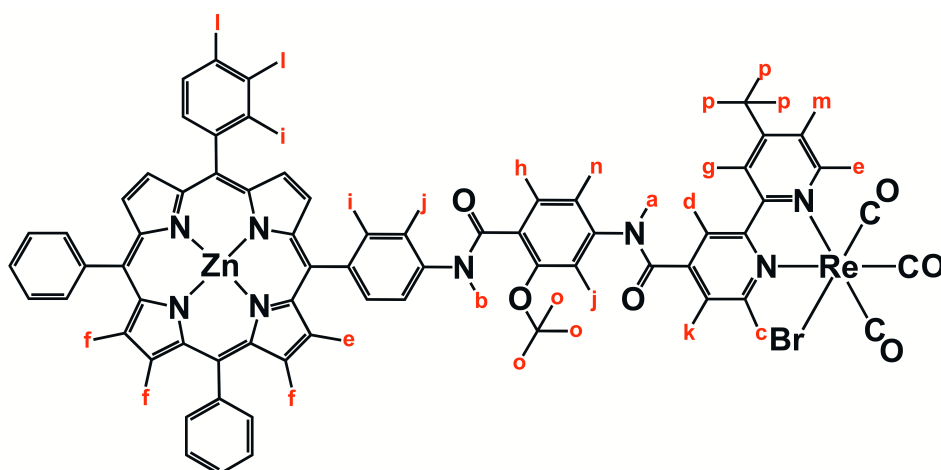
Fig. 59 ^{1}H NMR assignment of **Dyad 2 Br**.

The aliphatic/aromatic NOESY NMR spectrum is given in Fig. 60 and two example cross peaks have been highlighted: these are correlations between **j-o** and **g-p** indicating that **j** contains protons on the methoxybenzamide ring and that **g** is a proton on the pyridine ring with the methyl group. Proton **g** is not split and is therefore unlikely to be adjacent to another proton. It was assigned as the proton at the 3 position. For signal **j** to correlate with **o** it must be the nearest proton; the 3 position of the methoxybenzamide ring. The COSY spectrum (page 239) shows a strong coupling between **e-m** and a weaker cross peak between **g-m**. The weaker suggests a longer range coupling indicating **m** is on the same pyridine ring as **g** but at the 5 position. The coupling between **e** and **m** puts **e** at

the 6 position. The same deduction can be made from the couplings between **c-k** and **d-k**. The coupling between **h** and **n** suggests they are the protons on the methoxybenzamide ring. The exact positions were determined by a weak NOESY correlation between **a** and **n**. The porphyrin amide proton is unlikely to be close in space to the side of the ring with protons **h** and **n**, due to hindered rotation from the H-bond with the methoxy group. Proton **n** must therefore be correlating with the Bpy amide proton and was assigned as the 5 position, leaving **h** as the 6 position. The amide protons were also assigned from this deduction, making **a** the Bpy amide and **b** the porphyrin amide.
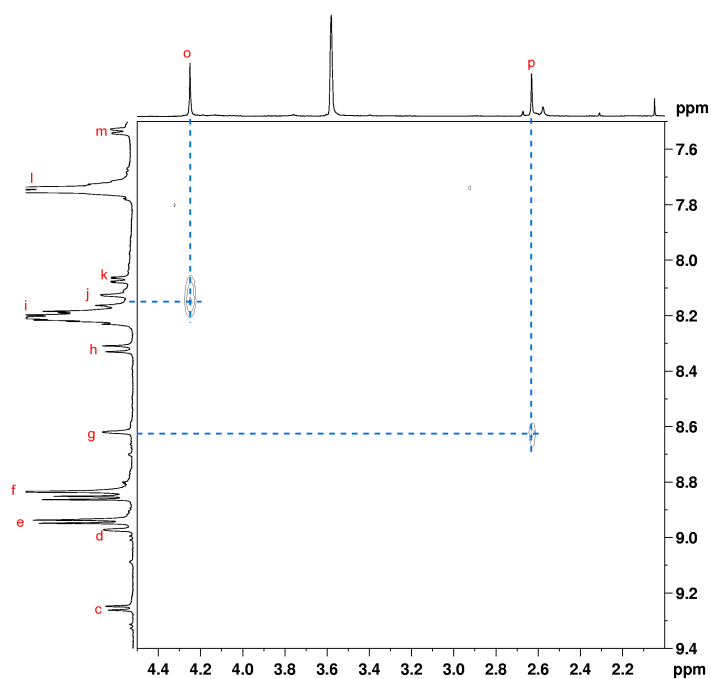
Fig. 60 ^{1}H-^{1}H NOE NMR spectrum of **Dyad 2 Br** (THF-d_8 400 MHz).

2.6.5   NMR spectroscopy of compound [Dyad 2 Pic][OTf]
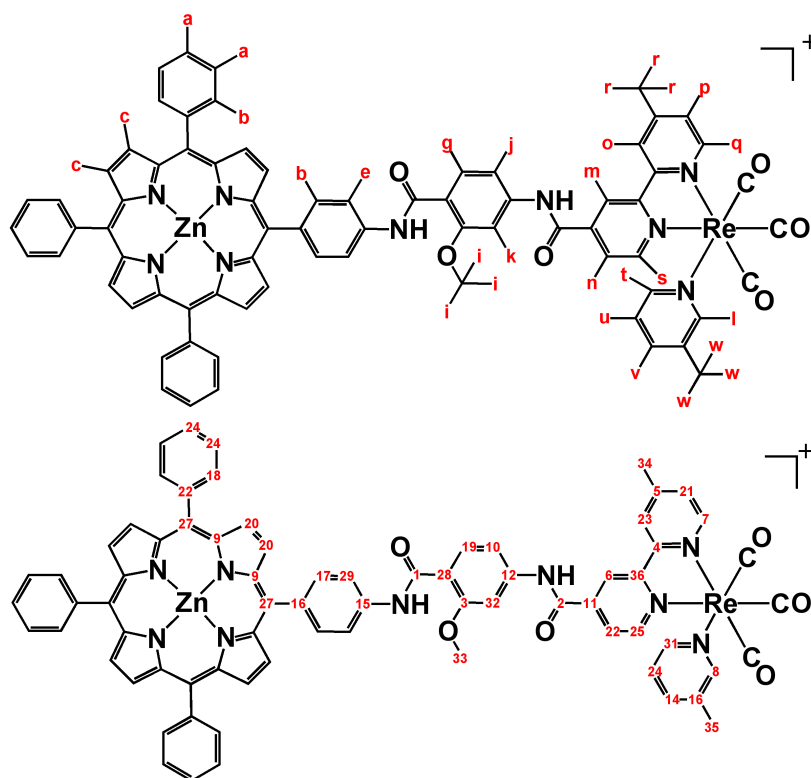
Fig. 61 ^{13}C and ^{1}H assignments of **[Dyad 2 Pic][OTf]**.

The bromide was substituted for 3-picoline to yield the final catalyst **[Dyad 2 Pic][OTf]**. Previous picoline dyads were successfully dissolved in CD$_2$Cl$_2$ for NMR experiments and so this was tried for **[Dyad 2 Pic][OTf]** but the spectra were poor. A few drops of CD$_3$OD was added and the spectrum became much sharper. In the presence of CD$_3$OD the amide signals become weak or cannot be observed at all due to exchange with deuterons. The methyl groups of the bipyridine and picoline are characteristic at δ = 2.7 and 2.2 respectively (**r** and **w**), identified between one-another by two-dimensional experiments. The methoxy group is also characteristic at δ = 4.25 (**i**). The aromatic region of the ^{1}H NMR spectrum is shown in Fig. 62 and in the solvent mixture described, many of the signals are not coincident. The β, *o*-phenyl and *m*-,*p*- phenyl protons are characteristic exhibiting multiplets at δ = 8.9, 8.2 and 7.75 respectively (**c**,**b** and **a**). One picoline signal is also characteristic as a doublet of doublets that is typically the most upfield signal in the aromatic region (δ = 7.2, **u**). These assignments were confirmed, and the remaining signals assigned using two-

74

dimensional NMR experiments. ^{1}H-^{1}H COSY and NOESY allowed tentative assignment of the whole spectrum and then the relationship with the carbon spectrum using HMQC and HMBC experiments confirmed these.
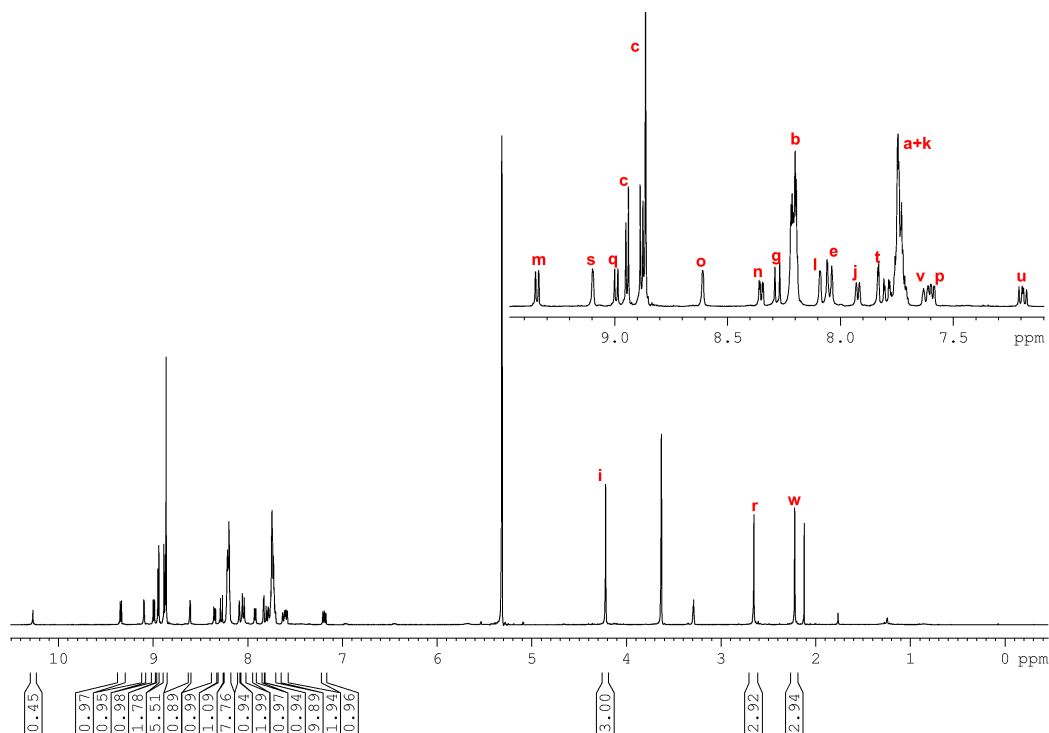
Fig. 62 ^{1}H NMR spectrum of **[Dyad 2 Pic][OTf]** (THF-d_8 400 MHz).

The COSY spectrum is shown in Fig. 63. Cross peaks are present with the picoline proton **u**. It is likely the signals coupling with the proton at δ = 7.2 are from protons of the picoline unit. Confirmation of the multiplet at δ = 8.2 being *o*-phenyl protons is given by the coupling to the *m*-phenyl protons at δ = 7.75.
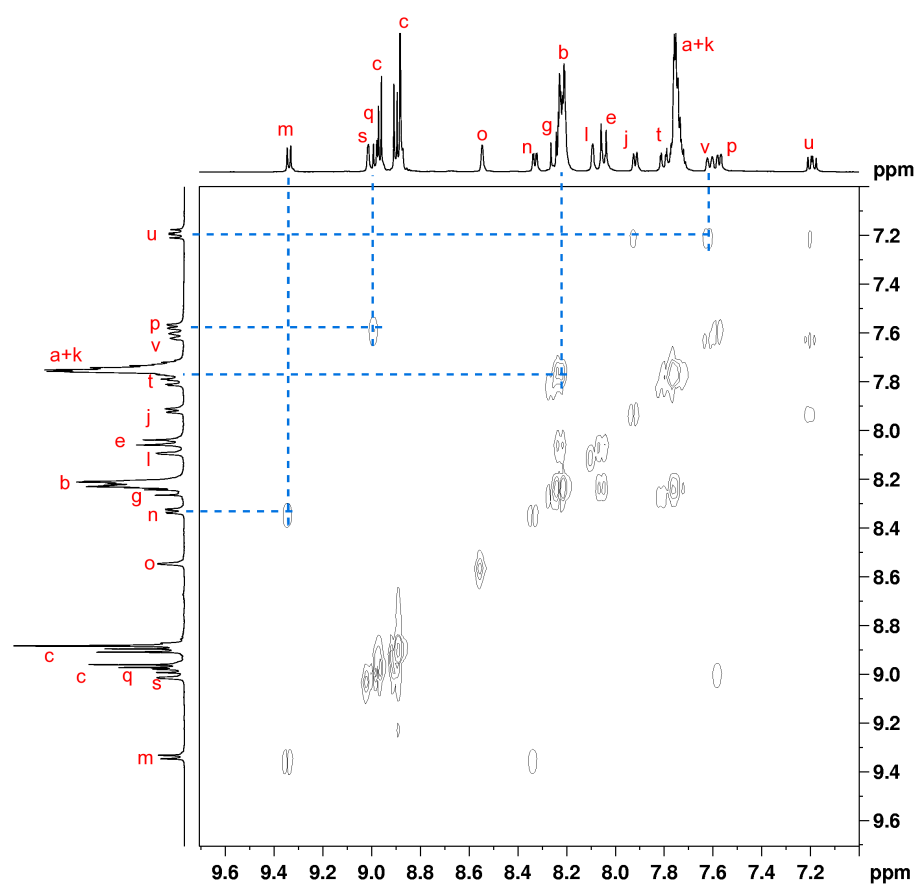
Fig. 63 ^{1}H-^{1}H COSY spectrum of **[Dyad 2 Pic][OTf]** (aromatic region) (THF-d_8 400 MHz).

The NOESY spectrum provides a handle with which to place signals for the bipyridine, picoline and methoxyphenyl protons. The three methyl groups are quite bulky and will typically show NOE with the nearest protons. Appendix page 240 shows a correlation between the methoxy protons and the multiplet at δ = 7.75 highlighting that there is a proton separate from the *m-,p-* phenyl protons hidden beneath it. This agrees with integration ratio of 10. The multiplet was also assigned to the proton nearest to the methoxy group, that at the 3 position of the methoxyphenyl moiety.

The ^{13}C spectrum contains many signals making the HMQC (appendix page 241) spectrum quite complicated. In this case all correlations have been assigned as the proton being directly bound to the carbon. Full assignment can be seen in Fig. 61.

The HMBC spectrum (Fig. 64) exhibits long-range couplings between carbon and proton leading to many more correlations. For clarity some example cross peaks have been annotated. The longer range couplings are essential for assigning carbon atoms that are not directly bound to a proton such as those labelled **4**, **36**, **11**, **28** and **2** (Fig. 65). Proton **m** correlates to carbon atoms **22**, **11** and **4**. This helps confirm the assignment of proton **m** and carbon atom **6** (via lack of HMBC correlation) and suggests the carbon signals may be from atoms **11**, **4** or **36**. The correlation between **s** and **36** confirms carbon **36** is in the bipyridine unit. The correlation between **n** and **2**, along with the chemical shift of **2**, helps to confirm that this signal is the carbonyl. A correlation between **g** and **28** was evidence for the assignment of **28** as the methoxyphenyl carbon in the 1 position. It was not possible to observe signals for the carbon atoms of the carbonyl ligands. No single correlation, or even two correlations in agreement, were used to assign the spectra. A careful assessment of all the NMR data along with logical deduction resulted in the complete assignment laid out in Fig. 65 and Fig. 61.
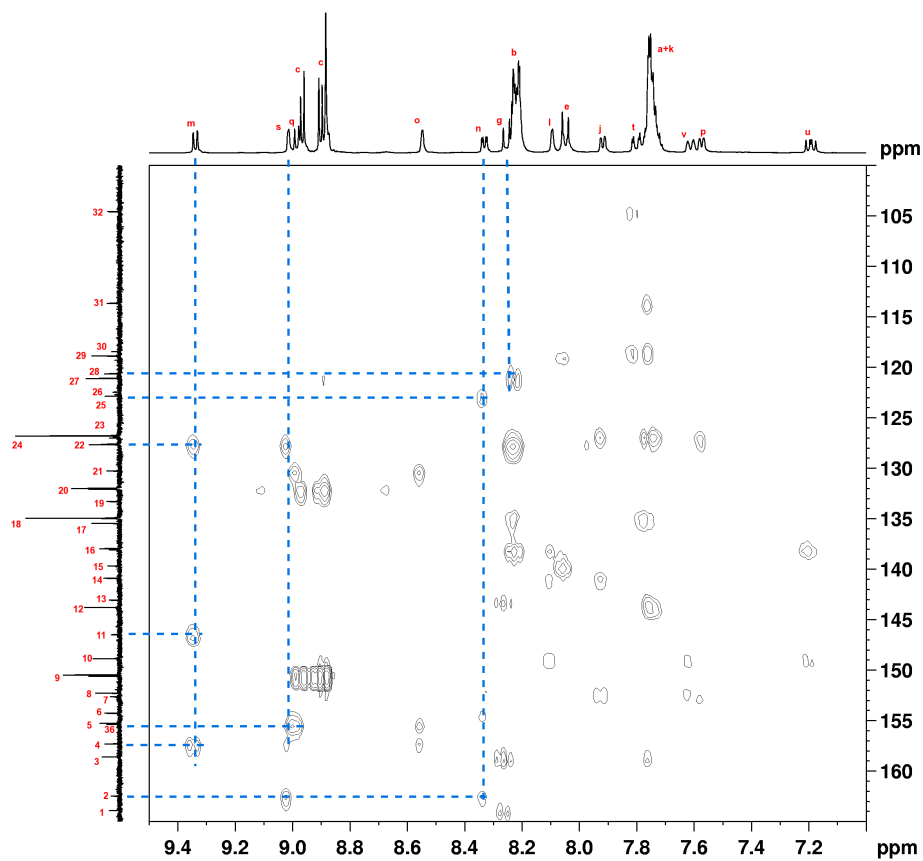
Fig. 64 ^{1}H -^{13}C HMBC spectrum of **[Dyad 2 Pic][OTf]** (THF-d_8 400 MHz).
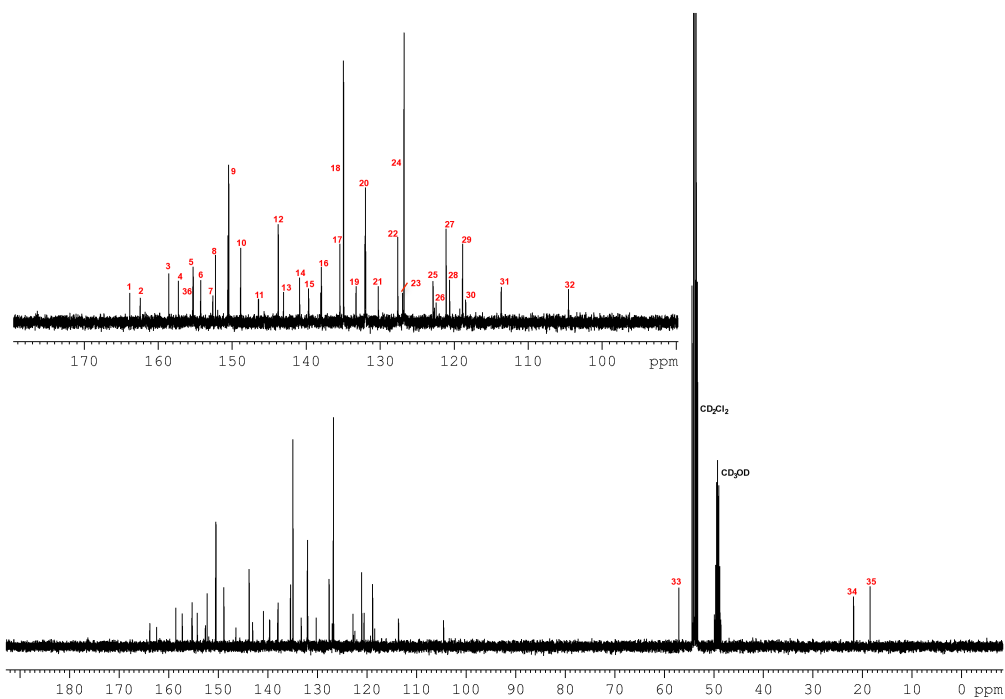
Fig. 65 ^{13}C{^{1}H} NMR spectrum of **[Dyad 2 Pic][OTf]** with assignments (THF-*d$_8$* 100.6 MHz).

Table 3 contains the signals for various groups present in compounds **2g**, **2h** and **[Dyad 2 Pic][OTf]**.

2g (CDCl$_3$)	2h (CDCl$_3$)	[Dyad 2 Pic][OTf] (CD$_2$Cl$_2$ + CD$_3$OD)	Assignment
2.50	2.49	2.65	Bpy CH$_3$
4.27	4.26	4.22	OCH$_3$
7.24	7.23	7.59	Bpy
7.25	8.39	8.28	*o*-methoxyphenyl
7.93	7.89	8.35	Bpy
8.10	8.06	8.05	*m*-amidophenyl
8.16	7.17 + 8.11	7.80 + 7.92	*m*-methoxyphenyl
8.34	8.33	8.61	Bpy
8.46	8.58	8.99	Bpy
8.58	8.41	8.09	Bpy amide
8.59	8.79	9.10	Bpy
8.89	8.90	9.34	Bpy
10.19	10.15	10.27	porphyrin amide

Table 3 NMR shifts (ppm) of compounds **2g**, **2h** and **[Dyad 2 Pic][OTf]**.

2.6.6   NMR spectroscopy of bipyridine appended porphyrins with methylene spacer
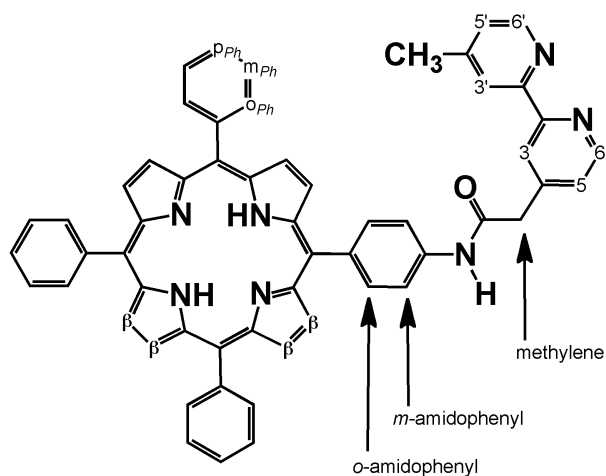
Fig. 66 Terminology for protons in bipyridine appended porphyrins with a methylene spacer.

The ^{1}H NMR spectrum of compound **3d** is given in Fig. 67. The spectrum contains several characteristic resonances that can immediately be assigned by their chemical shift, integral and splitting. The protons bound to the nitrogen atoms of pyrroles are present at δ = -2.8, the methyl group is the singlet at δ = 2.5 and the methylene group is the singlet at δ = 3.9. The multiplets at δ = 8.85, 8.2 and 7.75 are the β, *o*-phenyl and *m*-,*p*- phenyl protons respectively. The doublets each worth 2 protons at δ = 8.15 and 7.85 are from the amidophenyl ring. The signal with chemical shift close to that of the *o*-phenyl protons (δ = 8.15) is probably from the 2 and 6 positions and the signal with chemical shift close to that of the *m*-,*p*- phenyl protons (δ = 7.85) is probably the 3 and 5 positions. The remaining seven signals each worth one proton are from the bipyridine and the amide.
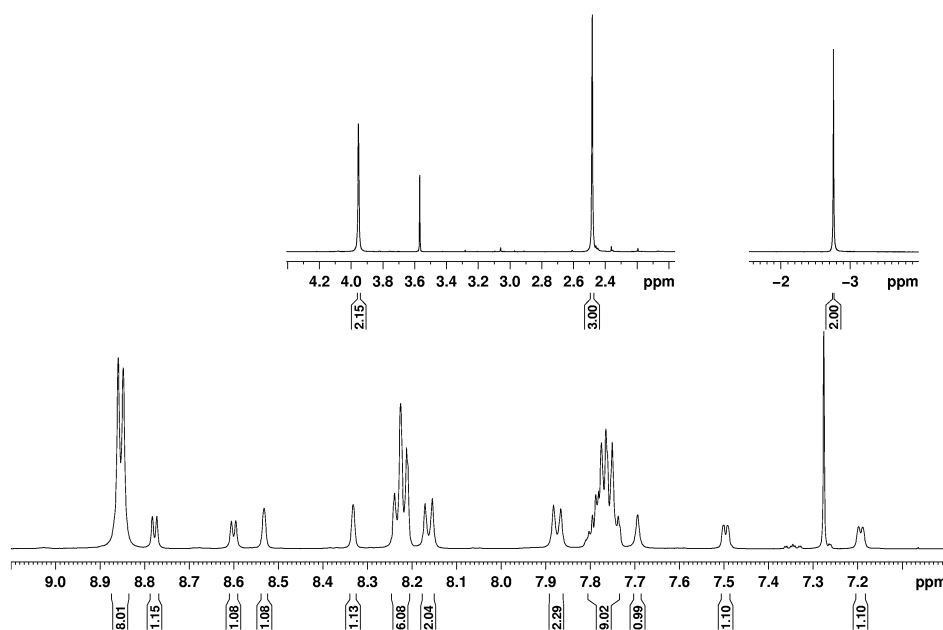
Fig. 67 ^{1}H NMR spectrum of **3d** (CDCl$_3$ 400 MHz).

Zinc was inserted into the porphyrin ring to produce **3e** and the ^{1}H NMR spectrum is shown in Fig. 68. The methylene, methyl, *o*-phenyl, m-,*p*- phenyl and β protons all give characteristic signals. The spectrum was run in THF and so the amide proton is characteristically downfield at δ = 9.7. The integration ratio of 2 for both the signals at δ = 8.09 and 8.12 suggests they are from the amidophenyl unit. The remaining signals must be the six bipyridine protons. A COSY spectrum (Appendix page 242) showed correlation between signals at δ = 8.55 and 7.21 and between signals at δ = 8.66 and 7.55 indicating these must be the pairs of Bpy protons at 5', 6' and 5, 6. The NOESY spectrum allows (Appendix pages 243 and 244) assignment of the amidophenyl signals. The signal at δ = 8.09 correlates with the amide suggesting it is the *m*-amidophenyl protons. Process of elimination would indicate that the signal at δ = 8.12 is the *o*-amidophenyl protons and the NOESY correlation with the β proton signal confirms this. The signal at δ = 7.21 correlates with the methyl and so the δ = 8.55 and 7.21 protons must be the 5', 6' pair. The signal at δ = 8.46 correlates with the methyl and so this must be the remaining unassigned proton on that pyridine ring. The same process can be applied to the other pyridine ring for NOE correlations to the methylene protons.

82
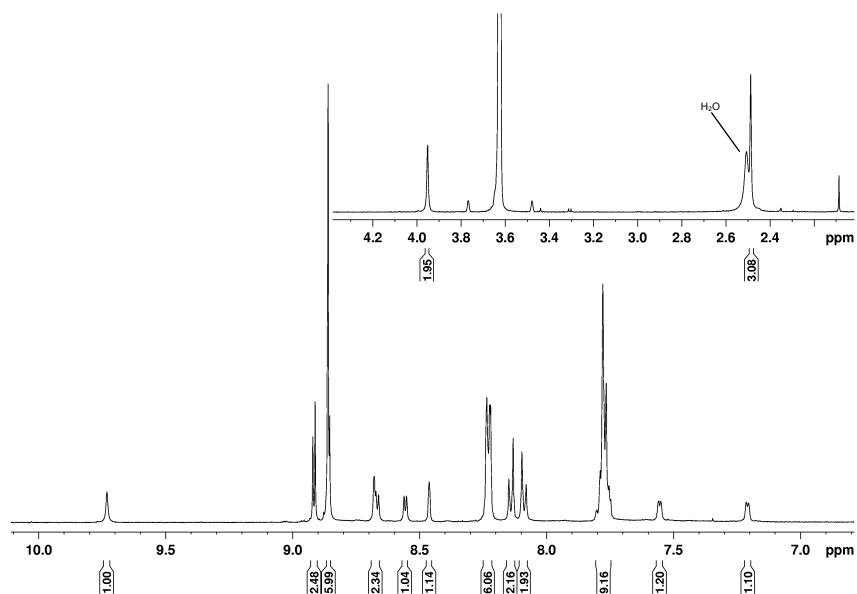
Fig. 68 ^{1}H NMR spectrum of **3e** (CDCl$_3$ 400 MHz).

2.6.7   NMR spectroscopy of Dyad 3 Br
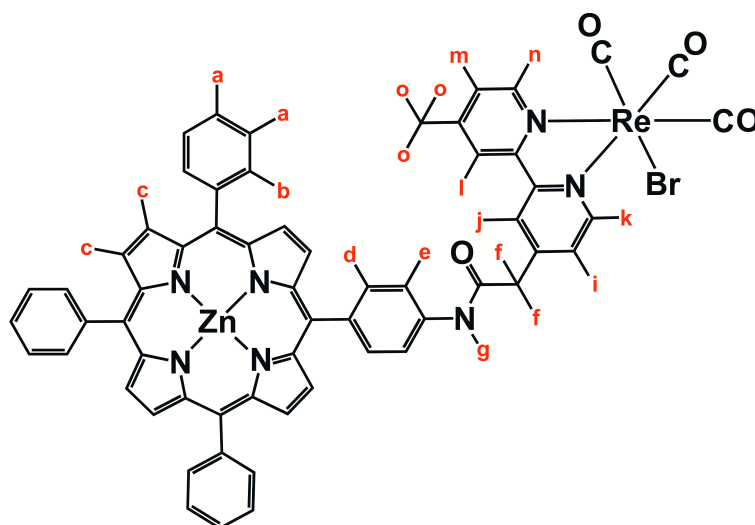
Fig. 69 ^{1}H NMR assignment of **Dyad 3 Br**.

Rhenium tricarbonyl bromide was coordinated to the bipyridine of **3e** to produce **Dyad 3 Br**. In THF the signals in the aromatic region are well resolved (Fig. 70). There are several characteristic signals that may be assigned on the basis of chemical shift, integration ratio and multiplicity. The singlets at δ = 2.6, 4.1 and 9.8 (**o**, **f** and **g**) are from the methyl, methylene and amide protons respectively. The signals labelled **c** are characteristic of the β protons coming at δ = 8.9 and

83

giving a total integration ratio of 8. The signals are split into sets of 2 and 6
protons due to the symmetry of the molecule. The chemical environment of the
two protons nearest the amidophenyl ring is slightly different to that of the other
six. Multiplets **b** and **a** are characteristic of the *o*-phenyl and *m-,p-* phenyl
protons respectively. Multiplet **a** has an integration ratio one higher than
expected indicating another proton is hidden underneath. Signals **d** and **e**
integrate to two each suggesting they are the two sets of protons on the
amidophenyl ring. The remaining six signals, each integrating to one proton, are
those on the bipyridine unit.
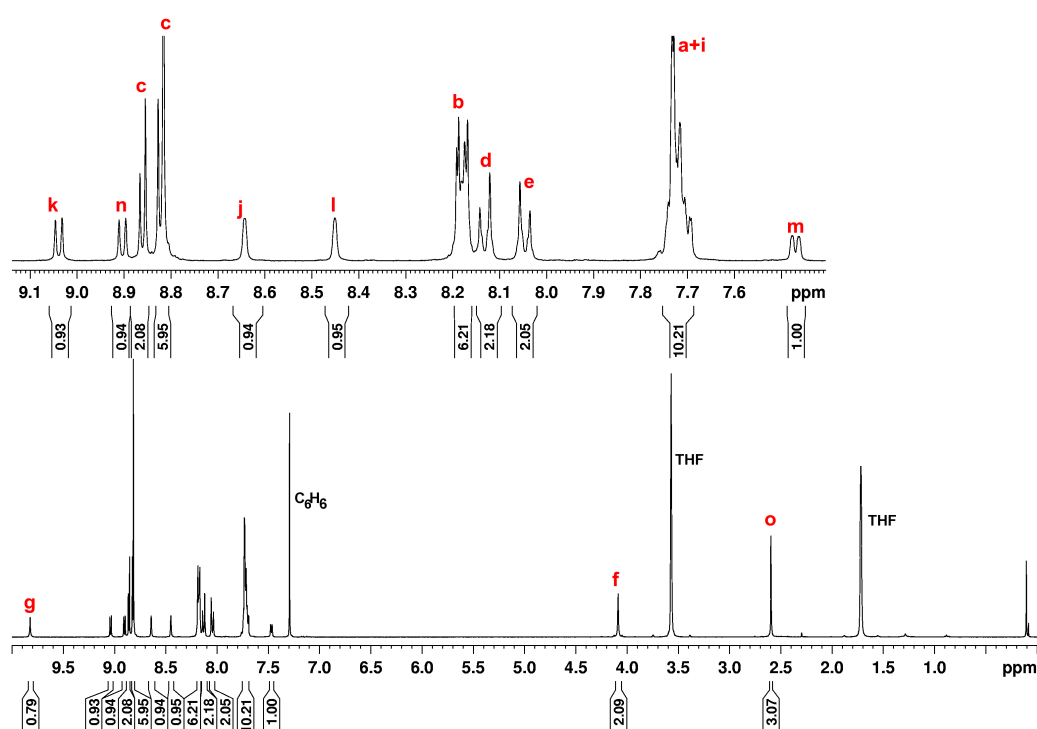
Fig. 70 ¹H NMR spectrum of **Dyad 3 Br** (THF-*d₈* 400 MHz).

¹H-¹H COSY and NOESY NMR spectroscopy was used to assign the remaining
signals. The COSY spectrum (Appendix page 245) indicates that there are
couplings with **m**, **n** and **k**, **i**. These must therefore be the 5,6 and 5',6' pairs. The
NOESY spectrum indicates that **j** and **i** are close in space to **f** and so **i** and **k** must
be the 5, 6 pair and **j** must be at the 3' position. **m** and **n** remain as the 5', 6' pair
and **l** as the proton at the 3 position. This is confirmed by NOESY correlations of
l and **m** with the methyl signal, **o**. To discriminate between the amidophenyl

proton pairs **d** and **e** it is possible to observe NOESY correlations between **d** and **c** and between **e** and **g**. **d** and **e** are therefore at the ortho and meta positions respectively. This is reinforced by signal **d** being closer in chemical shift to signal **b**.
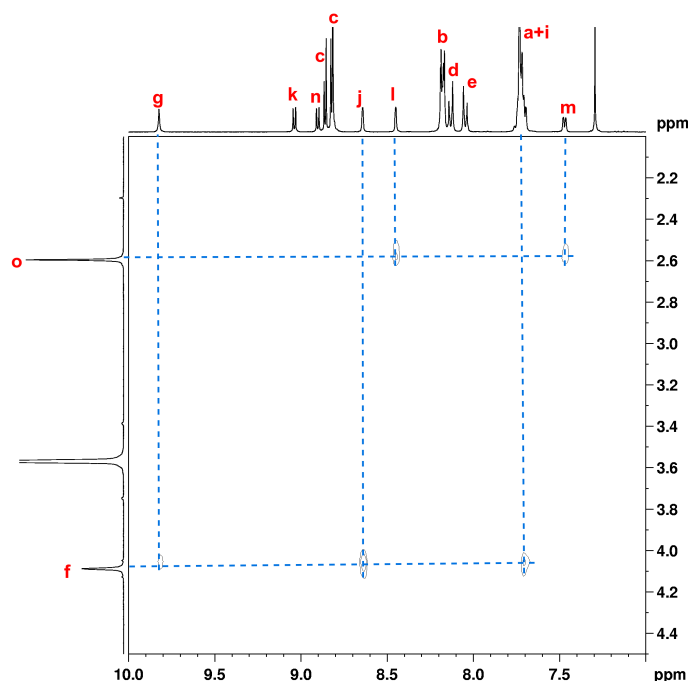
Fig. 71 ^{1}H-^{1}H NOESY spectrum of **Dyad 3 Br** (THF-d_8 400 MHz).

The HMQC NMR spectrum allowed for assignment of many of the carbon signals based on their correlation to the assigned proton spectrum. As an example the aliphatic region is shown in Appendix page 246. Correlations with protons **f** and **o** allowed assignment of carbon signals **25** and **26**. ^{13}C signals from atoms not directly bound to a proton can be assigned with the aid of longer range ^{13}C-^{1}H correlations given by a HMBC experiment. As an example the aromatic region is shown in Fig. 72 with a few example correlations highlighted. Amide proton **g** correlates with carbon **24,** which reinforces the assignment of **24** as the *m*-amidophenyl carbon. The correlation between **j** and **17** allowed the assignment of **17** as the Bpy 6 position. The correlations of **e** and **10** and of **c** and **7** allowed assignment of these quaternary carbons. It was not possible to observe signals for the carbon atoms of the carbonyl ligands.

85
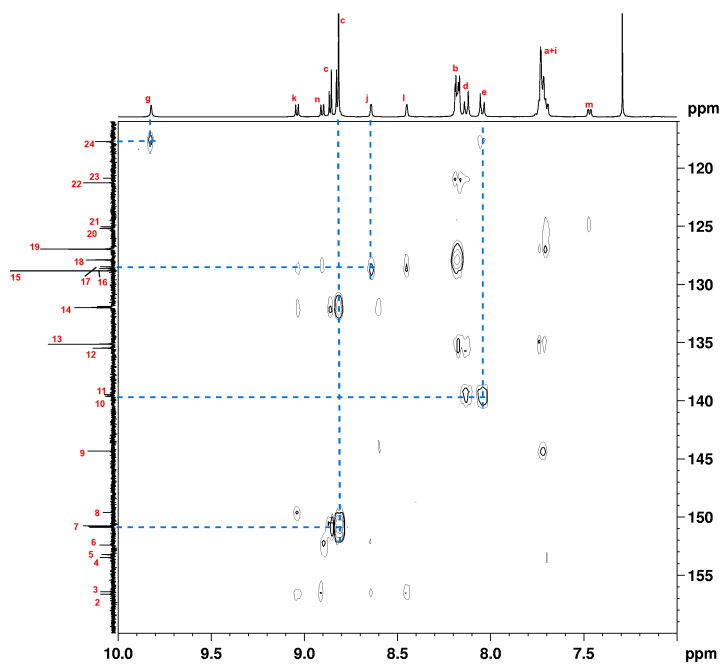
Fig. 72 ^{1}H-^{13}C HMBC NMR spectrum of **Dyad 3 Br** (THF-d_8 400 MHz).
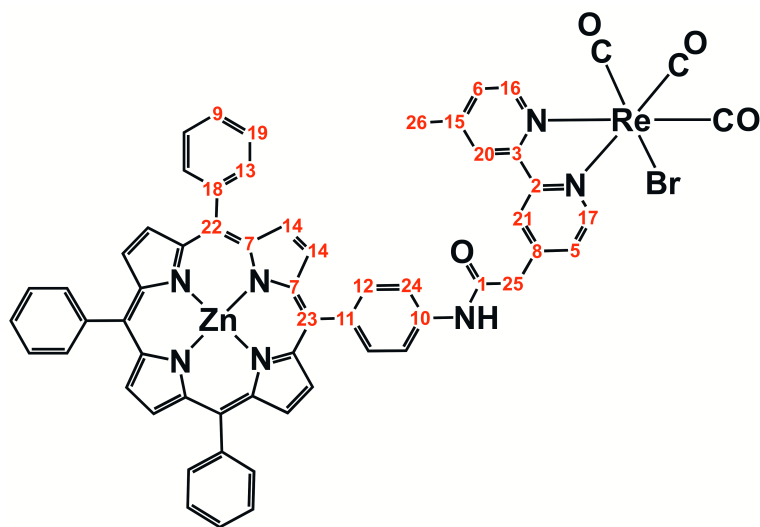
Fig. 73 ^{13}C NMR assignment of **Dyad 3 Br**.

2.6.8   NMR spectroscopy of [Dyad 3 Pic][OTf]
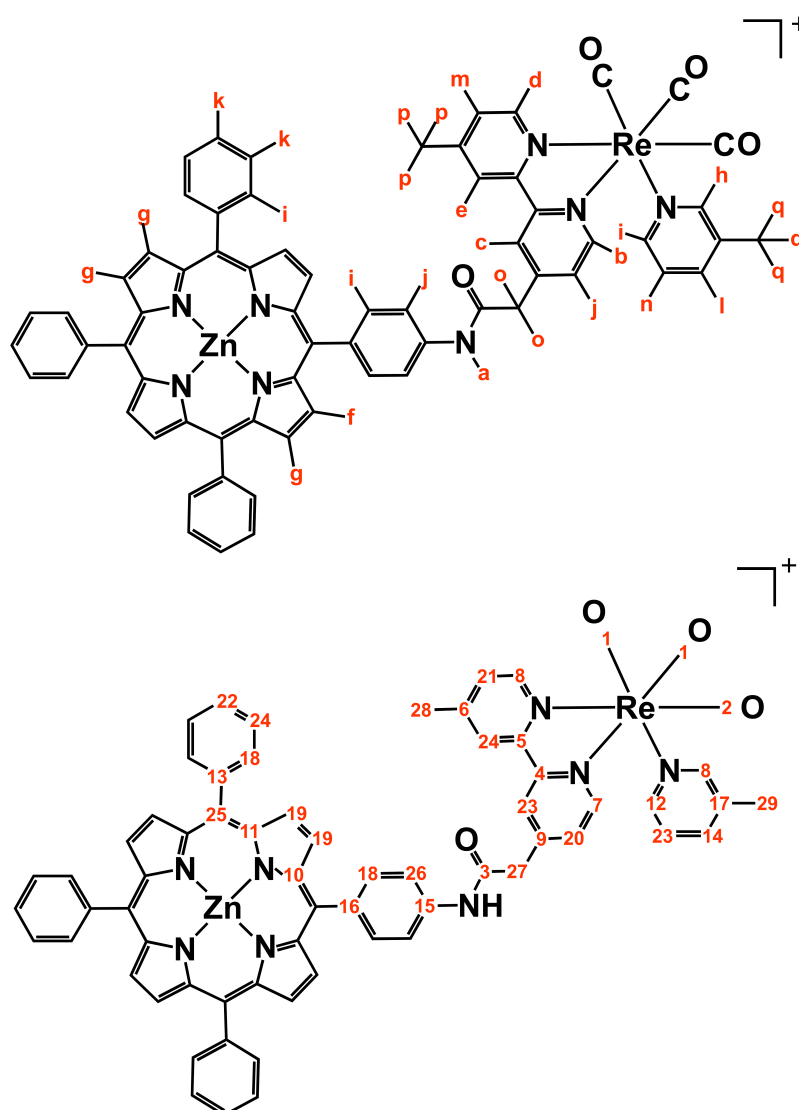
Fig. 74 ^{1}H and ^{13}C assignment of **[Dyad 3 Pic][OTf]**.

Substitution of bromide for picoline yielded **[Dyad 3 Pic][OTf]** and the ^{1}H NMR spectrum is shown in Fig. 75 and the signals have been annotated alphabetically for clarity. Several signals can be assigned on the basis of their chemical shift, integration ratio and multiplicity. The amide is downfield at δ = 10.45 (**a**). The two singlets at δ = 2.25 and 2.70 (**q** and **p**) are the methyl groups of the Bpy and picoline but at this stage cannot be told apart. The signal at δ = 4.26 (**o**) is the methylene group. The multiplets at δ = 8.9, 8.25 and 7.8 (**f**,**g**,**i** and **k**) are the β, *o*-phenyl and *m*-,*p*- phenyl protons respectively. The doublet of doublets at δ = 7.3 (**n**) is likely to be the picoline proton at the 5 position. The COSY spectrum (Fig.

87

76) shows this picoline proton correlates with two other signals that must be the protons at the 4 and 6 positions (**i** and **l**). The shift and integration of **j** suggests it contains two amidophenyl protons. The COSY correlation to *m*-amidophenyl indicates the other two amidophenyl protons are within that multiplet, which is logical as their chemical shift should be very similar. There are correlations between **m** and **d** and between **j** and **b** suggesting these signals arise from the 5,6 and 5',6' pairs of the Bpy. The NOESY spectrum (Appendix page 247) exhibits correlations between **o** and **c**, indicating that **c** is at the 3 position on the Bpy. There is also a correlation between **o** and **j** showing that **j** and **b** are the Bpy 5,6 protons and by process of elimination that **m** and **d** are the 5',6' protons. This is confirmed by correlation between **p** and **m**. If **p** correlates with known Bpy protons then it is likely to be the methyl of the Bpy and this is backed-up by other rhenium picoline dyads where the Bpy methyl is at higher shift than the picoline methyl. NOESY between **p** and **e** indicates that **e** is at the 3' position of the Bpy. Signals **h** and **l** correlate with **q**, suggesting that they are at the 2 and 4 positions of the picoline respectively.
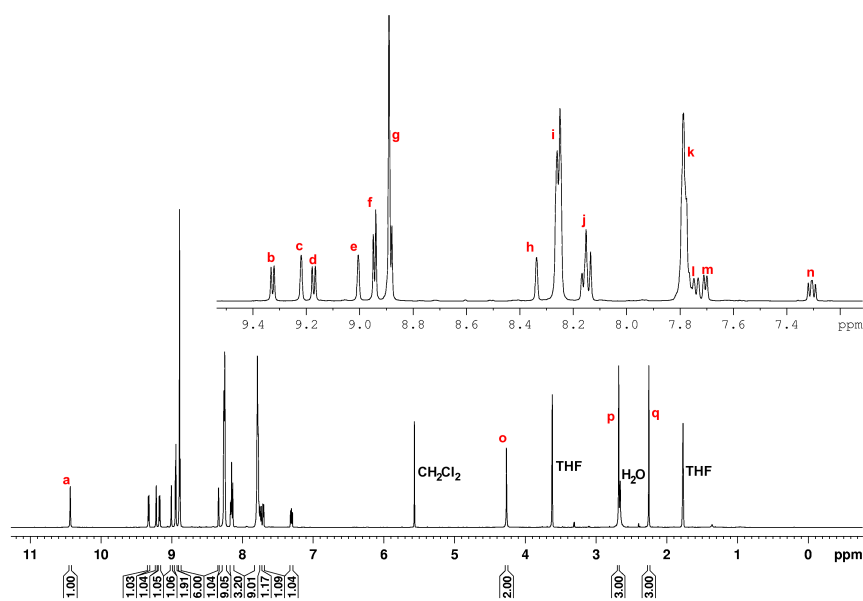
Fig. 75 ^{1}H NMR spectrum of **[Dyad 3 Pic][OTf]** (THF-d_8 400 MHz).
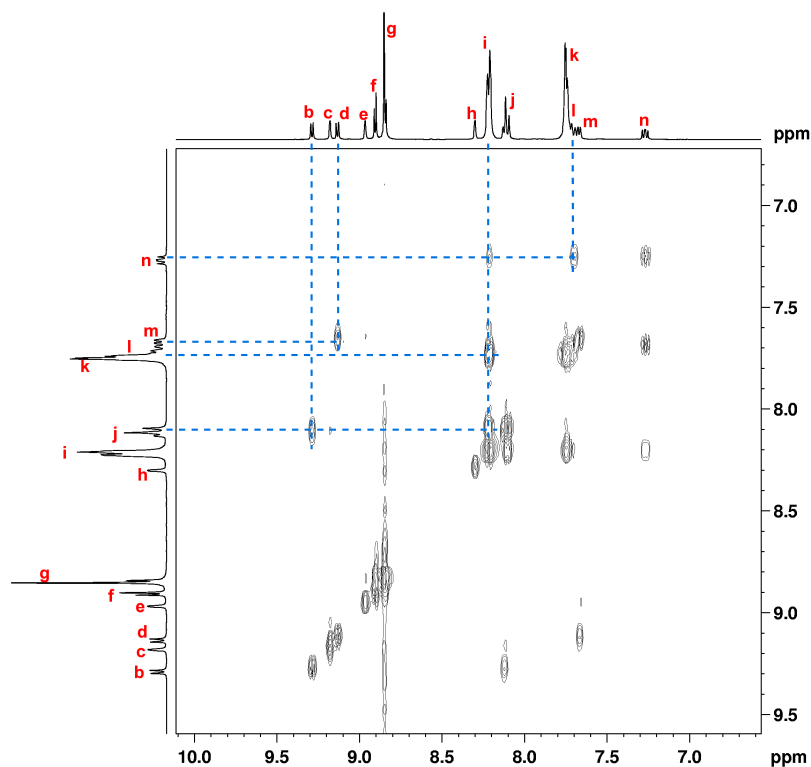
Fig. 76 ^{1}H-^{1}H COSY spectrum of **[Dyad 3 Pic][OTf]** (THF-d_8 400 MHz).

The carbon spectrum was assigned with the aid of HMQC and HMBC NMR experiments. The HMQC spectrum of the aromatic region is shown in Appendix page 248 and some examples have been highlighted. The aliphatic region also showed HMQC correlations that allowed assignment of the methyl and methylene groups. The HMBC spectrum (Fig. 78) allows for assignment of quaternary carbons via longer-range interactions. For simplicity a selection of examples have been highlighted. Quarternary carbons **4**, **5**, **9** and **15** were assigned due to correlation with protons **c**,**e**,**b** and **j** respectively. Carbon **17** was assigned as the 3 position on the picoline due to correlation with both protons **n** and **h**. In this case it was possible to observe signals for the carbonyl ligands.
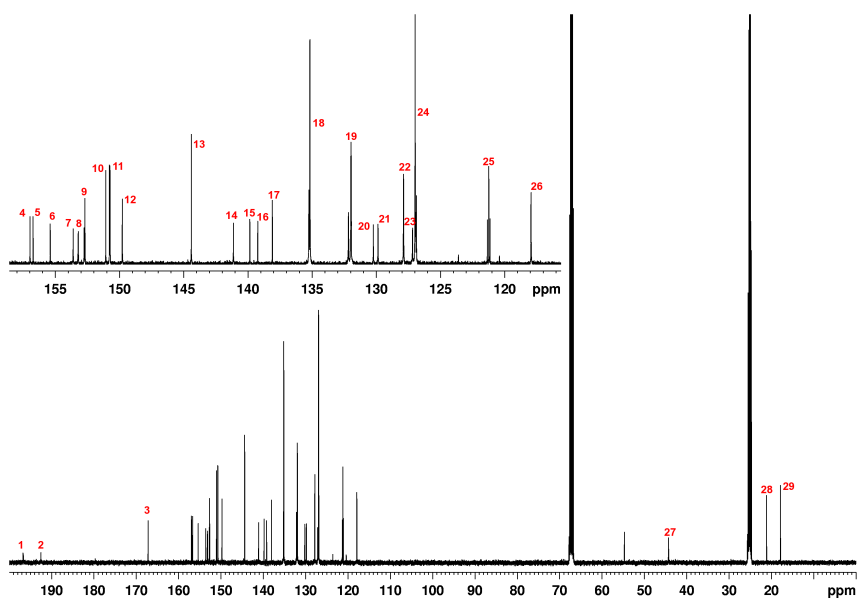
Fig. 77 ^{13}C{^{1}H} NMR spectrum of **[Dyad 3 Pic][OTf]** (THF-d_8 100.6 MHz).
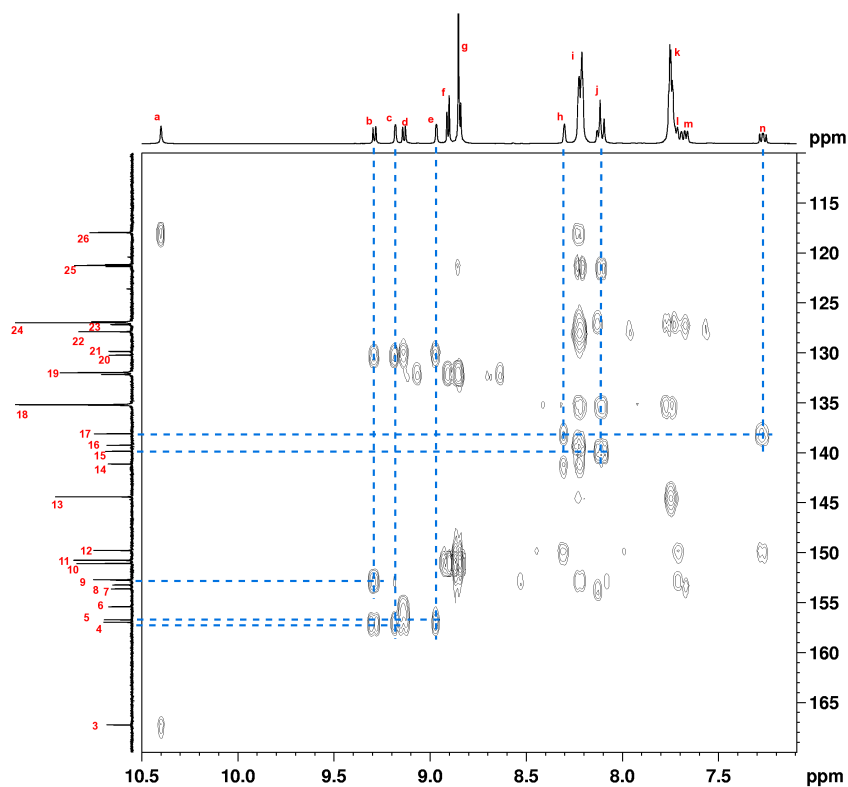
Fig. 78 ^{1}H-^{13}C HMBC NMR spectrum of **[Dyad 3 Pic][OTf]** (THF-d_8 400 MHz).

Table 4 contains the chemical shifts for various groups within compounds **3e**, **3f** and **[Dyad 3 Pic][OTf]**. It is apparent that the electron density on the Bpy increases on addition of rhenium bromide and then more so on substitution of bromide for picoline. Following this sequence, the shift of the Bpy CH_3, CH_2 and ring protons is either very similar to the previous compound or increases significantly. This increase in deshielding can also be seen in Fig. 79 where the spectra for the amide, CH_2 and CH_3 protons are stacked above one another.

3e (THF)	3f (THF)	[Dyad 3 Pic][OTf] (THF)	Assignment
2.49	2.60	2.68	Bpy CH$_3$
3.95	4.09	4.27	CH$_2$
7.21	7.47	7.71	Bpy
7.55	7.73	8.15	Bpy
7.78	7.73	7.79	*m-*, *p-* phenyl
8.09	8.05	8.15	*m*-amidophenyl
8.14	8.13	8.26	*o*-amidophenyl
8.23	8.18	8.26	*o*-phenyl
8.46	8.45	9.01	Bpy
8.56	8.64	9.17	Bpy
8.67	8.90	9.22	Bpy
8.67	9.03	9.33	Bpy
8.85	8.82	8.89	β pyrrole
8.92	8.86	8.95	β pyrrole
9.73	9.82	10.44	amide

Table 4 ^{1}H NMR shifts (ppm) for compounds **3e**, **3f** and **[Dyad 3 Pic][OTf]**.
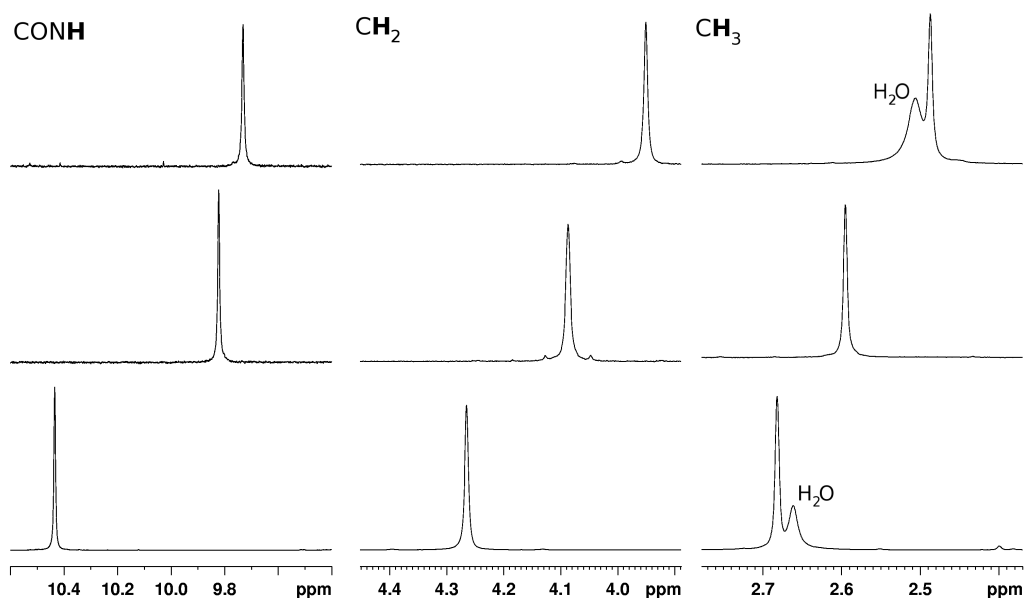
Fig. 79 ^{1}H NMR spectra (THF-d_8); top to bottom **3e**, **3f**, **[Dyad 3 Pic][OTf]**; left to right amide proton, methylene proton, methyl proton.

2.6.9 NMR spectroscopy of mononuclear rhenium complexes

The proton NMR spectrum of **6b** is shown in Fig. 80. There are three signals in the aromatic region that integrate in a 1:1:1 ratio indicating the presence of the bipyridine unit. The CH_3 and CH_2 groups of the ethyl are characteristic at $\delta = 1.4$ and 4.25 respectively. The CH_2 protons exhibit complex splitting due to $^3J_{HH}$ and $^3J_{HP}$ coupling. The CH_3 group is present as a triplet of doublets due to $^3J_{HH}$ and $^4J_{PH}$ couplings. The COSY spectrum of the aromatic region (Fig. 81) shows a coupling between the signals at $\delta = 7.53$ and 9.19 indicating that these are the 5,6 pair. The proton of the 5 position is typically observed 2 ppm to lower field than the 6 position in the Bpy structure. This agrees with the deshielding effect of the electronegative nitrogen atom. The signals at $\delta = 7.53$ and 9.19 were assigned as the protons at the 5 and 6 position respectively. The aliphatic region showed the expected coupling between CH_2 and CH_3 signals.
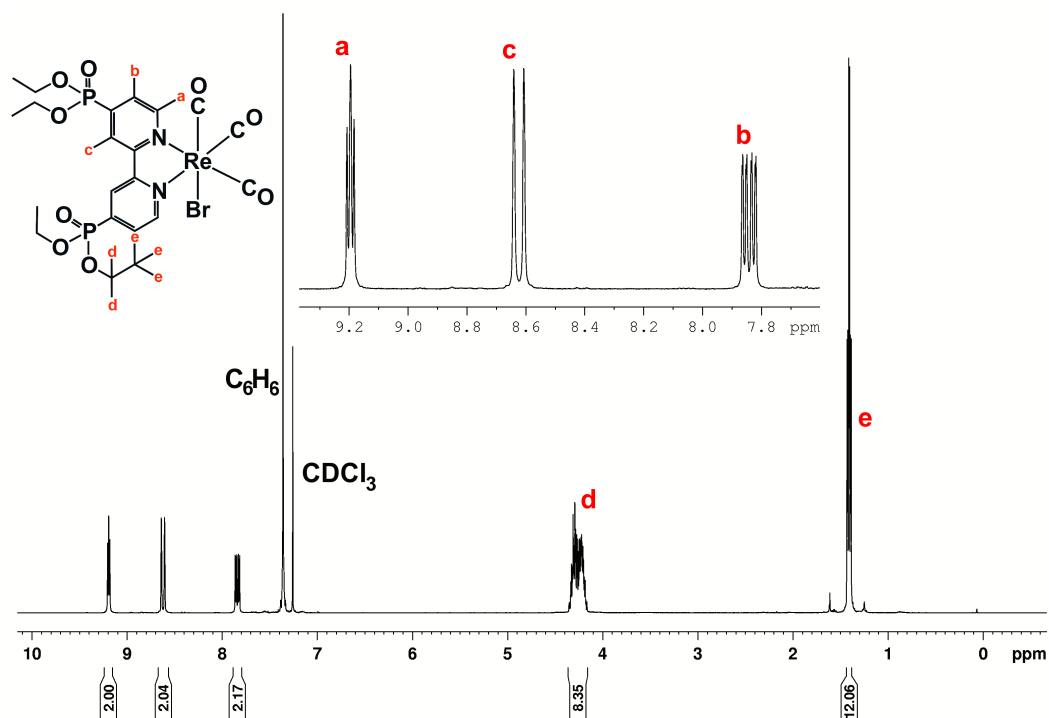
Fig. 80 ^{1}H spectrum of **6b** (CDCl$_3$ 400 MHz).
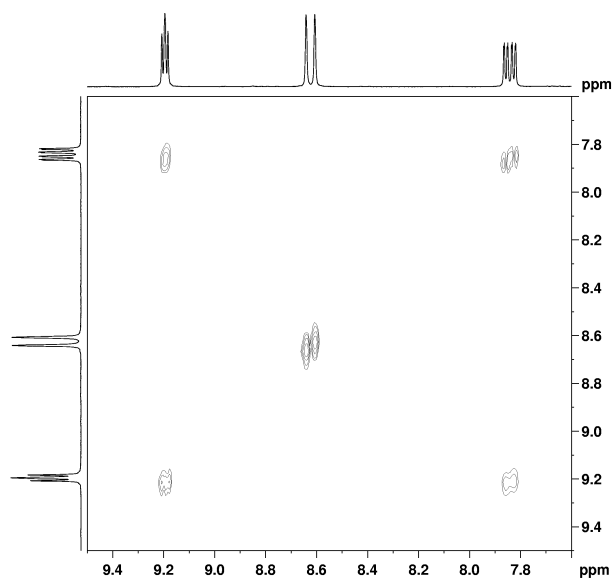
Fig. 81 ^{1}H-^{1}H COSY NMR spectrum of **6b** (CDCl$_3$ 400 MHz).

The ^{31}P{^{1}H} NMR spectrum (Appendix page 249) shows one signal as the compound has a plane of symmetry between the two phosphorus atoms. The ^{13}C{^{1}H} NMR spectrum (Fig. 82) exhibits five aromatic signals for the pyridine ring, two aliphatic signals for the ethyl groups and signals at δ = 155.5 and 196

94

which are thought to be the carbonyl groups. The signals at δ = 128.5 and 77 are due to residual C_6H_6 and $CDCl_3$ respectively. The HMQC spectrum allowed assignment of carbon signals for atoms bound directly to protons. The remaining unassigned ^{13}C signals were **4** and **6**, both of which showed HMBC correlation to proton **a** and nothing else. **4** and **6** were assigned on the basis of chemical shift.
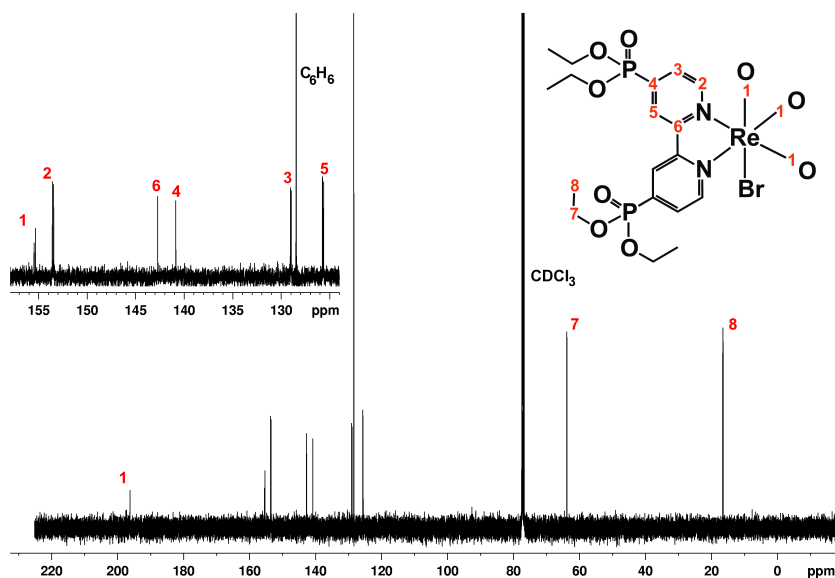
Fig. 82 $^{13}C\{^1H\}$ NMR spectrum of **6b** ($CDCl_3$ 100.6 MHz).

The bromide was substituted for picoline to produce compound **6c**. The ^1H and ^{13}C NMR spectra were fully assigned with the aid of two-dimensional NMR spectroscopy. The ^1H NMR spectrum is shown in Fig. 83 and exhibits several characteristic signals. In $CDCl_3$ the signals are mostly well separated apart from the multiplet at δ = 8.1 containing bipyridine protons and a picoline proton. However, the signals are not totally coincident and some of the individual peak shape is evident. In the aromatic region, the bipyridine and picoline protons can be told apart on the basis of integration ratio and multiplicity. Further upfield, the ethyl and picoline methyl protons are characteristic in multiplicity, chemical shift and integration ratio. The ethyl protons also exhibit complex splitting due to coupling with phosphorus. The $^{31}P\{^1H\}$ NMR spectrum (Fig. 85) exhibits two signals of typical chemical shift for phosphonate and PF_6 phosphorus environments. The splitting due to coupling with fluorine (712 Hz) provides extra confirmation of the PF_6 signal. The spectrum shows good purity. The

presence of PF$_6$ shows that a cationic rhenium species has indeed been formed. In the ^{13}C spectrum it was possible to observe signals for the carbonyl ligands.
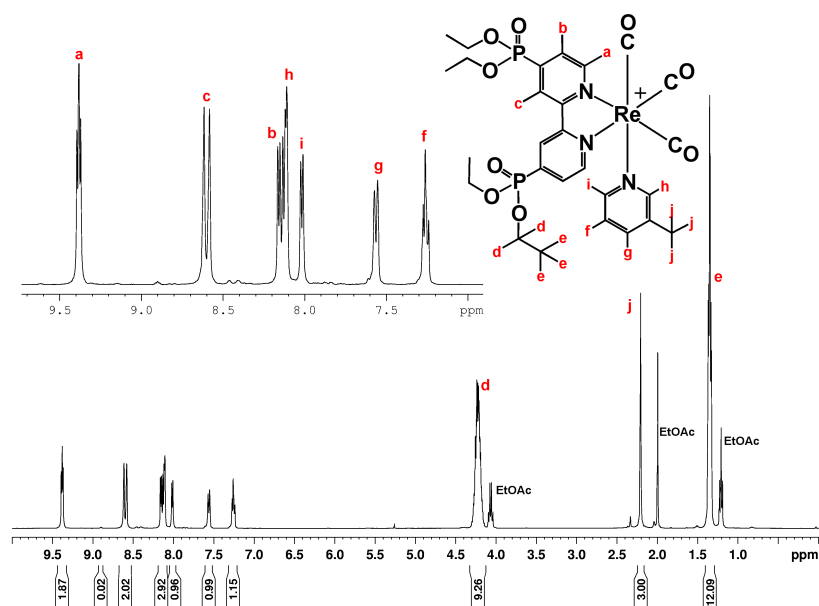
Fig. 83 ^{1}H NMR spectrum of **6c** with structural assignment (CDCl$_3$ 400 MHz).
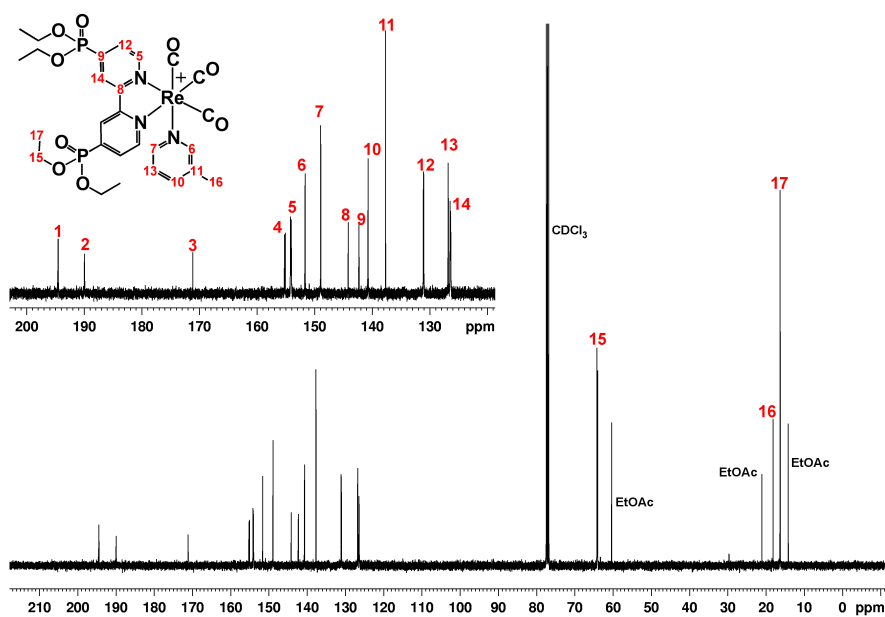
Fig. 84 ^{13}C{^{1}H} NMR spectrum of **6c** with structural assignment (CDCl$_3$ 100.6 MHz).
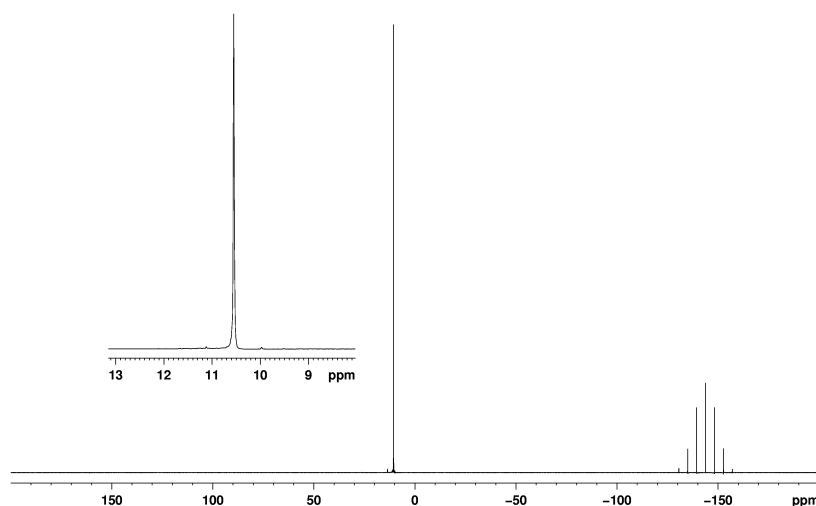
Fig. 85 ^{31}P{^{1}H} NMR spectrum of **6c** (CDCl$_3$, 109 MHz).

^{1}H-^{1}H COSY NMR spectroscopy (Appendix page 250) showed couplings between signals **a** and **b** suggesting they are the 5,6 proton pair on the bipyridine and therefore **c** must be at the 3 position. Signal **f** couples with **i** and **g** and must be the proton at the picoline 5 position. **g** and **h** both exhibit a longer range coupling to **j** suggesting they are the protons at the 4 and 2 positions respectively. **i** must therefore be the proton at the 6 position. In the HMQC NMR spectrum (example region in Fig. 86) all the proton signals show a correlation to a carbon signal and these carbon signals have been assigned accordingly. This leaves ^{13}C NMR signals **8,9,11,1,2** and **4**. **1,2**, and **4** are the furthest downfield, consistent with a carbonyl signal. **8,9** and **11** remain and must be the three quaternary carbons. In the HMBC NMR spectrum (Appendix page 251) **11** correlates with protons **h** and **f** and is assigned as the 3 position of the picoline. **8** and **9** must be the 2 and 4 position of the bipyridine but both correlate with proton **a**, confirming they are part of the bipyridine but providing no way of discriminating between the two. Typically the carbon of the 2 position is slightly downfield of the 4 position and the signals were assigned on this basis.

97
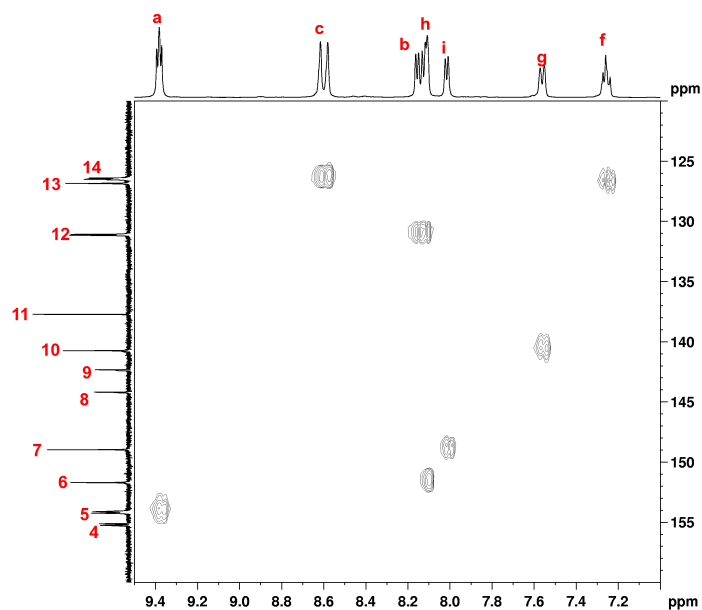
Fig. 86 ^{1}H-^{13}C HMQC NMR spectrum of **6c** (CDCl$_3$ 400 MHz).

The phosphonate ester groups were cleaved to produce the phosphonic acid **6d**. The ^{1}H NMR spectrum is typical of bipyridine and picoline and the ethyl groups have gone (Fig. 87). There is a slight bipyridine impurity and some residual ether from recrystallisation. A significant upfield shift in the ^{31}P signal indicates good purity and the formation of phosphonic acid (Fig. 88). The signal is broad, this may be because one group is deprotonated and one is not and exchange of the protons is occurring. The absence of a PF$_6$ ^{31}P signal suggests the overall charge of the complex has changed. It is likely one acid group is singly deprotonated resulting in a zwitterion complex that is neutral overall.
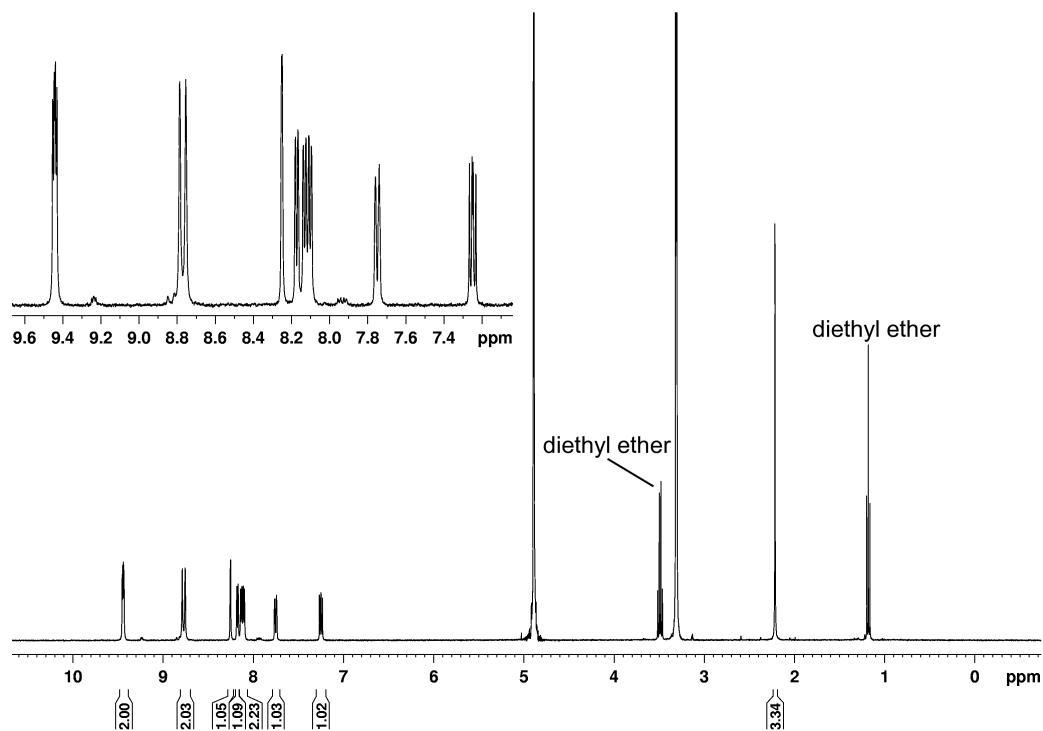
Fig. 87 ^{1}H NMR spectrum of **6d** in (CD$_3$OD 400 MHz).
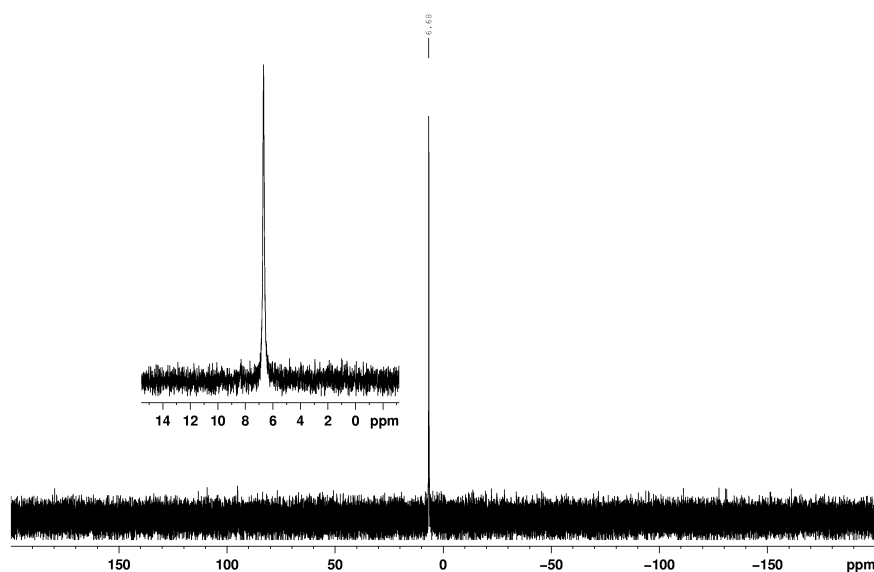
Fig. 88 ^{31}P{^{1}H} NMR spectrum of **6d** in (CD$_3$OD, 109 MHz).

Table 5 contains the chemical shifts for groups present in compounds **6b, 6c** and **6d**. The POEt groups are largely unaffected by substitution of bromide for picoline as the CH$_3$, CH$_2$ and ^{31}P signals are at very similar chemical shift. Introduction of the picoline ligand increases electron density on the Bpy as the

signals for the protons on the pyridine rings move to higher shift. Cleavage of the phosphonate ester to produce **6d** causes a significant downshift in the ^{31}P signal. This is shown graphically in Fig. 89.The Bpy signals are also shifted down indicating an increase in electron density. The picoline signals are barely different to those of **6c** suggesting changes to the periphery of the Bpy ligand have little effect on the axial ligand.

6b (CD$_3$OD)	6c (CD$_3$OD)	6d (CD$_3$OD)	Assignment
1.40	1.39		ethyl CH$_3$
	2.22	2.22	picoline CH$_3$
4.30	4.30		ethyl CH$_3$
	7.26	7.25	picoline
	7.76	7.75	picoline
	8.14	8.17	picoline
8.00	8.18	8.12	Bpy
	8.27	8.25	picoline
8.95	8.90	8.77	Bpy
9.27	9.55	9.44	Bpy
---	---	---	---
12.51	11.72	6.68	PO$_3$R(^{31}P)

Table 5 NMR shifts (ppm) for compounds **6b**, **6c** and **6d** (400 MHz).
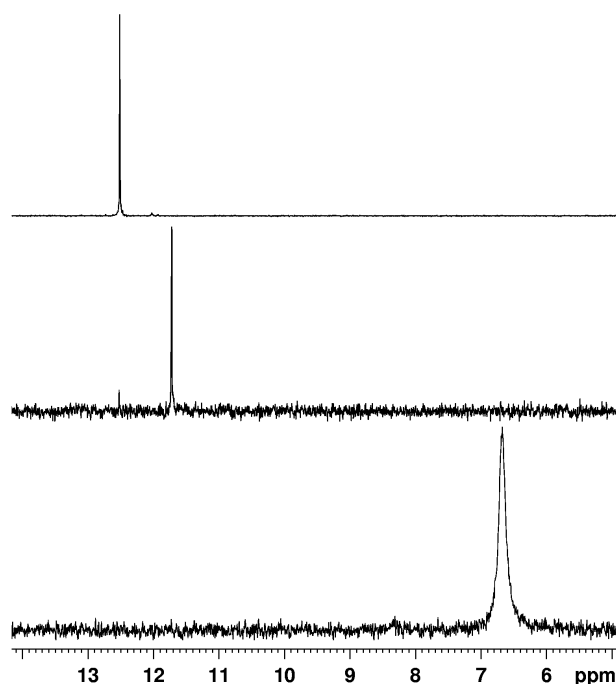
Fig. 89 ^{31}P{^{1}H} NMR spectra of **6b**, **6c** and **6d** (CD$_3$OD, 109 MHz).

2.6.10 NMR spectra of phosphonate porphyrins

Amino porphyrin was coupled to diethylphosphonoacetic acid to produce **7a**. All the proton signals are very characteristic in terms of chemical shift, integration ratio and splitting (Fig. 90). The internal ring protons are at $\delta = 2.8$. The CH$_2$ and CH$_3$ of the ethyl groups provide the signals at $\delta = 1.3$ and 4.3 respectively. The CH$_3$ signal is present as a triplet due to coupling with the CH$_2$. The CH$_2$ signal is more complex due to coupling with the CH$_3$ and phosphorus. The signal at $\delta = 3.15$ comes from the CH$_2$ adjacent to the amide and is present as a doublet due to coupling to phosphorus. The remaining signals in the aromatic region all arise from the porphyrin apart from the signal at $\delta = 9.2$ worth one proton due to the amide. The β, *o*-phenyl and *m,p*-phenyl protons can be observed as the multiplets at $\delta = 8.85$, 8.2 and 7.75 respectively. The remaining signal at $\delta = 7.95$ is due to the *m*-amidophenyl protons. The ^{31}P{^{1}H} NMR spectrum in Appendix page 252 shows one signal indicating purity and that the phosphonate group has been incorporated.

101
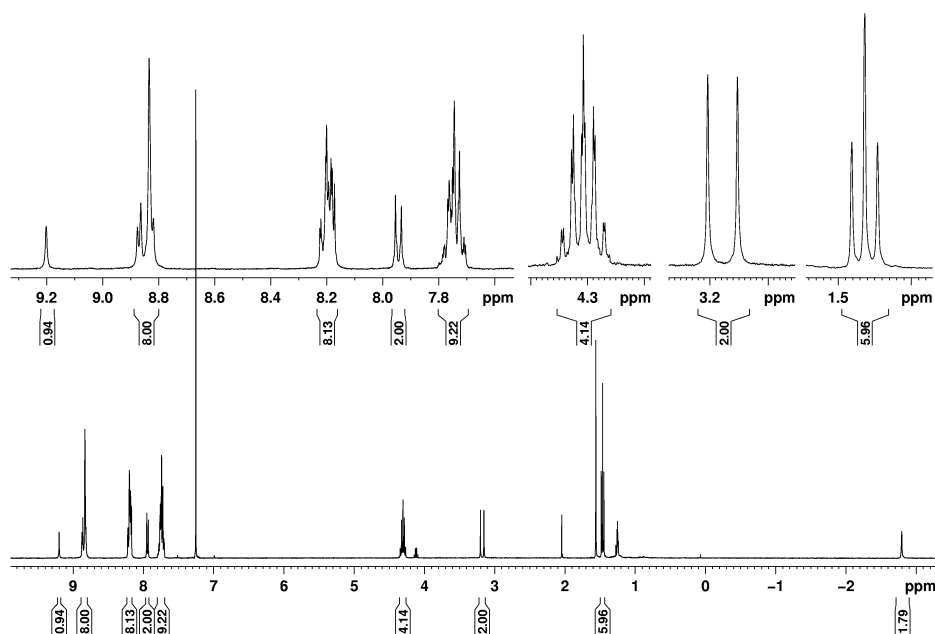
Fig. 90 ^{1}H NMR spectrum of **7a** (CDCl$_3$ 400 MHz).

Zinc was coordinated to the porphyrin core to yield **7b**. The signal at δ = -2.8 has been lost in agreement with coordination of zinc. The remaining structural protons are all the same as for **7a**. The CH$_2$ adjacent to the amide has shifted upfield by almost 0.5 ppm. The amide has moved significantly upfield by 0.8 ppm and the amidophenyl protons have also shifted. This suggests the protons in the functionalised arm of the porphyrin are very sensitive to the electronics of the macrocycle core, more so than the protons on the three phenyl groups around the ring. However the shift of the phosphorus is not much different (Appendix page 252) indicating it may be too remote or perhaps insulated from the electronics of the porphyrin by the CH$_2$ group. The CH$_2$, though almost as distant as the phosphorus, remains sensitive to the presence of the zinc. These shifts are tabulated in Table 6. The ^{31}P resonances for both **7a** and **7b** were sharp. The free acid compound **7c** is not included in the table because the spectra were run in CD$_3$OD as it was insoluble in CDCl$_3$.
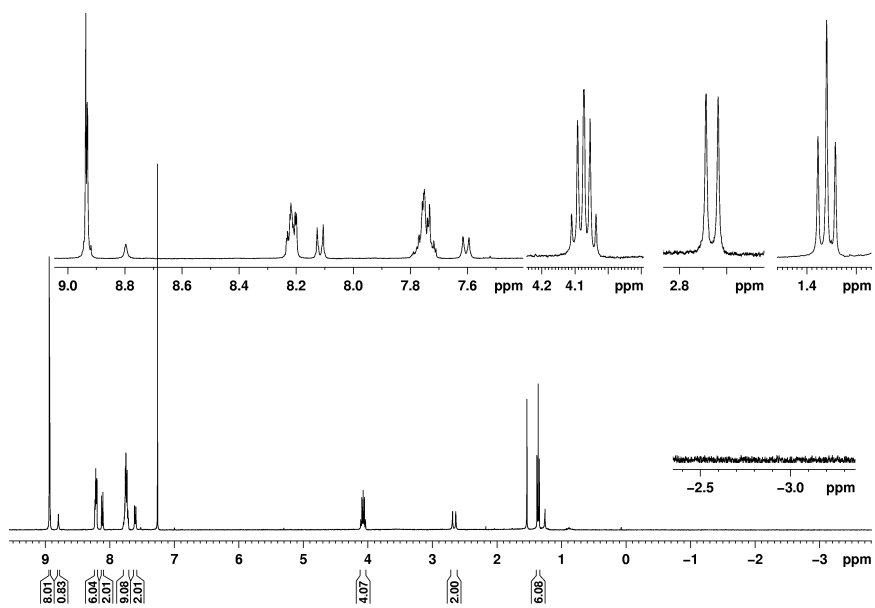
Fig. 91 ^{1}H NMR spectrum of **7b** (CDCl$_3$ 400 MHz).

7a (CDCl₃)	7b (CDCl₃)	Assignment
1.46	1.36	CH$_3$
3.18	2.66	CH$_2$
4.31	4.07	ethyl CH$_2$
7.74	7.75	*m-*, *p-* phenyl
7.94	7.60	*m*-amidophenyl
8.19	8.12	*o*-amidophenyl
8.19	8.21	*o*-phenyl
8.85	8.94	β-pyrrole
9.20	8.80	amide
---	---	---
23.54	22.68	^{31}P

Table 6 NMR shifts (ppm) for compounds **7a** and **7b**.

The phosphonate ester was cleaved to produce the free acid compound **7c** (Fig. 92). The transformation was performed in the presence of Et$_3$N to prevent demetallation. The absence of signals in the δ = -2.0 – -3.0 region demonstrate that this succeeded. However, a triethylammonium salt was formed and one equivalent is present in the spectrum. The acid group is therefore expected to exist singly deprotonated (Fig. 93). The CH$_2$ adjacent to the amide can be observed at δ = 3.0. The amidophenyl protons remain separated from the larger multiplets. Neither the amide proton nor the OH proton can be observed due to exchange with deuterons from the protic solvent. The ^{31}P signal is sharp and a

significant upfield shift confirms hydrolysis of the phosphonate ester (Appendix page 253). The spectrum is proton coupled and a triplet is observed due to coupling to CH_2 (J_{HP} = 19 Hz). Proton decoupling led to a singlet.
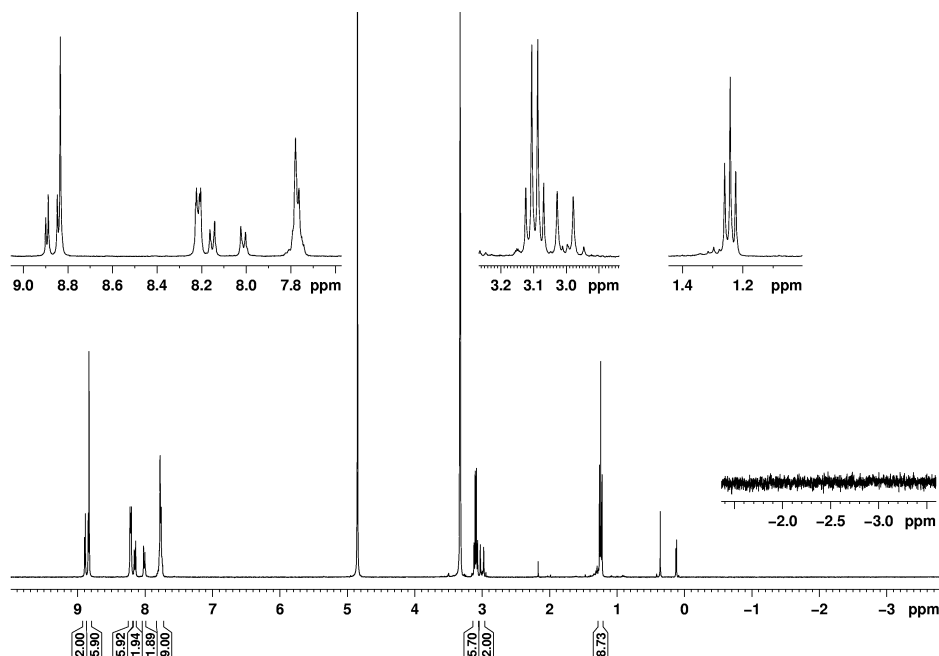
Fig. 92 ^{1}H NMR spectrum of **7c** (CD$_3$OD 400 MHz).
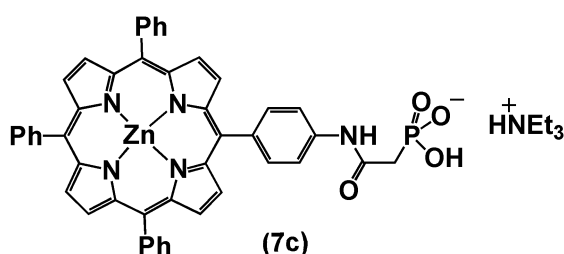
Fig. 93 Compound **7c** zinc porphyrin with phosphonic acid functionality. The preparation of this compound is performed in the presence Et$_3$N and ^{1}H NMR spectroscopy indicates one equivalent of HNEt$_3$ is present.

2.6.11 Mass spectrometry

The high resolution ESI-MS of **[Dyad 2 Pic][OTf]** is given in Fig. 94. There is one predominant signal with a high number of counts. The mass matches the calculation closely, with a difference of 2.4 mDa. The isotope pattern for a compound containing rhenium and zinc is quite complex and unique.

105

Furthermore for a compound with 73 carbon atoms there is a significant contribution from molecules with 72 ^{12}C and a ^{13}C. The only significant difference between the experimental and calculated isotope patterns is the half mass peaks present in the former. The half mass signals originate from dimers. Since **[Dyad 2 Pic][OTf]** contains 73 carbon atoms the probability of there being one ^{13}C is quite high; a dimer consisting of one molecule with an odd mass and one molecule with an even mass will give a combined odd mass. Division of an odd mass by the 2+ charge results in half mass values. A propensity to dimerise maybe advantageous for catalysis as many proposed mechanisms for CO_2 reduction by rhenium complexes suggest that two Re molecules must come to together. However, dimerization is less likely in catalytic solution as the concentration is low (0.05 mM) and coordinating solvent (DMF and TEOA) may interrupt intramolecular interactions. Overall the mass spectrum is good confirmation of having synthesised compound **[Dyad 2 Pic][OTf]** and provides some indication of purity.
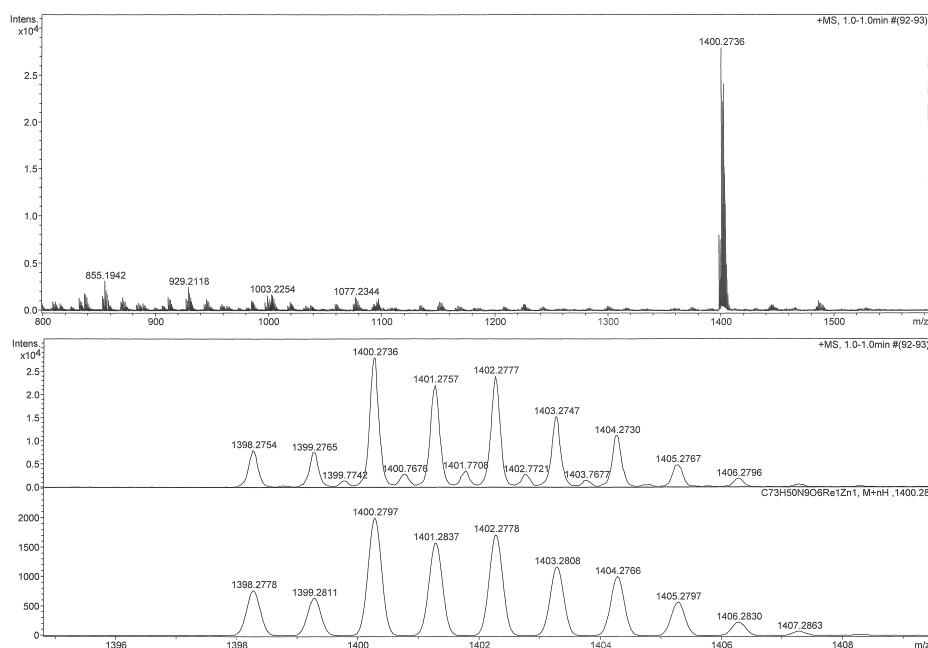
Fig. 94 HR-ESI-MS of **[Dyad 2 Pic][OTf]**, top: full scan, middle: observed and bottom: calculated isotope pattern.

The high resolution-ESI-MS of the dyad with the methylene spacer (**[Dyad 3 Pic][OTf]**) is shown in Fig. 95. The counts are low but the molecular ion can be

observed. An expansion of the isotope pattern reveals that the compound contains rhenium and zinc and matches the calculation in terms of mass. The mass spectra have been discussed with reference to the ^{185}Re and ^{64}Zn peaks. However, in this spectrum the low signal to noise distorts this signal and it does not have a sharp peak. Comparison between the observed and calculated signals at m/z = 1265 indicates a difference of mass of 2.3 mDa.
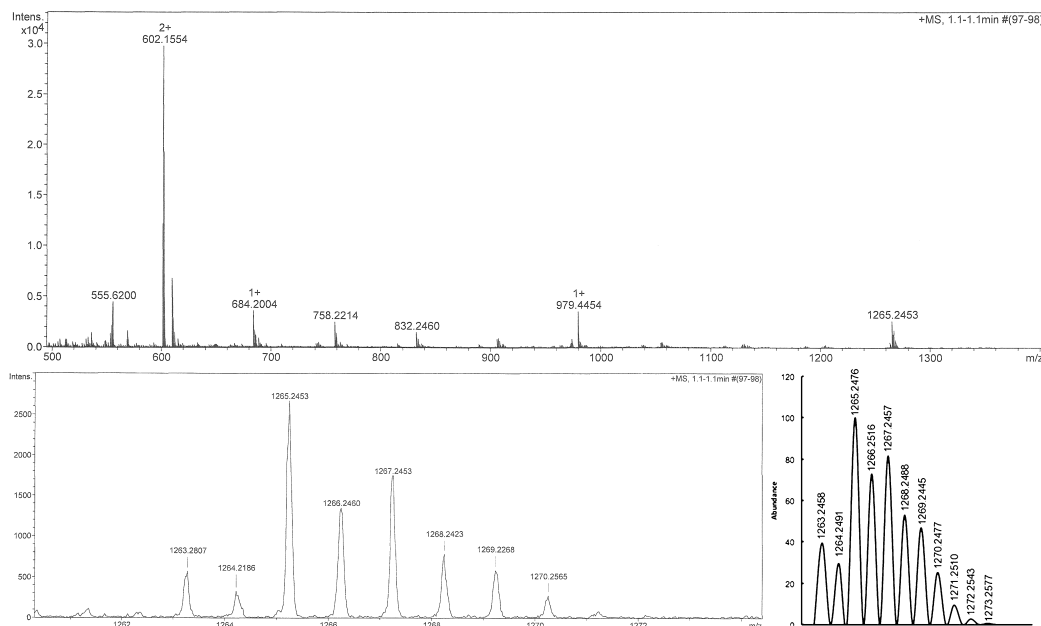
Fig. 95 HR-ESI-MS of **[Dyad 3 Pic][OTf]**, top: wide scan, bottom left: zoom on M$^+$, bottom right: calculated isotope pattern.

The ESI-MS of the mono-nuclear rhenium complex with phosphonic acid groups (**6d**) is given in Fig. 96. The rhenium atom is formally positively charged and the NMR spectrum indicated that the PF$_6$ counter-ion is no longer present. The complex alone must therefore be overall neutral and so an anionic unit must also exist (Fig. 97). A likely source of a negative charge in the molecule is deprotonation of one of the acid groups. A signal for **6d** was only observed in the negative ion mode indicating that a second deprotonation occurred instead of protonation to form the positive complex. The isotope pattern and masses agree with those calculated for the deprotonated species. The spectrum also suggests good purity and that the iodine of the ISi(CH$_3$)$_3$ has not substituted the picoline ligand as was observed with BrSi(CH$_3$)$_3$.

The zinc porphyrin with phosphonic acid group, **7c**, was observed in the negative ion mode of the ESI-MS. From ^{1}H NMR spectroscopy it is evident that one equivalent of triethylammonium is present. This suggests that the acid group exists singly deprotonated and as a salt. Observing **7c** as a negatively charged ion in the ESI-MS confirms this (Fig. 98).
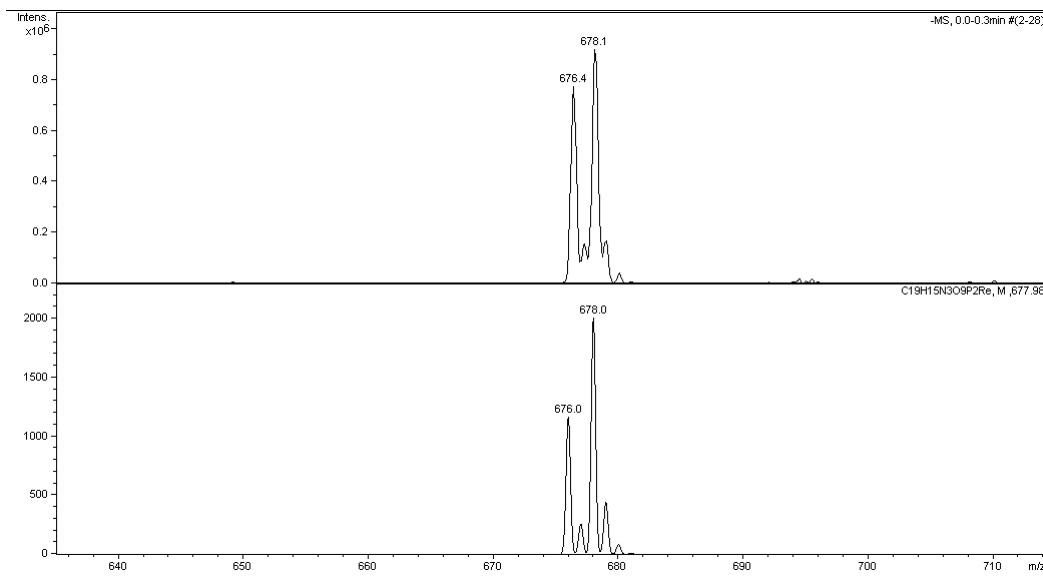
Fig. 96 Negative ion mode ESI-MS of **6d**. Top: observed spectrum, bottom: calculated spectrum.

(6d)
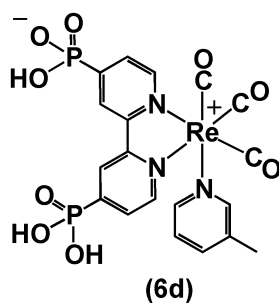
Fig. 97 Zwitterionic form of **6d**. The complex was detected in the ESI-MS in negative ion mode strongly suggesting a second deprotonation of an acid group.

108
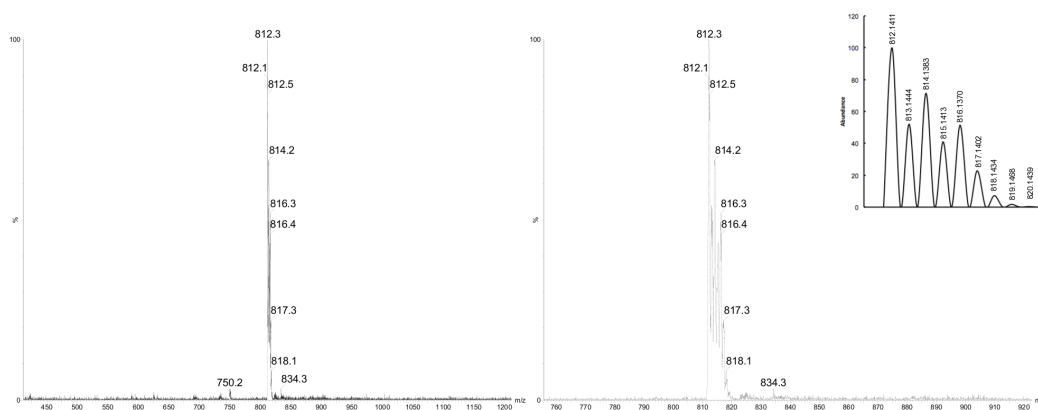
Fig. 98 ESI-MS of **7c**. Left: full scan, right: zoom of isotope pattern, inset: calculated isotope pattern.

2.6.12 Infrared spectroscopy

All compounds containing rhenium carbonyl groups were analysed by infrared spectroscopy. All spectra are focused on the carbonyl region, scanning from 1800 to 2100 cm^{-1}. The spectra are measured in solution unless otherwise stated. The choice of solvent was limited by solubility; all the bromides were run in THF and where possible the picoline compounds were run in CH$_2$Cl$_2$. The free acid compound **6d** was run in methanol. The IR spectrum of the methoxybenzamide spacer dyad with bromide ligand (**Dyad 2 Br**) is shown in Fig. 99. Group theory analysis of the rhenium centre allows for calculation of the number of bands expected based on symmetry. In all cases the three carbonyl ligands bind with *fac* geometry. The bromide complexes belong to the C$_S$ symmetry group producing three IR active modes (2A' + A''). The CO ligand is σ-donating and π-accepting in terms of electron density with respect to the metal. Electron density is accepted into an anti-bonding orbital, weakening the CO bond and causing a reduction in wavenumber. The IR spectra of carbonyl ligands are very sensitive to the electronics of the metal centre. It is clear from Fig. 99 that there is significant back donation from rhenium to CO as the signals are at much lower wavenumbers than those of free carbon monoxide (2143 cm^{-1}). The spectrum shows good purity with negligible additional CO stretches.

109
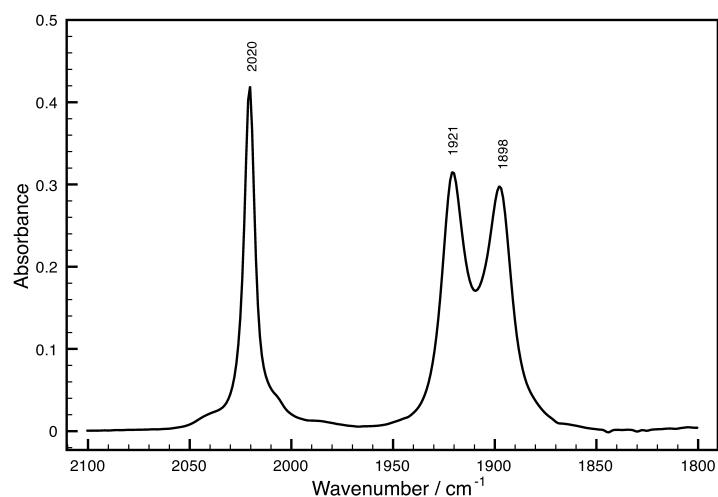
Fig. 99 Infrared spectrum of **Dyad 2 Br** in THF.

The IR spectrum of the methoxybenzamide spacer dyad with picoline ligand (**[Dyad 3 Pic][OTf]**) is shown in Fig. 100. The picoline complexes are of greater symmetry than the bromides. The picoline and two pyridine rings of the Bpy are similar in structure and electronics. The symmetry group of the picoline Bpy complexes is *pseudo*-C_3v as the three pyridine rings are not identical. The spectrum has two stretches, as predicted by group theory ($A_1 + E$) instead of the three seen for the bromides. The stretch at lower wavenumber is quite broad and two peaks can be made out, because the three pyridine rings are not identical. The stretches are at significantly higher wavenumber than for the bromide complexes because the rhenium centre is now formally cationic. Less electron density on the metal leads to a reduction in π-acceptance by the CO, the carbon-oxygen bond is stronger and so the stretching frequency increases. The spectrum also indicates all the bromide complex precursor has been consumed.
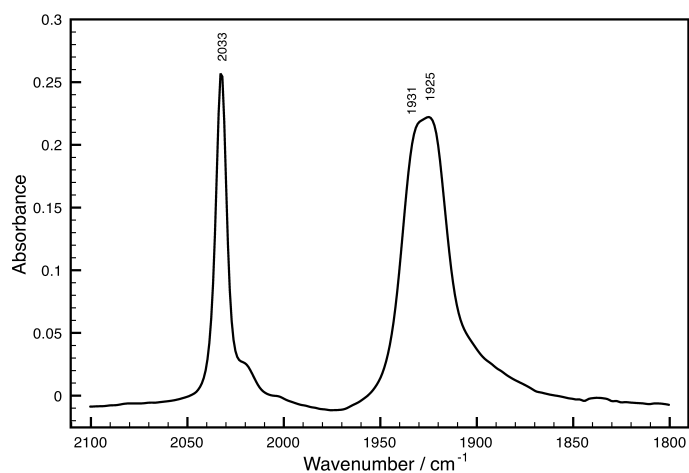
Fig. 100 IR spectrum of **[Dyad 2 Pic][OTf]** in THF.

The IR spectra of the rhenium bromides **Dyad 2 Br** and **6b** and the picoline complexes **[Dyad 3 Pic][OTf]**, **6c** and **6d** are very similar. ATR infrared spectra were run to analyse the organic components of the molecules as signals should arise from the amide C=O and N-H and from the Bpy imine C=N.

2e	2g	Dyad 2 Br	[Dyad 2 Pic][OTf]	Dyad 3 Br	[Dyad 3 Pic][OTf]	Assignment
		2021	2031	2021	2029	CO
		1891 (b)	1917 (b)	1935	1912 (b)	CO
				1892		CO
1670	1671	1665 (b)	1665 (b)	1668 (b)	1676 (b)	C=O
1600						NH$_2$ scissoring
	1590	1595	1594		1676 (b)	C=N
	1517	1521	1519	1525	1522	2° amide N-H
1514						N-H
1175 (s)						C-N

Table 7 Functional group IR signals of compounds **2e**, **2g**, **Dyad 2 Br**, **[Dyad 2 Pic][OTf]**, **Dyad 3 Br** and **[Dyad 3 Pic][OTf]** {(s) = sharp, (b) = broad}.

IR signals of the mononuclear rhenium complexes **6b**, **6c** and **6d** are given in Table 8. The CO stretches of the bromide are at higher wavenumbers than those of both the dyad bromides, in agreement with the incorporation of two electron-withdrawing phosphonate groups. The picoline complex also shows higher wavenumber stretches than either of the dyads. There is little difference in the wavenumbers of the P=O and P-O stretches suggesting that these bonds are relatively unaffected by changes in the axial ligand.

Comparison of the IR spectrum of the free phosphonic acid compound (**6d**) with that of **6c** shows the stretches are slightly higher in wavenumber due to the loss of the ethyl groups and their associated +I effect. The rhenium is even more electron deficient and back-bonding is further reduced. The P=O signal has significantly reduced in wavenumber indicating a weaker bond.

6b	6c	6d	Assignment
Solution			
2024	2036	2037	CO
1930	1927	1932	CO
1901			CO
ATR			
1258	1257	1156	P=O
1011	1014		P-OEt
975	971		P-OEt

Table 8 Functional group IR signals for compounds **6b**, **6c** and **6d**.

Table 9 contains the IR signals for compounds **7b** and **7c**. Cleavage of the PO-Et bonds produces **7c**. There is very little difference in the signals for C=O and N-H in agreement with the idea that the electronics of these groups are unaffected by the PO_3R group.

7b	7c	Assignment
1664	1657 (b)	C=O
1237 (b)	1020	P=O
1523	1523	2° amide N-H

Table 9 Functional group IR signals for compounds **7b** and **7c** {(b) = broad}.

2.6.13 X-ray crystallography

[Dyad 1 Pic][PF$_6$] was crystallised by layering hexane on dichloromethane. The structure is given in Fig. 101. There is disorder in one of the phenyl groups and the zinc atom sits out of the porphyrin ring by 0.257 Å (ESD .001 Å). It is typical in tetraphenyl porphyrin structures for the phenyl groups to be twisted with respect to the plane of the porphyrin. The C$_6$H$_4$ ring joined to the amide is 65.7° out of the plane of the porphyrin. The C$_6$H$_4$ ring is 69.3° out of the plane of the Bpy and as such, the Bpy is almost coplanar with the porphyrin, separated by only 9.2°. The two rings of the bipyridine are not quite coplanar as there is a twist of 8.3°. Only on acquiring X-ray data was is possible to identify that the compound exists as a dimer due to coordination of the amide carbonyl oxygen to the zinc (O-Zn bond length 2.215 Å).
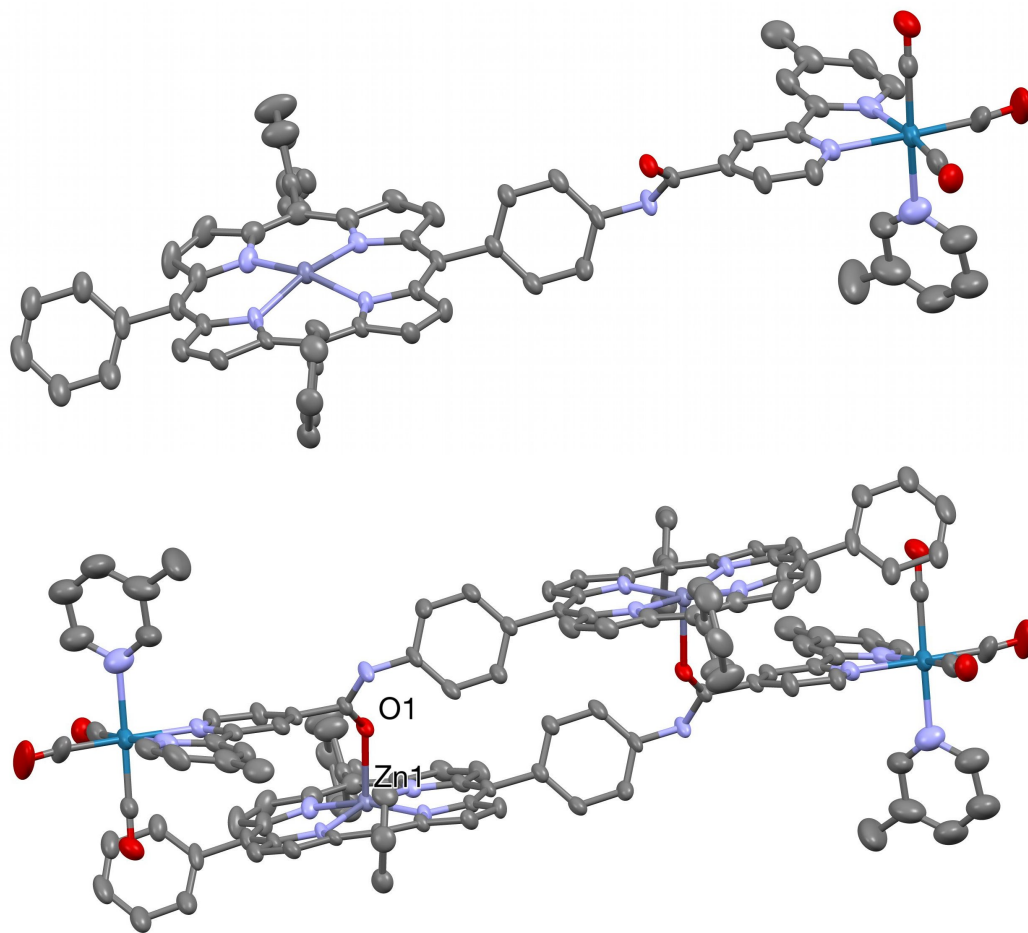
Fig. 101 X-ray crystal structure of **[Dyad 1 Pic][PF₆]**. Hydrogen atoms omitted for clarity. Disorder at one phenyl omitted for clarity. Thermal ellipsoids shown with probability of 50%. Top: monomer, bottom: dimer. Selected bond length (Å): Zn(1)-O(1): 2.216(4).

Compound **2d**, the free-base porphyrin with the methoxybenzamide spacer and nitro group was crystallised by slow evaporation of dichloromethane. The structure is shown in Fig. 102 and there was no disorder. There is a twist in the C_6H_4 unit with respect to the porphyrin of 50.54(10)°. The plane of the methoxybenzamide ring is only 10.99° out of the plane of the C_6H_4. It is possible to observe a hydrogen bond between the amide hydrogen and the methoxy oxygen, confirming NMR measurements. The plane of the six membered ring containing the hydrogen bond is 8.20° out of the plane of the methoxybenzamide ring.
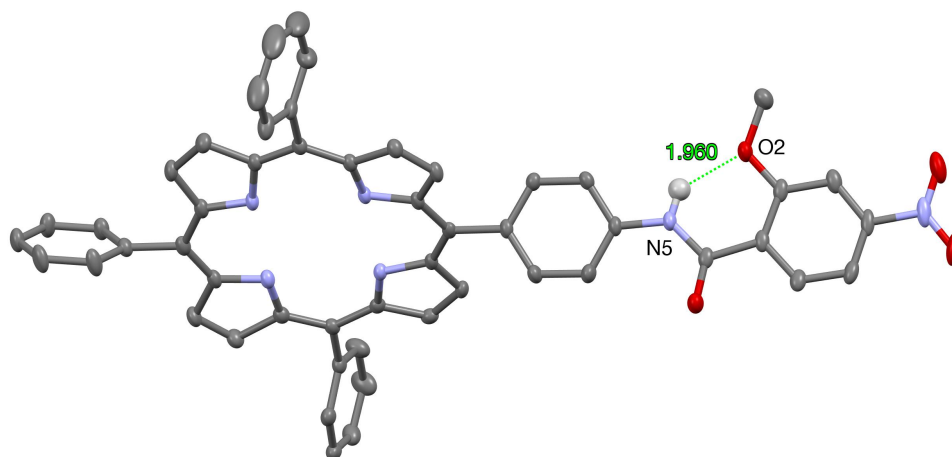
Fig. 102 X-ray crystal structure of **2d**. Selected hydrogen atoms removed for clarity. Hydrogen atom shown was located. Thermal ellipsoids shown with probability of 50%. Selected bond length (Å): O(2)-N(5): 2.658(4).

Plane 1	Plane 2	Twist / ° (ESD)
[Dyad 1 Pic][PF$_6$]		
Porphyrin	C$_6$H$_4$	65.7(3)
Bpy	C$_6$H$_4$	69.3(3)
Porphyrin	Bpy	9.2(2)
Bpy ring	Bpy ring	8.3(3)
2d		
Porphyrin	C$_6$H$_4$	50.54(10)
C$_6$H$_4$	Methoxybenzamide	10.99(11)
H-bond ring	Methoxybenzamide	8.20(10)

Table 10 Angles between planes in the crystal structures of **[Dyad 1 Pic][PF$_6$]** and **2d.**

Chapter 3. Electrochemistry and photochemistry

3.1 Electrochemistry

ReBpy(CO)$_3$X type complexes and metalloporphyrins exhibit well defined and well studied electrochemical behaviour. Under Ar in organic solvent the Re complexes typically show a one electron quasi-reversible reduction wave and, at more negative potential, an additional one electron irreversible reduction wave.[17] The first reduction has been investigated by spectroelectrochemistry and corresponds to the formation of a radical anion on the Bpy.[73] The irreversible nature of the second reduction can be explained by the strong labilising effect of the reduced diimine on the X ligand.[105] Typically ligand loss occurs unless a very strong π-accepting ligand is employed. Kubiak and co-workers showed that for the Re(tBu-Bpy)(CO)$_3$Cl catalyst the Cl is lost after the first reduction in contrast to Turner's study of Re(Bpy)(CO)Cl, which suggests Cl loss occurs as a result of the second reduction.[17] It seems the point at which the ligand is lost depends on the chemical nature of the catalyst. If the complex is catalytically active, purging with CO$_2$ will result in current enhancement prior to the second reduction wave. An example cyclic voltammogram from Ishitani and co-workers is shown in Fig. 103. The reduction potentials of the Re complexes are very sensitive to changes in structure at the bipyridine and this is illustrated by Table 11.
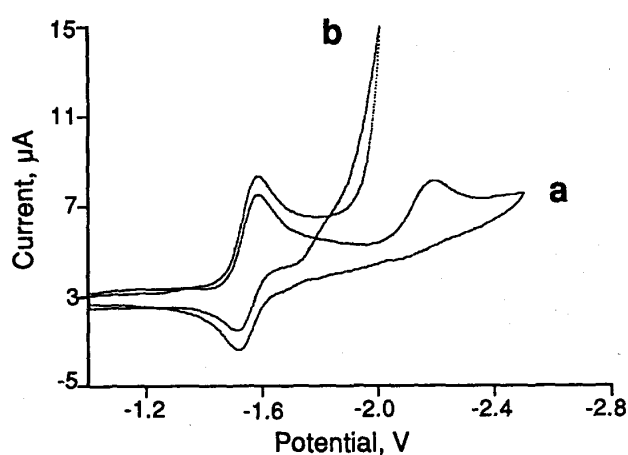
Fig. 103 CV of [Re(Bpy)(CO)$_3$\{P(OEt$_3$)\}]$^+$ in 0.1 M n-Bu$_4$NClO$_4$ in CH$_3$CN a) under Ar b) under CO$_2$.[30]

Complex	1st reduction potential (mV vs SCE)	2nd reduction potential (mV vs SCE)
Re(Bpy-COOH)(CO)$_3$Cl	-940	-1725
Re(Bpy)(CO)$_3$Cl	-1340	-1725
Re(Me$_2$Bpy)(CO)$_3$Cl	-1430	-1765
Re(Bpy-^{t}Bu)(CO)$_3$Cl	-1445	-1830
Re(Bpy-OMe)(CO)$_3$Cl	-1485	-1860

Table 11 Reduction potentials for ReL(CO)$_3$Cl complexes where L = Bpy with varying substituents at the 4 and 4' positions[17]. Electrolyte was 0.1 M Bu$_4$N PF$_6$ in CH$_3$CN.

The work herein is concerned with the photocatalytic reduction of CO_2. Current understanding of the photocatalytic mechanism is that rhenium is only reduced once, the second electron being supplied to CO_2 by another molecule of singly reduced Re complex. Furthermore the reduction potential is required for calculation of the driving force for electron transfer to the Re. Only the first reduction is relevant and therefore the following voltammetry will only explore the first reduction wave.

Zinc porphyrins typically exhibit two reversible oxidation waves and two reversible reduction waves.[106] This work looks at electron transfer from porphyrin to Re and so only the oxidation waves are investigated.

All cyclic voltammetry was performed in CH_2Cl_2 with Bu$_4$N$^+$ PF$_6^-$ electrolyte using ferrocene as internal standard. The working electrode, counter electrode and reference electrodes were Pt disc, Pt wire and Ag/AgCl respectively. Performing all the electrochemistry in the same conditions allows for

comparisons to be made as changes in solvent, electrolyte and reference electrode can significantly alter potentials.[107]

Cyclic voltammetry of zinc tetraphenyl porphyrin (ZnTPP) and $[Re(Bpy)(CO)_3Pic]^+$ was performed in exactly the same conditions in the Perutz group[108] and the redox potentials are given in Table 12. Typically 10 mg of compound was run in 5 mL of CH_2Cl_2. Solvent was lost by bubbling with Ar and for the more precious compounds less material was used. The concentration of the compounds tested by CV was in the range of 1-2 mM. CVs of **[Dyad 1 Pic][PF$_6$]** and **[Dyad 2 Pic][OTf]** and **[Dyad 3 Pic][OTf]** were also run. The CV of **[Dyad 2 Pic][OTf]** (Fig. 104) exhibits two quasi-reversible oxidations of the porphyrin and one quasi-reversible reduction. There is a signal prior to the reduction wave, which may be due to water in the compound (solvent and electrolyte were rigorously dried). The porphyrin is easier to oxidise than the simple ZnTPP, which is due to the +M effect of the nitrogen. The rhenium-centred reduction is at a less negative potential than the simple bipyridine complex due to the electron withdrawing effect of the carbonyl group. Both arguments can also be made for **[Dyad 1 Pic][PF$_6$]** and indeed there is very little difference in the oxidation and reduction potentials compared with **[Dyad 2 Pic][OTf]**.

[Dyad 3 Pic][OTf] (Fig. 105) shows two quasi-reversible oxidations at the porphyrin and a quasi-reversible reduction at the rhenium. The porphyrin oxidation potential is similar to dyad **[Dyad 2 Pic][OTf]** but the reduction of the rhenium centre is at a more negative potential than any of the dyads or the simple bipyridine complex. This is due to the +I effect of the additional CH_2 group. The shape of the rhenium-centered reduction wave is slightly different to the others as the current starts to rise again very shortly afterwards. This is probably because the reduction is at a negative enough potential to overlap with the first porphyrin reduction wave ($E_{1/2} = 1.84$ V for ZnTPP).

Complexes	$E_{1/2}^{ox}$/V	$E_{1/2}^{red}$/V	ΔE_p^{red}/mV
[ReBpy(CO)$_3$(Pic)][PF$_6$]	---	-1.57[108]	---
ReBpy(CO)$_3$Br		-1.86[108]	
ZnTPP	+0.38	---	---
ZnTPDHP	+0.14	---	---
[Dyad 1 Pic][PF$_6$]	+0.28	-1.44	91
[Dyad 2 Pic][OTf]	+0.32	-1.42	84
[Dyad 3 Pic][OTf]	+0.33	-1.68	101
Dyad 1 Br	+0.36	-1.63	120
Dyad 2 Br	+0.30	-1.60	134
2f (Dyad 3 Br)	+0.37	-1.83	127
6b	---	-1.45	124
6c	---	-1.19	70
7b	+0.27	---	---

Table 12 Redox half-wave potentials.
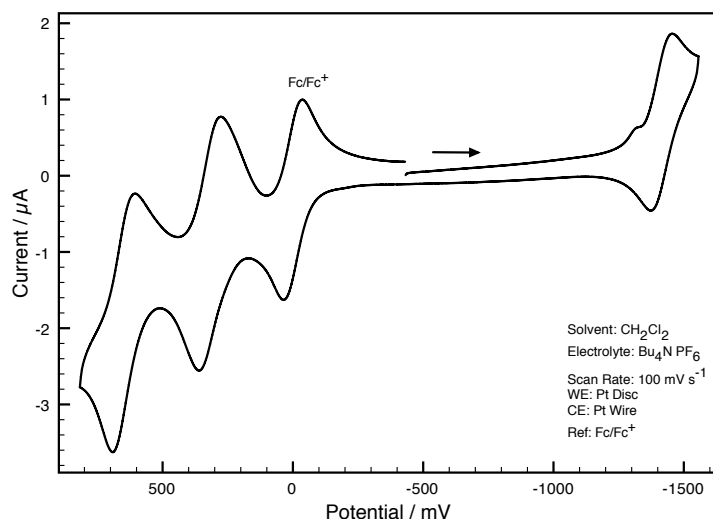
Fig. 104 Cyclic voltammogram of **[Dyad 2 Pic][OTf]**.
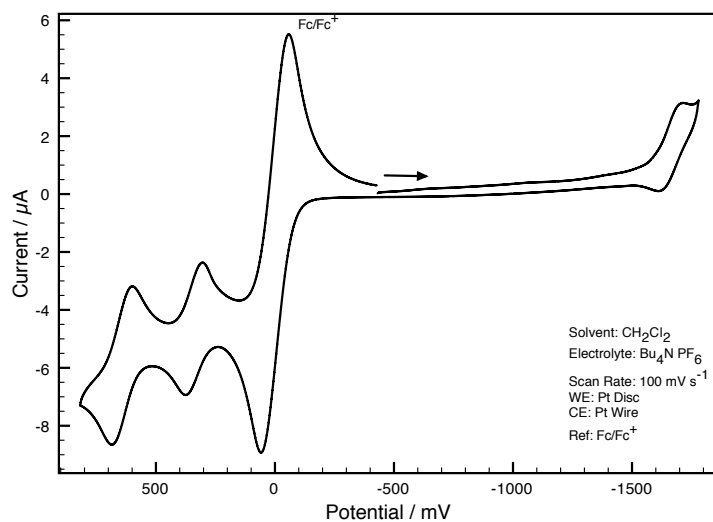
Fig. 105 Cyclic voltammogram of **[Dyad 3 Pic][OTf]**.

Dyad 2 Br is more difficult to reduce than **[Dyad 2 Pic][OTf]**. The reduction, based at the rhenium, is at more negative potential for the bromide because it is not cationic. The reduction of **Dyad 2 Br** is at a more negative potential than for the picoline complex and the difference is very similar to that between the **Dyad 1** complexes (0.18 and 0.19 V respectively). The reduction of **Dyad 3 Br** is at more reducing potential than **[Dyad 3 Pic][OTf]** and the difference is slightly less than for the other dyads at 0.15 V. All the bromide complexes show little or

no reversibility in the reduction signal indicating that reduction of rhenium is coupled to a chemical process.
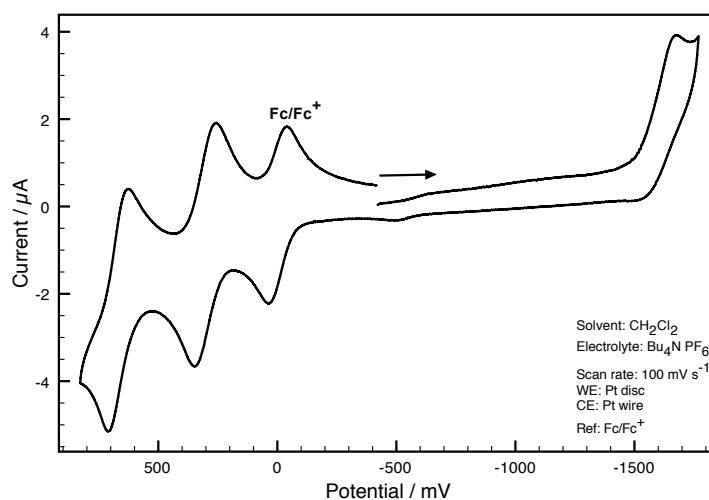
Fig. 106 Cyclic voltammogram of **Dyad 2 Br**.
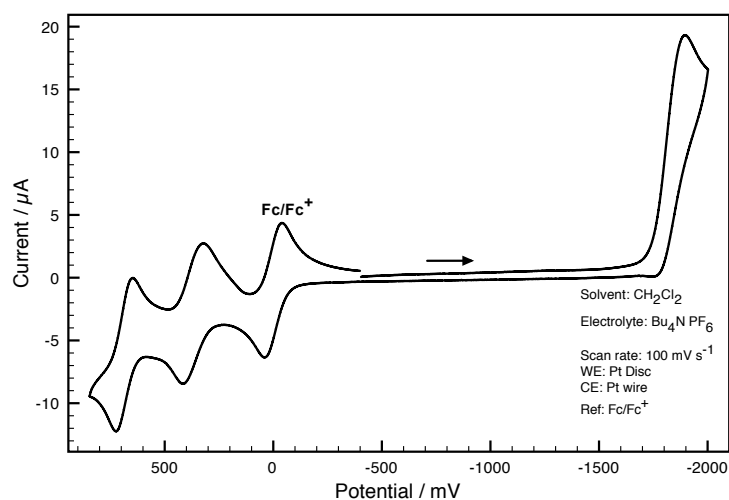
Fig. 107 Cyclic voltammogram of **Dyad 3 Br**.

The mono-nuclear rhenium complexes with phosphonate functionalised bipyridine were also tested by cyclic voltammetry. The reduction of the bromide complex is at a more reducing potential than for the picoline analogue but is more easily reduced than any of the dyad bromides. The phosphonate groups withdraw electron density stabilising the reduced rhenium species. The difference between the picoline and bromide complexes is larger than for the

dyads, 0.26 V. In terms of wave shape the bromide exhibits much greater reversibility than the dyad bromides, although peak separation does not suggest reversibility.
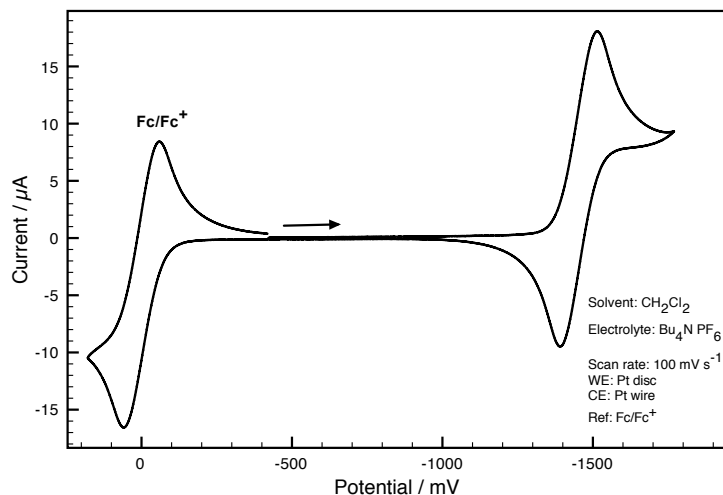
Fig. 108 Cyclic voltammogram of **6b**.
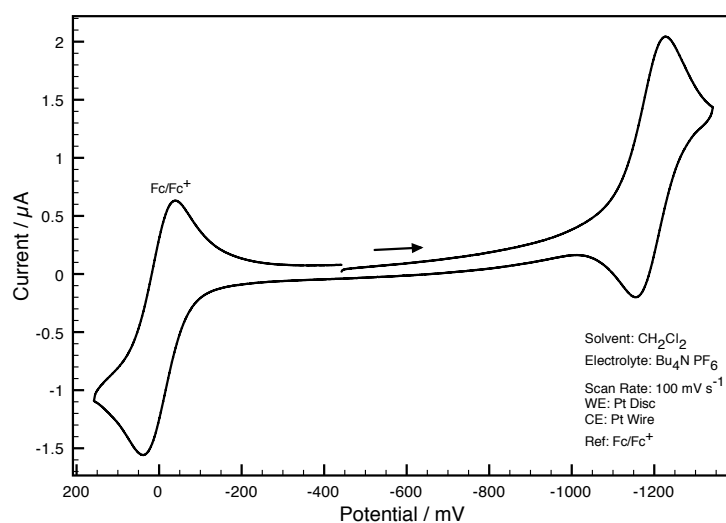
Fig. 109 Cyclic voltammogram of **6c**.

The cyclic voltammogram of **7b**, zinc tetraphenylporphyrin amide bound to a phosphonate ester, is shown in Fig. 110. The voltammogram exhibits the typical metalloporphyrin form. The first oxidation is quasi-reversible at +0.27 V, **7b** is 110 mV easier to oxidise than the simple ZnTPP. This suggests the additional amide-phosphonate unit can relieve a build up of positive charge at the porphyrin

core. A CV of the porphyrin with free phosphonic acid groups, **7c**, is discussed in the particle system chapter.
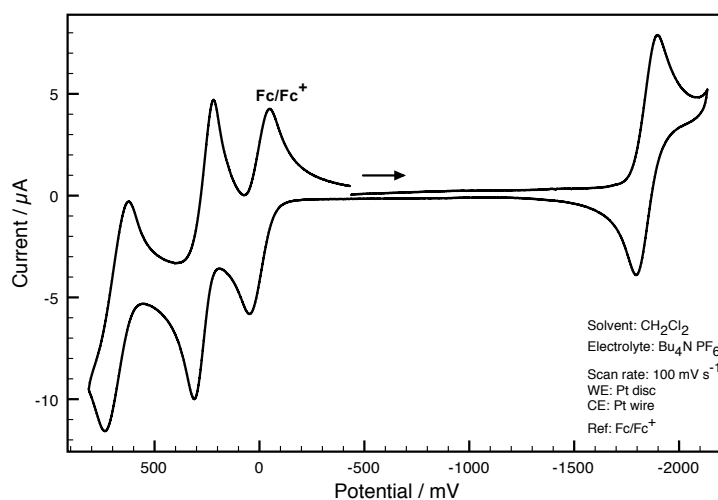
Fig. 110 Cyclic voltammogram of **7b**.

During photocatalytic runs it was observed by UV-Vis spectroscopy that significant changes in the structure of the porphyrin were occurring. A UV-Vis signal grew in that corresponded to a dihydroporphyrin species. Later NMR spectroscopic studies confirmed ZnTPP was hydrogenated to zinc tetraphenyldihydroporphyrin (ZnTPDHP) during irradiation in DMF/TEOA 5/1 mixtures. During catalysis ZnTPDHP appears in conjunction with the onset of catalysis and so voltammetry can tell us if ZnTPDHP is a plausible candidate for the active species. An authentic sample of ZnTPDHP was synthesised and cyclic voltammetry was run (Fig. 111, Table 12). ZnTPDHP shows two quasi-reversible oxidation waves ($\Delta Ep = 90$ and 89 mV). The first oxidation is achieved with a potential 240 mV less oxidising than that required for ZnTPP. It is apparent that ZnTPDHP is significantly more reducing (easier to oxidise) than ZnTPP and could be responsible for the onset of catalysis.
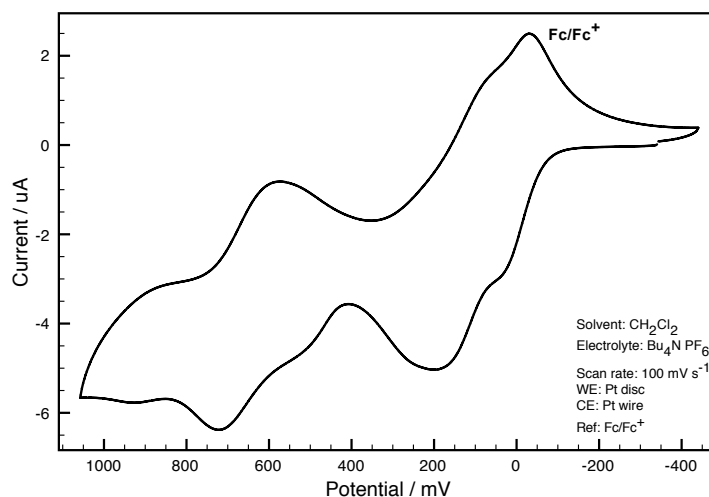
Fig. 111 Cyclic voltammogram of ZnTPDHP (**5a**).

3.2 Photochemistry

3.2.1 Porphyrin absorbance

Zinc tetraphenylporphyrin falls into the category of regular porphyrins. By definition the absorption and emission spectra are predominantly a result of the π electrons of the ring whereas the central metal plays a very minor role.[109] Photon absorption results in the population of any of the upper excited singlet states and leads to rapid radiationless decay to S_1, the lowest excited singlet state. This decay occurs on the picosecond timescale or faster. Once populated, S_1 can decay to the ground state either non-radiatively or radiatively via fluorescence. Alternatively intersystem crossing may occur, populating T_1 from which radiative (phosphorescence) or non-radiative decay can then occur. In some cases the S_1 state can be re-populated from T_1 via thermal repopulation or via triplet-triplet annihilation, this is observed as delayed fluorescence.
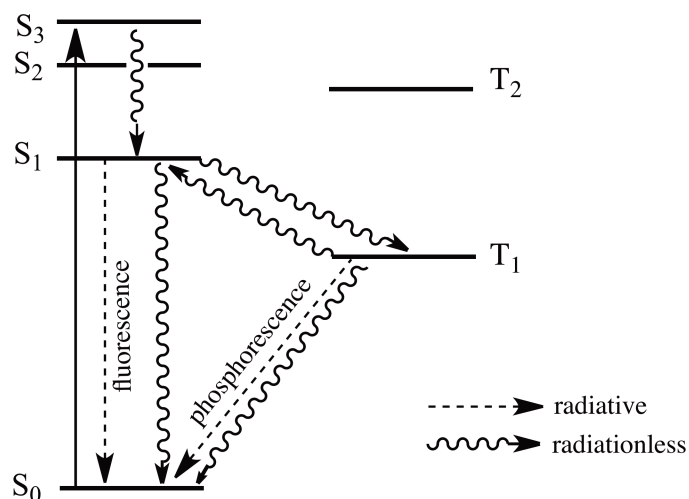
Fig. 112 Jablonski diagram for a regular porphyrin.[109]

The absorption spectra of regular metalloporphyrins exhibit two bands between 500 and 650 nm, referred to as 'Q bands'. The lowest energy band is the origin of the lowest excited singlet state and is denoted Q(0,0). The second, higher energy band is the vibrational overtone, denoted Q(1,0). The systems discussed in this thesis are exclusively irradiated in the Q bands. However, porphyrins cannot be discussed without mentioning the most intense band usually found between 400 and 430 nm and termed the 'B' or 'Soret' band. This band is the origin of the S_2 excited state and is denoted B(0,0). Typical UV-Vis absorption spectra for porphyrins used in this study are given in Fig. 113. The left spectrum is of a more dilute sample because the B(0,0) band absorbance at 420 nm is much more intense than the Q bands. On the right, the Q(1,0) and Q(0,0) bands can be observed. The singlet excited state of zinc porphyrin is usually on the order of several nanoseconds. The $^1(\pi,\pi^*)$ of ZnTPP was measured at 2.5 ns.[110]
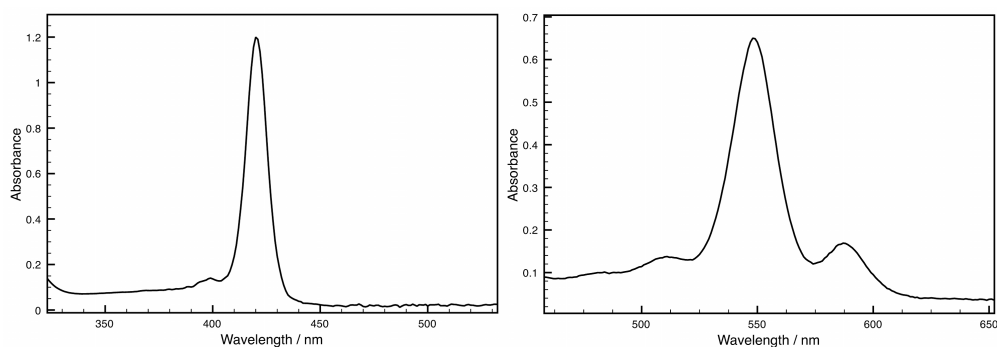
Fig. 113 UV-vis absorption spectra of **[Dyad 3 Pic][OTf]** in CH_2Cl_2. Left: Lower concentration, Soret band. Right: higher concentration, Q bands.

3.2.2   Fluorescence quenching in the dyads

It is important to test for quenching of the porphyrin emission by the rhenium centre because this is indicative of electron transfer. The zinc porphyrin-bipyridine ligand of **Dyad 2**, labelled **2h**, was measured for fluorescence. Then the entire **[Dyad 2 Pic][OTf]** was tested; a drop in fluorescence intensity indicates that electron transfer is occurring. Energy transfer can be ruled out because the porphyrin emits at much lower energy than the rhenium complex can absorb. The results are plotted in Fig. 114. The compound solutions were made to constant absorption with respect to the porphyrin Q bands. There is a significant drop in porphyrin emission when the rhenium is present (55% at 601 nm), confirming electron transfer from the excited porphyrin to the $Re(CO)_3Pic$ unit. This has also been observed in the **Dyad 1** motif.[74]

128
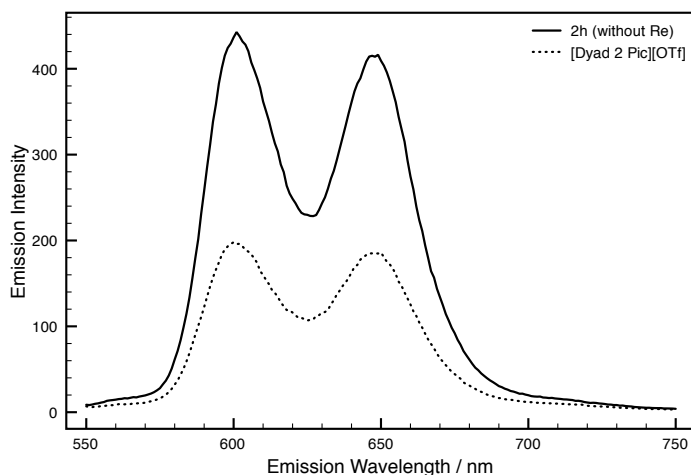
Fig. 114 Fluorescence of the **[Dyad 2 Pic][OTf]** zinc porphyrin with and without Re(CO)$_3$Pic in CH$_2$Cl$_2$. λ_{ex} = 420 nm. Solutions at approximately 1 x 10^{-5} M but diluted to equal absorbance.

[Dyad 3 Pic][OTf] was tested for emission quenching with and without rhenium in CH$_2$Cl$_2$. Compound **3e** is the zinc porphyrin-methylene-bipyridine ligand alone. The emission quenching due to the presence of the rhenium unit was 23% at 651 nm. This is less than half that of **[Dyad 2 Pic][OTf]** and suggests that the rate of electron transfer is slower in this dyad; radiative decay processes are kinetically favourable. **Dyad 3** has the most flexible link between porphyrin and bipyridine compared with **Dyad 2** and **Dyad 1** and is likely to exist in a wider range of conformers. Some conformations favour rapid electron transfer whereas the majority do not. **Dyad 3** also lacks a conjugated pathway for electron transfer compared with **Dyad 1** and **Dyad 2**.

3.2.3   Fluorescence quenching in two components systems

The simple ZnTPP was tested for fluorescence quenching by TEOA. One possible theory to explain the CO$_2$ reduction activity is that TEOA reductively quenches the excited porphyrin, providing an electron for the reduction. In this case no fluorescence quenching was observed with varying concentrations of TEOA (Fig. 115). To investigate whether the ZnTPP is transferring an electron to the Re catalyst emission quenching experiments were performed with ZnTPP in the presence and absence of [ReBpy(CO)$_3$Pic][PF$_6$]. It was not possible to

observe quenching of the ZnTPP by [ReBpy(CO)$_3$Pic][PF$_6$] (Fig. 116) indicating that the two component system may work differently to the dyads. The zinc tetraphenyldihydroporphyrin (ZnTPDHP) was tested for quenching by TEOA or [ReBpy(CO)$_3$3-picoline][PF$_6$]; the result was negative in both cases (Fig. 117). Electron transfer in two-component systems must be slower than the radiative relaxation of the porphyrin.
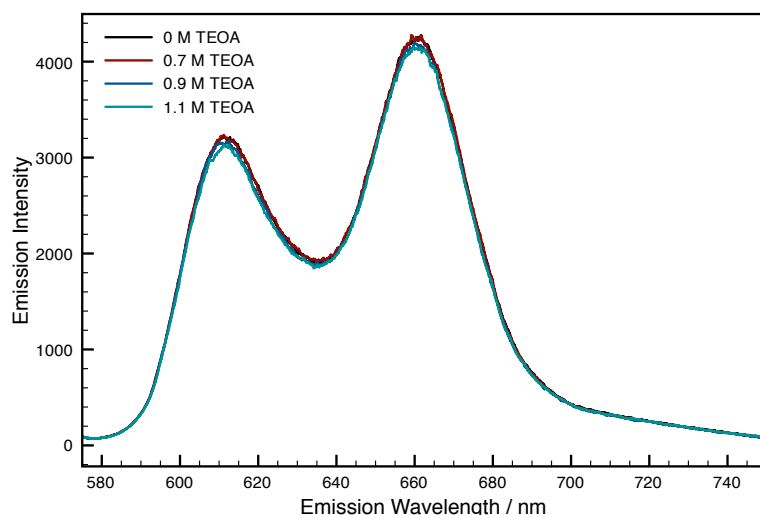
Fig. 115 Fluorescence of ZnTPP (0.05 mM) with varying concentrations of TEOA. λ_{ex} = 559 nm. In DMF.
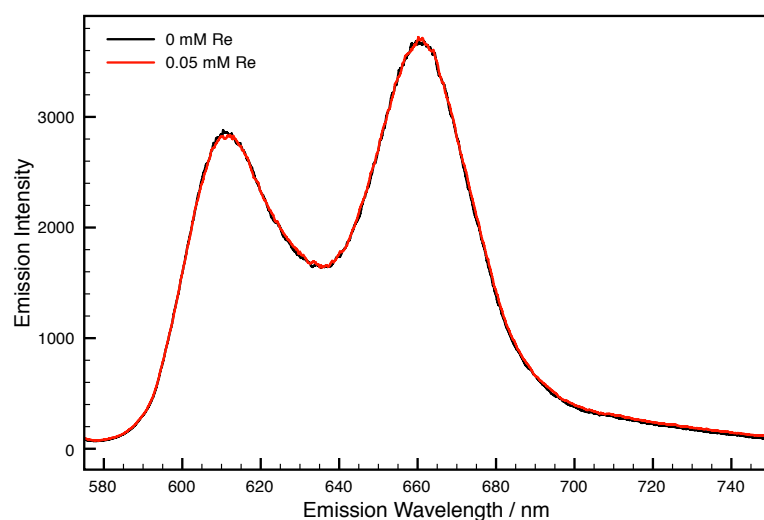
Fig. 116 Fluorescence of ZnTPP (0.05 mM in DMF) with and without [ReBpy(CO)$_3$Pic][PF$_6$]. λ_{ex} = 559 nm.
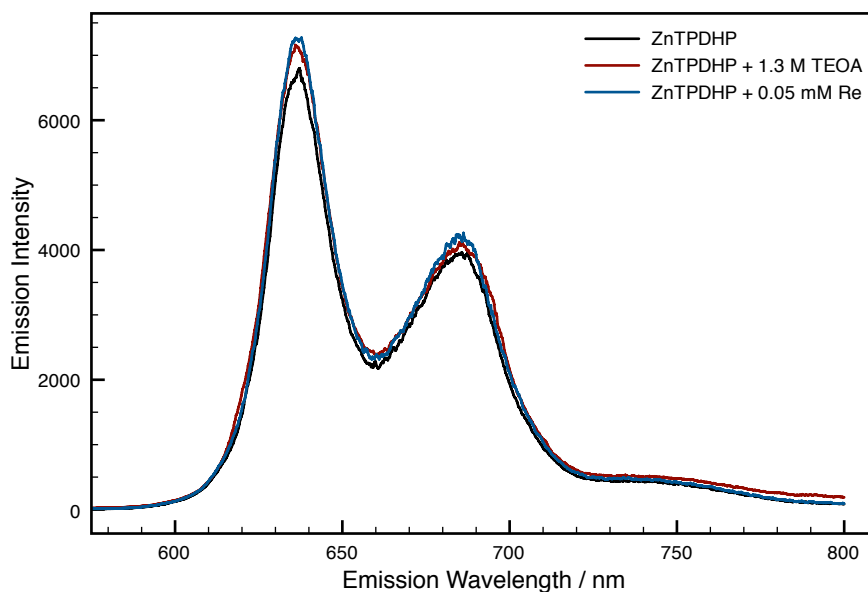
Fig. 117 Fluorescence of ZnTPDHP (0.05 mM) alone, with TEOA and with [ReBpy(CO)$_3$Pic][PF$_6$]. λ_{ex} = 623 nm. In DMF.

3.2.4   Remote site photo-substitution

To investigate if excitation of the porphyrin can induce chemistry at the rhenium centre, **[Dyad 2 Pic][OTf]** (2 mM) was irradiated with $\lambda > 520$ nm in the presence of Br$^-$ ([Bu$_4$N][Br] at 31 mM) in de-aerated DMF/Et$_3$N 5/1. IR spectra were taken at one-minute intervals (Fig. 118). The picoline ligand was completely substituted within 10 min of irradiation. This is clear from the splitting of the lower wavenumber signal into two. Substitution of the Pic for bromide reduces the symmetry of the complex and increases the number of CO stretches expected from two to three. The wavenumbers of the signals also drop due to the rhenium centre changing from formally positive to neutral, as demonstrated by the characterisation data of **Dyad 2 Br** and **[Dyad 2 Pic][OTf]** in the Synthesis chapter. The back bonding to the CO ligands is increased, weakening the C-O bond and reducing the vibrational frequency. This is further evidence that electron transfer can occur from porphyrin to rhenium. The system was tested for thermal substitution in the dark and in the absence of electron donor. Approximately 50% of the Pic was thermally substituted by bromide over the course of 7 days indicating that irradiation significantly accelerates remote site ligand substitution.
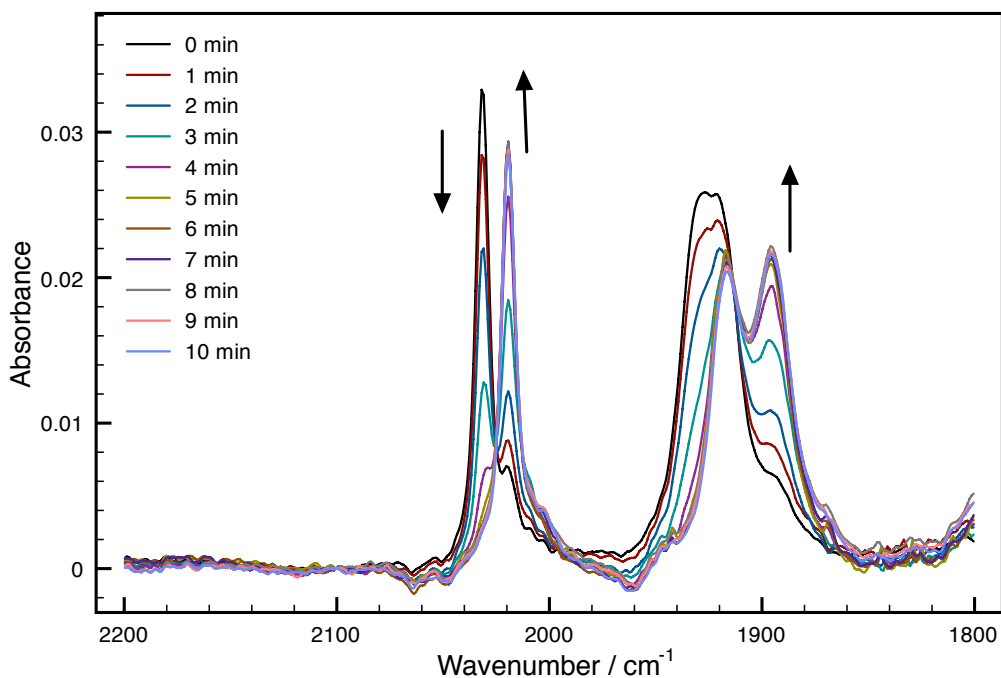
Fig. 118 Remote site photosubstitution in **[Dyad 2 Pic][OTf]**. The Pic ligand is substituted for bromide within 10 min in the presence of Et$_3$N as electron donor ($\lambda > 520$ nm).

3.2.5   Driving force for electron transfer

The change in free energy on inter- or intra-molecular electron transfer from the excited state of the sensitiser to rhenium can be estimated using Eq. 1, where E$_{ox}$ and E$_{red}$ are taken as the potentials for the first oxidation of the sensitiser and first reduction of the rhenium, respectively. The potentials were estimated from cyclic voltammograms measured in CH$_2$Cl$_2$. For E$_{00}$, we take the highest energy emission maximum of the sensitiser, measured at room temperature.

$$\Delta G_{ox}{}^* = E_{ox} - E_{red} - E_{00}$$

Eq. 1 Calculating driving force for photoinduced electron transfer.

The potentials, emission maxima, driving forces and maximum turnover numbers for CO are given in Table 13. Taking just the picoline complexes, the greater the driving force for electron transfer, the lower the maximum turnover number. This is not the case for bromide complexes where the **Dyad 1 Br** produces the lowest

maximum turnover number but does not have the highest driving force. The bromides continue to confuse as the most active system is **Dyad 3 Br**, yet the driving force is not favourable for electron transfer.

Complexes	$E_{1/2}^{ox}$ / V	$E_{1/2}^{red}$ / V	E_{00} / eV	ΔG_{ox}^{*} / eV	Max TON
ZnTPP + [ReBpy(CO)₃Pic] [PF₆]	0.38[108]	-1.57[108]	2.06	-0.11	100
ZnTPP + ReBpy(CO)₃Br	0.38[108]	-1.86[108]	2.06	+0.18	62[108]
ZnTPDHP + [ReBpy(CO₃)Pic] [PF₆]	0.14	-1.57[108]	1.97	-0.26	50
[Dyad 1 Pic][PF₆]	0.28	-1.44	2.07	-0.35	23
Dyad 1 Br	0.36	-1.63	2.07	-0.08	26
[Dyad 2 Pic][OTf]	0.32	-1.42	2.06	-0.32	35
Dyad 2 Br	0.30	-1.60	2.07	-0.17	30
[Dyad 3 Pic][OTf]	0.33	-1.68	2.07	-0.057	360
Dyad 3 Br	0.37	-1.83	2.08	0.12	270

Table 13 First oxidation and first reduction potentials (vs Fc/Fc⁺), lowest energy emission maxima and driving force of electron transfer for the catalytic systems tested. All in CH_2Cl_2.

3.2.6   Time resolved infrared spectroscopy

[Dyad 2 Pic][OTf] and **[Dyad 3 Pic][OTf]** were investigated by TRIR spectroscopy using a setup described elsewhere.[111] **[Dyad 1 Pic][OTf]** had been investigated with time resolved infrared spectroscopy (TRIR). A down frequency shift in the TRIR signals indicated the direction of charge separation was from porphyrin to rhenium. Formation of a charge-separated state was observed and the lifetime was measured at 23.7 ps in propionitrile and 53 ps in THF.[73] The ground state bleach recovered in 52 ps (CH_3CN). **[Dyad 2 Pic][OTf]** was investigated by TRIR spectroscopy in CH_2Cl_2. Infrared difference plots and the growth and decay of signals corresponding to the ground state and charge separated state are given in Fig. 119 and Fig. 120. Similar to **[Dyad 1 Pic][OTf]**, a down frequency shift in the TRIR signals indicated the direction of charge separation was from porphyrin to rhenium The ground state reached the maximum bleach within the response time of the instrument; **[Dyad 2 Pic][OTf]** exhibits ultrafast charge separation occurring in a timescale less than one picosecond. The kinetics of the ground state recovery have been fitted to a bi-exponential function. The shorter component has a lifetime of 42 ps and the longer component has a lifetime of 515 ps. Dilution of the solution from 1.5 mM down to 0.2 mM did not change the TRIR kinetics, demonstrating that the longer component is not the result of an intermolecular interaction.
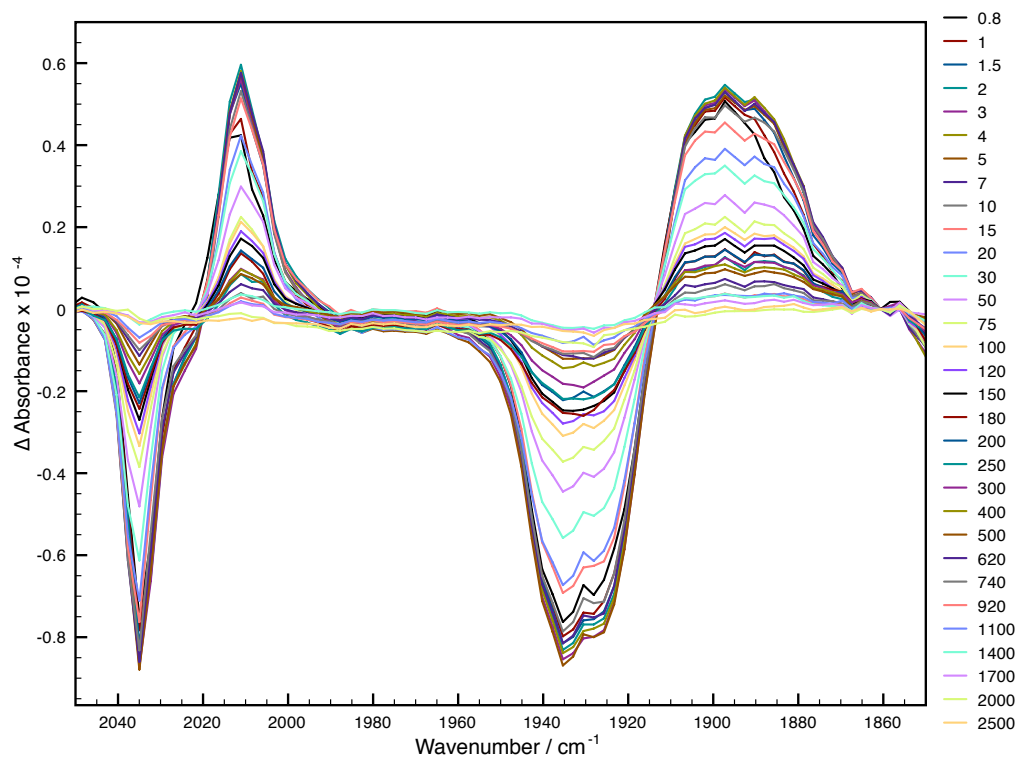
Fig. 119 TRIR spectra of **[Dyad 2 Pic][OTf]** at 1.5 mM in CH_2Cl_2. λ_{ex} = 560 nm.
Probe delay times in picoseconds.
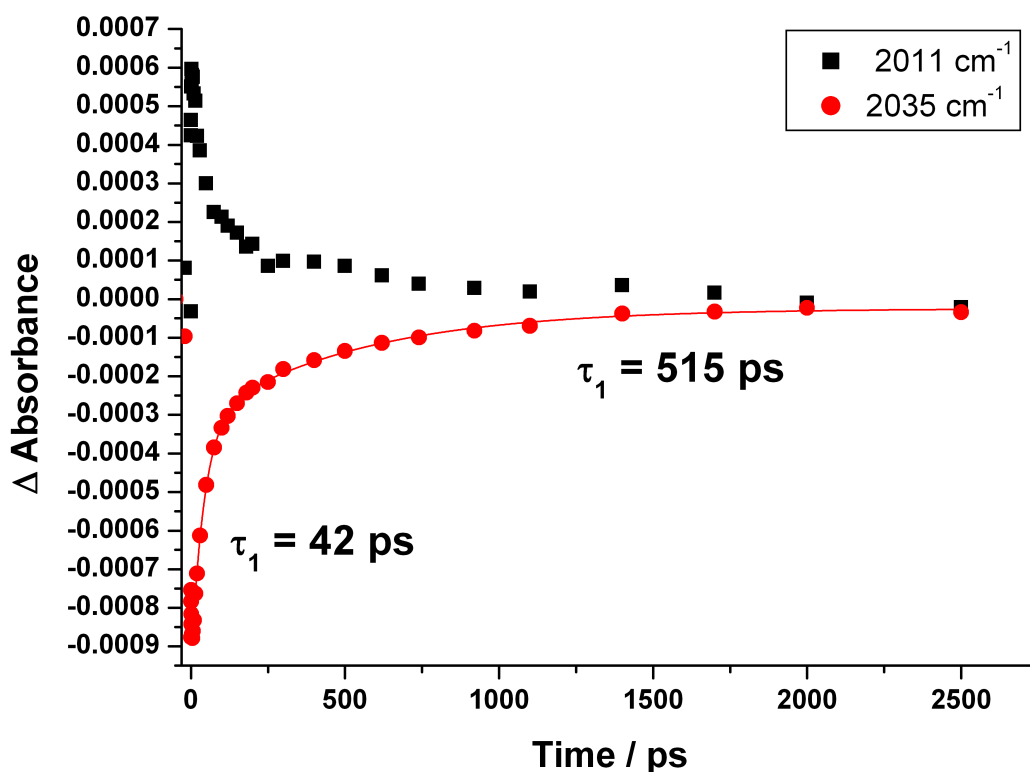
Fig. 120 TRIR kinetics of **[Dyad 2 Pic][OTf]** in CH_2Cl_2 following 560 nm excitation.

[Dyad 3 Pic][OTf] was also investigated by TRIR spectroscopy and the difference spectra and TRIR kinetics are given in Fig. 121 and Fig. 122. As with the other dyads, a down frequency shift in the TRIR spectra indicates porphryin to rhenium charge transfer. The kinetics of **[Dyad 3 Pic][OTf]** are significantly different to those of **[Dyad 1 Pic][OTf]** and **[Dyad 2 Pic][OTf]**. It was possible to observe the bleaching of the ground state within the instrument response time. The charge-separated state grows in over a timescale of 12 ps and subsequently decays over 335 ps. Electron transfer is significantly slower in both directions for **[Dyad 3 Pic][OTf]**. The slower component of the parent recovery in **[Dyad 2 Pic][OTf]** is longer lived but considering the area under the curve, this time period corresponds to a relatively very small signal at 2011 cm^{-1}. Introduction of the methylene spacer into the metalloporphyrin rhenium dyad has reduced the rate of electron transfer. The rate of forward electron transfer has been reduced to a lesser extent than the rate of back electron transfer.
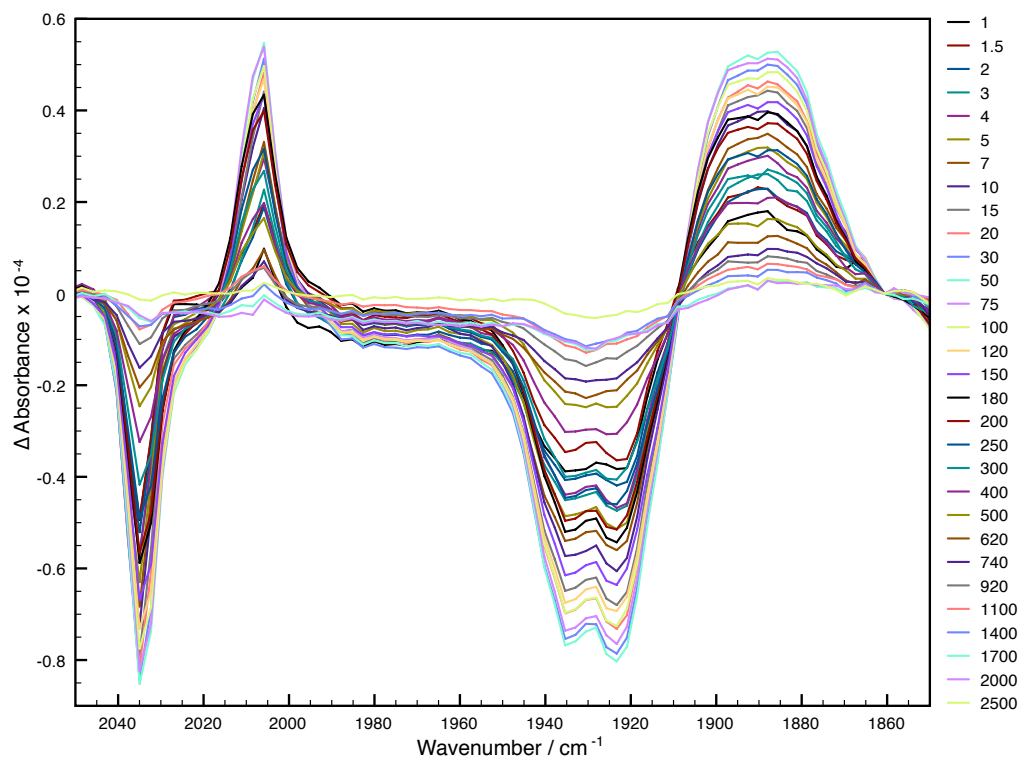
Fig. 121 TRIR spectra of **[Dyad 3 Pic][OTf]** in CH_2Cl_2. λ_{ex} = 560 nm. Probe

delay times in picoseconds.
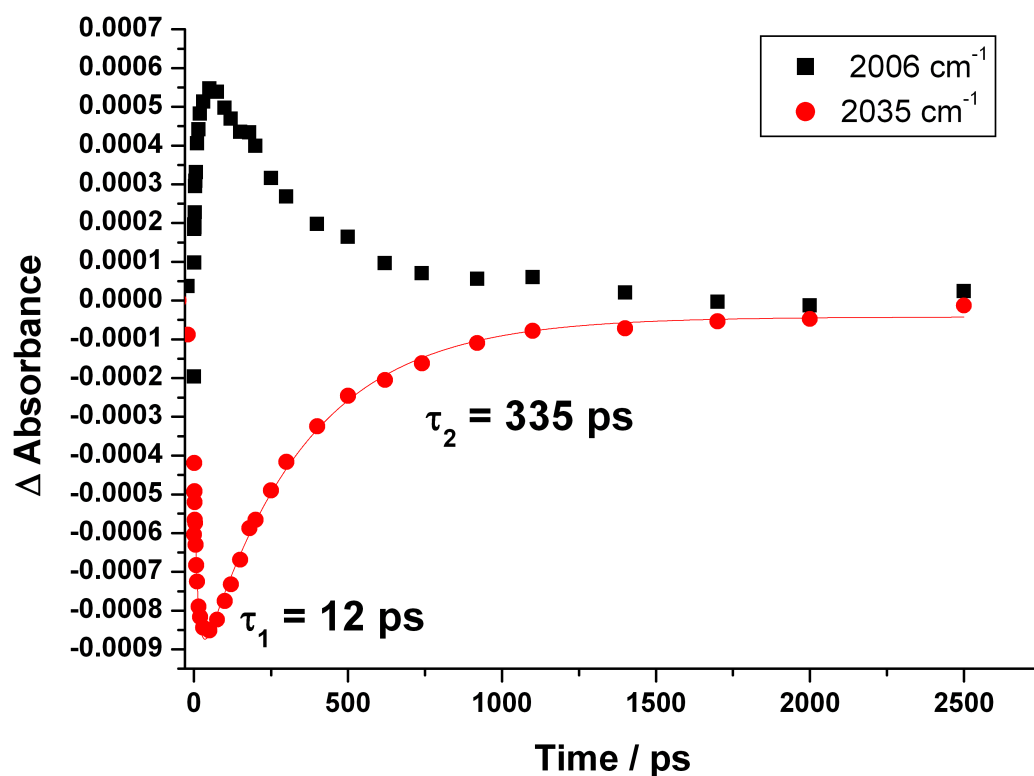
Fig. 122 TRIR kinetics of **[Dyad 3 Pic][OTf]** in CH_2Cl_2 following 560 nm excitation.

3.2.7 Conclusions

The literature demonstrates that changes to the Bpy have a significant effect on the first reduction potential. This is consistent with the less negative reduction potentials observed for the mono-nuclear rhenium complexes with phosphonate ester functionalities. Accordingly the first reduction of the **Dyad 3** motif requires more negative potentials than **Dyads 1** and **2**, which is in agreement with having distanced the electron withdrawing carbonyl group from the Bpy.

It is also established that changes to the axial ligand on the rhenium complexes have a significant effect on the electrochemistry. The bromide complexes of the dyads show reduced reversibility and require more negative potentials at the first reduction compared with the Pic complexes. This is consistent with a formally neutral rhenium centre compared to the positive Re of the Pic complexes. The electrochemistry of the porphyrin unit is less affected by changes in the spacer of the dyad or the axial ligand on the rhenium. However, the ZnTPDHP

(dihydrogenated porphyrin), can be oxidised at significantly less positive potentials than zinc porphyrins. As a catalytic intermediate this can have mechanistic implications.

The driving force for electron transfer was estimated for all systems. There is little correlation between turnover number of CO and the propensity for electron transfer from porphyrin to rhenium. Broadly, a decrease in driving force leads to more efficient catalysis. This is counter intuitive but there are many different factors, aside from the driving force for electron transfer, contributing to differences in the molecules. The two-component mixture with ZnTPDHP as sensitizer has a much higher driving force for electron transfer but the turnover number is half that than with ZnTPP. One explanation is the decomposition pathway of the porphyrin. The porphyrin can sensitize the rhenium and then is also active once it has been hydrogenated to ZnTPDHP. It could therefore be capable of double the yield of sensitisation prior to complete bleaching. The ZnTPDHP intermediate may also explain the activity of some of the bromide complex systems for which the driving force for electron transfer is positive. Once the porphyrin has been hydrogenated to ZnTPDHP electron transfer is more favourable.

All the porphyrin complexes synthesised have UV-Vis absorption and emission spectra consistent with metalloporphyrins. All the dyads show quenching when the rhenium unit is present compared with the free bipyridine. The degree of quenching decreases in the order **[Dyad 1 Pic][PF$_6$]** (85% in toluene) > **[Dyad 2 Pic][OTf]** (55% in CH$_2$Cl$_2$) > **[Dyad 3 Pic][OTf]** (23% in CH$_2$Cl$_2$). This suggests that the rate of electron transfer is also reduced in this order. It is possible to conclude that the more active the catalyst, the slower the electron transfer. Slow electron transfer in the forward direction is unlikely to be advantageous for catalytic activity but if back electron transfer is also slowed, charge separation lifetimes may be increased.

ZnTPP and ZnTPDHP exhibit no quenching in the presence of TEOA or [ReBpy(CO)$_3$Pic][PF$_6$]. This suggests that the rate of emission of both sensitisers is greater than reductive quenching by TEOA or oxidative quenching by the

rhenium complex. This is plausible as the quenching would be diffusion limited; a much slower process than emission. This raises the question of how these system produce CO under visible light. It may be because the catalysis experiments use a high intensity lamp for many hours and so enough porphyrin excited state is continually produced that the rhenium complex can eventually come in contact and quench it. The catalytic conditions may favour formation of a ZnTPP and [ReBpy(CO)$_3$Pic][PF$_6$] complex prior to excitation.

[Dyad 2 Pic][OTf] exhibits remote site photoactivity. Irradiation of the complex in DMF/Et$_3$N with $\lambda > 520$ nm in the presence of Br$^-$ showed complete substitution of the picoline ligand in 10 min. This is consistent with electron transfer.

The current theories of the CO$_2$ photo-reduction mechanism by rhenium complexes, and our mass spectrometry results, suggest that the axial ligand is substituted by solvent (DMF or TEOA). Since [ReBpy(CO)$_3$(DMF)]$^+$ or [ReBpy(CO)$_3$(TEOA)]$^+$ have a cationic rhenium centre, the most relevant data obtained so far for indicating the driving force in the catalytically active species is for the picoline complexes. The picoline and bromide complexes of **Dyad 1** and **Dyad 2** show the same activity within error, in agreement with the concept that in both cases the catalysts are ultimately the solvent complexes. Ligand substitution will presumably require an additional photon, but this may only need to happen once before the catalytic cycle can ensue. Therefore it would not be possible to observe an affect on the quantum yield of CO production and subsequently TON. Photosubstitution in **Dyad 1 Br** was not observed in DMF/Et$_3$N in the presence of Pic. However, it is necessary to investigate photosubstitution in the catalytic conditions with TEOA.

There is a significant difference in activity between the picoline and bromide complexes of **Dyad 3**. **Dyad 3 Br** is the only dyad for which the driving force for electron transfer is unfavourable and yet, for the time that it is active, it produces CO at a higher rate than **[Dyad 3 Pic][OTf]**. This may disprove the concept that the catalysts are ultimately the same complex. However, as discussed in the Introductory chapter, Ishitani finds picoline ligands have an effect on the stability

of his Ru-Re dyads. In his case it is detrimental but for our systems the effect has not been investigated. If Pic stabilises the dyads, then it may be possible to explain the increased efficiency despite a lower TOF. The Pic catalysts should be run in the presence of bromide and the bromides in the presence of Pic. The Introductory chapter outlines the findings of other groups, which suggest that the axial ligand needs to provide a fine balance of coordination ability. It must be capable of substitution but also re-coordination. Should this be true, then alterations to this ligand have a much more complex impact than simply the change in reduction potential.

TRIR spectroscopy has confirmed that photoinduced charge separation from porphyrin to rhenium Bpy occurs in **[Dyad 2 Pic][OTf]** and **[Dyad 3 Pic][OTf]**. The recovery of the ground state indicates that the charge separated state lifetime for **[Dyad 2 Pic][OTf]** is of the order of 42 ps and for **[Dyad 3 Pic][OTf]** is 335 ps. This is consistent with the CO_2 photoreduction activity. The charge separation lifetime of **[Dyad 2 Pic][OTf]** is similar to that of **[Dyad 1 Pic][OTf]** and so is the turnover number of CO. The **[Dyad 3 Pic][OTf]** charge separation lifetime is significantly greater than the other two dyads along with the turnover number of CO.

Chapter 4.   Photocatalytic CO₂ Reduction

The development of a system that can recycle carbon dioxide powered solely by sunlight is a necessity for the future. The energy required for our everyday lives is obtained largely from the combustion of oil. The oil will eventually run out and burning it produces the greenhouse gas carbon dioxide. Various alternative energy sources will need to be used in combination to meet our future needs. Solar power is clean and using it to recycle CO_2 can allow use to store it in chemical fuels of high energy density. This means we could continue to oxidise hydrocarbons but in a carbon neutral way. Hydrocarbons remain attractive because they offer very high energy density, we have an established infrastructure for their utilisation and we have highly efficient engines due to decades of optimisation. We also need to find an alternative for the carbon based molecular building blocks we currently obtain from crude oil. These building blocks are essential for modern civilisation as they are used to make products such as plastics and life-saving drugs. Producing CO from CO_2 is useful because it can be used as a fuel but it is also a feedstock for various industrial processes (Fig. 123). The Fischer-Tropsch process uses CO to produce hydrocarbons; varying chain lengths are produced depending on the catalyst used. The hydroformylation of alkenes with CO produces aldehydes, which can be further processed to produce alcohols, plasticizers, detergents, flavourings and perfumes.[112] CO can also be used to produce ammonia, a feedstock for fertiliser production.[112]
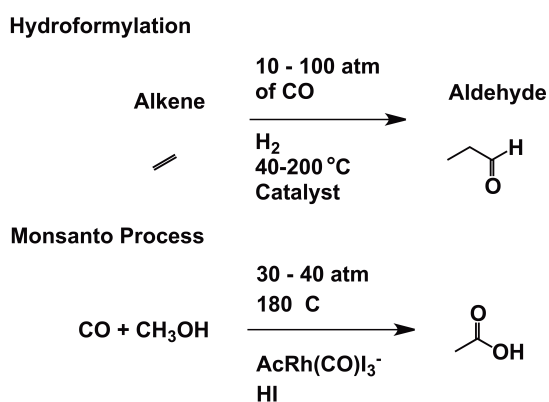
Fig. 123 Examples of major industrial process for which CO is a feedstock.[112]

Porphyrins strongly absorb visible light and rhenium bipyridine tricarbonyl complexes can catalytically convert carbon dioxide to carbon monoxide. Emission quenching and remote site photosubstitution experiments indicate that the light energy absorbed by the porphyrin is received by the rhenium via electron transfer. The dyads should be capable of visible light powered CO_2 reduction. Indeed similar systems based on palladium porphyrins have shown catalytic CO production from CO_2.[75] There are also numerous examples of rhenium catalysts sensitised to visible light with $[Ru(Bpy)_3]^{2+}$ that produce several hundreds of turnovers of CO.[33, 113]

4.1   Catalysis experiments

4.1.1   Conditions

The dyads were tested for CO_2 reduction activity under long wavelength low energy visible light. The reduction of CO_2 requires two electrons (Fig. 124) and so a sacrificial electron donor is required, in this case triethanolamine is used. The generic equation for CO_2 reduction to CO and how this relates to our system, is given in Fig. 124. The catalyst was dissolved in a 5 to 1 mixture of DMF and triethanolamine because this is the optimum solvent and amount of electron donor yet found for rhenium catalysts. The catalysts were used at a concentration of 0.05 mM as this is the optimum concentration found for $[Ru(Bpy)_3]^{2+}$-sensitized rhenium systems and it gives the porphyrin Q(1,0) band an absorbance around 1.

$$CO_2 + 2H^+ + 2e^- \longrightarrow CO + H_2O$$

$$CO_2 + 2H^+ + 2N(C_2H_4OH)_3 + h\nu \xrightarrow[\text{DMF}]{\text{ZnTPP-BpyRe(CO)}_3\text{X}} CO + H_2O + 2N(C_2H_4OH)_3^{\bullet+}$$
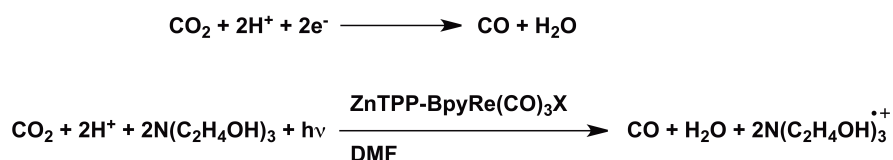
Fig. 124 The equation for CO_2 reduction to CO.

Optical filters were necessary to control the wavelengths of light reaching the sample. A $\lambda > 520$ nm filter was used along with a water filter and a 660 short pass filter ($\lambda < 660$ nm) to reduce the heat coming from the lamp. This combination of filters irradiated all samples with $520 < \lambda < 660$ nm. The heat of

the lamp combined with the heat filters held the sample directly in the beam at 33 °C. The sample was placed as close as possible to the light source so that photocatalytic reactions would be complete in a reasonable time.

4.1.2   Measurements

The reaction was performed in a custom cell with the reaction solution in a quartz cuvette, so that the solution could be analysed by UV-Vis spectroscopy throughout the catalytic reaction. A headspace above the cuvette acted as a CO_2 reservoir and aliquots were removed for analysis by gas chromatography. Methane was used as internal calibrant via a response factor obtained with known quantities of CO (Fig. 125).
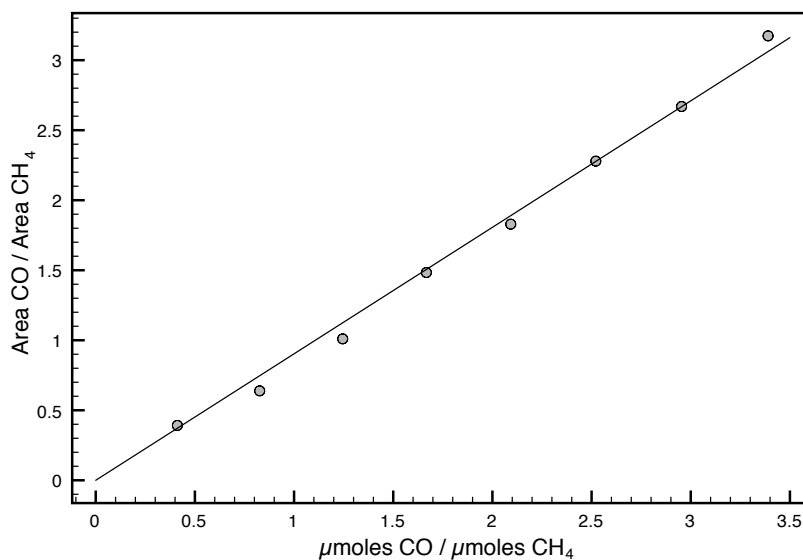
Fig. 125 Calibration plot for CO and CH$_4$ peak area ratios.

A side arm from the headspace allowed for transfer of the gas to an IR cell where the CO could be identified by infrared spectroscopy. The catalysis would be run either until the quantity of CO ceased to increase or until the porphyrin Q bands had bleached.

144

4.1.3   Reproducibility

The reproducibility of the CO measurement system was investigated. Maintenance of the GC is crucial to maintain a flat baseline and therefore fewer artefacts distorting the peak area measurements. The signal to noise ratio could usually be increased by baking out the column and detector. Leaving the GC constantly on with a flow of He helped maintain good signal to noise on a day-to-day basis. Fresh catalytic solutions were necessary and were stored in a freezer (-20 °C) for use within four weeks. The solutions were protected from ambient light up until being placed in front of the lamp.

4.1.4   Control experiments

[Dyad 1 Pic][PF₆], **[Dyad 2 Pic][OTf]** and **ZnTPP + [ReBpy(CO)Pic][PF₆]** were tested without CO_2 (under Ar) and without triethanolamine. In all cases catalytic quantities of carbon monoxide were not produced.

4.2   CO₂ photoreduction with Dyad 1

Dyad 1 had previously been synthesised in the Perutz group but testing for CO_2 reduction with Et_3N gave negative results. Despite proof that reductive quenching of the porphyrin by Et_3N does occur, tests using Et_3N as electron donor yielded no CO. Throughout the literature triethanolamine (TEOA) is used as electron donor for many photocatalytic systems including CO_2 reduction by rhenium complexes. It was possible to gain up to 23 turnovers of CO from **[Dyad 1 Pic][OTf]** in a mixture of DMF/TEOA 5/1 (Fig. 126). **Dyad 1 Br** was also synthesised and tested for photocatalytic CO_2 yielding 25 turnovers of CO in the same time frame; within error therefore identical in performance to the picoline complex. The bromide and picoline ligands produce a neutral and a positive rhenium centre respectively. The driving force for electron transfer from porphyrin to rhenium is significantly increased when 3-picoline is the axial ligand. However, CO_2 reduction activity does not improve. The curve also exhibits some sigmoidal character suggesting that there is an induction period prior to catalysis.

145
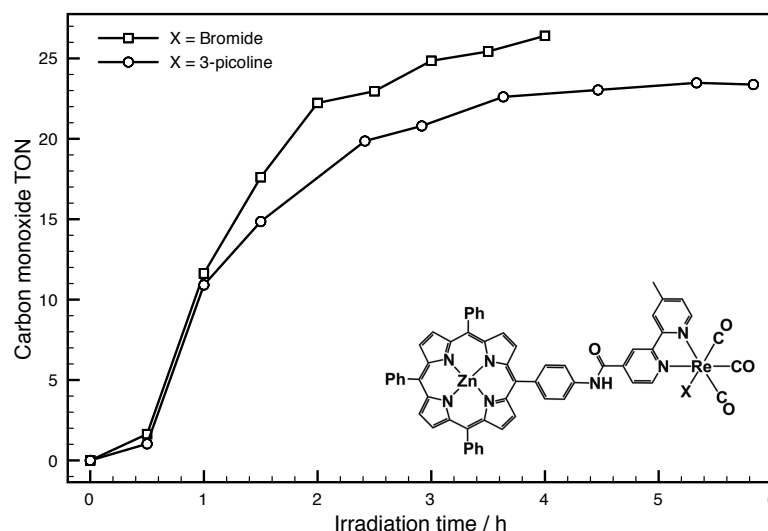
Fig. 126 CO photo-production by **[Dyad 1 Pic][PF$_6$]** and **Dyad 1 Br** under the standard conditions.

The UV-Vis spectrum can give information about structural changes of the porphyrin during the reaction. Fig. 127 shows the UV-Vis spectrum of **[Dyad 1 Pic][PF$_6$]** during CO_2 photoreduction. The plot is scaled to show the Q-band region as major changes were observed here. During irradiation the Soret band decreased in intensity and there was a minor decrease in intensity at 350 nm. Q(1,0) band at 560 nm exhibits a significant reduction in absorbance. The greatest rate of depletion of this band is between 30 and 60 min of irradiation and this is also when the greatest rate of CO production occurs. It is plausible that the catalytic induction period is caused by production of zinc tetraphenyldihydroporphyrin (ZnTPDHP). There is growth of a new peak at 625 nm, which, by comparison with authentic samples, is ZnTPDHP (Fig. 130). This indicates that the porphyrin is reduced during irradiation, with electrons that probably originate from the TEOA. The peak at 600 nm first increases and then decreases in intensity. The difference spectra can make it easier to assign (Fig. 128); the peak at 600 nm does bleach but a peak grows in at 610 nm corresponding to zinc tetraphenylisotetrahydroporphyrin (ZnTPTHP: λ_{max} 418, 498, 562, 607 nm in pyridine and see Fig. 131 for UV-Vis comparison of Zn porphyrin and associated hydrogenation products).[114] The kinetics of the changes in the Q bands for both the picoline and bromide complexes are given in Fig. 132. There is little difference between the two complexes but in all cases the

146

bromide complex absorbance bands decay less rapidly until the 200 to 250 min region when they overtake the picoline complex. The band at 610 nm has contributions from porphyrin and dihydroporphyrin but should give some indication of the tetrahydroporphyrin growing in and decaying. The 630 nm band is produced exclusively by the dihydroporphyrin giving a clear plot of growth and decay of this species.
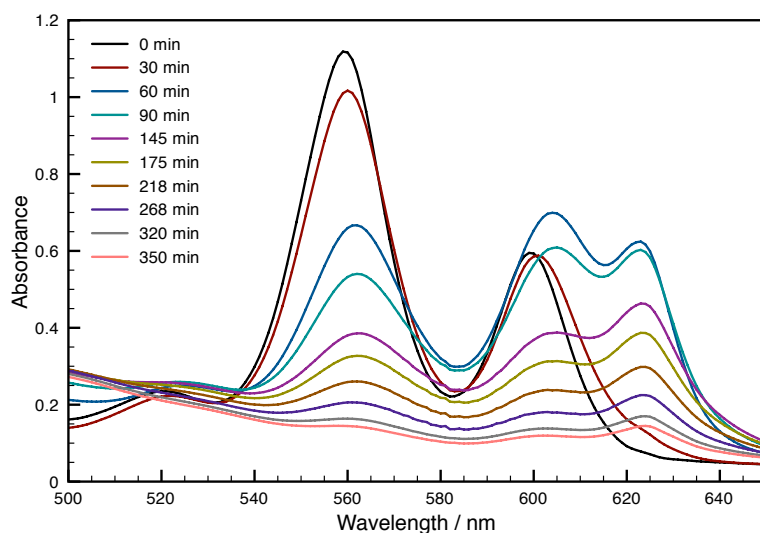
Fig. 127 UV-Vis spectrum of **[Dyad 1 Pic][PF₆]** complex during CO_2 photoreduction.
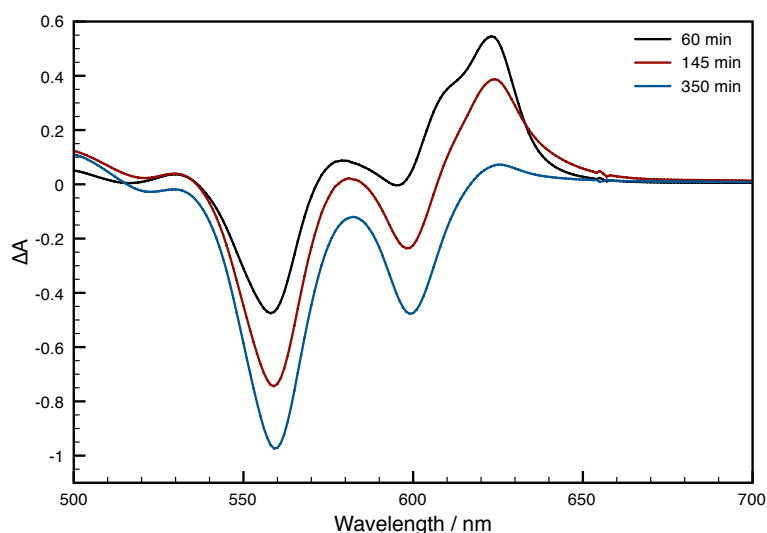
Fig. 128 Difference spectra for the UV-Vis absorption of **[Dyad 1 Pic][PF₆]** during catalysis at 60, 145 and 350 min.

Zinc tetraphenyldihydroporphyrin   Zinc tetraphenylisotetrahydroporphyrin
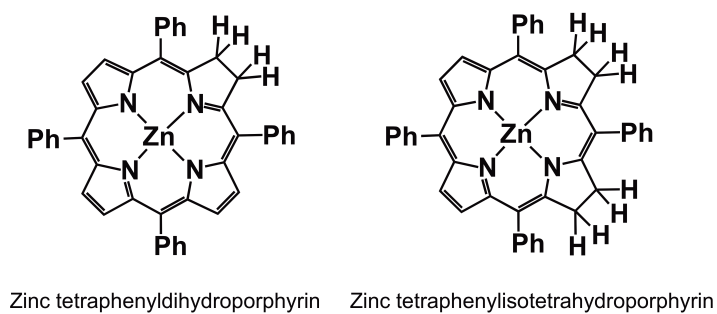
Fig. 129 Structures of hydrogenated porphyrins: zinc tetraphenyldihydroporphyrin (ZnTPDHP) and zinc tetraphenylisotetrahydroporphyrin (ZnTPTHP).
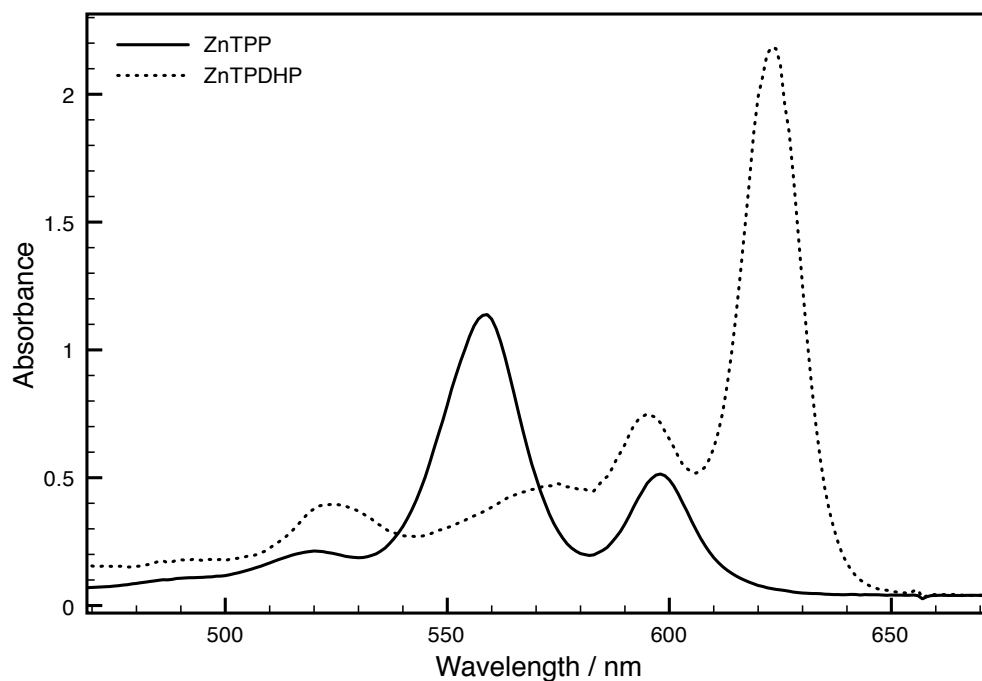
Fig. 130 UV-Vis absorption spectra of authentic ZnTPP and ZnTPDHP in DMF/TEOA (5/1) and at 0.05 mM.
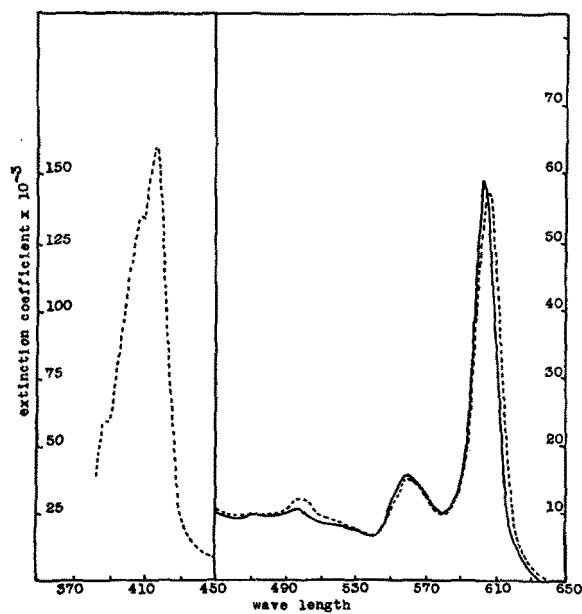
Fig. 131 UV-vis spectrum zinc tetraphenylisotetrahydroporphyrin in —— benzene and ---- pyridine.[115]
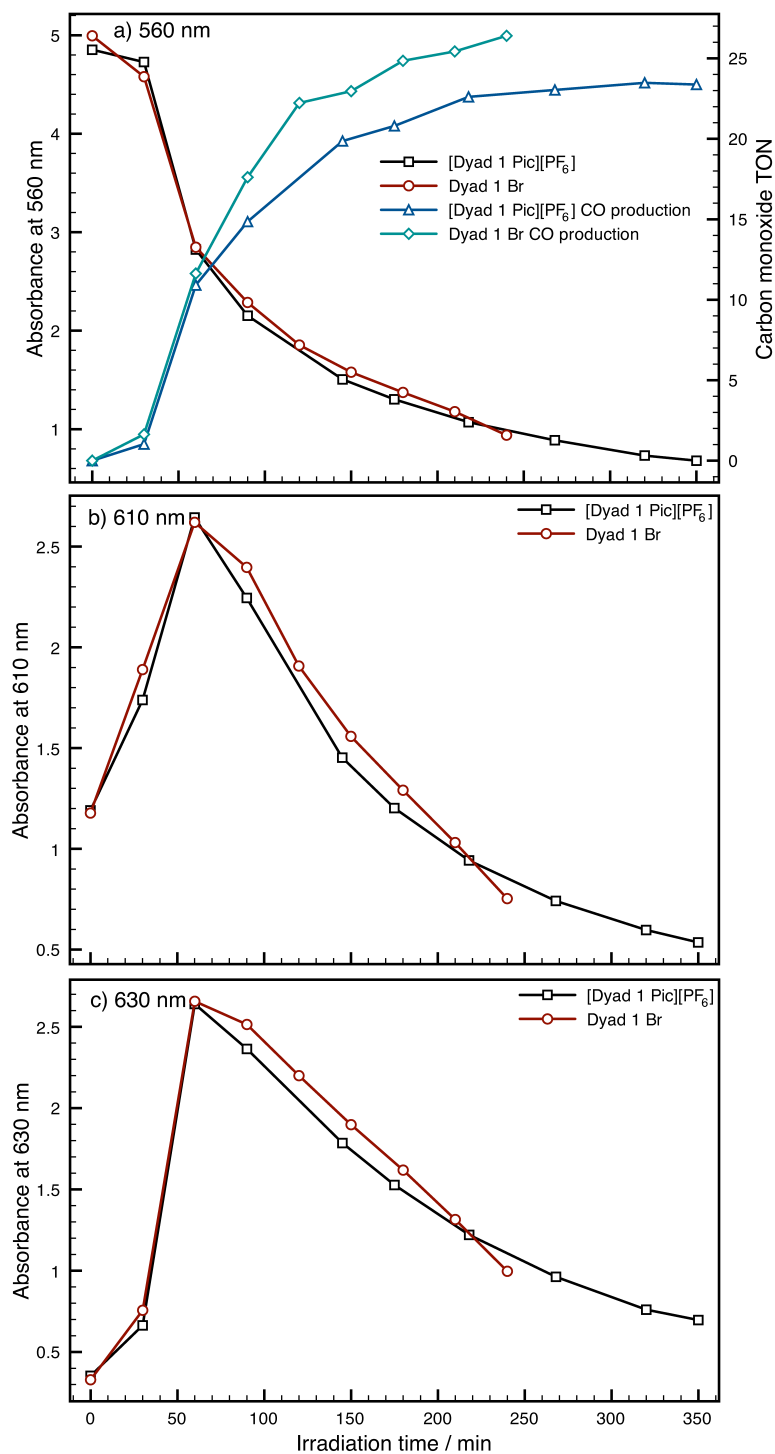
Fig. 132 Growth/decay kinetics for **[Dyad 1 Pic][PF₆]** and **Dyad 1 Br** Q bands.

4.3 *CO₂ photoreduction with Dyad 2*

The second dyad containing a methoxybenzamide spacer was designed to generate charged-separated states with longer lifetimes. It was shown that the

ratio of forward to back electron transfer is a function of donor-acceptor separation.[116] The methoxybenzamide spacer provides a significant increase in separation over the **Dyad 1** motif but should retain efficient electron transfer due to the possibility of conjugation. **Dyad 2** was synthesised with bromide and with 3-picoline as axial ligand on the rhenium. The picoline complex was able to produce turnover numbers up to 35. The initial rate was more than double that of **Dyad 1**. The bromide and picoline complexes show identical activity for the initial 4 h of irradiation but the porphyrin of the picoline complex did not photo-bleach as soon and produced a further 5 turnovers in 4 h.
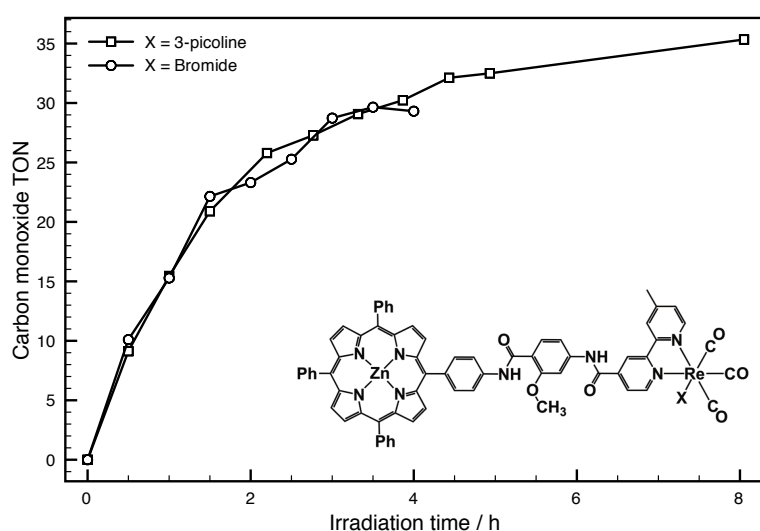
Fig. 133 CO photo-production by **[Dyad 2 Pic][OTf]** and **Dyad 2 Br**.

The UV-Vis spectrum of **[Dyad 2 Pic][OTf]** during photocatalysis is similar to that of **[Dyad 1 Pic][PF₆]** (Fig. 134 and Fig. 135). Depletion of the band at 560 nm is most rapid during the first 30 min of irradiation, corresponding with the period of most rapid CO production. The intensity of each of three Q bands was plotted against time for the picoline and bromide complexes in order to make comparisons of the kinetics. The solutions were made to the same concentration but the bromide Q bands show lower absorption coefficients (Fig. 136). The top plot for the 560 nm band shows little difference between the two complexes except that the bromide depletes more rapidly. The 610 nm and 630 nm bands show that isotetrahydroporphyrin and dihydroporphyrin are also formed with **[Dyad 2 Pic][OTf].** The plots also indicate that more

dihydroporphyrin is generated for the picoline complex and that it is also longer lived.
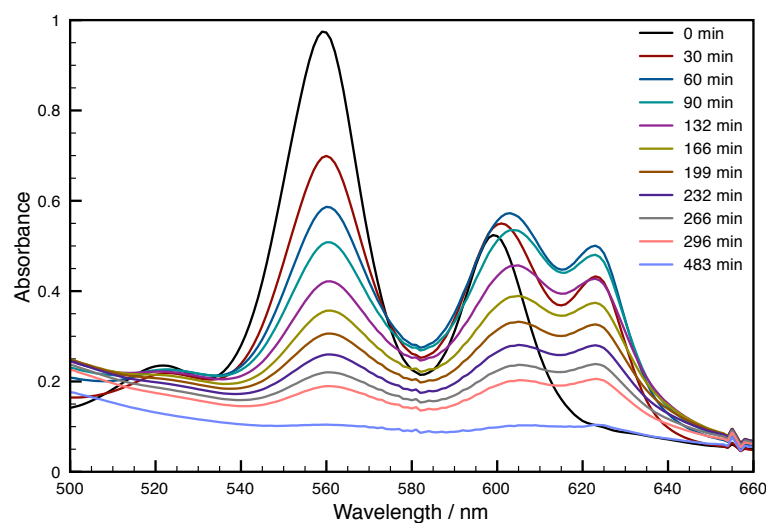
Fig. 134 UV-Vis absorption spectrum of **[Dyad 2 Pic][OTf]** complex during CO_2 photoreduction.
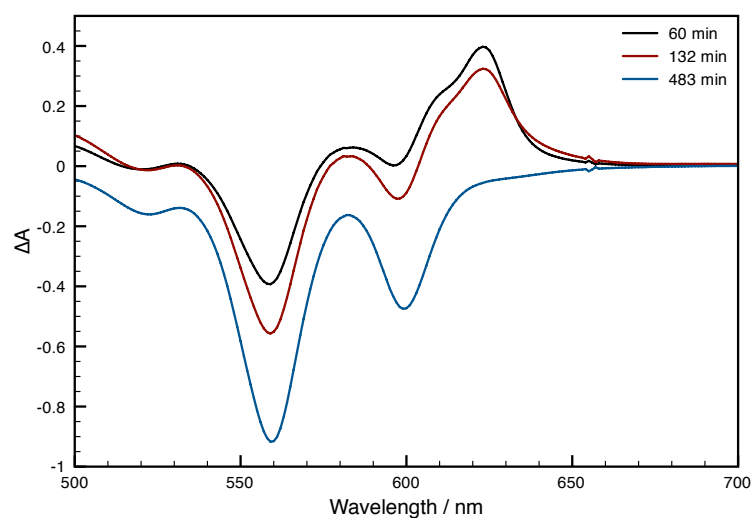
Fig. 135 Difference spectra for the UV-Vis absorption of **[Dyad 2 Pic][OTf]** during catalysis at 60, 132 and 483 min.
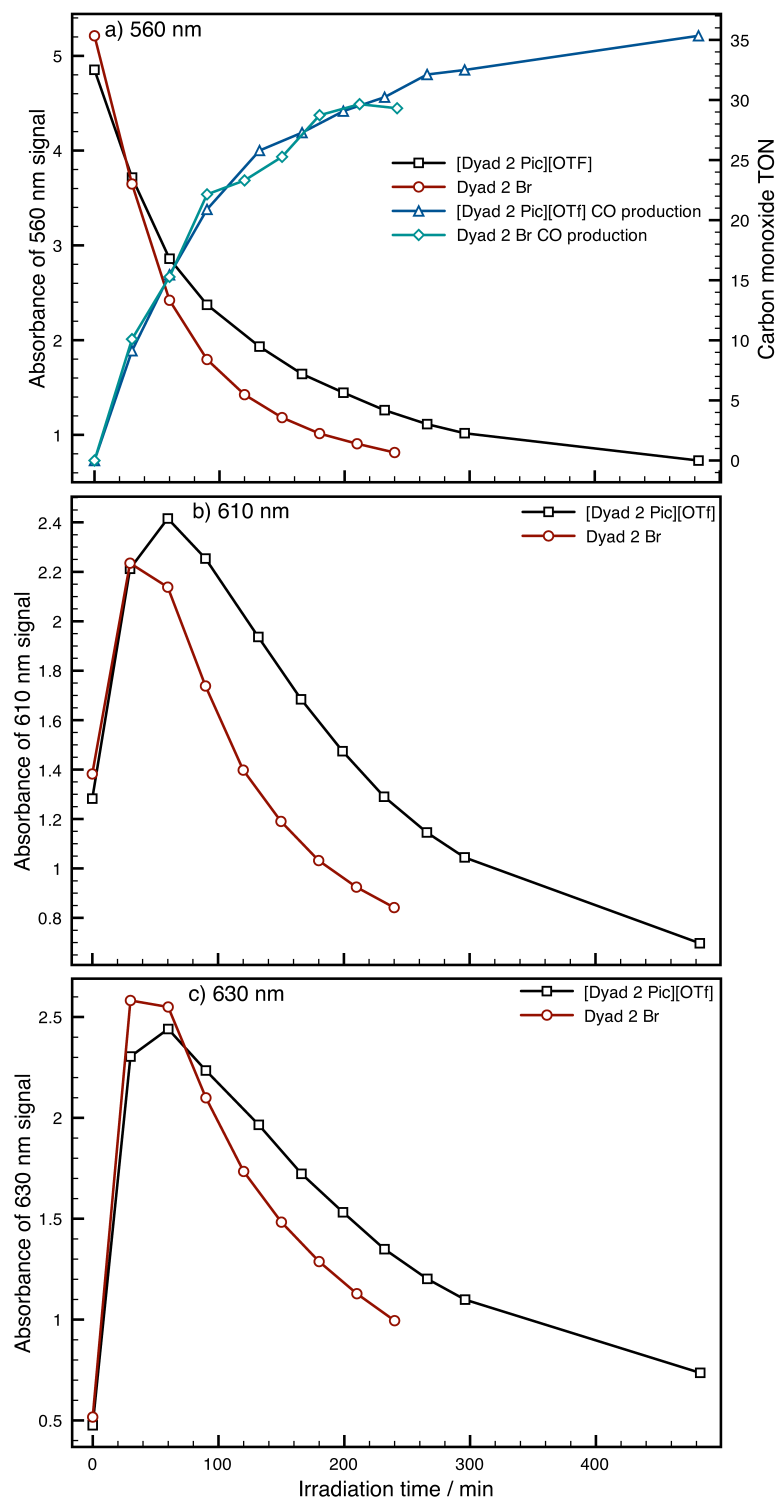
Fig. 136 Growth and decay dynamics of the Q bands at a) 560 nm b) 610 nm and

c) 630 nm for **[Dyad 2 Pic][OTf]** and **Dyad 2 Br**.

4.4   CO₂ photoreduction with Dyad 3

The dyad motif with a methylene spacer was tested for CO_2 photoreduction. The activities of the bromide and picoline complexes of **Dyad 3** are given in Fig. 137.
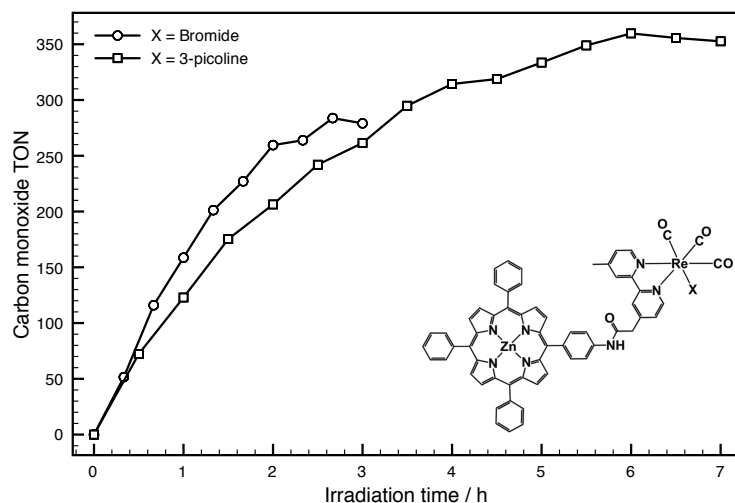
Fig. 137 CO photo-production by **[Dyad 3 Pic][OTf]** and **Dyad Br**.

The UV-Vis spectrum of the reaction solution was taken throughout catalysis (Fig. 138). The changes in the Q bands are similar to those of the other two dyads (Fig. 139). The main difference is that the ratio of the signal at 610 nm to that of the signal at 630 nm is significantly greater. Therefore **[Dyad 3 Pic][OTf]** shows greater conversion to isotetrahydroporphyrin than the other dyads. It is possible to rule out some other reduction products of the porphyrin such as tetrahydroporphyrin (hydrogenated pyrroles on opposing corners of the porphyrin) or phlorin as these both exhibit intense absorptions at wavelengths higher than 630 nm and this region of the spectra is empty. For the **Dyad 3** motif only, there is a significant growth in the signal at 300 nm but it has not been possible to assign this.
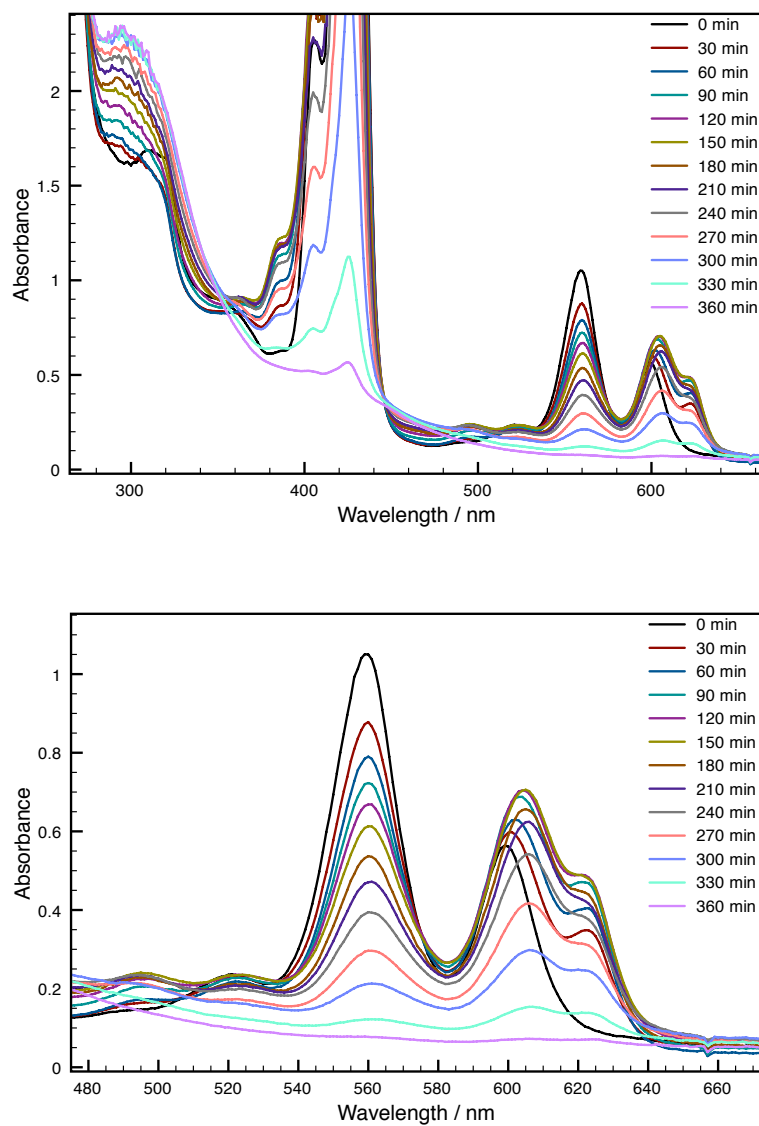
Fig. 138 UV-Vis absorption spectra of **[Dyad 3 Pic][OTf]** during CO_2 photoreduction.
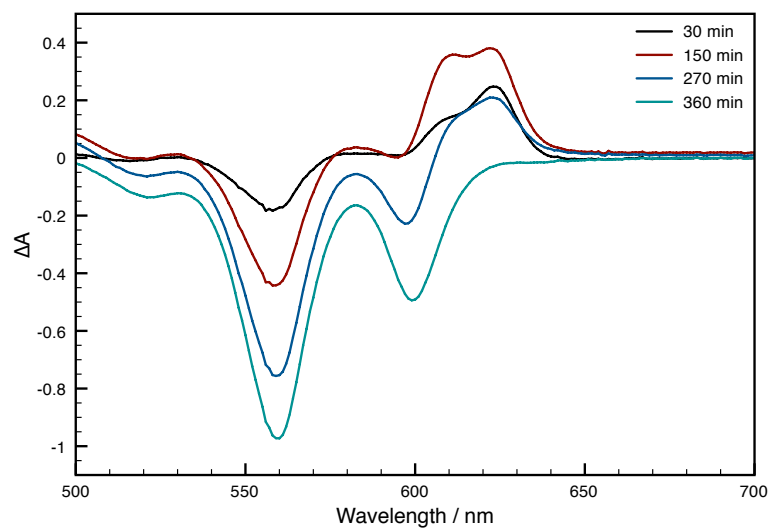
Fig. 139 Difference spectra for the UV-Vis absorption of **[Dyad 3 Pic][OTf]**
during catalysis at 30, 150, 270 and 360 min.
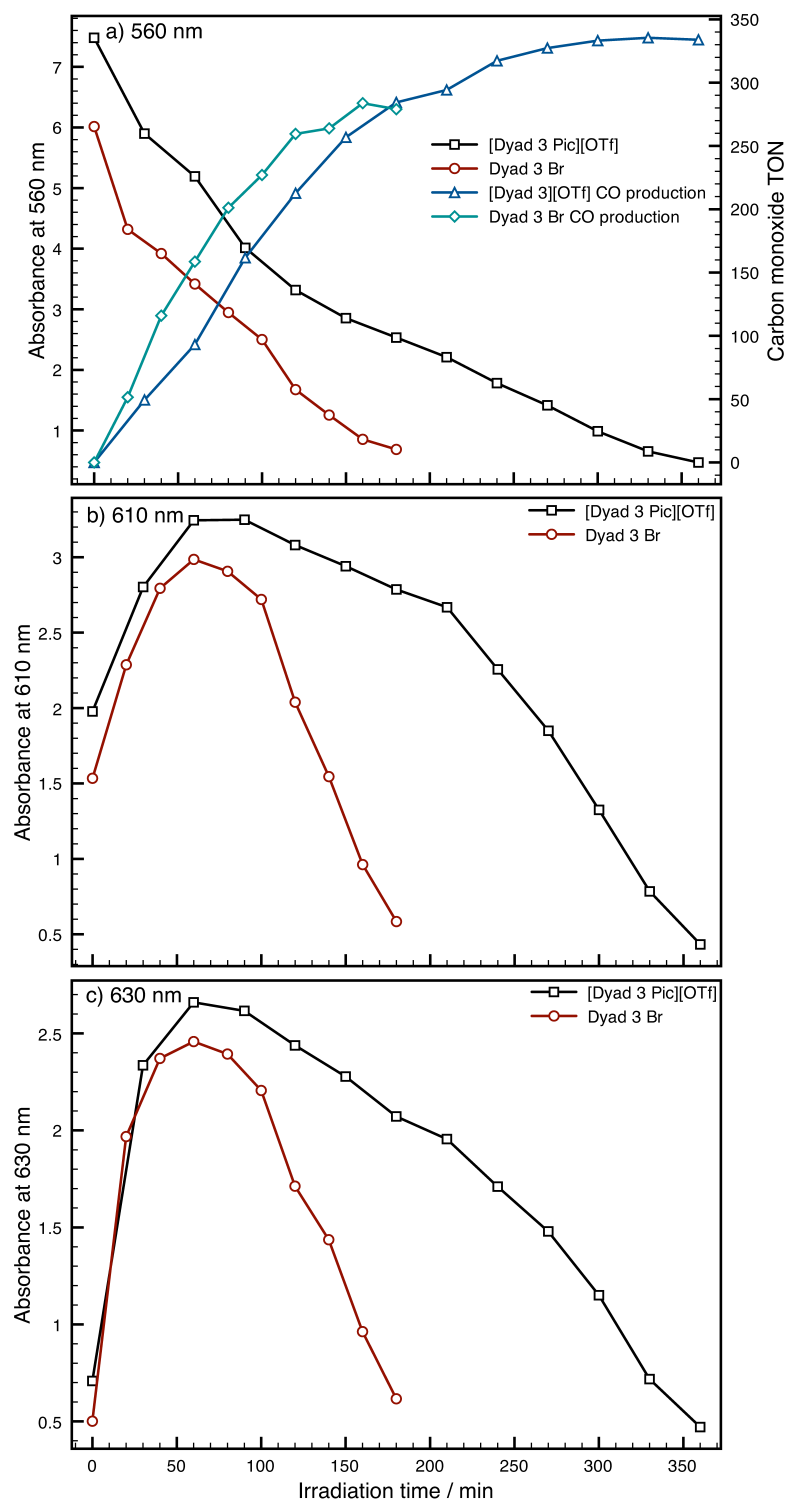
Fig. 140 Grow/decay kinetics for a) 560 nm b) 610 nm c) 630 nm bands of **[Dyad 3 Pic][OTf]** and **Dyad 3 Br**.

4.5 Dyad inter-comparison

4.5.1 Porphyrin degradation

The growth and decay of the Q bands for the three picoline dyads has been plotted in Fig. 141. **[Dyad 3 Pic][OTf]** is the most active and it appears that slow decay of the band at 560 nm is important. There is some contribution in this region from dihydroporphyrin and isotetrahydroporphyrin but the porphyrin absorption is dominant. This suggests that either porphyrin is important for activity or sustained quantities of hydroporphyrin and isotetrahydroporphyrin, or both. The most striking difference is in the absorption at 610 nm, for which **[Dyad 3 Pic][OTf]** shows a large growth and a long lifetime. This indicates isotetrahydroporphyrin is important for activity. The signal at 630 nm originates exclusively form dihydroporphyrin. The least active dyad produces the most dihydroporphyrin but it bleaches most rapidly.
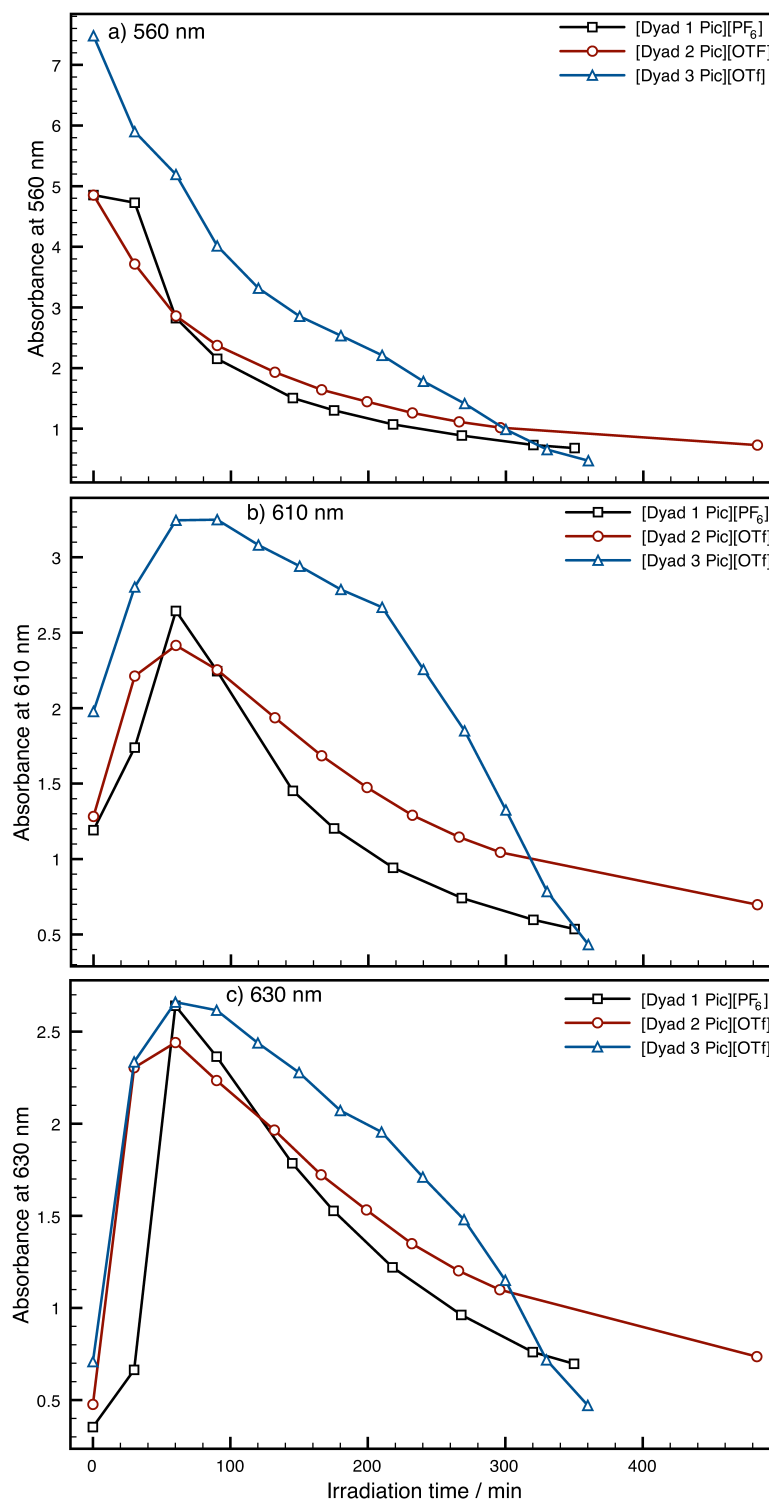
Fig. 141 Ratiometric growth/decay of Q bands at a) 560 nm b) 610 nm c) 630 nm for **[Dyad 1 Pic][PF$_6$]**, **[Dyad 2 Pic][OTf]** and **[Dyad 3 Pic][OTf]**.

4.5.2 Turnover frequency

The turnover frequencies (TOF) of each catalyst are given in Table 14. The overall TOF is the rate until maximum TON is reached and the maximum TOF is the fastest rate within the catalyst CO production profile. Generally the more active catalysts in terms of TON are also the most active catalysts in terms of TOF. The main exception is **Dyad 3 Br**, which shows a much lower TON than **[Dyad 3 Pic][OTf]** but significantly higher overall and maximum TOF. The bromide catalysts all produce CO at a higher rate than their picoline counterparts.

Catalyst	Overall TOF / h^{-1}	Maximum TOF / h^{-1}	Max TON
[Dyad 1 Pic][PF$_6$]	5	10	23
Dyad 1 Br	7	15	26
[Dyad 2 Pic][OTf]	4	14	35
Dyad 2 Br	8	15	30
[Dyad 3 Pic][OTf]	60	97	360
Dyad 3 Br	106	151	270

Table 14 Overall and maximum turnover frequencies for all catalytic systems along with maximum turnover number for CO.

4.6 CO₂ photoreduction with two components

The two separate components, ZnTPP and [Re(Bpy)(CO)$_3$Pic][PF$_6$], were tested for CO$_2$ reduction and produced turnovers up to 120.[108] The UV-vis spectra are similar to those of the dyads. Re(Bpy)(CO)$_3$Br was also tested with ZnTPP and produced up to 65 turnovers.

The plot in Fig. 142 gives the TON for all three dyads with picoline ligands and the two separate components, composed of ZnTPP and $[ReBpy(CO)_3Pic][PF_6]$.
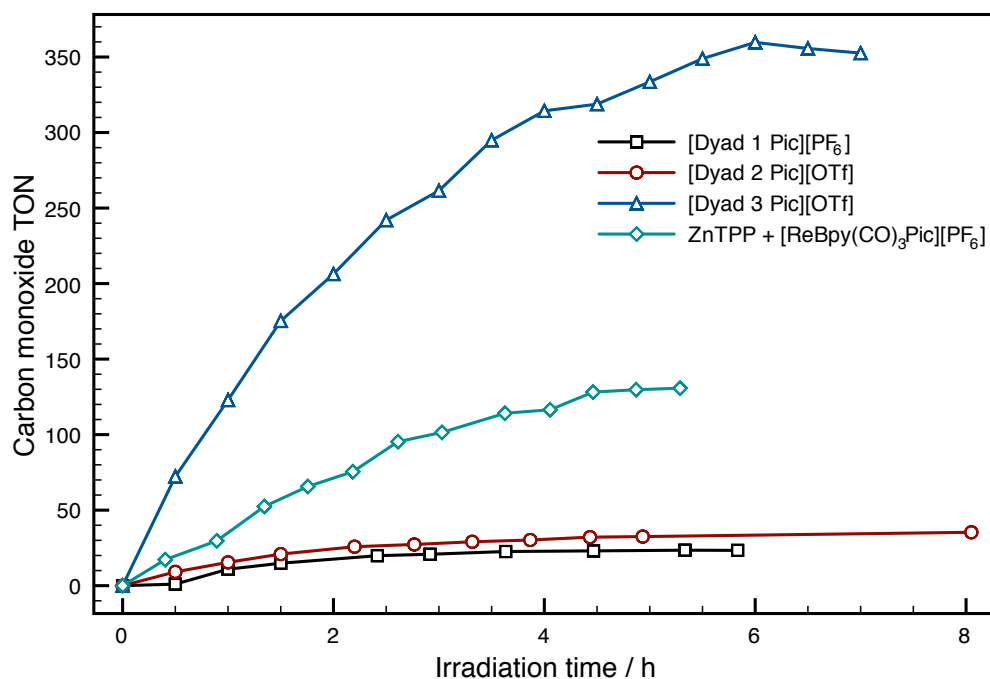
Fig. 142 Carbon monoxide TON for **[Dyad 1 Pic][PF₆]**, **[Dyad 2 Pic][OTf]**, **[Dyad 3 Pic][OTf]** and ZnTPP + $[ReBpy(CO)_3Pic][PF_6]$.

4.7 CO₂ photoreduction products

The photocatalytic reactions produced carbon monoxide, which was identified and quantified by gas chromatographic analysis. The only identifier for CO in the GC is retention time. To provide unambiguous identification of the gas produced the headspace was measured with IR spectroscopy. An example spectrum is shown in Fig. 143 of the headspace from a photoreaction with **[Dyad 3 Pic][OTf]**.
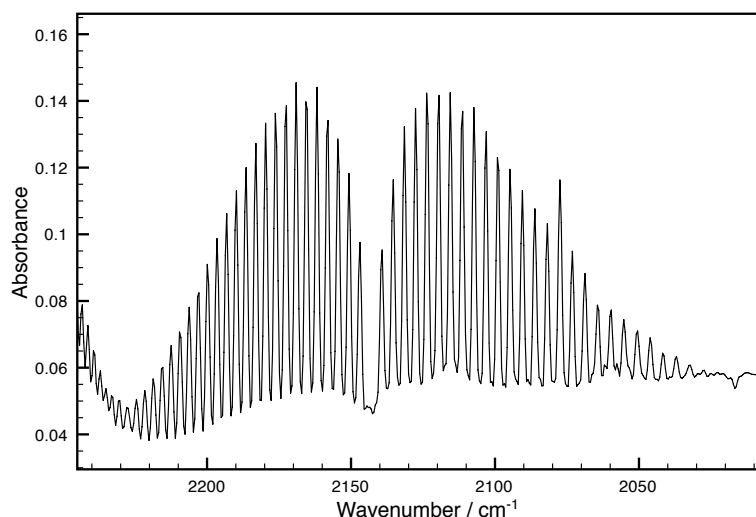
Fig. 143 Gas phase infrared spectrum of photoreduction cell headspace after 420 min irradiation.

It was necessary to investigate the selectivity of the catalytic system for CO_2 reduction products other than CO. Infrared spectroscopy was employed to detect formate or formic acid type species in the reaction solution. The background solution of CO_2 dissolved in DMF/TEOA is likely to interfere with signals from alternative CO_2 reduction products, even with background subtraction. The reaction solution was diluted five times with CH_2Cl_2 to reduce the interfering signals. An authentic sample of sodium formate was measured in DMF/TEOA and CH_2Cl_2 in a ratio of 20:80 respectively. The sodium formate was poorly soluble and so formic acid was used instead. Despite the solvent mixture it was possible to observe a signal at 1713 cm⁻¹. The two component system of ZnTPP and [ReBpy(CO)₃Pic][PF₆] was tested. In Fig. 144 the above spectrum shows the reaction mixture at 0 h irradiation and below, the reaction mixture after 2 h irradiation, both diluted five times in CH_2Cl_2. Both spectra are plotted on top of an authentic sample of formic acid in an identical solution. After 2 h irradiation no formic acid can be detected and certainly less than ten turnovers can have been produced.

162
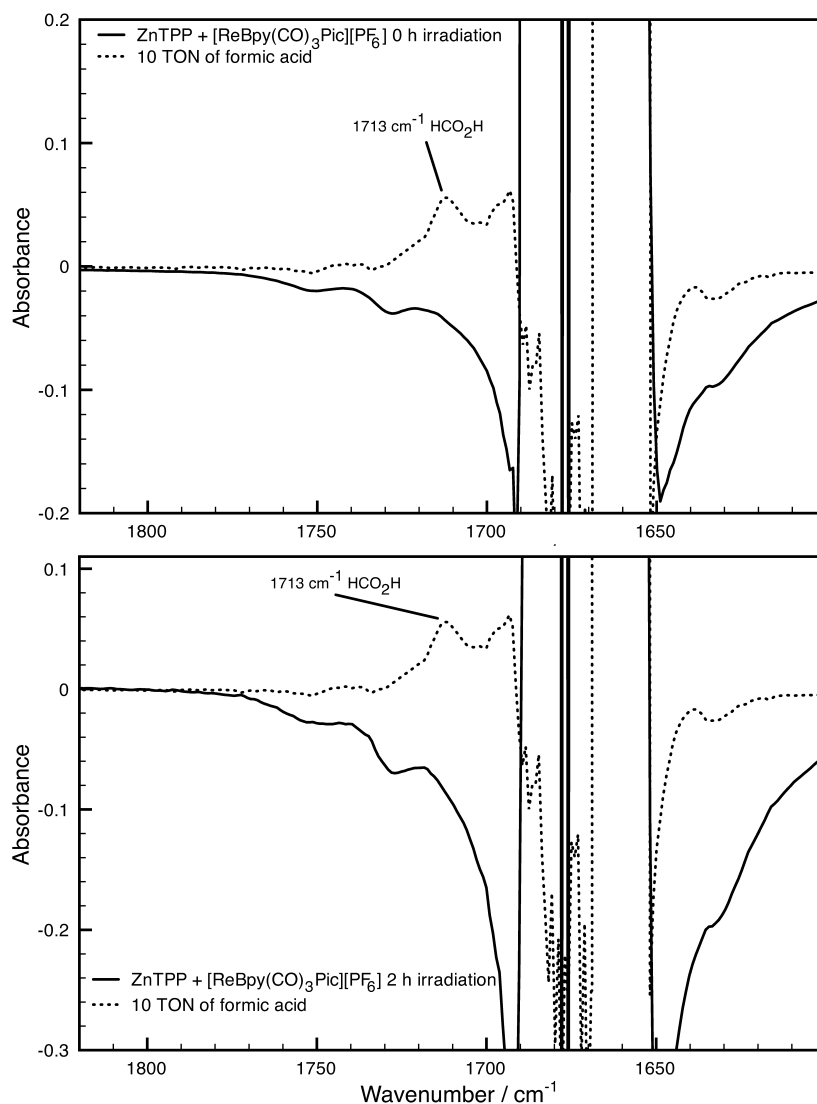
Fig. 144 Above: 0 h irradiation, below: 2 h irradiation. Both plotted on top of 10 turnovers of formic acid.

4.8   Structural changes during the photo-reaction

4.8.1   Photoreduction of the metalloporphyrin

Since a chlorin species is formed during the reaction it was necessary to identify what chemical group is saturating the pyrrole double bond. It could be simple hydrogenation, but in the presence of amines it has been shown that fragments of amine can add to the pyrrole.[117] A higher concentration mixture of ZnTPP in DMF/TEOA was irradiated so that ESI-mass spectrometry of the reaction mixture could be performed. The isotope pattern matches best with calculations

163

for a mixture of ZnTPP, ZnTPDHP and ZnTPTHP (Fig. 145). To further confirm the chemical structure of the dihydroporphyrin NMR experiments were performed. A large-scale (50 mg) photolysis was performed of ZnTPP in DMF/TEOA under Ar and the product was exhaustively extracted into ether after addition of water. The ether was removed and the product dried under vacuum. NMR spectra were then taken of the product in CDCl₃ and compared to spectra of an authentic sample of ZnTPDHP (Fig. 146). The lower spectrum is that of the photoreaction mixture and the three intense signals of ZnTPP can be seen at δ = 8.95, 8.25, 7.75 ppm. Five weaker signals can be made out quite clearly at δ = 8.48, 8.33, 8.05, 7.85, 7.65 ppm and they correspond well in shift, multiplicity and integration ratio to those in the above spectrum of ZnTPDHP. Importantly, a singlet can be observed at δ = 4.1 ppm corresponding to the four protons on the pyrrole.
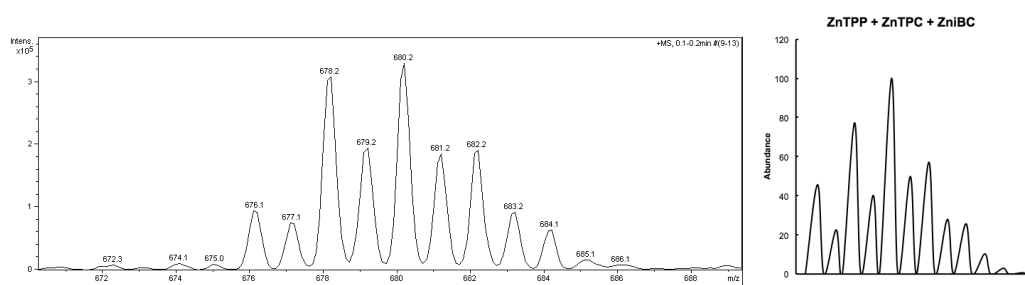
Fig. 145 Left: ESI-MS of ZnTPP in DMF/TEOA after irradiation with $\lambda >$ 520 nm, right: calculated isotope pattern for ZnTPP, ZnTPDHP and ZnTPTHP on top of one another.
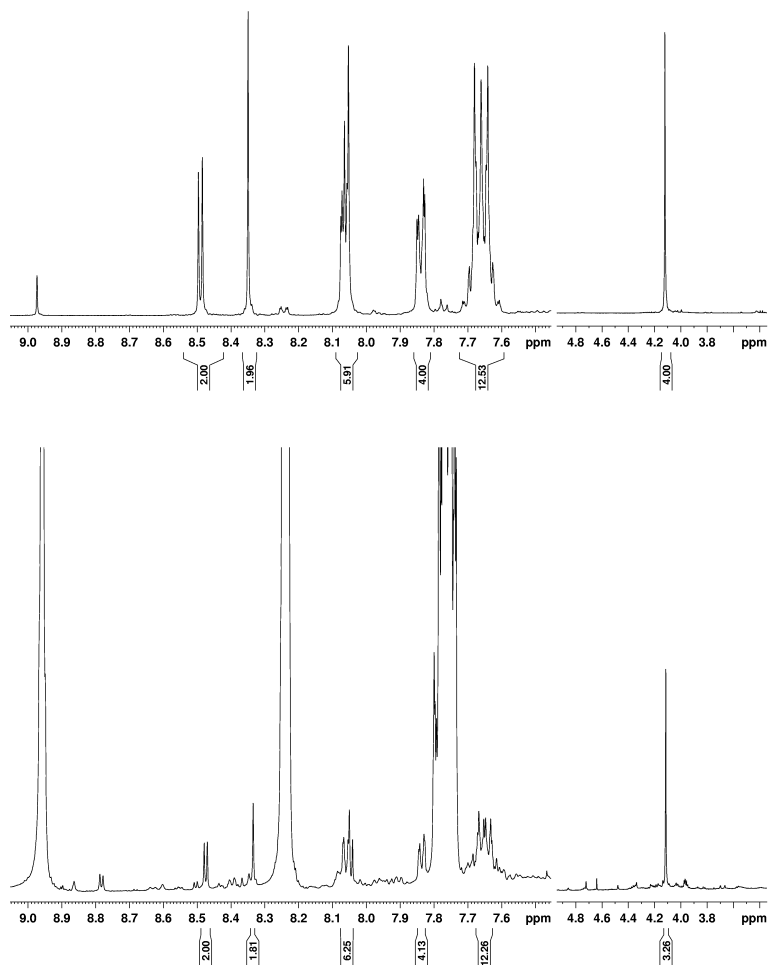
Fig. 146 Above: Authentic ZnTPDHP, below: photoreaction mixture of ZnTPP in DMF/TEOA 5/1.

To determine whether ZnTPDHP is active for sensitizing CO_2 reduction two experiments were conducted (by Marius Campiân). **[Dyad 1 Pic][PF₆]** was irradiated with $\lambda > 520$ nm for 20 min to produce a typical quantity of dihydroporphyrin. The irradiation wavelengths were then changed to $\lambda > 620$ nm to exclusively excite the dihydroporphyrin. CO was produced but the turnovers were half that when just $\lambda > 520$ nm light is used. The second experiment was to test a two component system of ZnTPDHP and [Re(Bpy)(CO)₃3-Picoline][PF₆] for CO_2 photoreduction ($\lambda > 520$ nm). In this case 50 turnover numbers of CO was produced in comparison to 100 when using ZnTPP. Both experiments indicate that ZnTPDHP is active for sensitising the rhenium complex for CO_2 reduction. Despite the increased driving force for

electron transfer outlined in the electrochemistry chapter, ZnTPDHP only produces around half the turnover number experienced with ZnTPP. It is proposed that ZnTPP is more active because it can sensitise rhenium as the porphyrin, then as the dihydroporphyrin and then it bleaches. The dihydroporphyrin can only sensitize as dihydroporphyrin and then it bleaches. Both may include an additional stage as isotetrahydroporphyrin.

Fig. 147 is a general scheme for the photo-reduction of metalloporphyrins. The bottom hydrogenation route of the scheme appears to apply to our data. With the aid of two electrons and two protons the porphyrin becomes hydrogenated to dihydroporphyrin and then stepwise to isotetrahydroporphyrin and onto the hexahydroporphyrin. However, looking at the top route, the scheme also indicates that the porphyrin hydrogenated at the meso position can transform either directly or via tetrahydroporphyrin to dihydroporphyrin. Neither of these species are observed in our spectra but may be involved if the steady state concentration is very low due to rapid conversion. The scheme suggests that the isotetrahydroporphyrin further hydrogenates to hexahydroporphyrin. ZnTPP photo-reduction experiments in benzene with piperidine observed the hexahydroporphyrin in the UV-vis spectra with a peak at 642 nm (Fig. 148).[115] For our system in DMF/TEOA 5/1 it is not possible to say from the UV-vis spectra if hexahydroporphyrin is formed.
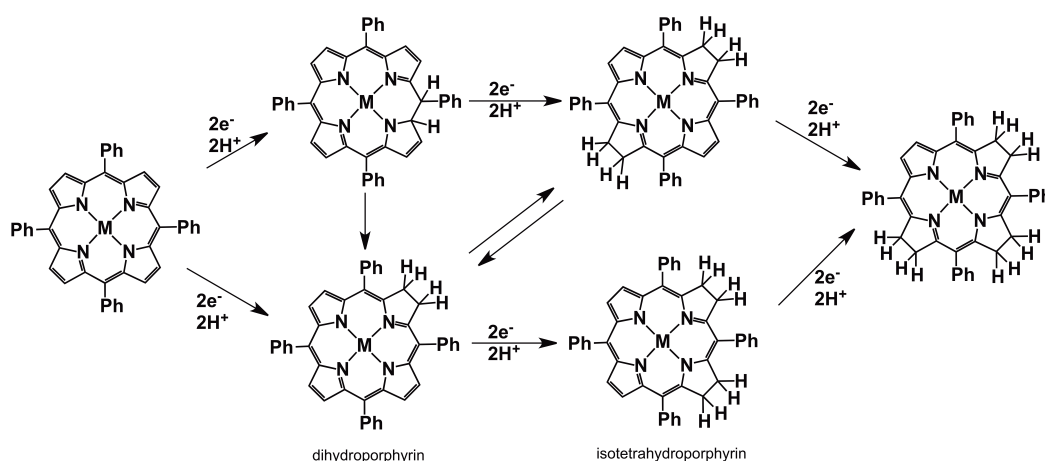
Fig. 147 General scheme for the photo-reduction of metalloporphyrins.[109]
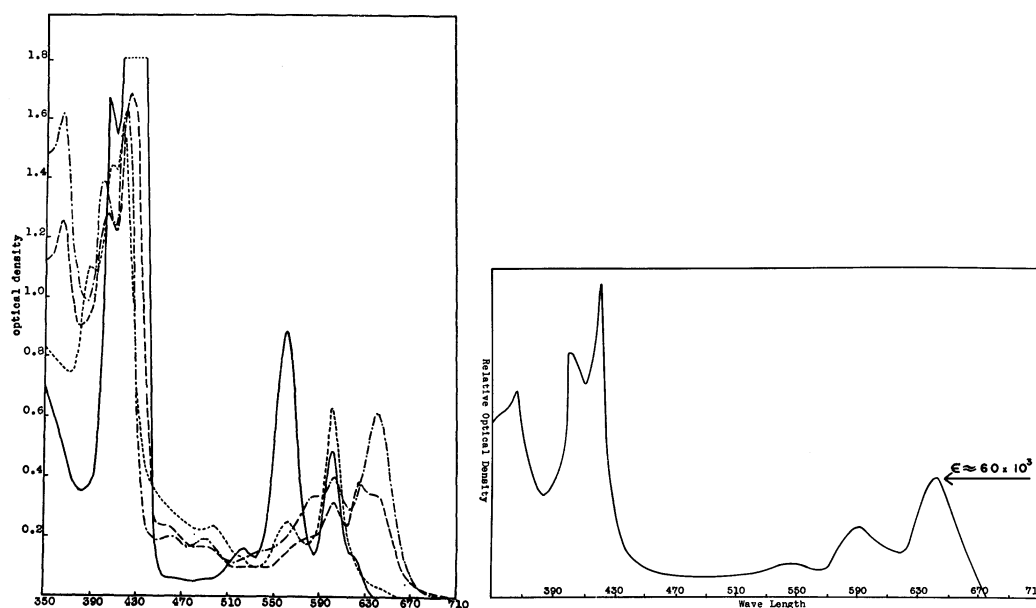
Fig. 148 UV-vis spectra, left: photo-reduction of ZnTPP by benzoin in benzene plus 0.5% piperidine. ——— start, -------- 3 ½ min, -.-.-.-.-.- 12 min sunlight. …….. overnight in the dark with oxygen. Right: Sketch of zinc hexahydroporphyrin spectrum.[115]

4.8.2 Structural changes at the rhenium centre

It was possible to probe structural changes at the rhenium centre using mass spectrometry. The ZnTPP + [ReBpy(CO)₃Pic][PF₆] system was tested (Fig. 149) and the rhenium was observed with picoline (M^+) and without picoline but with TEOA ([M^+ - picoline + TEOA]$^+$). **[Dyad 2 Pic][OTf]** was investigated (Fig. 150) and both M^+ and [M^+ - picoline + TEOA] could be observed. Moreover, in this case it was possible to observe [M^+ - picoline]$^+$ and a mass corresponding with [M^+ - picoline + TEOA + CO₂]$^+$. Four signals corresponding to the same molecular transformations could be observed for **[Dyad 1 Pic][PF₆]**.

167
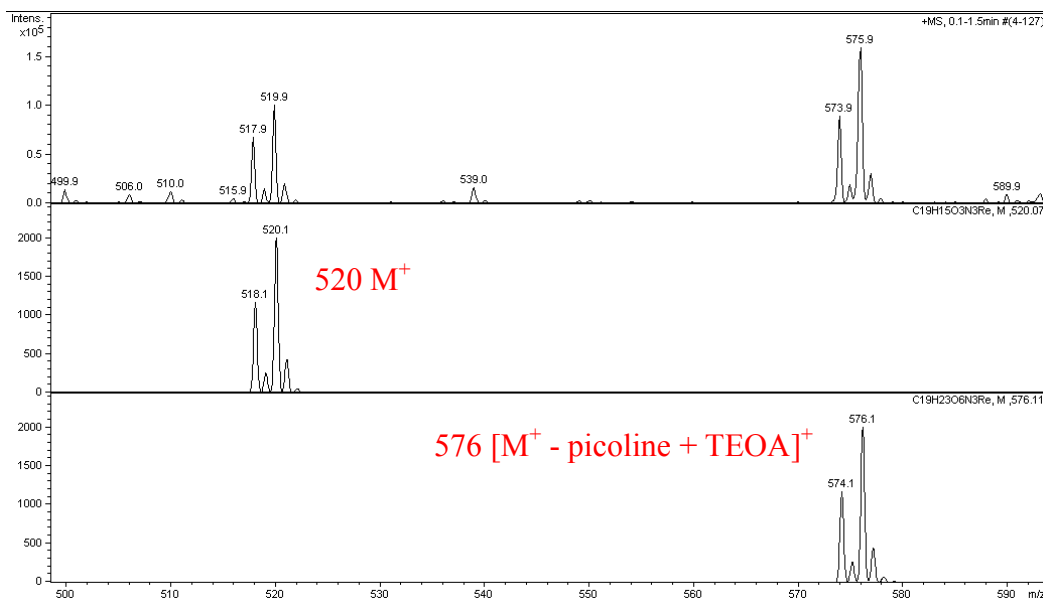
Fig. 149 ESI-MS of ZnTPP + [ReBpy(CO)₃Pic][PF₆] after 5 min irradiation. Top: observed, middle: calculated for M^+, bottom: calculated for $[M^+ -$ picoline + TEOA$]^+$.
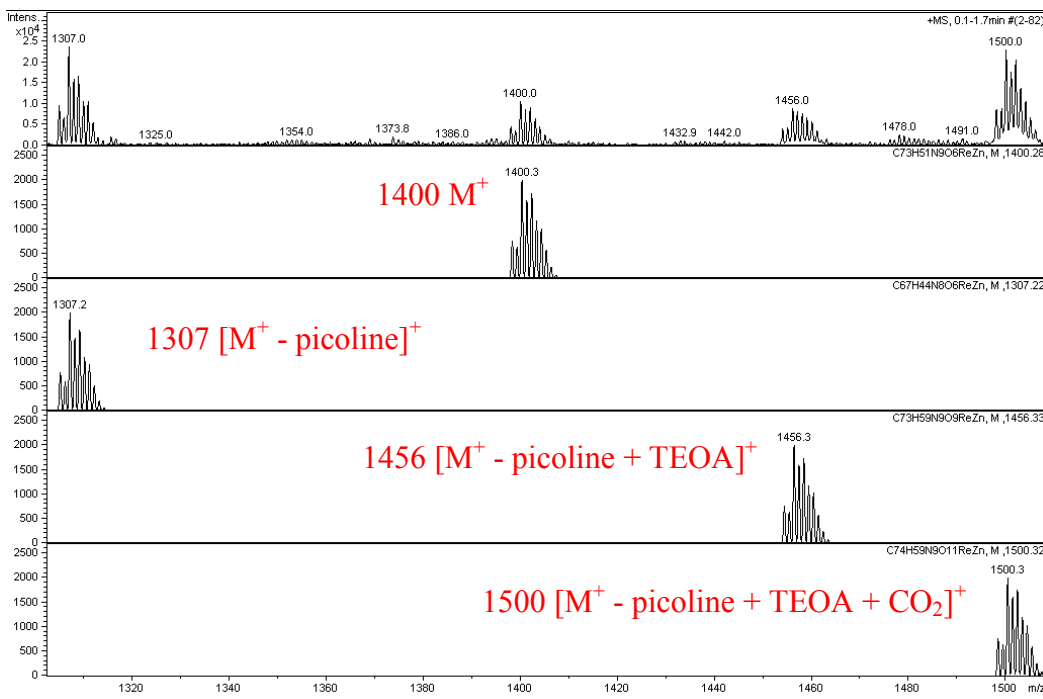
Fig. 150 ESI-MS of **[Dyad 2 Pic][OTf]** after 5 min irradiation. From top to bottom: observed, calculated for M^+, calculated for $[M^+ -$ picoline$]^+$, calculated for $[M^+ -$ picoline + TEOA$]^+$ and calculated for $[M^+ -$ picoline + TEOA + CO₂$]^+$.

The two-component system was investigated by infrared spectroscopy during photocatalysis. The spectrum after 10 min irradiation is shown in Fig. 151. The signal is weak due to the low concentration of the rhenium complex. A background spectrum was taken of DMF/TEOA 5/1. However, as irradiation progresses other species such as oxidation products of the TEOA are produced making the background spectrum less able to correct for the solvent mixture. Nonetheless there is a clear change in the symmetry of the complex as the lower wavenumber peak has split in two. This indicates that the picoline has been substituted, probably by DMF or TEOA. This shows good agreement with the ESI-MS data in which a TEOA complex was observed. The IR spectra were the same after 5 min and 15 min irradiation.
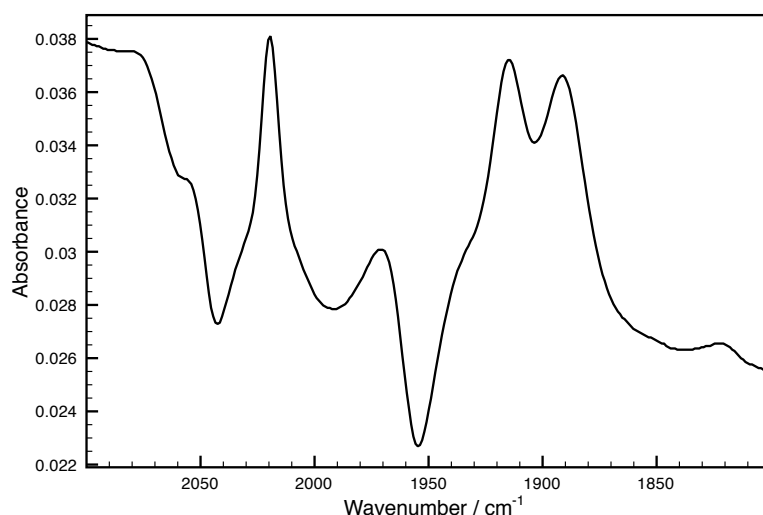
Fig. 151 IR spectrum of ZnTPP + [ReBpy(CO)$_3$Pic][PF$_6$] in DMF/TEOA 5/1 saturated with CO$_2$, after 10 min irradiation.

4.9 Conclusions

Zinc porphyrin combined with [ReBpy(CO)$_3$X]$^{0/+}$ type complexes is an active combination for visible light-powered CO$_2$ reduction. Electrons are transferred from the photo-excited porphyrin to the rhenium Bpy. Covalent attachment of the porphyrin to the rhenium Bpy (the dyads) will overcome the kinetic limitations of diffusion to give faster electron transfer. Changes in the chemical nature of the unit between the donor and acceptor will alter the rates of electron

transfer in the forward and backward directions. **[Dyad 1 Pic][PF$_6$]**, with the simple amide bond, is the least active system. This is probably because the rate of charge recombination increases as well as the rate of charge separation, due to the chemical spacer being small. Introduction of a large spacer, which in theory could increase charge separation and reduce charge recombination, gave **[Dyad 2 Pic][OTf]**. This showed a slight increase in CO$_2$ photo-reduction activity on **[Dyad 1 Pic][PF$_6$]**. The increase in activity is probably due to the increased distance between donor and acceptor causing an increase in the charge separation lifetime. The chemical nature of the spacing unit (methoxybenzamide) will also have an impact. The methoxy group and the additional amide bond will affect the electronics of the spacer. Flexibility is also important as it can determine the conformers available in solution. The methoxybenzamide group is relatively rigid and the main source of flexibility is likely to be rotation about the porphyrin C$_6$H$_4$ and the Bpy-CONH bond as evidenced by X-ray crystallography (Fig. 152).
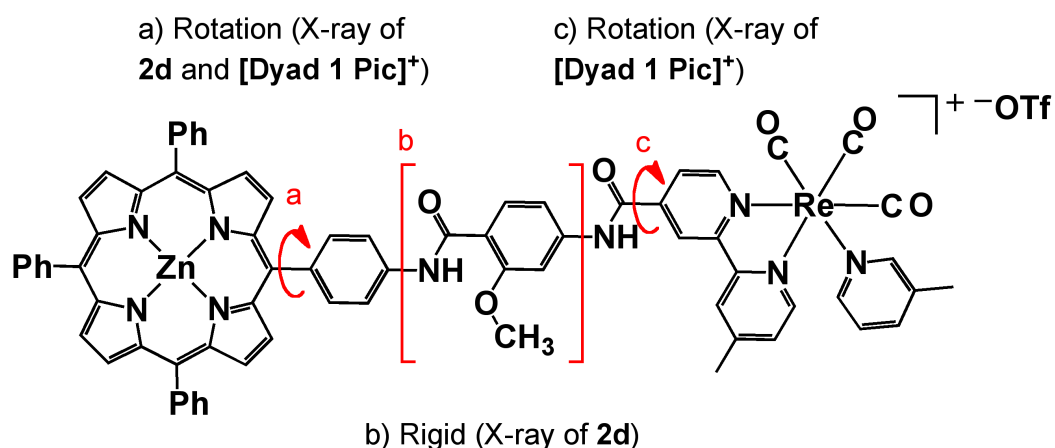
Fig. 152 Possible flexibility in the structure of **[Dyad 2 Pic][OTf]** and sources of evidence.

[Dyad 3 Pic][OTf] is the most active photocatalyst. In this case the spacer is a CH$_2$ unit, providing greater separation than in **Dyad 1** but less than in **Dyad 2**. There are two most likely reasons for the source of increased activity. First, the electronics of the CH$_2$ group. The catalytic activity of the rhenium catalysts is very dependent on changes in the electronics of the Bpy and the addition of

carbonyl groups is detrimental for CO$_2$ reduction activity. **Dyad 3** does not have the carbonyl group directly attached to the Bpy. This is backed-up by the second most active system, the two separate components, in which there is also no carbonyl group on the Bpy. Addition of carbonyl groups to this system significantly reduced activity. However, other factors must be taken into account with the two separate components. The second main factor in the activity of **Dyad 3** is likely to be the flexibility of the CH$_2$ group. A range of conformers is possible, some of which could have the rhenium unit bent back near the porphyrin allowing through-space electron transfer instead of through-bond (Fig. 153). In this way, **Dyad 3** may operate like the two-component system but tethered together and therefore overcoming diffusional limits.
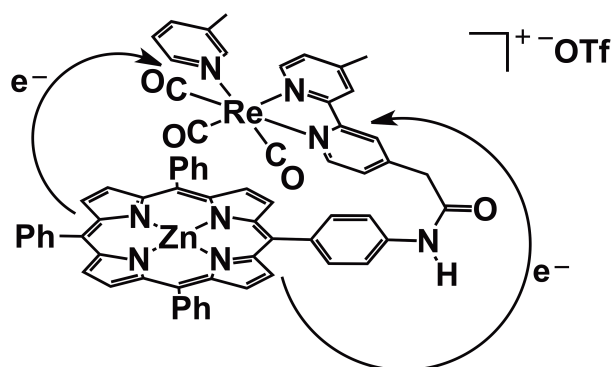
Fig. 153 Possible conformation of **[Dyad 3 Pic][OTf]**.

For systems of lower activity, there is no difference between the picoline or bromide complexes. However for **Dyad 3** there is a significant difference in activity. This suggests that the factors leading to low activity dominate and the charge on the rhenium has negligible affect. Once these have been overcome to some degree, the charge on the rhenium becomes important. The bromides form a neutral complex and the driving force for electron transfer is low relative to the positively charged picoline complexes. The answer is not quite this simple as the driving force for **Dyad 3 Br** is in fact negative despite producing TON = 270. From the mass spectrometric and infrared experiments of the reaction mixtures we know that the axial ligand is substituted and that this begins within the first five minutes of irradiation. The bromides were not tested but the literature shows

$[Ru(Bpy)_3]^{2+}$ sensitized systems with a chloride ligand on the rhenium also undergo ligand substitution.

Several reaction intermediates have been identified. The porphyrin is hydrogenated at one of the pyrrole groups during the photoreaction to produce dihydroporphyrin. There is also UV-vis spectroscopic evidence of reduction of a second pyrrole, and from the mass spectrometric studies this probably occurs via hydrogenation, although this has not been shown by NMR spectroscopy. The UV-Vis spectra do tell us that saturation is at two adjacent pyrroles. We can also deduce from these spectra that saturation at opposite pyrroles does not occur nor does saturation at the meso position. Mass spectrometric studies tell us the picoline ligand at the rhenium is substituted. The TEOA complex can be observed along with the complex with no sixth ligand. This could be a result of DMF complexes also forming and then decomposing in the mass spectrometer.

Chapter 5.   Particle System

5.1 Introduction

The photocatalytic systems consist of a porphyrin sensitiser and a rhenium catalyst. The porphyrin donates electrons to the rhenium, which is an electron acceptor. The rhenium can then perform catalytic reduction chemistry using the transferred electron. In one of the dyads of this type charge separation has been shown to occur but is short-lived and extending the lifetime should improve catalytic activity.

Some metal oxides, in the form of extended solids, are semiconductors. The occupied orbitals are grouped as the 'valence band' (VB) and the unoccupied orbitals as the 'conduction band' (CB). When the semiconductor absorbs light an electron is promoted from the VB to the CB. Once in the CB the electron can travel away from the site of excitation and therefore away from the hole left in the VB, providing charge separation. Many metal oxide semiconductors absorb in the UV and high-energy visible parts of the spectrum. Dyes can be attached to the surface of the metal oxides to sensitise them to visible light. If the excited state redox potential is reducing enough, an electron is injected directly into the CB when the dye is excited. Once in the CB, charge separation can occur as above. If particles of metal oxide are used, an electron acceptor can be attached to the same unit and, if the potentials are matched, it will receive the electron injected by the sensitiser. The charge separation capability of metal oxide structures can be exploited for molecular donors and acceptors.

In recent years charge separation has been achieved by anchoring sensitiser and catalyst onto metal oxide particles through which the electron may travel[44, 118-121]. Methodology from dye sensitised solar cells has been exploited to anchor catalyst and sensitiser to the surface of the semiconducting particle. The dye, upon excitation and reductive quenching, injects electrons into the conduction band. Once within the conduction band the excited electron is long lived and can travel through the particle and into the catalyst. In a successful system[121] (Fig. 154) consisting of a cobalt complex electron acceptor, TiO_2 nanoparticles and a

$[RuBpy_3]^{2+}$ derivative sensitiser, electron injection occurs in 180 ps whereas back electron transfer takes 1 ms. Importantly the photoelectron in the TiO_2 conduction band has a half-lifetime of 0.8 s. Whilst electrons in a semiconductor conduction band are not the same as the dyad charge separated state, the duration for which the electron is available to the catalyst is high, particularly as electron transfer from the $TiO_{2(CB)}$ to the catalyst occurs in 10 µs. In this particular example direct electron transfer between Ru and Co is not considered significant.
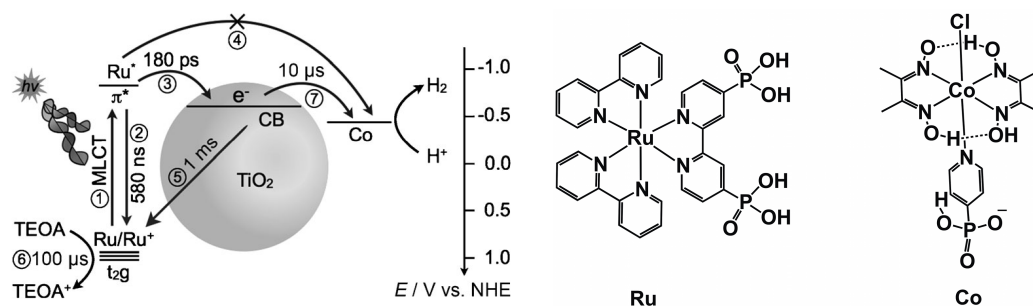
Fig. 154 Kinetics of electron transfer in a donor-TiO_2-acceptor system.[121]

The lifetime of the charge separated state in the first dyad from the Perutz group was measured at tens of picoseconds.[73] Greater efficiencies in catalysis should be possible by significantly increasing the lifetime of charge separation. The separation of the zinc porphyrin and rhenium catalyst by TiO_2 nanoparticles was investigated. Anchoring groups were introduced to the molecules so that they may bind to the surface of the particle and provide efficient charge transfer. There are several types of anchoring group available including carboxylates, phosphonates, sulfonates, catelcholates, acetylacetonates, siloxanes, salicylate and hydroxamates.[122-124] The most heavily studied to date are carboxylates and phosphonates. Phosphonates were selected for this work as they provide stronger binding, which is stable over a wider pH range[125] and less susceptible to dissociation especially in organic solvents.[124] Furthermore there is synthetic methodology already established for the introduction of phosphonates to zinc porphyrins and to 2,2'-bipyridine. Designs were made for the porphyrin and rhenium complexes to incorporate anchoring groups (Fig. 155). Anchoring groups were introduced to only one side of the molecules to prevent binding to more than one particle and subsequent aggregation.

It was shown from mass spectrometric studies that **6d** is probably zwitterionic, existing with one acid group deprotonated and a formally positive rhenium centre. The PO_3H^- groups are electron withdrawing as confirmed by IR spectroscopy. The simple Bpy complex $[ReBpy(CO)_3Pic][OTf]$ exhibited CO stretching frequencies of 2033 and 1924 cm^{-1} (in THF) whereas for **6d** they were 2037 and 1932 cm^{-1} (in CH_3OH). In general the IR, UV and NMR spectra for **6d** are much as for complexes without PO_3H^-.

Mass spectrometry suggests the PO_3H group of **7c** exists deprotonated as the molecular ion could only be observed in negative ion mode. The NMR and UV spectra are much as for other asymmetric porphyrins.
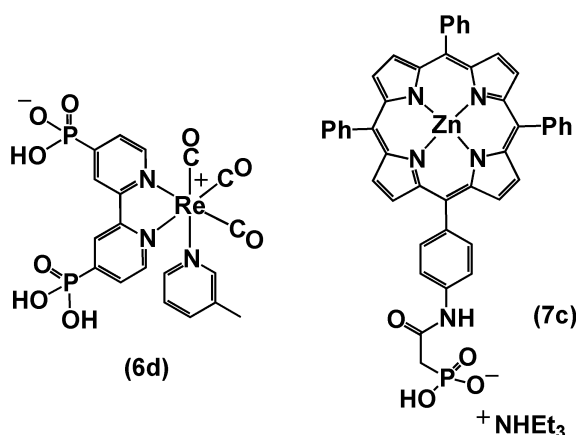
Fig. 155 Catalyst and dye with phosphonic acid anchoring groups.

For systems of this type to be active and efficient via charge transfer *through* the particle, the redox potentials of the dye excited state, catalyst and the metal oxide conduction band must be matched such that sufficient driving force for electron transfer is available. The electrochemical and emission data available when designing the system was for a rhenium analogue with the simple 2-2'bipyridine and the zinc tetraphenyl porphyrin with a bipyridine group attached. The reduction potential of the rhenium complex was -0.84 V vs NHE and the excited state redox potential of the porphyrin was -1.05 V vs NHE. The conduction band of TiO_2 is at -0.703 V vs NHE.[126] The data available tell us that the excited porphyrin should be able to inject electrons into the conduction band of the TiO_2 but the conduction bands of the TiO_2 cannot reduce the rhenium. However, the

electrochemistry was performed in THF and converted[107] from vs Fc/Fc$^+$, these compounds are not the ones we propose to use and the electronic structure will be perturbed when the complexes are anchored onto metal oxide surfaces. Therefore the values are only approximations. Furthermore, it is known that the introduction of an electron withdrawing group on the Bpy will reduce the reduction potential. A methoxycarbonyl group at the 4 and 4' positions of the bipyridine reduces the reduction potential relative to the simple Bpy by 410 mV.[108] If the PO_3 groups have a similar effect, the reduction of the rhenium complex could be as low as -0.43 V vs NHE.

The particle system has other advantages beyond charge separation. The compounds are immobilised and so the system is heterogeneous. This means catalysis can be tested for in any suspending medium as the complexes no longer need to be solubilised. To date, the optimum solvent for CO_2 photoreduction by Re complexes is DMF, the importance of which is two fold 1) The Re complex with phosphonic acid groups is not DMF soluble 2) if possible we need an alternative, ideally water; the particle systems could be suspended in water but also the rhenium complex with two phosphonic acid groups is water soluble. Electrocatalytic CO_2 reduction by Nafion-immobilised Re complexes in water has been observed.[127]

5.2   *Electrochemistry of 6d*

The electrochemistry of **6d** was investigated in order to determine the first reduction potential and if catalysis occurs in both organic solvent and in water. For organic solvents **6d** only dissolved satisfactorily in DMSO. The cyclic voltammogram can be seen in Fig. 156. There is a quasi-reversible reduction wave followed by a reversible wave at $E_{1/2}$ = -934 and -1663 mV vs Fc/Fc$^+$ with ΔEp = 198 and 81 mV respectively. Two reduction waves are typical of ReBpy(CO)$_3$X type complexes.[60] Closer inspection of the first reduction peak shows it is wide, unsymmetrical and has a large peak separation. It is probably a compound peak consisting of several processes. These may be reduction, ligand loss and/or decomposition. There is also a non-reversible peak at -1473 mV, which may be a process related to a minor product from the first reduction peak.

Importantly the first reduction has $E_{1/2}$ = -0.934 V vs Fc/Fc$^+$ or = -0.304 V vs NHE (+0.63 V[107]) making the Re reducible by TiO_2 by 0.40 V. On addition of CO_2 the re-oxidation peak of the first wave is lost suggesting a reaction is occurring. There is also current enhancement at the second reduction wave where Re complexes typically show catalysis. The catalytic reduction of CO_2 to CO requires protons. In efforts to increase catalysis, **6d** was tested for stability to trifluoroacetic acid (3.3 mM) as a proton source, but it did not prove stable to TFA in DMSO monitoring by UV-Vis spectroscopy.
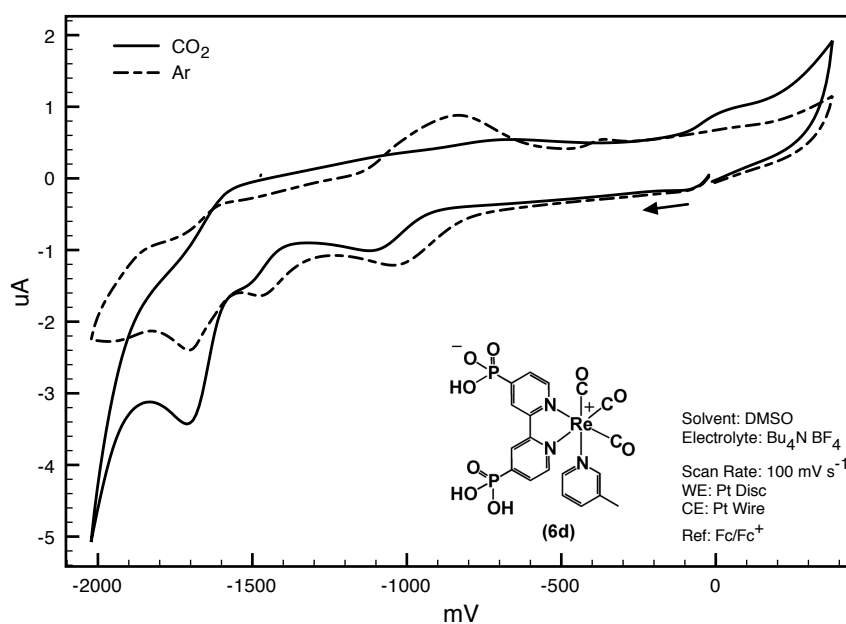
Fig. 156 Cyclic voltammogram of **6d** in DMSO. Bu$_4$N BF$_4$ electrolyte with Pt disc working electrode, Pt wire counter electrode and Fc/Fc$^+$ added as internal standard. Scan rate was 100 mV s^{-1}.

Cyclic voltammetry of **6d** was run in phosphate buffered water (pH 7) and agrees well with previous work[127] (Fig. 157). Comparing electrolyte alone (blue) and with **6d** under Ar (black) it is apparent that a large amount of current is passed on addition of **6d**. Such a large wave is likely to be catalytic H$^+$ reduction. A significant current is also passed with electrolyte alone which is probably electrolysis of water. Under CO_2 a current increase manifests itself as the appearance of a shoulder and a broadening around -1300 mV. These results suggest **6d** is an active CO_2 and H$^+$ reduction electrocatalyst which would agree

with the electrocatalytic production of H_2 and CO seen with $ReBpy(CO)_3X$ type complexes in Nafion.[127] In order to add weight to this conclusion and to quantify activity, bulk electrolysis needs to be performed. Interestingly on the forward reduction scan under CO_2 a shoulder develops around -1200 mV indicating additional catalytic current. However, on the reverse scan the other side of this shoulder exhibits lower current for a given potential than the wave under Ar. The reduction product (e.g. CO or HCO_2H) is probably building up round the electrode and inhibiting the catalyst.
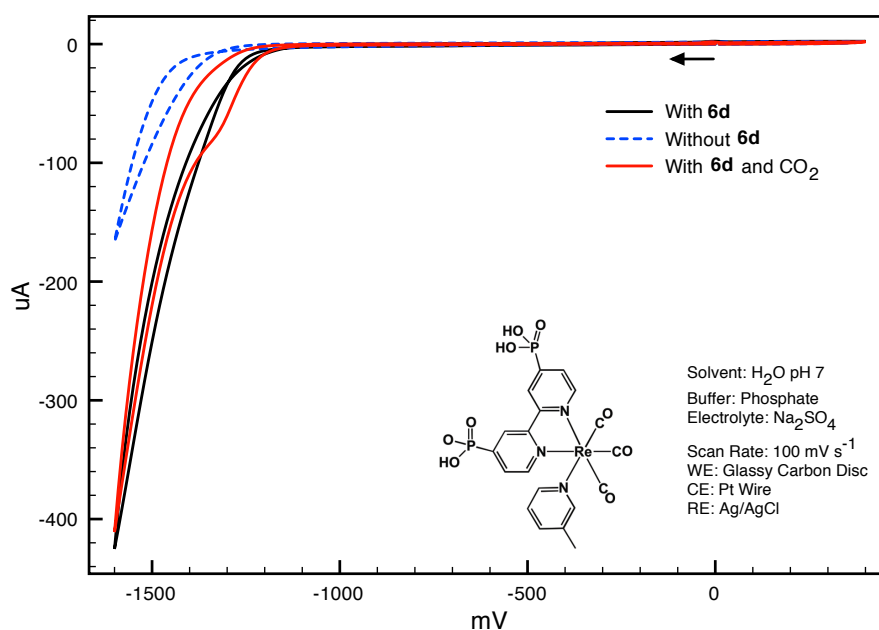
Fig. 157 Cyclic voltammetry of **6d** in H_2O buffered with phosphate to pH 7. Na_2SO_4 was used as electrolyte. The working electrode was glassy carbon, the counter electrode was Pt wire and the reference electrode was Ag/AgCl. The scan rate was 100 mV s^{-1}.

Cyclic voltammetry of **6d** loaded on mesoporous indium tin oxide electrodes (herein referred to as *m*-ITO) was investigated. Anchoring a catalyst to an electrode can be advantageous because the catalyst is immobilised, kinetic limitations of diffusion to the electrode can be overcome and it may provide some stabilisation of the molecule during catalysis. Making an electrode coating porous can significantly increase the surface area to which the catalyst can bind, resulting in increased current densities. *m*-ITO electrodes were fabricated and the

catalyst pre-loaded in methanol. Once dry, the electrodes were investigated by cyclic voltammetry in acetonitrile (Fig. 158). Individual redox processes cannot be observed but there is a current increase on addition of CO_2. The oxidation sweep also exhibits lower current under CO_2 than under Ar, as seen for the free catalyst in H_2O.
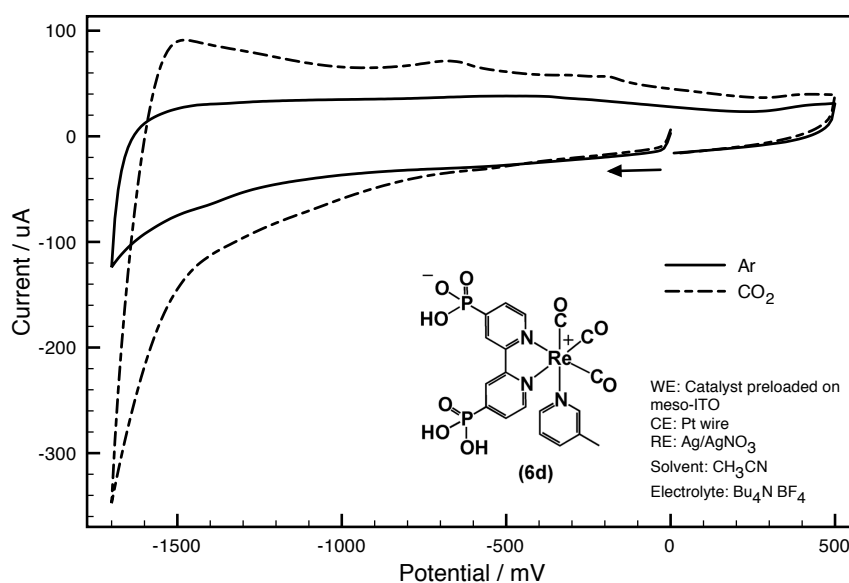
Fig. 158 Cyclic voltammetry of **6d** loaded onto mesoporous indium tin oxide electrodes.

5.3 *Electrochemistry of 7c*

The zinc porphyrin functionalised with a phosphonic acid group, **7c**, was investigated by cyclic voltammetry. The experiment was run in CH_2Cl_2 for comparison with other data but **7c** was not very soluble leading to weak current responses. The CVs with and without ferrocene internal standard are given for clarity (Fig. 159). The CV without ferrocene shows a non-reversible wave followed by a pseudo-reversible wave at +66 and $E_{1/2}$ = +144 mV vs Fc/Fc$^+$ respectively. Addition of ferrocene appears to introduce reversibility to the wave at +66 mV. However, this additional wave could be ferrocene-mediated electrochemistry; the ferrocene is oxidised and in turn oxidises the porphyrin. The CV was performed in CH_2Cl_2 to allow for comparison with the other porphyrins studied. **7c** was not very soluble in CH_2Cl_2 and began to precipitate

179

out and coat the electrodes. A coating of porphyrin on the electrode might prevent other large porphyrin molecules reaching the surface yet allow the smaller ferrocene molecule through. The peak shapes of the second oxidation wave are very symmetrical with respect to the baseline compared with the typical 'duck' shape. This resembles peak shapes seen in film electrochemistry where the electrode is coated with analyte. Crucially with the first oxidation at +696 mV vs NHE, the porphyrin is relatively easy to oxidise. Using the equation $E*_{ox} = E_{ox} - E*_{00}$, the excited state redox potential of **7c** was calculated as -1.31 V vs NHE. Crucially, **7c** should be able to inject electrons into the TiO_{2CB}. It is possible to estimate the driving force for electron transfer from porphyrin to particle using the equation $\Delta G_{ox}* = E_{ox} - E_{red} - E_{00}$. The driving force is -0.61 eV indicating that electron transfer to TiO_2 is favourable. This is only an estimate due to conversion from potentials vs Fc/Fc^+ to vs NHE. Since the excited state redox potential of **7c**, the conduction band of TiO_2 and the reduction of **6d** are at -1.31, -0.703[126] and -0.304 V vs NHE respectively, electron transfer from dye to particle to catalyst should be possible.
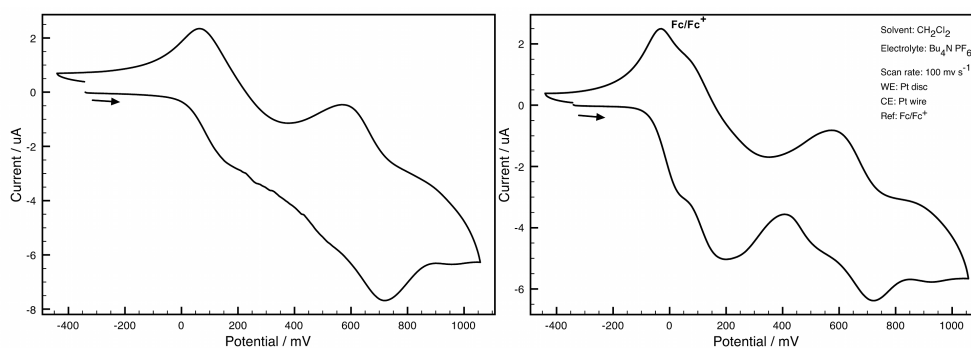
Fig. 159 Cyclic voltammetry of **7c** in CH_2Cl_2.

5.4 Characterisation of particles

5.4.1 Binding

The compounds with phosphonate groups were tested for binding to metal oxide surfaces. The metal oxide used was 25 nm particles of TiO_2 as a 75/25 mixture of the anatase and rutile morphologies. A solution of the compound was made, a

UV-Vis spectrum was taken and then metal oxide particles were added. After stirring for 1 h the suspension was centrifuged to settle the particles and the supernatant removed. This was then syringe-filtered (Millipore filter attached to a syringe) to remove any remaining particles and a UV-Vis spectrum was taken. The absorbance is indicative of the concentration and so the fraction of compound removed from solution by binding to the metal oxide can be determined. Example spectra are shown in Fig. 160 and Fig. 161 for **6d** and **7c** respectively. The Re complex **6d** bound to TiO_2 quantitatively and the porphyrin **7c** bound > 90%.
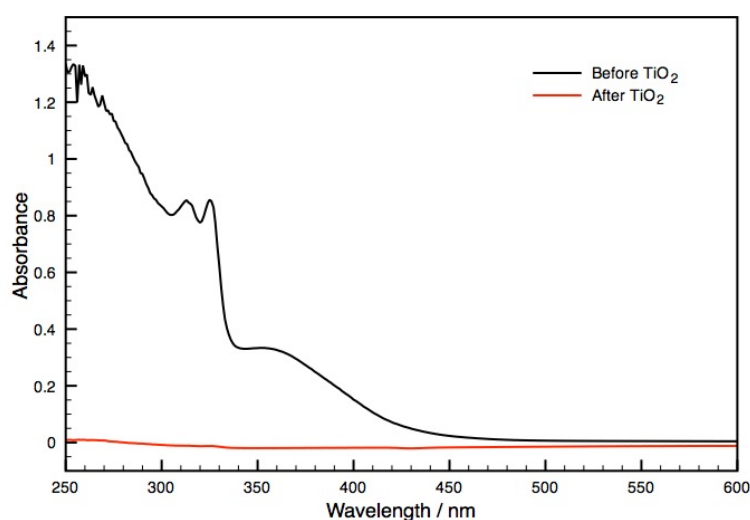
Fig. 160 UV-Vis spectra of a H_2O solution of **6d** before and after exposure to TiO_2.
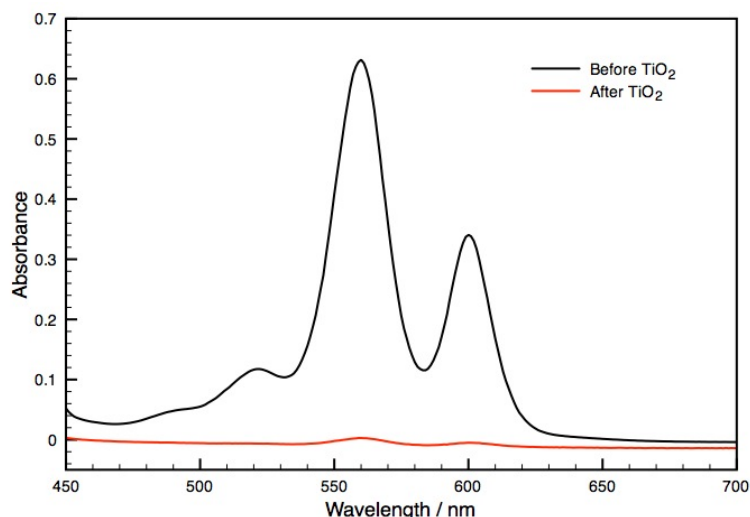
Fig. 161 UV-Vis spectra of a CH₃OH solution of **7c** before and after exposure to TiO₂.

5.4.2   Diffuse reflectance UV-Vis spectroscopy

To observe the rhenium complex **6d** and the porphyrin **7c** on the particle surface diffuse reflectance UV-Vis spectroscopy was utilised. A Kubelka Munk correction[128] was employed which accounts for scattering or reflection from the material beneath the coloured layer being analysed. A background spectrum of TiO₂ was used. The rhenium complex exhibits much weaker absorbance than the porphyrin and had to be at double the loading of the porphyrin to obtain K/S of 0.35 where the porphyrin gave K/S of 1.9. The spectrum of **6d** on TiO₂ (Fig. 162) shows absorption of wavelengths as long as 500 nm. The spectrum on the particles is significantly different to that of **6d** in solution (Fig. 160) indicating that the electronics of the complex have changed. The major changes are probably at the Bpy as this is where the anchoring groups are and the presence of the Bpy is responsible for the rhenium complex absorption in the longer wavelength UV range and the visible. The IR spectrum of **6d** on the particle (Fig. 164) indicates that although the electronics at the rhenium centre are altered, the difference is not as drastic as in the UV-vis. The structure of the porphyrin is retained as the Soret and three Q bands can be observed. The Q bands maintain similar wavelengths and relative intensities as in solution (Fig. 161).
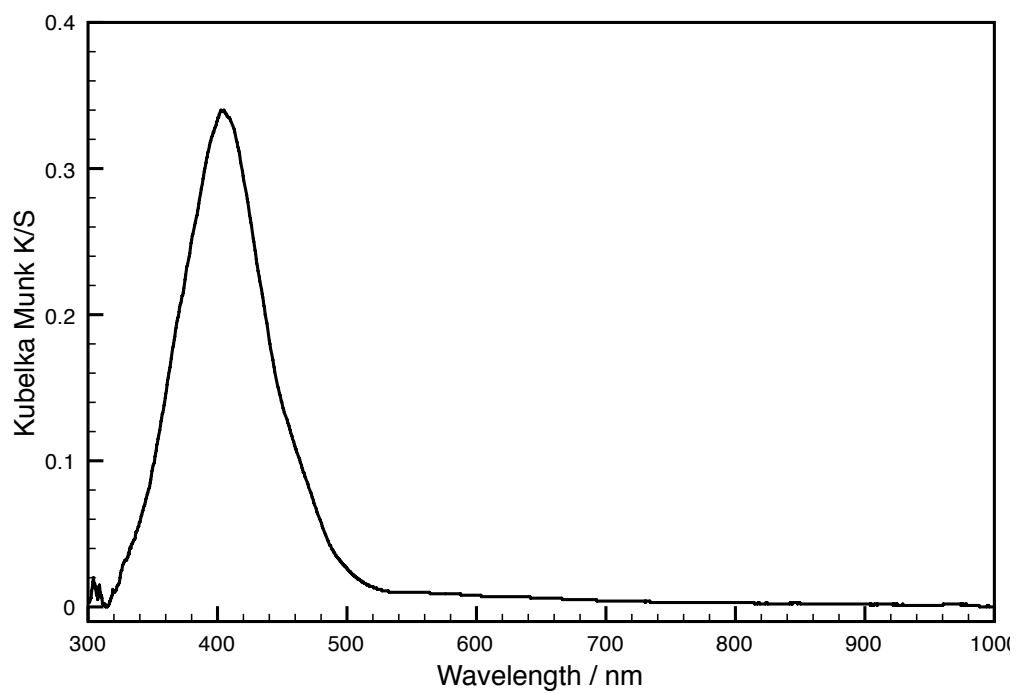
Fig. 162 Diffuse reflectance UV-Vis spectrum of 0.2 µmoles **6d** per 5 mg TiO_2.
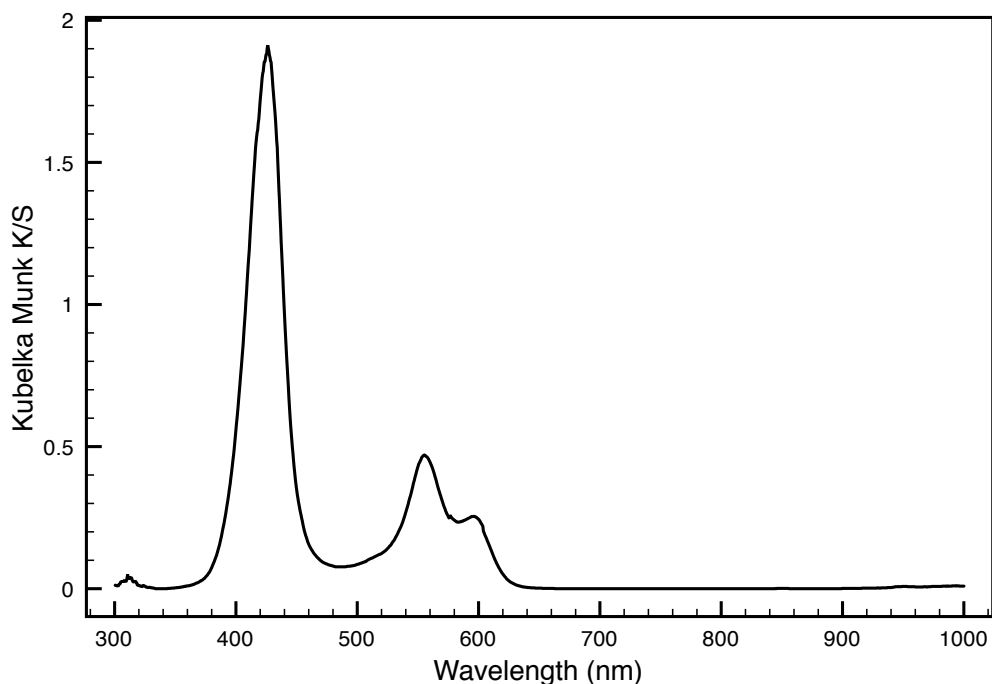
Fig. 163 Diffuse reflectance UV-Vis spectrum of **7c** on TiO_2.

5.4.3   Infrared spectroscopy

TiO_2 particles loaded with **6d** were formed into KBr discs and IR spectra were taken (Fig. 164). TiO_2 alone was run and a ratio of which was taken from the subsequent spectra of Re-TiO_2. The concentration of **6d** is very low but metal carbonyl signals are intense at 2027 and 1916 cm^{-1}. The signal is weak and so the signal to noise is low; nonetheless two clear peaks can be seen in the carbonyl region with a shape and wavenumber comparable with **6d** in methanol solution (2037 and 1932 cm^{-1}). There are also 3 peaks around 1100 cm^{-1} that compare well with literature values[129] for P-O and P=O on TiO_2. This not only tells us the compound is present on the surface of the particles but that it also retains the pseudo C_3v symmetry and therefore the picoline ligand. Since the cationic charge of the rhenium centre is retained the reduction potential for the complex should remain favourable. In methanol solution the IR spectrum of **6d** has peaks at 2037 and 1932 cm^{-1}, on binding to TiO_2 the frequency drops indicting an increase in electron density on the rhenium centre. This is encouraging for electron transfer from TiO_{2CB} to **6d**.

184
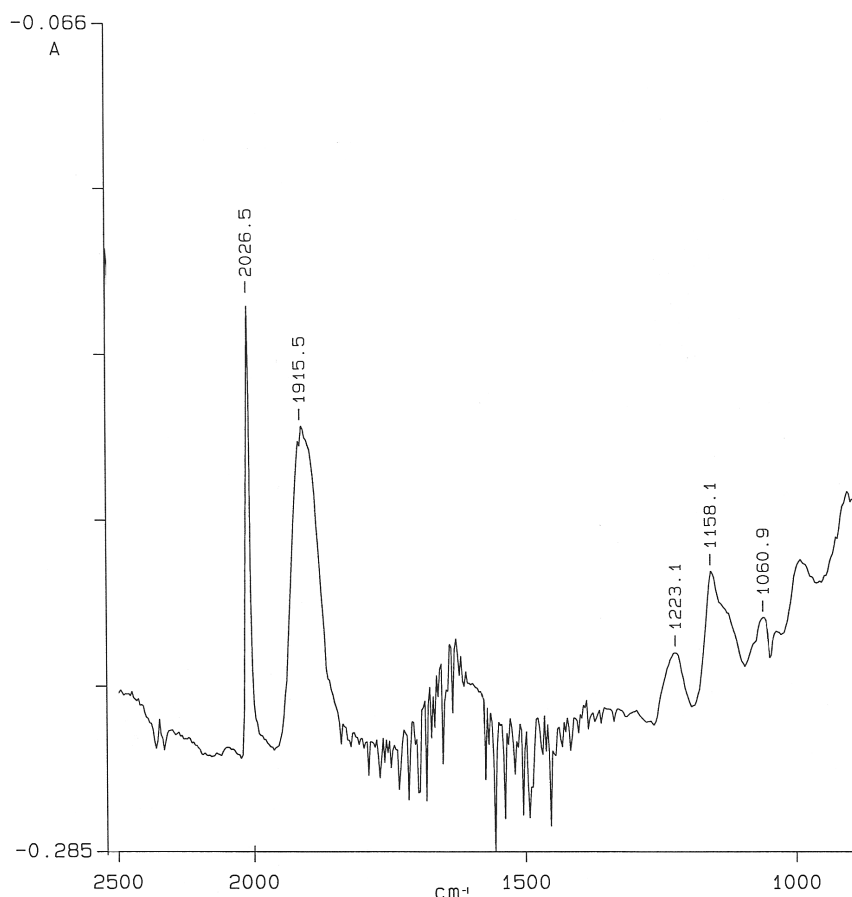
Fig. 164 IR spectrum (KBr disc) of TiO_2 modified with **6d**.

5.4.4   Solid state NMR

To further characterise the rhenium complex on the particles magic angle spinning solid state NMR experiments were performed. To provide a comparison the bipyridine ligand with two phosphonic acid groups was also run alone and on TiO_2. Due to limited material it was not possible to run the rhenium complex **6d** alone. The ^{31}P spectra are shown in Fig. 165. The diphosphonic acid Bpy alone shows one strong signal indicating that there is only one phosphorus environment, agreeing well with the solution phase spectra. Once on TiO_2 (blue) there are predominantly two phosphorus environments plus a myriad of smaller peaks. Multiple phosphorus environments suggest that the acid groups have several binding modes. There are many different ways the catalyst may bind; each acid group has three oxygen atoms through any combination of which it may attach, the TiO_2 is a mixture of anatase and rutile and so the catalyst may be bound to one morphology or both, un-bound acid groups may be in different

protonation states and the complexes maybe bound to the TiO_2 as isolated molecules or they may perturb one-another depending on their proximity. Rhenium bound to the Bpy (**6d**) appears to develop a third major phosphorus environment. The signal at $\delta - 1$ has a shoulder on the right hand side that appears to be of similar intensity to the signal at δ 5.
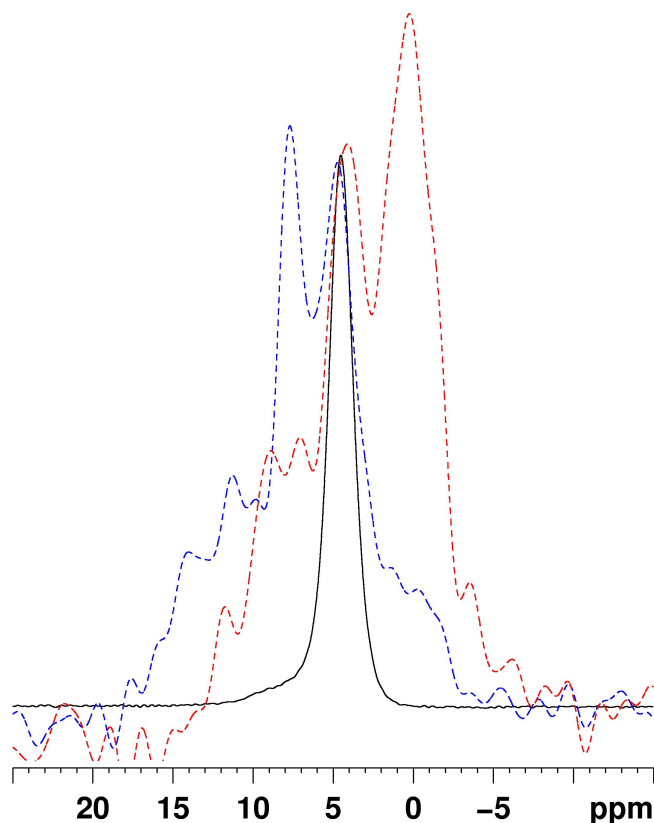
Fig. 165 ^{31}P MAS NMR of phosphonic acid Bpy (black), phosphonic acid Bpy on TiO_2 (blue) and **6d** on TiO_2 (red).

The ^{13}C MAS NMR spectra are shown in Fig. 166 and suffer from a poor signal to noise ratio due to the low concentration of the sample. The spectra are less informative than the ^{31}P spectra but it is possible to say that **6d** is bound to the TiO_2 and that the bipyridine structure is retained.
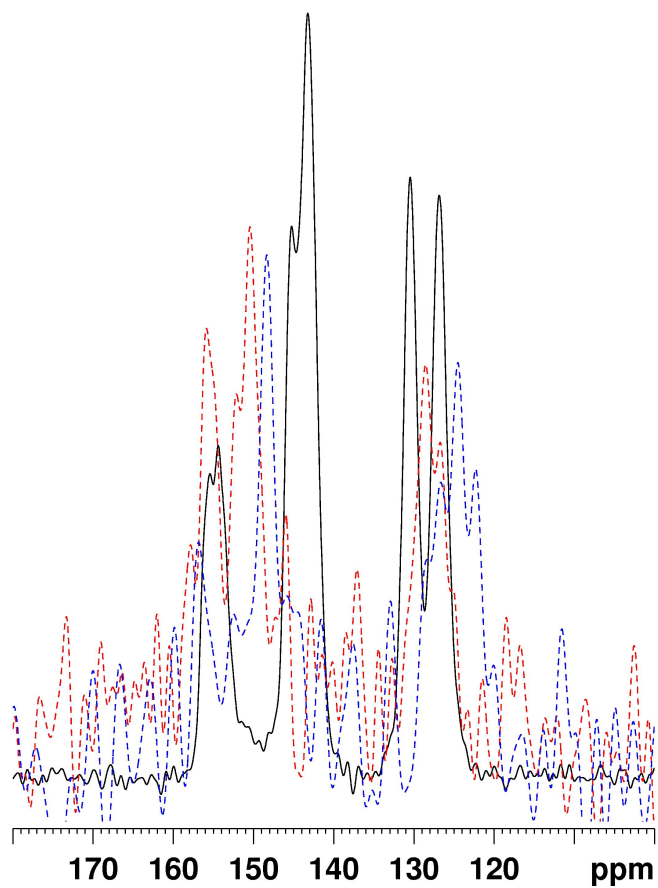
Fig. 166 ^{13}C MAS NMR spectra of phosphonic acid Bpy (black), phosphonic
acid Bpy on TiO$_2$ (blue) and **6d** on TiO$_2$ (red).
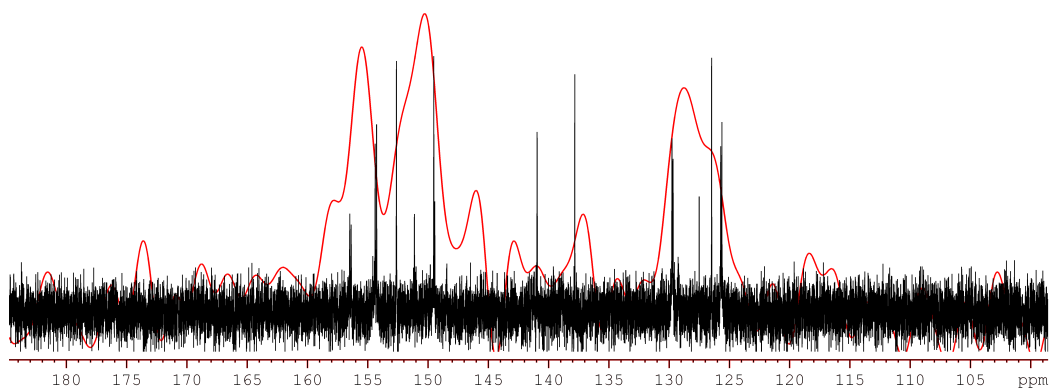
Fig. 167 ^{13}C spectra. Red: MAS-NMR **6d** on TiO$_2$ at 0.2 μmol per 5 mg TiO$_2$.
Black: D$_2$O solution of **6d**.

5.4.5   Porphyrin fluorescence

The fluorescence of the porphyrin **7c** was measured in the absence and presence of TiO$_2$ and compared with simple ZnTPP with and without TiO$_2$ (Fig. 168). The fluorescence quenching of **7c** by TiO$_2$ is significantly greater than for ZnTPP; 87% and 31% respectively. This suggests that functionalization of the porphyrin with the phosphonic acid group significantly increases interaction with the particle.
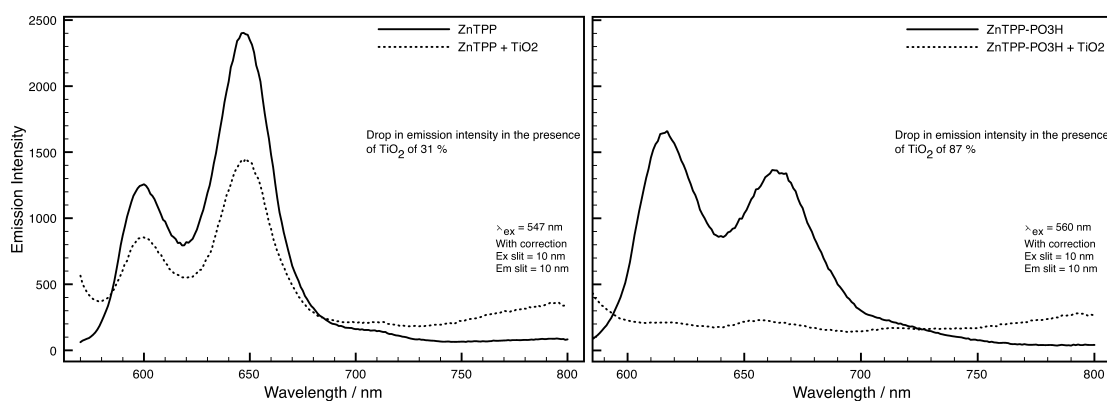
Fig. 168 Emission spectra of ZnTPP and **7c** in the presence and absence of TiO$_2$.
Spectra taken in CH$_2$Cl$_2$ and 1.5 mg of TiO$_2$ was added to 3 mL of solution.
Concentration made as 10^{-5} M then the samples were diluted/reduced if
necessary to match in absorbance.

5.4.6   Characterisation

The rhenium complex **6d** appears to bind very strongly with TiO$_2$. The compound is removed from solution by TiO$_2$ and can be observed on the surface by IR, DRUV and MAS-NMR spectroscopy. The IR and MAS-NMR data suggest that the complex remains intact and largely unaltered on the surface. The stretching frequency of the carbonyls indicates that the electron density on the rhenium appears to increase slightly. The ^{31}P and Bpy ^{13}C signals are retained in the MAS-NMR spectra but the picoline cannot be so clearly observed. The IR spectra indicate that the picoline is present because the symmetry of three pyridine species and three carbonyl groups is retained. The DRUV spectrum suggests a significant alteration in the electronics of the complex as it now shows

one broad absorption with a peak at 400 nm. The solution spectrum showed an absorbance tail up to 400 nm with peaks at 350 nm. A shift in the absorbance of a complex once anchored onto TiO_2 is known and there are several examples of blue shifted spectra.[130-132] The blue shifts have been attributed to deprotonation of the anchoring groups.[130] Red shifts in the absorbance spectrum appears to be rare. Dubois and co-workers recently immobilised a $Re(Bpy)(CO)_3Cl$ catalyst on SiO_2 via amidopropyl linkers at the 4,4' positions of the Bpy.[133] The surface immobilised complex appeared to be red shifted. However, a Re catalyst with amidopropyl groups on the Bpy but not attached to SiO_2 also showed absorbance in a very similar region indicating the red shift was due to this additional chemical group. The UV-Vis absorption was broadened slightly when immobilised on SiO_2 but the extent of change in the band shape was minimal compared with Re-TiO_2.
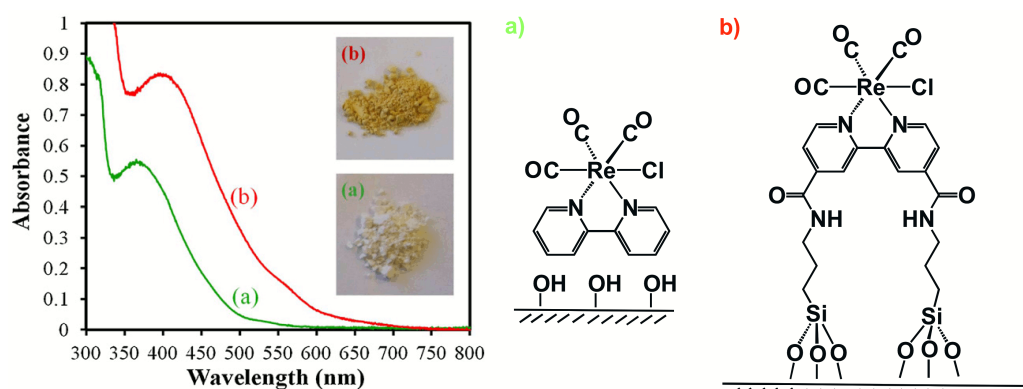
Fig. 169 Left: UV-Vis spectra and photographs of Re catalyst a) physically absorbed in SiO_2 b) covalently attached to SiO_2. Right: Chemical structures of absorbed and bound Re catalysts.[133]

5.5 *CO₂ photoreduction*

In previous work on particle-supported systems, solutions of the catalyst or sensitizer were made in the same solvent used for catalysis. A suspension of particles in the solvent/sacrificial electron donor mixture would be made and the solution of catalyst or sensitizer simply injected; the system would then self-assemble. The full photocatalytic system is assembled fresh every time, and it is a simple route to adding more equivalents of one of the components. However,

the Re complex **6d** does not dissolve in DMF and so the particles had to be pre-loaded (herein referred to as Re-MO$_x$). The IR characterisation of Re-TiO$_2$ was performed weeks after the particles were loaded indicating that the complex is stable on TiO$_2$.

Rhenium photocatalysts absorb the shorter wavelengths of visible light and will perform catalysis under $\lambda > 400$ nm. The Re-TiO$_2$ was first tested with $\lambda > 420$ nm and the system produced a turnover number of 80 in 22 h (Fig. 173). There have been few reports of TNs for Re catalysts under visible light but, as far as we know, this is the highest efficiency achieved. There are a few similar experiments in the literature. When discussing these here, the TN is assumed to be when catalysis had ceased. Ishitani's ReBpy(CO)$_3$PPh$_3$ gave a TN = 12 under $\lambda > 330$ nm (1997) and ReBpy(CO)$_3$P(OEt)$_3$ exhibited a TN = 8 in 18 h under $\lambda = 365$ nm[30], these were the most active of all he tested.[53] Lehn tried ReBpy(CO)$_3$Cl under $\lambda > 400$ nm with additional NEt$_4$Cl to enhance activity and observed TN = 48 in 4 h.[8] The TiO$_2$ may be increasing the stability of the Re catalyst but we have used lower energy light than the previous reports and so this may reduce degradation of the catalyst.

To further understand the effect of anchoring the catalyst onto TiO$_2$ **6d** was tested in a DMSO/DMF mix to allow dissolution and then compared with Re-TiO$_2$ (Fig. 170). **6d** is inactive for CO production unless on the surface of TiO$_2$. One explanation is that **6d** alone cannot produce the MLCT state required for CO$_2$ reduction because of the deprotonated state of one of the PO$_3$ groups. The PO$_3$ groups withdraw electron density and should reduce the driving force for MLCT formation by relieving negative charge build up on the Bpy. However, the presence of a formal negative charge on one of the PO$_3$ groups may inhibit electron transfer from rhenium to Bpy. Once loaded onto the TiO$_2$ the O$^-$ can bind with Ti and the negative charge can delocalise into the TiO$_2$.
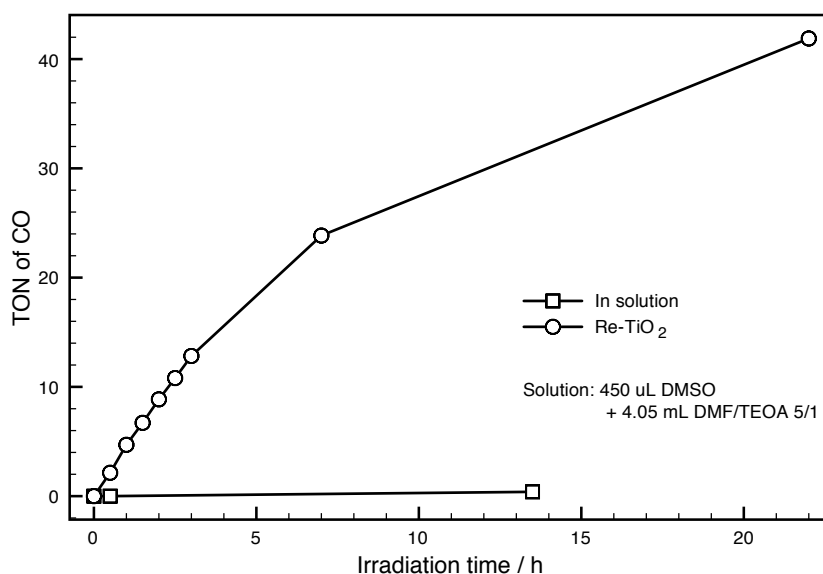
Fig. 170 CO_2 photoreduction **6d** vs Re-TiO$_2$ $\lambda > 420$ nm.

To test for sensitisation of Re-TiO$_2$ by **7c**, the wavelength of light was increased until Re-TiO$_2$ no longer produced CO. Re-TiO$_2$ was active up to $\lambda > 455$ nm and CO production stopped at $\lambda > 515$ nm. Re-TiO$_2$ with **7c** was tested for CO_2 reduction under $\lambda > 515$ nm (Fig. 171). The system gave TON = 32 after 94 h. UV-vis spectra could not be taken of the suspension during catalysis however by-eye it was apparent from the purple to green colour change that hydroporphyrins were probably being formed (Fig. 172). Intriguingly the green colour never bleached despite days of irradiation. Compared with the dyads and the two separate components the system is slow (maximum TOF = 2 h^{-1}, **Dyad 3 Br** = 151 h^{-1}) and inefficient but sensitisation has been demonstrated around MO$_x$ nanoparticles. The cyclic voltammetry suggests the TiO$_2$ can reduce the Re and so the electron transfer mechanism through the conduction band of the particle, the origin of the expected increase in lifetime of charge separation, is possible. The limitation may lie with the porphyrin. It has been reported that introduction of a methylene spacer between the dye and phosphonate group decreases the electron injection quantum yield significantly (from 1 ± 0.1 to 0.5 ± 0.1).[134] Porphyrins also suffer from aggregation via π-π stacking due to high planarity and aromaticity. Aggregates of zinc porphyrins on TiO$_2$ nanoparticles showed an increase in energy transfer rate between molecules and decreased the excited state lifetimes.[123] However, aggregation increased the quantum yield of

191

electron injection.[135] Aggregation can be reduced by the use of co-adsorbates such as chenodeoxycholic acid or by introducing bulky groups onto the porphyrin.
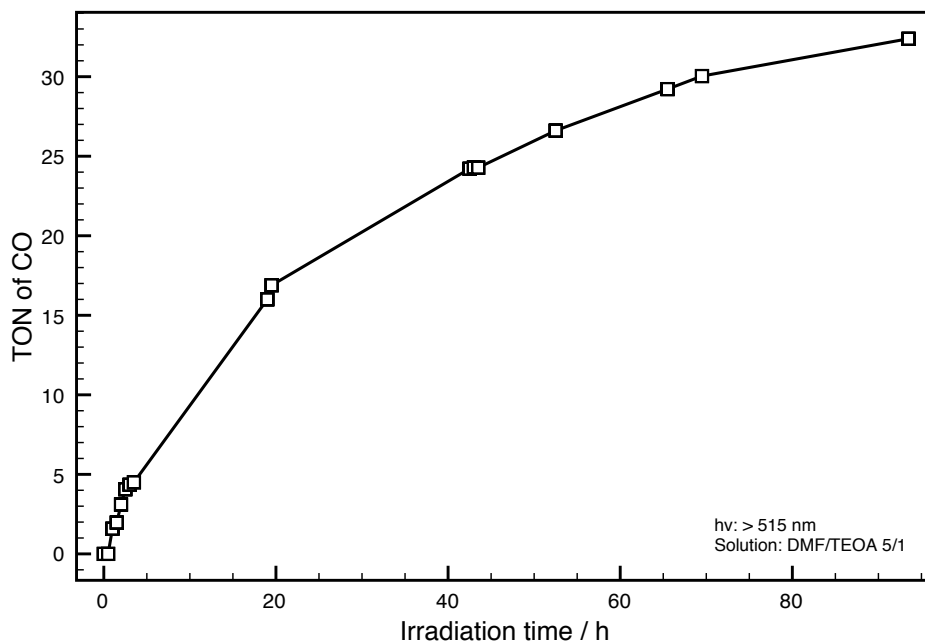
Fig. 171 CO_2 photoreduction Re-TiO$_2$ + **7c**, $\lambda > 515$ nm.
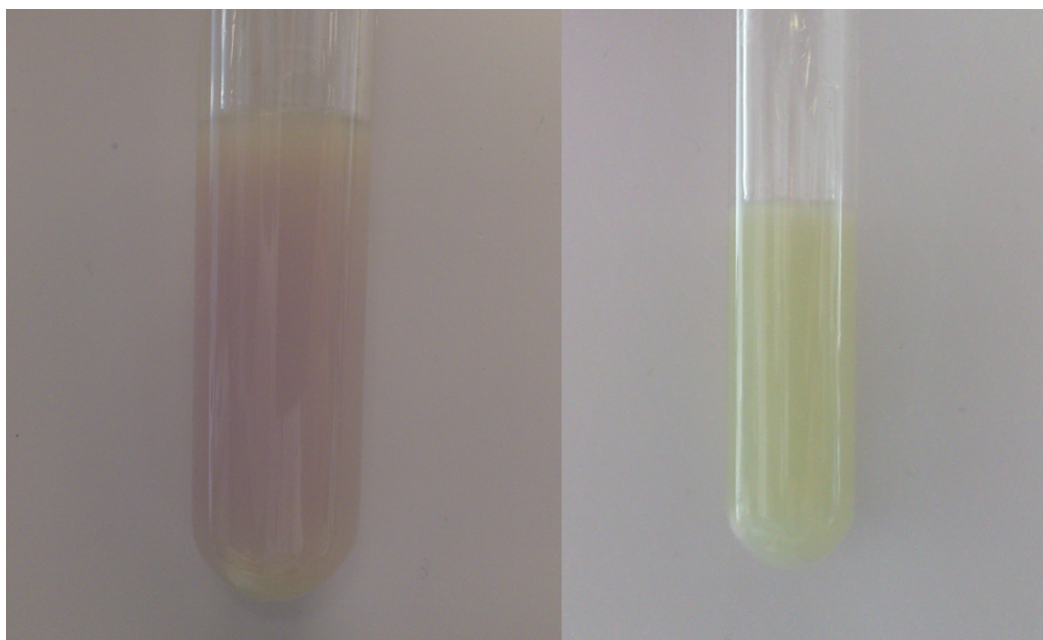
Fig. 172 Photographs; left: Re-TiO$_2$ + **7c** 0 h irradiation, right: after 2.3 h
irradiation with $\lambda > 520$ nm.

Current theories regarding the mechanism of CO_2 photoreduction by homogenous Re catalysts suggest that two molecules must come together to complete the catalytic cycle; a carboxylate bridged dimer is formed.[34] This is not possible if the catalyst is immobilised. There are six possible reasons for the activity of Re-TiO$_2$; 1) the mechanistic theories are wrong; 2) our particular rhenium molecule is mechanistically unique compared with those studied; 3) bound **6d** is in equilibrium and constantly comes on and off TiO$_2$; 4) **6d** falls off during catalysis; 5) the catalyst molecules on the surface are close enough to one another that a Re-COO-Re interaction can occur; 6) The particles aggregate enough that a Re-COO-Re interaction is possible between particles. To investigate reason 5 the Re loading was doubled (0.2 µmoles per 5 mg TiO$_2$) but this resulted in slightly less activity (Fig. 173). 2xRe-TiO$_2$ probably has a very similar TON to Re-TiO$_2$ but the slight reduction is because more molecules are competing for light. This suggests that activity is not dependent on Re-Re proximity. Reasons 1-3 would be challenging to explore. Reason 4 could be tested by removing the particles from the solution after catalysis and running a UV-Vis spectrum. Reason 6 is unlikely as the particles are dispersed initially with sonication and then stirred throughout the catalytic run, but aggregates could be detected using dynamic light scattering.
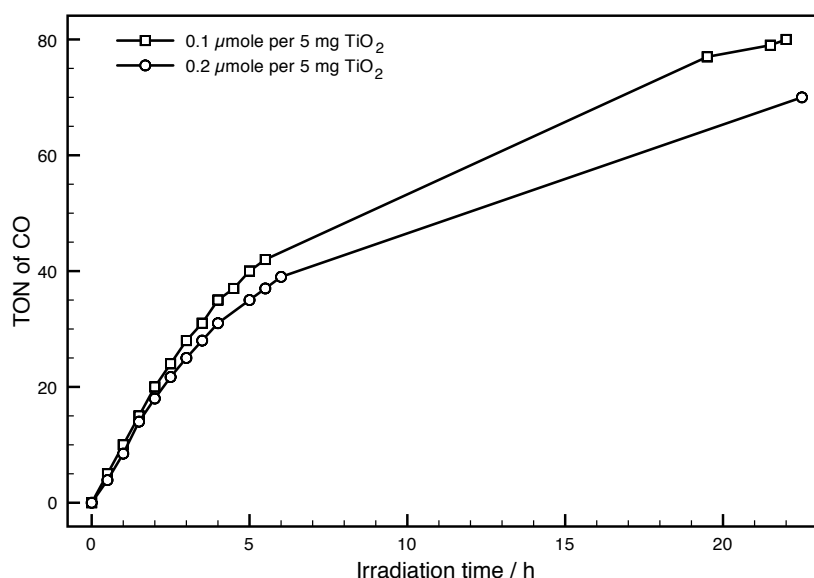
Fig. 173 Turnover numbers of CO for two different loadings of catalyst on TiO$_2$; 0.1 µmoles and 0.2 µmoles **6d** per 5 mg TiO$_2$. Irradiated by $\lambda > 420$ nm.

In order to test the significance of the rhenium catalyst being bound to the particle surface, **7c** loaded on TiO_2 was tested with [ReBpy(CO)$_3$Pic][PF$_6$], a catalyst without anchoring groups. The system produced no more than 2 turnovers of CO after 50 h of irradiation.

The conduction band of ZnO is in a similar position to that of TiO_2[136] and so **6d** was loaded onto ZnO and tested with **7c** under $\lambda > 515$ nm. The system was active (Fig. 174) but produced a TON of only 16 and became inactive after 3 h. One reason could be that ZnO is unstable in acidic conditions and can form Zn^{2+}/dye aggregates lowering electron injection efficiencies.[136]

Particle: ZnO
Catalyst: **6d**
Dye: **7c**
Solution: DMF/TEOA 5/1
Light: hv > 515 nm
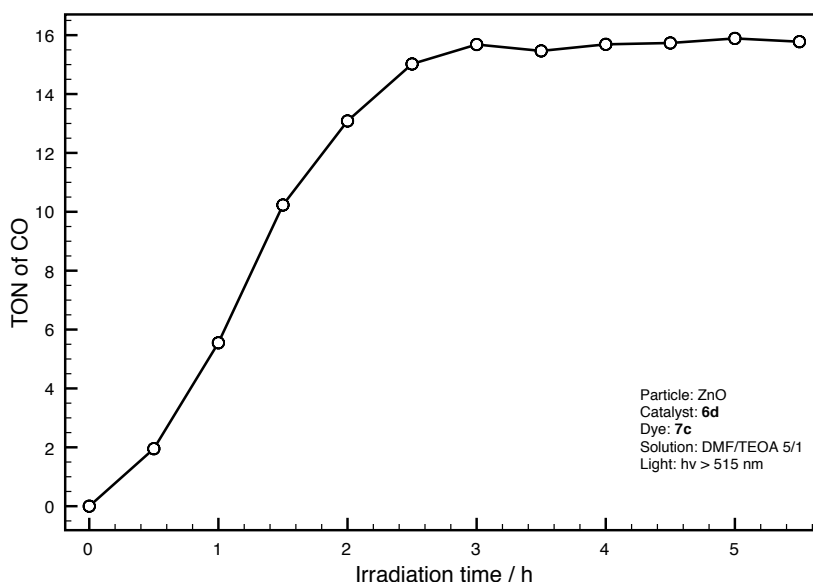
Fig. 174 **6d** and **7c** on ZnO, $\lambda > 515$ nm.

A sample of CdS loaded ZnO was investigated for sensitisation of **6d**. CdS is yellow and has a band gap of 2.42 eV[137] or 512 nm. Extended solids can be less susceptible to photo-degradation compared with dyes existing as discrete molecules. Photolysis with $\lambda > 420$ nm was used and the system does appear to be active but less than Re-TiO_2 under the same wavelengths of light. A DRUVS spectrum was taken to confirm the absorption profile of the CdSZnO but despite the reported band gap of 512 nm there is little absorption in this region or at all for $\lambda > 400$ nm (Fig. 176).
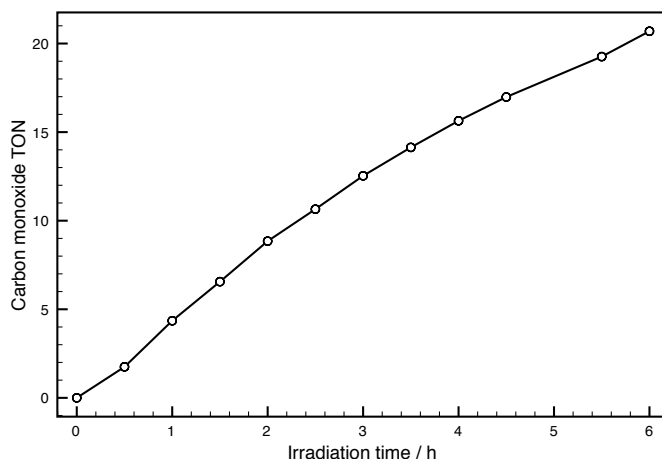
Fig. 175 Re-ZnO-CdS catalytic system, $\lambda > 420$ nm.
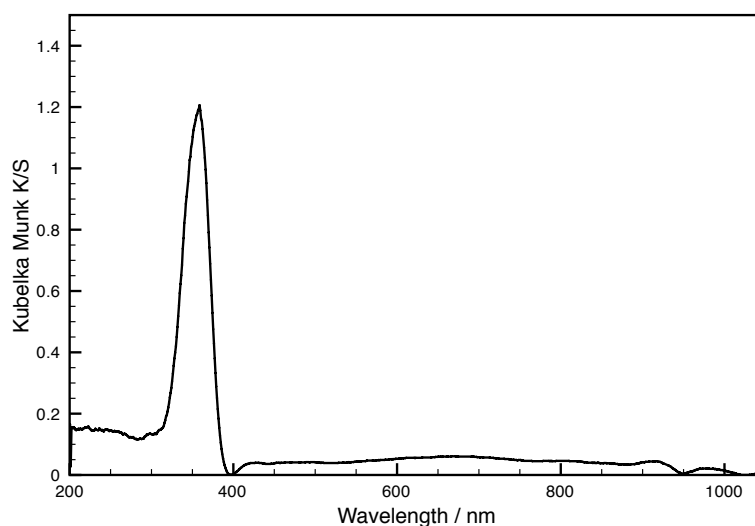
Fig. 176 DRUVS of CdS-ZnO.

5.6 Conclusions and further work

A cationic rhenium bipyridine tricarbonyl complex and a zinc porphyrin have been synthesised with phosphonic acid groups. Both compounds bind tightly to TiO$_2$. Electrochemical investigations suggest that the porphyrin should be capable of injecting electrons into the conduction band of the TiO$_2$ and this should in turn be able to reduce the rhenium complex. Both complexes have been characterised on the particles and appear to remain intact. However, the electronic structure of the rhenium complex appears to be significantly altered as the UV-vis absorption is red shifted and the band shape is very different.

Electrochemical investigations indicate that **6d** is a catalyst for CO_2 reduction and probably also H^+ reduction. The rhenium complex is capable of photocatalytic CO_2 reduction once anchored onto the TiO_2 ($\lambda > 420$ nm). Catalysis is slow (overall TOF = 4 h^{-1}) but relatively efficient with a turnover number of 80. The **6d** loading was doubled in order to increase the proximity of the molecules to one another. Catalysis did not improve despite the mechanistic theory outlined in the introduction that suggests two rhenium complexes form a bridged dimer to perform CO_2 reduction. The red shift in the UV-Vis spectra of **6d** on the TiO_2 surface was confirmed by catalytic activity being maintained up to $\lambda < 500$ nm. Activity ceased at $\lambda > 515$ nm. On introduction of the porphyrin CO production resumed with $\lambda > 515$ nm. Again, catalysis was slow (maximum TOF 2 h^{-1}) and relatively inefficient at TON=32 but competitive with the **Dyad 1** and **Dyad 2** motifs. It is not possible to say if electron transfer is occurring through the particle conduction band or simply between molecules on the surface. A purple to green colour change suggested the porphyrin was being hydrogenated. Interestingly the green colour did not bleach after days of irradiation suggesting inhibition of the porphyrin degradation pathway. ZnO particles performed significantly worse than TiO_2. Testing the analogue of **6d** without PO_3H groups with **7c** on TiO_2 did not produce catalytic CO_2 reduction. This indicates that the catalyst must be bound to the particle surface for activity. It also suggests that **7c** on TiO_2 alone does not produce CO.

Improvements to the structure of the rhenium and porphyrin complexes could be made. The rhenium catalysts are strongly affected by changes made to the Bpy; usually electron-withdrawing groups cause a reduction in activity. A catalyst with just one PO_3H group for anchoring to the particle may be more active. It is also likely that it would be more flexible on the surface, which would be advantageous if two catalyst molecules must come together for CO_2 reduction. A porphyrin with the PO_3H group attached directly to the conjugated core should improve efficiency as the CH_2 spacer and rotations in the C_6H_4 group will reduce electronic communication with the particle.

Chapter 6.   Conclusions and further work

6.1 Synthesis

6.1.1   Conclusions

Two novel metalloporphyrin-rhenium dyads have been synthesised and methodology has been developed for the preparation of a methoxybenzamide spacer dyad and a methylene spacer dyad. Steps for introducing methoxybenzamide units to the porphyrin have been optimized and now make the introduction of multiple spacer units viable.

6.1.2   Further Work

Both methoxybenzamide spacer and methylene spacer motifs could be elaborated on by introduction of different metals to the porphyrin and to the Bpy. It has previously been demonstrated that charge separation occurs in an analogue of **Dyad 1** with Mg in the porphyrin.[73] Within the field of CO_2 reduction alone a range of metal-bipyridine complexes are capable of catalysis, including manganese[21], ruthenium[42] and osmium.[35] The spacer between porphyrin and rhenium can be investigated further. The success of the methylene spacer for CO production may be built upon by introduction of an ethylene spacer. The synthetic methodology toward the methoxybenzamide spacer catalyst is well placed for the introduction of multiple methoxybenzamide units.

6.2 Electrochemistry and photochemistry

6.2.1   Conclusions

Cyclic voltammetry has shown that the picoline complexes can be reduced at significantly less negative potential than the bromides. This is consistent with reduction of a formally positive rhenium centre versus a formally neutral rhenium centre. **Dyad 3** requires more negative potentials to reduce the rhenium by 0.26 Vand this is probably because the carbonyl group is not directly attached to the Bpy. There is little difference in the oxidation potential of the porphyrin between the dyads. The redox potentials and the porphyrin emission data allow

the driving force for electron transfer from porphyrin to rhenium to be estimated. Broadly, an increase in driving force for electron transfer leads to a less efficient catalyst, in terms of TON of CO. This is somewhat counter intuitive but there are other differences in the molecules aside from the redox potentials that can affect catalytic efficiency such as the chemical nature of the spacer.

Interestingly, the **Dyad 3 Br** has a positive change in free energy for electron transfer from excited porphyrin to Re yet exhibits high catalytic efficiency. This could be due to formation of the ZnTPDHP intermediate via hydrogenation of the porphyrin. ZnTPDHP can be oxidised at less positive potentials by 0.24 V than porphyrin and so the free energy change for electron transfer is more negative.

In all three dyads the presence of rhenium leads to quenching of the porphyrin emission. The degree of quenching decreases in the order **[Dyad 1 Pic][PF$_6$]** (85% in toluene) > **[Dyad 2 Pic][OTf]** (55% in CH_2Cl_2) > **[Dyad 3 Pic][OTf]** (23% in CH_2Cl_2). This suggests electron transfer rates also decrease in this order and therefore the more rapid process of emission can dominate. A decrease in electron transfer rate in the back direction would be advantageous for efficient photocatalysis. The order for the degree of emission quenching is consistent therefore with the trend in activity.

The TRIR spectroscopy revealed that the lifetime of the charge separated state in **[Dyad 2 Pic][OTf]** is similar to that of **[Dyad 1 Pic][OTf]**, 42 ps in CH_2Cl_2 versus 23.7 ps in propionitrile or 53 ps in THF.[73] This is consistent with the similar catalytic activity seen in these complexes. In both cases charge separation occurred on the sub-picosecond timescale. The TRIR spectroscopy of **[Dyad 3 Pic][OTf]** on the other hand, was quite different. The growth of the charge separated state could be observed and took place over 12 ps. The lifetime of this state was 335 ps. The methylene spacer has slowed electron transfer in the dyad, both in the forward and backward directions. The charge separation lifetime is approximately seven times greater in **[Dyad 3 Pic][OTf]** and this corresponds with a significantly higher activity for CO_2 photoreduction.

6.2.2   Further Work

[Dyad 3 Pic][OTf] could be tested for remote site photosubstitution. The bromide complex of each dyad should also be investigated. This would help explain the activity of these complexes, particularly **Dyad 3 Br** for which the free energy change of electron transfer is positive.

6.3   *Photocatalytic CO$_2$ reduction*

6.3.1   Conclusions

It has been demonstrated that zinc porphyrins can sensitise rhenium bipyridine tricarbonyl species for CO$_2$ reduction with low energy visible light. The rhenium complexes alone cannot reduce CO$_2$ with $\lambda > 520$ nm but in the presence of zinc porphyrin catalytic quantities of CO are produced. The covalent attachment of zinc porphyrin to the Bpy on the Re to produce dyads should overcome the kinetic limitations of diffusion. The dyads exhibit electron transfer from porphyrin to rhenium and this is likely to be the photochemical mechanism by which visible light induced CO$_2$ reduction is possible. The covalent attachment of porphyrin to rhenium may also increase rates of charge recombination. Six dyads were tested and they exhibit activities both above and below that of the two separate components. The dyads were designed with different bridging ligands separating the porphyrin and rhenium units. Increasing the distance between donor and acceptor in structures capable of electron transfer should in theory increase charge separation. However, the ability of the bridge to conduct electrons, along with the flexibility and range of conformers available, will have an impact as well. Two variations of each dyad were synthesised, with either bromide or picoline as ligand on the rhenium. Bromide has a negative charge and forms a neutral rhenium complex. Picoline is neutral and forms complexes with a formal positive charge on the rhenium. The driving force for electron transfer is significantly higher for positively charge rhenium centres.

The **Dyad 1** motif has an amide bond between porphyrin and rhenium. The separation between donor and acceptor is relatively small. The amide bond has good π-orbital overlap and is a good electron conductor. The bipyridine and

199

C_6H_4 groups will have good π-orbital overlap if the whole system is coplanar but the crystal structure indicates that in the solid state, this is not the case. In solution a range of conformers is likely to be present that will favour electron transfer to different extents. **Dyad 1** is the least active system and despite the difference in driving force, the bromide and picoline complexes are equally active. This suggests the impact of the structure of the bridge significantly outweighs the impact of the charge on the rhenium unit. The shortness of the bridge probably allows rapid charge recombination and the twists in the structure may hamper efficient electron transfer in either direction.

The **Dyad 2** motif has the same structure as **Dyad 1** except for the addition of a methoxybenzamide spacer group. The separation between donor and acceptor is greater than in **Dyad 1**. The spacer group was designed to be planar and the crystal structure of **2d** suggests that in **Dyad 2** this is the case. The methoxybenzamide spacer is expected to conduct electrons well and so the limitations in conduction in **Dyad 2** should be essentially the same as in **Dyad 1**; the twist of the C_6H_4 with respect to the porphyrin and the twist of the bipyridine with respect to the bridge. **Dyad 2** outperforms **Dyad 1** in photocatalysis. The bromide and picoline complexes of **Dyad 2** are essentially the same in activity. The difference in activity between **Dyad 1** and **Dyad 2** is probably predominantly due to the increased distance between donor and acceptor and therefore an increased lifetime of charge separation. However, effects from the electronics of the methoxy group and additional amide cannot be ruled out. It would be difficult to diagnose the impact of the methoxy group as a **Dyad 2** analogue without the methoxy would remove the hydrogen bond and therefore the planarity of the methoxybenzamide bridge.

Dyad 3 outperforms all the other systems as either the bromide or the picoline complex. The methylene bridge is significantly different to the other dyads and cannot be compared as closely. The separation between donor and acceptor is between that of **Dyads 1** and **2** but the activity does not fall between the two. The difference in the electronics and flexibility between the structures must play a significant role. The CH_2 is expected to be less conducting than a planar aromatic system because the electrons of the bonds cannot easily delocalise and therefore

transport charge. **Dyad 3** contains the same C_6H_4 and Bpy groups as the other dyads; providing the same degree of hindrance to electron transfer due to conformations in which electrons cannot delocalise. The significant increase in activity is probably due to the flexibility and lower conductivity of the spacer group. Conformations must be possible that overcome the limitations of diffusion but allow long-lived charged separation. The rhenium unit could flex backwards towards the porphyrin and therefore intramolecular electron transfer could occur through-space and not through-bond (Fig. 177). The reduced conductivity of the spacer will slow charge separation and recombination. If the latter is more affected than the former then high activity would be expected.
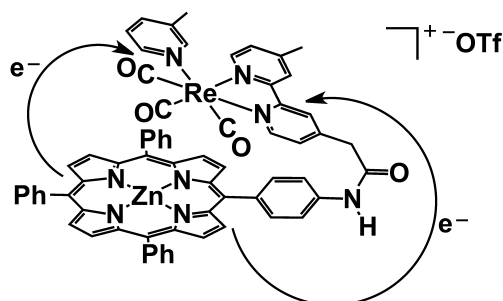
Fig. 177 Possible conformation of **Dyad 3** favouring through space electron transfer.

It is also known that the addition of carbonyl groups to the bipyridine of rhenium electrocatalysts causes a reduction in activity.[17] In systems sensitised by zinc porphyrin, Bpy with methoxycarbonyl groups is essentially inactive compared to a turnover number of 120 with the simple Bpy.[108] In **Dyad 3** the carbonyl group is not directly attached to the Bpy. The rhenium bipyridine unit of **Dyad 3** resembles more the Me_2Bpy complex, with two electron donating groups attached. The Me_2Bpy complex is an efficient CO_2 reduction electrocatalyst, outperforming the simply Bpy complex.[17] **Dyad 1** and **Dyad 2** have a mixture of electronic effects on the Bpy, possessing an electron withdrawing CONHR group and an electron donating CH_3 group. Efforts to optimise the two component system by making structural alterations to the porphyrin and rhenium units has thus far not yielded a more efficient system than the simple zinc tetraphenyl porphyrin and $[ReBpy(CO)_3Pic]^+$.[108] Electron withdrawing groups on the Bpy,

which should favour the formation of a reduced rhenium complex, led to a significant reduction in the catalytic activity.

The bromide complexes are also active for CO_2 photoreduction. The plots of turnover number versus time are very close to those of the picoline analogues. In the case of **Dyad 2**, the activity of the bromide overlays very closely on that of the picoline complex. This suggests that the catalysts posses a very similar active species. ESI-MS data demonstrated that TEOA substitutes the picoline of the picoline complexes during photocatalysis. Perhaps under the catalytic conditions the bromide ligand can also be substituted, yielding a cationic Re as in the picoline complexes. The porphyrin was hydrogenated during catalysis to produce a sensitizer with a greater driving force for reducing the rhenium. This may play a role in the activity of bromide complexes. However, the close agreement in CO production against time for both the bromide and picoline complexes would rule out a separate induction period for bromides.

There are several findings of importance for the mechanism of CO_2 photoreduction by the porphyrin rhenium dyads. TEOA was found not to quench ZnTPP, consistent with the porphyrin emission outcompeting diffusion limited quenching. All three dyads exhibit porphyrin to rhenium charge separation and this must initiate the photocatalysis. The charge separation occurs on the picosecond timescale and can outcompete the porphyrin emission, whereas quenching by TEOA cannot. The lifetime of the hole on the porphyrin is presumably long enough that it can oxidise TEOA. The hole lifetime may not correlate with the lifetime of charge separation in the conditions of catalysis as the electron on the rhenium is consumed by CO formation.

6.3.2   Further Work

Structural optimisation of the dyads is synthetically demanding. A more simple approach is to optimise the two component system first. It is easier to make separate porphyrin and rhenium complexes. To create different combinations of the components is also more simple as they just need to be mixed.

The dihydrogenated (ZnTPDHP) and tetrahydrogenated (ZnTPTHP) products of the porphyrin can be observed by UV-Vis spectroscopy in the catalytic reaction mixtures. The ZnTPDHP intermediate has been synthesised and tested for CO_2 reduction activity with [ReBpy(CO)$_3$Pic][PF$_6$]. The ZnTPTHP could also be synthesised and tested for activity (Fig. 178).
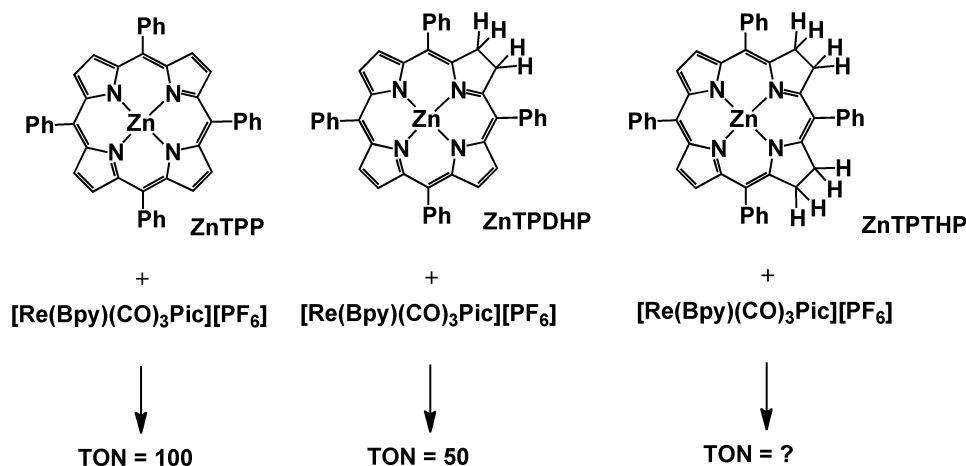
Fig. 178 Activity of the photoreaction intermediates consisting of porphyrin with various degrees of hydrogenation.

Efficient electron transfer from porphyrin to rhenium is hindered by rotation around the C_6H_4 unit between the porphyrin core and the amide. This could be overcome by fusing one phenyl group with an adjacent pyrrole via bromination followed by a Pd mediated cyclisation.[138] This would force the C_6H_4 (subsequently C_6H_3) to be coplanar with the porphyrin (Fig. 179). Achieving any regioselectivity for the subsequent nitration reaction could be challenging.
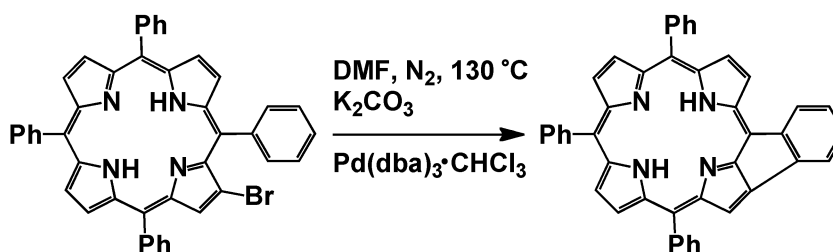
Fig. 179 Pd mediated cyclisation, forcing the phenyl to be co-planar with the porphyrin core.

6.4 Particle System

6.4.1 Conclusions

A [ReBpy(CO)$_3$Pic]$^+$ complex with phosphonic acid groups was successfully synthesised. The compound exhibits typical characterisation data for complexes of this type. It binds strongly to the surface of TiO$_2$ and has been characterised on the particles via several different techniques. It was possible to observe the metal carbonyl stretching frequencies by IR spectroscopy in KBr discs. The compound appears to be stable on TiO$_2$. The frequencies of the CO stretches drop on binding to TiO$_2$ suggesting an increase in electron density at the rhenium centre. This is encouraging if electron transfer is to occur in the direction of TiO$_2$ to Re. Diffuse reflectance UV-Vis spectroscopy shows that there is a significant change in the electronics of the complex when bound to TiO$_2$. An absorbance signal is observed with a completely different shape to the solution UV-Vis spectrum and at higher wavelengths. A red shift in the absorbance of the rhenium complex is encouraging for visible light induced CO$_2$ reduction. A large change in the UV-Vis spectrum but not such a large change in the IR spectrum can be reconciled by considering the origin of the signals. The binding of the complex to TiO$_2$ occurs at the Bpy. The presence of the Bpy is responsible for the signal in the UV-Vis observed with rhenium complexes of this type and so this is consistent with binding at the Bpy. The IR signal originates from the C-O bond, which is remote from the binding site and will be less affected by whether the complex is on or off TiO$_2$.

The rhenium complex bound to TiO$_2$ is active for CO$_2$ reduction under various wavelengths of light between 420 and 500 nm. Typically rhenium complex of this type can exhibit visible light photochemistry up as far as 455 nm but CO$_2$ reduction with wavelengths longer than 420 nm has, to our knowledge, never been demonstrated before. The Re-TiO$_2$ structure exhibits relatively high efficiency producing a turnover number of CO of 80. Activity for an immobilised rhenium catalyst raises questions around the mechanistic theories that invoke a carboxylate bridged dimer.[34]

A zinc porphyrin has been successfully synthesised with a phosphonic acid group. The complex binds strongly to TiO_2 and retains the Soret and Q bands observed in the solution UV-Vis spectrum. The Re-TiO_2 structure cannot produce CO with $\lambda > 515$ nm but introduction of the porphyrin results in CO production. The system is slow and relatively inefficient ($TON_{CO} = 35$) but the concept of sensitisation around a metal oxide nanoparticle has been proven. Interestingly the porphyrin goes from purple to green during catalysis, indicative of hydrogenation, but it does not ever bleach at the reaction times investigated (up to 3 d). This indicates that the TiO_2 provides some stabilisation of the porphyrin.

6.4.2   Further Work

Time resolved infrared (TRIR) spectroscopic studies are possible on KBr discs. We have demonstrated that an IR spectrum can be taken of the rhenium catalyst on TiO_2 in a KBr disc. A TRIR investigation could detail the kinetics of the excited states of the catalyst and indicate whether the Re centre is reduced in the presence of electron donor on the TiO_2 surface. However, the very low concentration of the complex when on TiO_2 in a KBr disc will make the signal very weak.

To optimise the system it would be of interest to investigate new porphyrin and Re structures. The Re complexes typically suffer from depleted catalytic activity when electron-withdrawing groups are introduced to the Bpy. However, the particle system cannot be assembled without them. The electron withdrawing effect could be minimised by creating a catalyst with only one PO_3H group. A proposed synthetic route is given in Fig. 180 with the preparation of mono-bromo Bpy described by Klemm and co-workers.[139] This may also make the catalyst more flexible on the surface of the TiO_2, which could be advantageous if the CO_2 bridged dimer intermediate proposed by Fujita et al.[34] is correct.
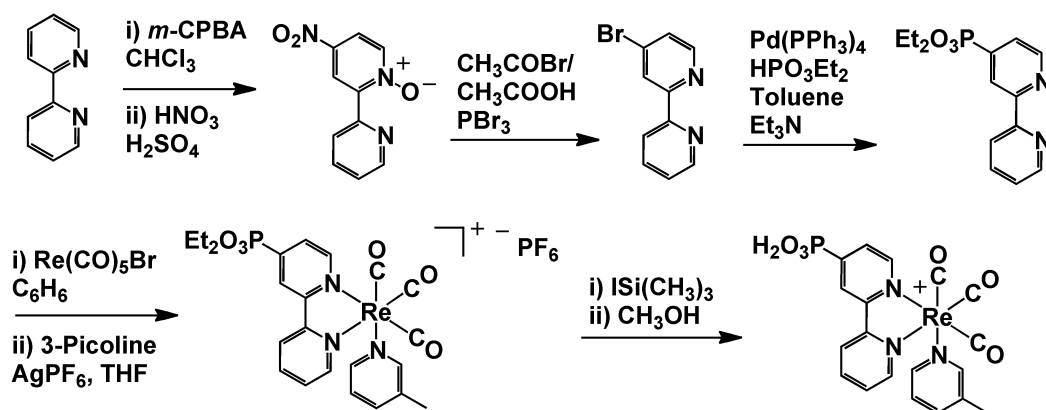
Fig. 180 Preparative route for a Re photocatalyst with one phosphonic acid group.

It has also been proposed that methylene spacers between zinc porphyrins and the phosphonic acid anchoring group reduces charge injection efficiency into the TiO_2 conduction band. It is also likely that rotations in the C_6H_4 unit in the structure of **7c** will also reduce electronic communication with the TiO_2. An optimised structure would have the phosphonic acid group attached directly to the porphyrin core. Since the aggregation of porphyrin dyes is problematic, introducing tertiary butyl functionalities to the phenyl groups will be advantageous. These groups will also help 'push' electron density toward the TiO_2 via the $+I$ effect. A proposed synthetic route is given in Fig. 181, including the established route to zinc iodo porphyrin with tertiary butyl groups established by Odobel and co-workers[140] and the introduction of PO_3Et_2 to zinc iodo porphyrin by Guilard et al.[141]
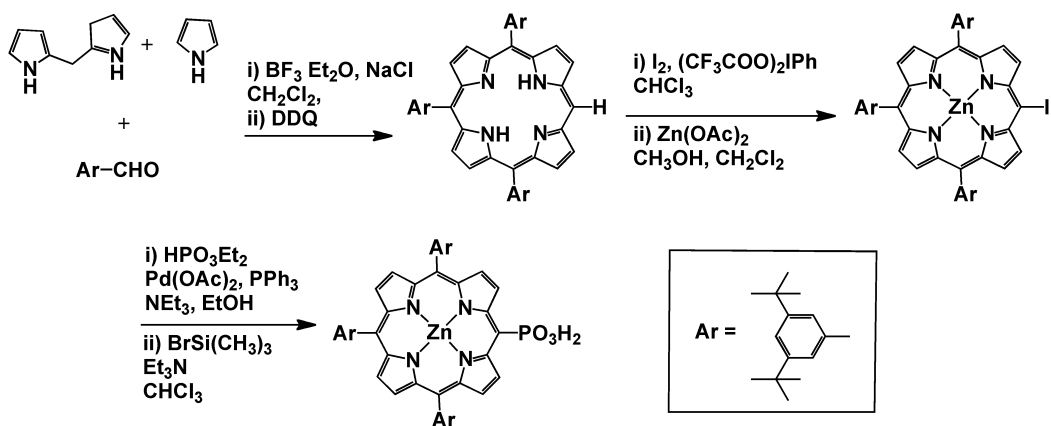
Fig. 181 Preparation of a zinc porphyrin with a phosphonic acid group bound directly to the aromatic core. The structure also contains six tertiary butyl groups to increase the driving force for porphyrin oxidation and reduce aggregation.

Chapter 7.   Experimental

7.1 General Procedures

Chemicals were obtained from the following suppliers: diisopropylamine, 2.5 M
n-butyl lithium in hexanes (Acros); pyridine, EDTA, AgOTf, 4,4'-dimethyl-2,2'-
bipyridine, sodium sulphide, celite 512 medium, trifluoroacetic acid, BrTMS,
Et_3N, 2-chloro-methylpyridinium iodide, triethanolamine, anhydrous DMF,
ITMS, CeO_2 particles (< 25 nm), $SrTiO_3$ particles (< 100 nm), methyl
chloroformate, $SnCl_2$, 2-methoxy-4-nitrobenzoic acid, PMHS, KF, $AgPF_6$,
$Pd(PPh_3)_4$, PPh_3, $P(OEt)_3$, diethylphosphonoacetic acid, copper (II) acetate
(Aldrich); $Pd(OAc)_2$ (Alfa Aesar) 3-picoline (BDH Chemicals); CO_2 CP grade
(BOC); titania P25 (~21 nm, anatase: rutile 80:20) (Evonik); $SOCl_2$, silica 60
(Fluka); Na_2SO_4, Na_2CO_3, $NaHCO_3$, NaOH, HCl, KOH, ammonium hydroxide
(Fisher); $Zn(OAc)_2.H_2O$, CH_3CO_2Na, $NaNO_2$ (Fisons); 4 Å molecular sieves
(Merck), tetraphenylporphyrin (Frontier); dicyclohexylcarbodiimide (Lancaster);
$Re_2(CO)_{10}$ (Strem); ZrO_2 (Sky Spring Nanomaterials, Inc); dibromobipyridine,
tetraphenylchlorin (TCI).

Solvents for general use were obtained from Fisher. Solvents were dried by
refluxing over sodium wire (C_6H_6, THF, toluene) or over CaH_2 (CH_2Cl_2). DMF
was dried using a Pure Solv 400-3-MD (Innovative Technology).

CD_2Cl_2, CD_3OD, DMSO-d_6 and $CDCl_3$ were used as obtained (Aldrich) and
THF-d_8 was dried over K.

Pyridine was dried over 4 Å molecular sieves and diisopropylamine was distilled
from sodium hydroxide. Methyl chloroformate was distilled prior to use. n-BuLi
was titrated against n-benzylbenzamide prior to use.

Routine separation of porphyrins by flash chromatography was performed on a
Combi*Flash R*f system using 24 g Redi*Sep R*f silica columns (Teledyne Isco), and
dry-loading the samples on silica (Fluka).

7.2   Physical Measurements

7.2.1   Nuclear magnetic resonance (solution)

NMR spectra were run on a Bruker AV500 (^{1}H at 500 MHz) spectrometer, Bruker ECS400 (400 MHz) at York or a Bruker 400 MHz at Cambridge. ^{1}H NMR spectra were referenced to residual protiated solvent at δ 7.26 (CDCl$_3$), δ 1.72 ([^{2}H$_8$] THF), δ 5.32 (CD$_2$Cl$_2$) and δ 3.31 (CD$_3$OD).[142] ^{13}C NMR spectra were referenced to the solvent δ 77.16 (CDCl$_3$), δ 25.31 ([^{2}H$_8$] THF), δ 53.84 (CD$_2$Cl$_2$) and δ 49.00 (CD$_3$OD).[142] ^{31}P and ^{19}F NMR spectra were pre-calibrated to an external reference.

7.2.2   Nuclear magnetic resonance (solid)

Solid state NMR experiments: All experiments were performed in Cambridge using standard SSNMR methodology on a Bruker 9.4 Tesla Avance-400 spectrometer with a double resonance probe, at frequencies of 400.1 MHz (^{1}H), 161.9 MHz (^{31}P) and 100.5 MHz (^{13}C) and at a magic angle spinning (MAS) rate of 12.5 kHz, with samples packed into 4 mm zirconia rotors. All samples were characterized using standard cross polarization (CP) MAS techniques (^{1}H π/2 pulse length 2.5 μs, ^{1}H cross polarization field 70 kHz, ^{1}H-^{31}P cross polarization contact time 10 ms, ^{1}H-^{13}C cross-polarization contact time 2.5 ms, broadband TPPM decoupling during signal acquisition at a ^{1}H field strength of 100 kHz).

7.2.3   Fabrication of meso indium tin oxide electrodes

Fabriaction of meso indium tin oxide electrodes: ITO coated glass was cut into slides 10 mm x 20 mm and these were sonicated for 60 minutes in isopropanol followed by HPLC grade acetone. Once dry, Scotch tape was used to mask an area of 5 mm x 5 mm. 5 M acetic acid was added to 42 mg of ITO until the suspension weighed 200 mg, this was sonicated for 20 min immediately before use. 2 μL was pipetted onto the 5 mm x 5 mm masked area on the ITO slide and allowed to dry for 1 h. The Scotch tape was then removed and the slides heated in an oven ramped to 350 °C at a rate of 2 °C min^{-1} and held at 350 °C for 20 min.

7.2.4   Absorbance and emission spectroscopy

IR spectra were recorded on a Mattson RS FTIR instrument, averaging 64 scans at resolution 2 cm^{-1}. ATR-IR spectra were an average of 32 scans. The KBr discs of the particle were taken with a Perkin Elmer RX I instrument at the University of Cambridge. UV−visible absorption spectra were measured using an Agilent 8453 spectrometer in 10 mm x 10 mm quartz cuvettes. The emission spectra were measured using a Hitachi F- 4500 fluorimeter, and all samples were either degassed by three freeze−pump−thaw cycles or de-aerated by purging the sample with Ar. Correction was applied for instrument response and all measurements were made in 10 mm x 10 mm quartz cuvettes.

7.2.5   Diffuse reflectance UV-Vis spectroscopy

Diffuse reflectance UV spectra were recorded on an Ocean Optics HR2000+ High Resolution Spectrometer with DH-2000-BAL Deuterium/Helium light source (200-1100 nm). An R400-7-UV-Vis reflection probe was used to record diffuse reflectance spectra. Spectra were recorded in Spectra Suite software using an integration time automatically determined by the software, box car smoothing width of 30, and 10 scans to average. Kubelka Munk correction[128] was applied via the Spectra Suite in-built procedure and TiO$_2$ was used as background.

7.2.6   Mass spectrometry

ESI mass spectra were recorded on a Bruker micrOTOF instrument with a sample flow rate of 0.2 mL/min, nebuliser gas pressure of 1.5 bar, dry gas flow of 8 L min^{-1} and a dry gas temperature of 180 °C. EI mass spectra were run on a Waters GCT premier with a source temperature of 180 °C, electron energy of 70 eV and a trap current of 200 μA. Some compounds and the reaction mixture ESI mass spectra were run on a Bruker Esquire 6000 via direct infusion using a syringe pump at 240 μL min^{-1}. Nebuliser gas and dry gas flows and temperatures were optimised for each individual sample along with the spray voltage. The ESI-MS of compound **7c** was run on a Quatro LC by Micromass (Cambridge). Mass values are quoted for ^{64}Zn, ^{185}Re and ^{79}Br.

7.2.7 Cyclic voltammetry

Cyclic voltammetry was performed in CH_2Cl_2 with 0.1 M $[Bu_4N][PF_6]$ (TBAP) electrolyte. The setup comprised reference electrode (Ag/AgCl, 3 M), working electrode (platinum disc) and counter electrode (platinum wire). Ferrocene was used as internal standard. All scans were made at 100 mV s^{-1}. Cyclic voltametric experiments used a BASi Epsilon with C3 cell stand.

7.2.8 X-ray crystallography

Compound **2d**

Empirical formula	$C_{52.6}H_{37.2}Cl_{1.2}N_6O_4$
Formula weight	859.29
Temperature/K	110.00(10)
Crystal system	orthorhombic
Space group	Fddd
a/Å	23.5964(4)
b/Å	37.3470(6)
c/Å	40.0789(6)
α/°	90.00
β/°	90.00
γ/°	90.00
Volume/Å^3	35319.7(9)
Z	32
ρ_{calc}mg/mm^3	1.293
m/mm^{-1}	0.152
F(000)	14303.4

Crystal size/mm^3	$0.1818 \times 0.1617 \times 0.1159$
2Θ range for data collection	5.76 to 50.7°
Index ranges	-25 ≤ h ≤ 28, -44 ≤ k ≤ 44, -45 ≤ l ≤ 48
Reflections collected	26924
Independent reflections	8081[R(int) = 0.0340]
Data/restraints/parameters	8081/6/606
Goodness-of-fit on F^2	1.035
Final R indexes [I>=2σ (I)]	R$_1$ = 0.0578, wR$_2$ = 0.1587
Final R indexes [all data]	R$_1$ = 0.0712, wR$_2$ = 0.1693
Largest diff. peak/hole / e Å^{-3}	0.85/-1.07

Table 15 Crystal data and structure refinement for **2d**.

Diffraction data were collected at 110 K on an Oxford Diffraction SuperNova diffractometer with Mo-K$_a$ radiation (λ = 0.71073 Å) using an EOS CCD camera. The crystal was cooled with an Oxford Instruments Cryojet. Diffractometer control, data collection, initial unit cell determination, frame integration and unit-cell refinement was carried out with "Crysalis".[143] Face-indexed absorption corrections were applied using spherical harmonics, implemented in SCALE3 ABSPACK scaling algorithm.[144] OLEX2[145] was used for overall structure solution, refinement and preparation of computer graphics and publication data. Within OLEX2, the algorithm used for structure solution was direct methods.[146] Refinement by full-matrix least-squares used the SHELXL-97[147] algorithm within OLEX2.[145] All non-hydrogen atoms were refined anisotropically. Hydrogen atoms were placed using a "riding model" and included in the refinement at calculated positions except for the N-H hydrogens which were placed by difference map after all other atoms had been located and refined. The crystal contained dichloromethanes of crystallisation at two sites in the asymmetric unit. One was partially occupied and modelled with an

occupancy of 0.1875; the carbon of this DCM was restrained to be approximately isotropic. The other was disordered and modelled with the carbon in two different positions with relative occupancies of 0.814:0.186(12).

Compound **[Dyad 1 Pic][PF₆]**

Empirical formula	$C_{67.5}H_{49}Cl_5F_6N_8O_4PReZn$
Formula weight	1609.94
Temperature/K	110.00(10)
Crystal system	triclinic
Space group	P-1
a/Å	12.9474(5)
b/Å	15.8804(5)
c/Å	17.3277(6)
α/°	98.752(3)
β/°	92.264(3)
γ/°	106.821(3)
Volume/Å³	3357.4(2)
Z	2
ρ_{calc}mg/mm³	1.593
m/mm⁻¹	2.452
F(000)	1602.0
Crystal size/mm³	0.1612 × 0.091 × 0.0831
2Θ range for data collection	5.7 to 54.2°
Index ranges	$-16 \leq h \leq 16, -20 \leq k \leq 20, -22 \leq l \leq 18$
Reflections collected	25307

Independent reflections	14802[R(int) = 0.0307]
Data/restraints/parameters	14802/25/880
Goodness-of-fit on F^2	1.074
Final R indexes [I>=2σ (I)]	$R_1 = 0.0658$, $wR_2 = 0.1871$
Final R indexes [all data]	$R_1 = 0.0808$, $wR_2 = 0.1989$
Largest diff. peak/hole / e Å^{-3}	4.12/-1.79

Table 16 Crystal data and structure refinement for **[Dyad 1 Pic][PF$_6$]**.

Diffraction data were collected at 110 K on an Oxford Diffraction SuperNova diffractometer with Mo-K$_α$ radiation ($λ = 0.71073$ Å) using a EOS CCD camera. The crystal was cooled with an Oxford Instruments Cryojet. Diffractometer control, data collection, initial unit cell determination, frame integration and unit-cell refinement was carried out with "Crysalis".[143] Face-indexed absorption corrections were applied using spherical harmonics, implemented in SCALE3 ABSPACK scaling algorithm.[144] OLEX2[145] was used for overall structure solution, refinement and preparation of computer graphics and publication data. Within OLEX2, the algorithm used for structure solution was charge flipping using SUPERFLIP.[148] Refinement by full-matrix least-squares used the SHELXL-97[147] algorithm within OLEX2.[145] All non-hydrogen atoms were refined anisotropically. Hydrogen atoms were placed using a "riding model" and included in the refinement at calculated positions except for the N-H hydrogens which were placed by difference map after all other atoms had been located and refined.

The hexafluorophosphate was disordered over two sites. For one of these, the phosphorus was centred on a special position and for the other the occupancy was 50% with a dichloromethane of crystallisation occupying the site at other times. One of the phenyl groups on the porphyrin ring was disordered and modelled in two positions with refined occupancies of 0.817:0.183(12). The

ADPs of equivalent carbons in the disordered phenyl were constrained to be equal, e.g. C51 & C51A.

In addition to the ordered dichloromethanes of crystallisation, the crystal also contained some disordered solvent, believed to be a mix of hexane and dichloromethane for which a suitable discrete model could not be obtained. This was accounted for using the solvent mask algorithm within OLEX2 (this solvent space had a volume of 213.1 Å^3 and was estimated to contain 17.3 electrons).

There was also some evidence of twinning from some relatively large residual-density peaks, but it was not possible to model this.

7.3 Photocatalysis

7.3.1 Photoreaction cell

Photocatalysis was performed in a custom made cell comprising of a 10 mm x 10 mm quartz cuvette with a headspace of a minimum volume of 10 mL. Above the headspace was a ground glass joint, which was sealed with a size 21 septum. Sampling was made through this septum for GC. The headspace had a sidearm, isolated by a Young's tap, joining it to a gas phase IR cell with CaF_2 windows. The IR cell was connected to a vacuum joint via a second Young's tap. The IR cell was put under vacuum. At the end of a catalytic run the headspace was opened to the IR cell and the gas produced from the reaction would be drawn through and could be subjected to IR spectroscopy.

7.3.2 Catalytic solutions

The catalytic solution was typically 0.05 mM making the porphyrin Q band at 560 nm, Q(1,0), at absorbance 1 by UV-vis spectroscopy. 10 mL of a 0.25 mM DMF solution of the catalyst would be made. These stock solutions allowed the catalysts to be weighed out in amounts greater than 1 mg. They were stored in a freezer at -25 °C and could be used up to a month later without noticeable degradation in catalytic performance, their UV-vis spectrum or mass spectrometric analysis. The 0.05 mM catalytic solution was made from the stock

by diluting 2 mL into 10 mL. To make a 10 mL solution in DMF/TEOA 5/1, 1.87 g TEOA was weighed into a 10 mL volumetric flask, approximately 2 mL of DMF was added so the catalytic stock was not being added to neat TEOA. Then 2 mL of stock was added followed by DMF up to the 10 mL mark. The catalytic solutions were protected from light as much as possible and stored in the freezer. They would not be used later than two weeks after making. 3 mL of catalytic solution was added to the photoreaction cuvette and this was bubbled with CO_2/CH_4 95/5 for 10 min, protected from light throughout this time.

7.3.3   Lamp and filters

Irradiation of all samples was performed with an ILC 302 Xe arc lamp. Light from the lamp was directed through a water filter (10 cm) and a 660 nm short pass filter to remove heat, such that any sample directly in the beam was at a temperature of 33 °C. Various optical filters were added, typically to remove shorter wavelength light. These included $\lambda > 520$ nm and $\lambda > 620$ nm cut-off filters.

7.3.4   Gas chromatography method

The amount of CO produced was determined by GC analysis using a UnicamProGC+ (ThermoONIX) with a thermal conductivity detector. Air, CO, CH_4 and CO_2 were separated on a Restek ShinCarbonST 100/120 micropacked column (2 m, 1/16" OD, 1.0 mm ID) fitted with "pigtails" of Restek intermediate-polarity deactivated guard column on either end (fused silica, 0.53 mm ID, 0.69 ± 0.05 mm OD). The carrier gas was ultra high purity He (N6.0, BOC gases) passed through a GC triple filter (Focus Technical) to remove trace impurities prior to the column. The GC method began with 1 min at 40 °C followed by a 5 °C/min gradient up to 120 °C (16 min). Injections (200 μL) were made manually with a Hamilton gastight locking syringe (500 μL) at 220 °C with a 30 mL/min split flow. The carrier gas was kept at constant pressure (165 kPa). The detector block and transfer temperatures were 200 and 190 °C respectively, at a constant voltage of 10 V with makeup and reference flows of 29 and 30 mL/min respectively. The amount of CO was determined using a calibration plot (Fig. 182). Known volumes of CO were mixed with a mimic

experimental solution (3 mL DMF:TEOA 5:1 (v/v), headspace and solution were purged with CO_2/CH_4 (99/1) and sampled to GC. Quantification was by comparison of integrations of the CO peak against a 1% CH_4 internal standard and later with 5% CH_4. Corrections were made for temperature and the change in headspace pressure at each injection.
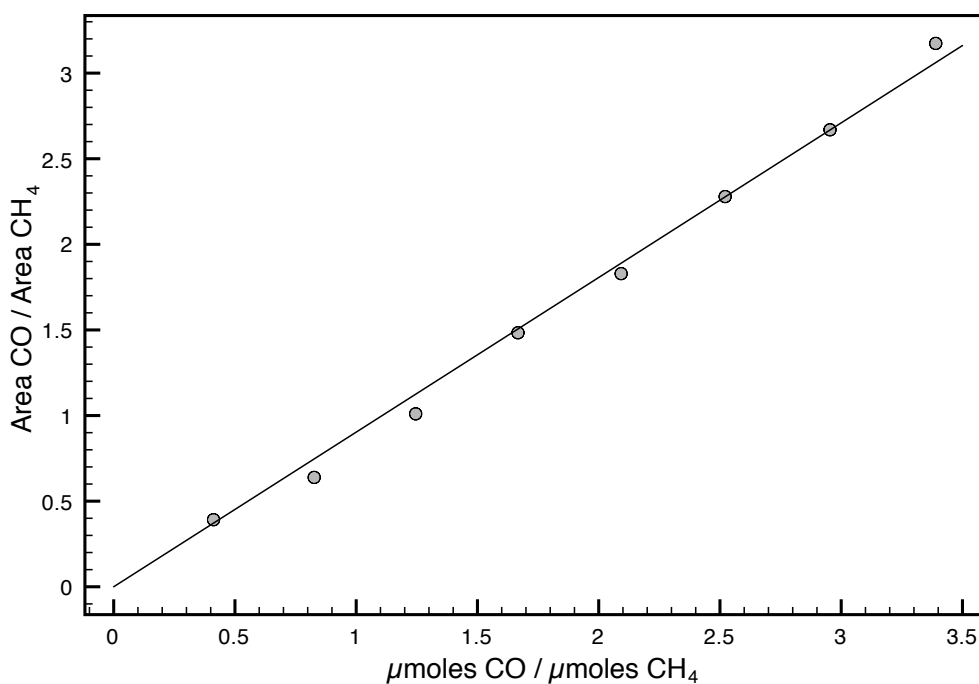
Fig. 182 Calibration for quantification of CO by gas chromatography.

7.3.5   Turnover number calculations

The headspace of the photoreaction cell was measured. Two cells were predominantly used in this work with headspaces of 12150 and 11700 µL. The cell was then purged with CO_2 and CH_4 supplied in the ratio 95/5. Working at 1 atm, the volumes of CO_2 and CH_4 could be calculated by splitting the headspace volume into a 95/5 ratio. The ideal gas law was then employed to calculate the number of moles of each gas. The temperature for this calculation was known from placing a thermometer directly in the beam of the lamp and was constantly 33 °C. The temperature of an item directly in the beam is higher than the air around and so a thermometer adjacent to the cell throughout a reaction was not satisfactory. The pressure, required for calculating the moles of gas, was

taken from the electronics department website where local daily readings of the atmospheric pressure are taken (http://weather.elec.york.ac.uk). The gas constant was taken to be 0.08206 atm L mol^{-1} K^{-1}. The number of moles of CO_2 or CH_4 in the syringe aliquot was then calculated by dividing the moles in the headspace by the fraction of the headspace taken by the syringe. The starting moles of CO are set to zero. The ratio of the areas of the peaks for CO and CH_4 are taken from the GC software. These are converted to the ratio of moles of the gases by use of the calibration plot line gradient. The number of moles of CO is then calculated by multiplying the molar ratio by the moles of CH_4 calculated before. The moles of CO produced can then be divided by the number of moles of catalyst to yield a turnover number. Subsequent calculations are performed in the same way but compensate for the number of moles of each gas removed by each syringe.

The calculations were incorporated into a Microsoft Excel spreadsheet developed with Alvaro Martinez and Marius Câmpian (Fig. 183).

Date	07/11/2012		For 5% CH4
Dye			
Catalyst	Dyad 3		
Lamp	Blue		
Filters (nm)	Heat filter + > 520 nm		

Constants		t/mins	t/s	Time/h	Sample	μmoles CO2	μmoles CH4	μmoles CO2	μmoles CH4	μmoles CO	CO	CH4	CO/CH4	CO/CH4	μmoles CO	μmoles CO	TON
Gases constant / atm·L·mol⁻¹·K⁻¹	0.08206	0	0	0.00	A	460.370	24.230	7.458	0.393	0.000	220828	0	0	0.000	0.000	0.000	0
		30	0	0.50	B	452.913	23.838	7.337	0.386	0.118	56266	203992	0.27582454	0.305	7.280	7.398	49
External parameters		30	0	1.00	C	445.575	23.451	7.218	0.380	0.221	102159	194616	0.52492601	0.581	13.630	13.969	93
		30	0	1.50	D	438.357	23.071	7.101	0.374	0.381	168910	183396	0.92101245	1.020	23.527	24.247	162
Pressure / mbars	1015.6	30	0	2.00	E	431.256	22.698	6.986	0.368	0.497	221512	181436	1.22088229	1.352	30.682	31.899	213
(http://weather.elec.york.ac.uk/)		30	0	2.50	F	424.270	22.330	6.873	0.362	0.595	247680	166794	1.4849455	1.644	36.714	38.525	257
Pressure / atm	1.00232	30	0	3.00	G	417.397	21.968	6.762	0.356	0.651	273104	165260	1.65257171	1.830	40.196	42.659	284
Temperature / K	306.15	30	0	3.50	H	410.635	21.612	6.652	0.350	0.664	291277	169974	1.71365621	1.897	41.007	44.134	294
T0 / celcius	33	30	0	4.00	I	403.983	21.262	6.544	0.344	0.709	294676	158542	1.85866206	2.058	43.756	47.592	317
Tf / celcius	33	30	0	4.50	J	397.438	20.918	6.438	0.339	0.722	313826	163186	1.9231184	2.129	44.540	49.098	327
System parameters		30	0	5.00	K	391.000	20.579	6.334	0.333	0.724	300869	153370	1.96172002	2.172	44.698	49.980	333
		30	0	5.50	L	384.666	20.246	6.231	0.328	0.718	308542	156060	1.97707292	2.189	44.318	50.318	335
Headspace volume / μL	12145.9	30	0	6.00	M	378.435	19.918	6.131	0.323	0.703	305074	155088	1.96710255	2.178	43.380	50.083	334
Syringe volume / μL	200																
Parameters used																	
Calibration plot (Areas ratio vs. molar ratio) slope	0.90317																
Catalyst present (μmoles)	0.15																

Fig. 183 Spreadsheet incorporating CO turnover calculations.

7.4 Synthesis

4'-methyl-2,2'-bipyridine-4-carboxylic acid[149], Re(CO)$_5$Br[150], 5-(4-aminophenyl)-10,15,20-triphenylporphyrin[83], **Dyad 1 Br** and **[Dyad 1 Pic][PF$_6$]**[71, 151], 4,4'-diethyl phosphate-2,2'-bipyridine[102], **2d**[88], and zinc tetraphenylchlorin[101] were synthesised by literature methods. The synthesis of zinc tetraphenyldihydroporphyrin was modified to include a water wash (5x) to remove Zn(acac)$_2$ and subsequent drying under high vacuum.

7.4.1   5-[4-[(2-methoxy-4-amino-carboxyamidyl)phenyl]phenyl]-10,15,20-triphenyl porphyrin (2e)
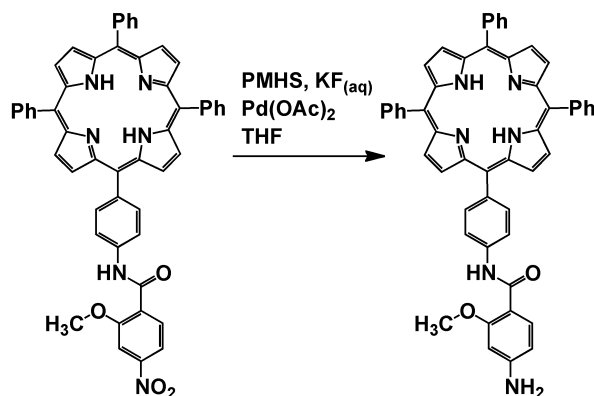
To a flame-dried 500 cm^3 RBF under Ar was added **2d** (2.48 g, 3.07 mmol) and Pd(OAc)$_2$ (33.7 mg, 153 μmol). Dry degassed THF was added (140 cm^3) with stirring. The system was purged with N$_2$. A solution of KF (356 mg, 6.14 mmol) in degassed H$_2$O (6.43 cm^3) was added. A balloon of Ar was fitted and PMHS (740 μL, 12.2 mmol) was added dropwise (gas evolved). The solution was stirred at RT for 2.75 h after which it was judged complete by TLC. When following by TLC, the first spot was starting material, the third was product and a second rather intense spot was observed at approximately 1 h but this disappeared by 2.75 h.

The reaction was opened to air, diluted with 10 – 20 cm^3 ether and stirred for 5 min. Water and ether was added and the product back-extracted into ether. This was filtered through a mixed plug of neutral alumina (bottom layer) and Celite (top layer) flushing with EtOAc followed by CH$_2$Cl$_2$/CH$_3$CN. The product was purified by column chromatography (Si-60, CH$_2$Cl$_2$/CH$_3$CN 10/1) (2.15 g, 2.76 mmol, 90%). ^{1}H NMR and ESI-MS matched data reported previously.[88]

7.4.2   5-[4-[(2-methoxy-4-(4-methyl-2,2'-bipyridine-4'-carboxyamidyl) carboxyamidyl) phenyl] phenyl]-10,15,20-triphenyl porphyrin (2g)
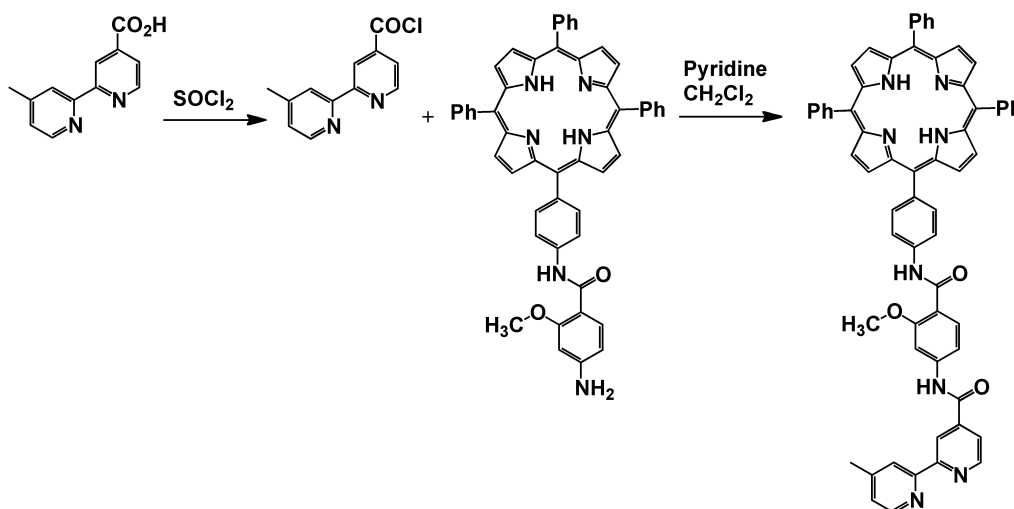
4-methyl-2,2'-bipyridine-4-carboxylic acid (52.7 mg, 0.248 mmol) was heated at reflux in $SOCl_2$ (4.65 cm^3) under Ar for 2 h. Excess $SOCl_2$ was removed under reduced pressure revealing a yellow solid, which was dried for a further 0.5 h. Porphyrin **2e** (193 mg, 0.248 mmol) was dissolved in the minimum amount of dry CH_2Cl_2 and added by cannula to the yellow solid. Dry pyridine was added (7.75 cm^3) and the solution heated at reflux for 2 h under Ar and then left overnight at RT. The solvent was removed under reduced pressure and the product was re-dissolved in CH_2Cl_2, washed with saturated $NaHCO_3$ solution, brine and water followed by drying over Na_2SO_4. The solvent was removed and the product purified by column chromatography (Si-60, CH_2Cl_2, Et_3N, CH_3OH). The second fraction was collected and the solvent removed yielding the desired compound (103 mg, 0.105 mmol, 53%)

^{1}H NMR (500 MHz, CDCl$_3$): δ −2.76 (2 H, s, pyrrole NH); 2.50 (3 H, s, bpy CH$_3$); 4.27 (3 H, s, OCH$_3$), 7.24 (1 H, m, bpy); 7.25 (1 H, m, *o*-methoxyphenyl); 7.75 (9 H, m, *m-/p*-phenyl); 7.93 (1 H, dd, 1.81 and 5.08 Hz, bpy); 8.10 (2 H, d, 8.09 Hz, *m*-amidophenyl); 8.16 (2H, d, 1.91 Hz, *m*-methoxyphenyl); 8.21 (8H, m, *o*-phenyl + *o*-amidophenyl); 8.34 (1 H, s, bpy); 8.46 (1 H, d, 8.45 Hz, bpy); 8.58 (1 H, s, bpy amide); 8.59 (1 H, d, 5.24 Hz, bpy); 8.83 (6H, m, β-pyrrole); 8.89 (3 H, m, bpy, β-pyrrole); 10.15 (1 H, s, porphyrin amide)

$^{13}C\{^1H\}$ **NMR** (100.6 MHz, THF-d_8): δ 21.14; 56.68; 104.21; 113.13; 118.74; 120.83; 122.55; 125.89; 127.59; 128.58; 133.54; 135.35; 135.75; 140.42; 143.40; 144.62; 149.70; 150.69; 159.03; 163.58; 165.33

ESI-MS: *m/z* = 975.3758 ([M + H$^+$]$^+$, 100%), (M + H$^+$; $C_{64}H_{47}N_8O_3$ requires 975.3766, difference 0.8 mDa)

IR (ν/cm^{-1}) (ATR) 1671 (C=O), 1590 (C=N), 1517 (N-H), 1471, 1404, 1314, 1244, 1031, 965, 799, 702

7.4.3   5-[4-[(2-methoxy-4-(4-methyl-2,2'-bipyridine-4'-carboxyamidyl) carboxyamidyl) phenyl] phenyl]-10,15,20-triphenyl porphyrinatozinc(II) (2h)
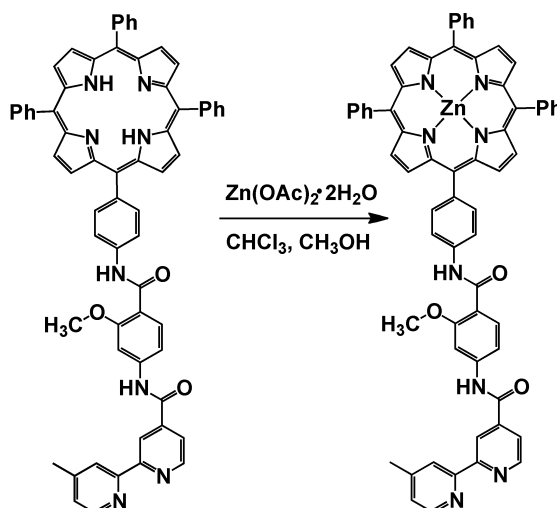
In a modification of a literature procedure,[71] porphyrin **2g** (260 mg, 0.267 mmol) was dissolved in 15% CH$_3$OH in CHCl$_3$. Zinc acetate dihydrate (264 mg, 1.20 mmol) was added and the solution heated at reflux for 1 h and then allowed to cool. The product was diluted further with CH$_2$Cl$_2$ and washed with a solution of 1% EDTA (m/v) in 10% Na$_2$CO$_3$ solution and then with water. The product solution was dried over MgSO$_4$ and the solvent removed (244 mg, 0.235 mmol, 88%).

^{1}**H NMR** (500 MHz, CDCl$_3$) δ 2.49 (3 H, s, bpy CH$_3$); 4.26 (3 H, s, OCH$_3$); 7.17 (1 H, d, 8.07 Hz, 5-methoxyphenyl); 7.23 (1 H, m, bpy 5'); 7.75 (9 H, m, *m-/p*-phenyl); 7.89 (1 H, d, 4.23 Hz, bpy 5); 8.06 (2 H, d, 8.31 Hz, *m*-amidophenyl);

8.11 (1 H, s, 3-methoxyphenyl); 8.21 (8 H, m, *o*-phenyl); 8.33 (1 H, s, bpy 3');
8.39 (1 H, s, 6-methoxyphenyl); 8.41 (1 H, s, bpy amide); 8.58 (1 H, d, 4.93 Hz,
bpy 6'); 8.79 (1 H, s, bpy 5'); 8.90 (1 H, d, 5.07 Hz, bpy 6); 8.95 (6 H, m, β-pyrrole); 9.02 (2 H, d, 4.93 Hz, β-pyrrole); 10.15 (1 H, s, porphyrin amide)

ESI-MS: *m/z* = 1037.2904 ([M+H$^+$]$^+$, 98%), (M + H$^+$; C$_{64}$H$_{45}$N$_8$O$_3$Zn requires 1037.2901, difference 0.7 mDa)

7.4.4   5-[4-[(2-methoxy-4-([rhenium (I) tricarbonyl (bromide)]4-methyl-2,2'-bipyridine-4'-carboxyamidyl) carboxyamidyl) phenyl] phenyl]-10,15,20-triphenyl porphyrinatozinc(II) (Dyad 2 Br)
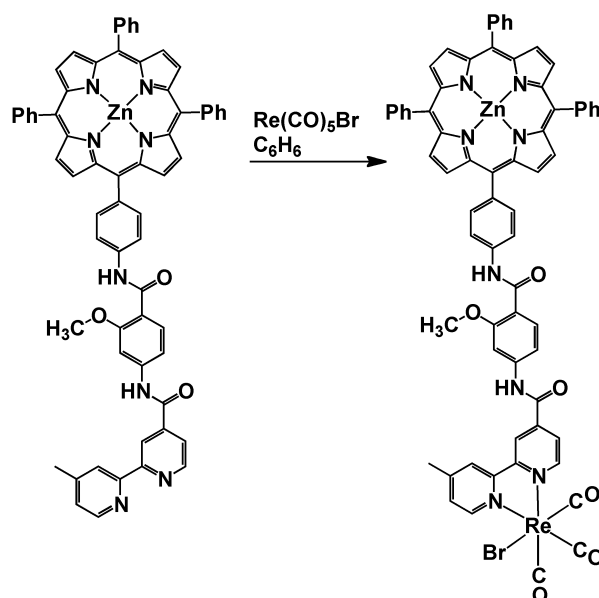
In a modification of a literature procedure,[87] porphyrin **2h** (109 mg, 0.105 mmol) and Re(CO)$_5$Br (43 mg, 0.105 mmol) were placed in a Schlenk tube under Ar and dry benzene (15 cm^3) was added by cannula. The mixture was heated to 65 °C under argon for 12 h. The solution was filtered and the solvent was removed to yield the desired product (142 mg, 0.102 mmol, 97%).

^{1}H NMR (400 MHz, THF-d_8): 2.67 (3 H, s, bpy CH$_3$); 4.29 (3 H, s, OCH$_3$); 7.45 (1 H, d, 8.34 Hz, 5-methoxyphenyl); 7.58 (1 H, d, 5.68 Hz, 5-Bpy); 7.79 (9 H, m, *m-/p*-phenyl); 8.11 (1 H, d, 5.68 Hz, 5'-Bpy); 8.20 (3 H, m, 3-methoxyphenyl + 3-amidophenyl); 8.24 (8 H, *m*-phenyl + *m*-amidophenyl); 8.37 (1 H, d, 8.52 Hz, 6-methoxyphenyl); 8.67 (1 H, s, 3-Bpy); 8.89 (6 H, m, β-pyrrole); 8.98 (3 H, m,

β-pyrrole + 6-Bpy); 9.04 (1 H, s, 3'-Bpy); 9.30 (1 H, d, 5.50 Hz, 6'-Bpy); 10.23 (1 H, s, porphyrin amide); 10.30 (1 H, s, Bpy amide).

^{13}C{^{1}H} NMR (100.6 MHz, THF-d_8): δ 20.40; 55.83; 117.68; 120.51; 121.51; 124.27; 124.83; 124.84; 126.23; 127.14; 128.23; 131.25; 132.79; 134.41; 134.75; 138.87; 142.97; 143.65; 145.33; 150.05; 152.02; 153.75; 155.15; 157.11; 158.19; 162.43; 162.98

ESI-MS: *m/z* = 1407.1208 ([M + Na$^+$]$^+$, 24%), (M + Na$^+$; $C_{67}H_{44}N_8O_6ZnReBrNa$ requires 1407.1280, difference 7 mDa)

IR (ν/cm^{-1}) (THF) 2020 (s), 1920 (s), 1898 (s) (ν(CO)). (ATR) 2021 (CO), 1891 (CO), 1665 (C=O), 1595 (C=N), 1521 (N-H), 1404, 1312, 1236, 1203, 1178, 1070, 993, 797, 752, 718, 700

7.4.5   5-[4-[(2-methoxy-4-([rhenium (I) tricarbonyl (3-picoline)]4-methyl-2,2'-bipyridine-4'-carboxyamidyl) carboxyamidyl) phenyl] phenyl]-10,15,20-triphenyl porphyrinatozinc(II) triflate ([Dyad 2 Pic][OTf])
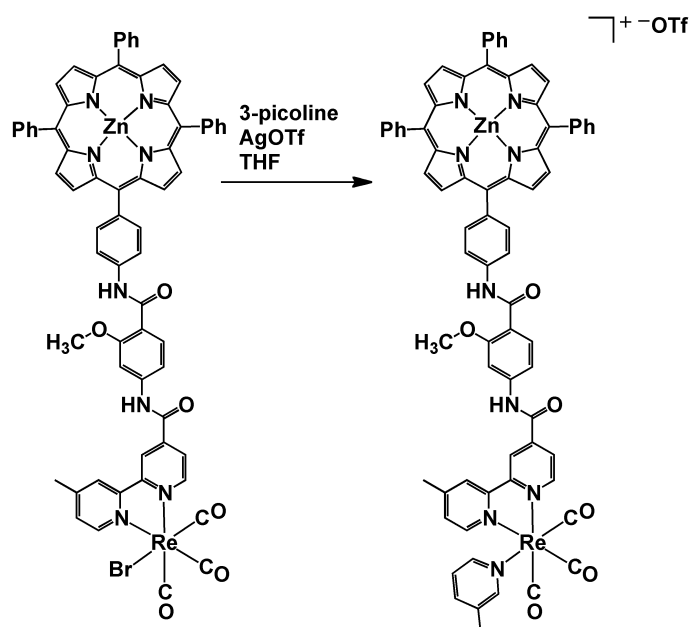
In a modification of a literature procedure,[151] **Dyad 2 Br** (142 mg, 0.102 mmol) was dissolved in a mixture of dry THF (13 cm^3), 3-picoline (0.63 cm^3) and AgOTf (130 mg, 0.504 mmol) and heated at reflux under Ar for 1 h. The solution was filtered and evaporated to dryness. The residue was then dried under vacuum

overnight. The product was purified on Sephadex LH20 eluting with THF (60 mg, 0.039 mmol, 54%)

¹H NMR (500 MHz, CD_2Cl_2 + CD_3OD): δ 2.22 (3 H, s, pic CH_3); 2.65 (3 H, s, bpy CH_3); 4.22 (3 H, s, methoxy CH_3); 7.19 (1 H, dd, 5.70 and 8.17 Hz 5-pic); 7.59 (1 H, dd, 0.71 and 5.76 Hz, bpy 5'); 7.62 (1 H, d, 7.84 Hz, 4-pic); 7.75 (10 H, m, *m-/p*-phenyl + 3-methoxyphenyl); 7.83 (1 H, d, 1.85 Hz, 6-pic); 7.92 (1 H, d, 5.50 Hz, 5-methoxyphenyl); 8.05 (2 H, d, 7.92 Hz, *m*-amidophenyl); 8.09 (1 H, s, bpy amide); 8.22 (8 H, m, *o*-phenyl); 8.28 (1 H, d, 8.55 Hz, 6-methoxyphenyl); 8.35 (1 H, dd, 1.72 and 5.68 Hz, bpy 5); 8.61 (1 H, s, bpy 3'); 8.89 (6 H, m, β-pyrrole); 8.96 (2 H, d, 4.60 Hz, β-pyrrole); 8.99 (1 H, d, 5.81 Hz, bpy 2'); 9.10 (1 H, d, 1.40 Hz, bpy 3); 9.34 (1 H, d, 5.75 Hz, bpy 6); 10.27 (1 H, s, porphyrin amide)

¹³C{¹H} NMR (100.6 MHz, CD_2Cl_2 + CD_3OD): δ 19.49 (picoline CH_3); 21.87 (Bpy CH_3); 57.06 (OCH_3); 104.57 (methoxybenzamide-3); 113.67 (picoline-6); 118.47; 118.91 (*m*-amidophenyl); 120.66 (methoxybenzamide-1); 121.15 (porphyrin meso); 122.46; 122.89 (Bpy-6'); 126.82 (*m, p*- phenyl); 127.04 (Bpy-3); 127.69 (Bpy-5' + *i*-phenyl); 130.26 (Bpy-5); 132.06 (β-pyrrole); 133.31 (methoxybenzamide-6); 134.95 (*o*-phenyl); 135.44 (*o*-amidophenyl); 137.95 (*i*-amidophenyl + picoline-3); 139.69 (*p*-amidophenyl); 140.89 (picoline-4); 143.02; 143.84 (methoxybenzamide-4); 146.46 (Bpy-4'); 148.86 (methoxybenzamide-5); 150.44 (α -pyrrole); 152.29 (picoline-2); 152.68 (Bpy-6); 154.20 (Bpy-3'); 155.29 (Bpy-4); 157.26 (Bpy-2); 158.62 (methoxybenzamide-2); 162.38 (Bpy carbonyl); 163.86 (amidophenyl carbonyl)

ESI-MS: *m/z* = 1398.2754 (M⁺, 30%), (M+; $C_{73}H_{51}N_9O_6ZnRe$ requires 1398.2778, difference 2.4 mDa)

IR (ν/cm⁻¹) (THF) 2032 (s), 1923 (s, broad) (ν(CO)). (ATR) 2031 (CO), 1917 (CO), 1665 (C=O), 1594 (C=N), 1519 (N-H), 1485, 1405, 1241, 1159, 1071, 1029, 993, 795, 752, 701

7.4.6 4'-methyl-2,2'-bipyridine-4-acetic acid (3a)
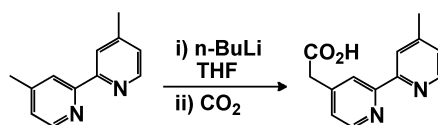
Procedure 1 A modification of that by Ciana.[98] A 250 cm^3 RBF was flame dried and flushed with Ar. THF (3 cm^3) and diisopropylamine (2.1 cm^3) were added and the mixture cooled to -78 ˚C. 2.5 M butyllithium in hexanes (6 cm^3) was added via syringe and the mixture was stirred for 0.75 h. A solution of 4,4'-dimethyl bipyridine (3 g) in THF (72 cm^3) was added, the solution turned black and was stirred for 2 h at -78 ˚C. Dry CO_2 $_{(g)}$ was set bubbling through a flame dried RBF charged with Et_2O (30 cm^3) and cooled to -78 ˚C. The black lithiated bipyridine solution was added to the Et_2O/CO_2 mixture via cannula and a yellow precipitate soon appeared. The reaction was left under an atmosphere of CO_2 overnight and allowed to RT. Et_2O was added (30 cm^3) and the product extracted with 3 M NaOH (3 x 30 cm^3). The alkaline layer was then acidified to pH 1 with concentrated HCl and cooling. The product was then extracted with Et_2O (30 cm^3) and buffered to pH 5 with solid CH_3CO_2Na. A saturated aqueous solution of $Cu(CH_3CO_2)_2$ was added causing precipitation of a blue Cu complex. The solid was filtered off with a microfiber filter paper and washed with water, ethanol and ether and then air-dried. The product was suspended in water (60 cm^3) and H_2S bubbled through for 0.33 h resulting in a dark brown colour. The product was filtered through celite, concentrated to 9 cm^3 and filtered again. The solution was evaporated to dryness under reduced pressure to yield a yellow oil. Recrystallisation twice from ethanol/hexane yielded pure **3a** (569 mg, 2.682 mmol, 16%). Analysis was in agreement with the literature.[98]
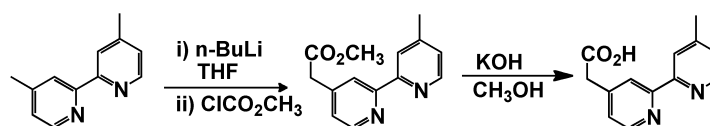
Procedure 2 A modification of that by Tomioka.[99] To a flame dried 100 mL RBF was added THF (5 mL) and freshly distilled diisopropylamine. The mixture was cooled to -78 ˚C and freshly titrated n-butyl lithium (1.1 eq) was added.

Dimethylbipyridine (1 g, 5.43 mmol) was dissolved in THF (20 mL) and added my cannula. The mixture was stirred at -78 °C for 2 h and then freshly distilled methyl chloroformate (0.6 mL) in THF (2 mL) was added by syringe. The reaction was stirred at -78 °C for 1 h and then at RT for 2 h. The mixture was then washed with saturated NaHCO$_3$ solution and extracted into ethyl acetate. The extracts were washed with brine and dried over Na$_2$SO$_4$. The product was purified on Si eluting with 2% Et$_3$N in pentane and 0 – 10 % EtOAc. The second fraction was collected and the solvent removed to yield the desired product **3b** (257 mg, 0.858 mmol, 22%).

^{1}H NMR (400 MHz, CDCl$_3$): δ 2.45 (3 H, s, Bpy CH$_3$); 3.72 (3 H, s, OCH$_3$); 3.73 (2 H, s, CH$_2$); 7.15 (1 H, dd, 0.80 and 5.03 Hz Bpy); 7.28 (1 H, dd, 1.68 and 5.06 Hz Bpy); 8.24 (1 H, s, Bpy); 8.33 (1 H, s, Bpy); 8.54 (1 H, d, 4.92 Hz Bpy); 8.63 (1 H, d, 5.01 Hz, Bpy).

The methyl ester **3b** was hydrolysed to produce the free acid. A 50 mL RBF was charged with **3b** (284 mg), which was dissolved in the minimum amount of methanol. KOH (131 mg) was added. The reaction was stirred at 35 °C for 2 h. The solvent was removed and the solid taken up in H$_2$O and titrated to pH 7 with a 10 % solution of HCl. The H$_2$O was removed and the product used without purification.

^{1}H NMR (400 MHz, CD$_3$OD): δ 2.43 (3 H, s, Bpy CH$_3$); 3.58 (2 H, s, CH$_2$); 7.24 (1 H, dd, 0.73 and 5.08 Hz, Bpy); 7.38 (1 H, dd, 1.51 and 5.08 Hz, Bpy); 8.03 (1 H, s, Bpy); 8.17 (1 H, s, Bpy); 8.45 (1 H, d, 5.03 Hz, Bpy); 8.48 (1 H, d, 5.08 Hz Bpy).

7.4.7   5-[4-(4-methylene carboxyamidyl, 4'-methyl-2,2'-bipyridine-) phenyl]-10,15,20-triphenyl porphyrin (3d)
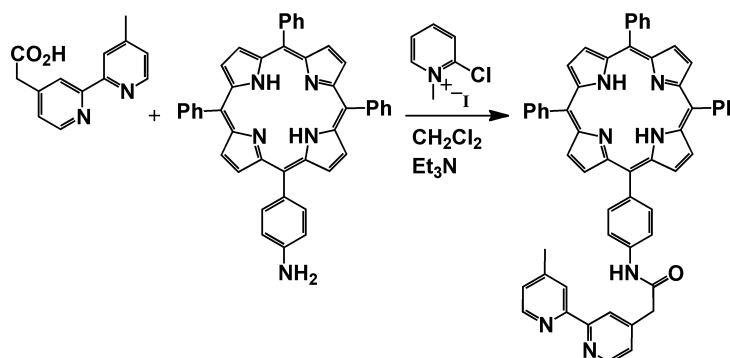
A 50 cm^3 RBF was charged with **1b** (125 mg, 0.219 mmol) and CH$_2$Cl$_2$ (15 cm^3) and cooled to 0 ˚C. A solution of 4'-Methyl-2,2'-bipyridine-4-acetic acid and 2-chloromethyl pyridinium iodide in CH$_2$Cl$_2$ (15 cm^3) was added, followed by Et$_3$N dropwise. The mixture was stirred at 0 ˚C for 5 min and then warmed to RT. After stirring at RT for 0.5 h TLC showed negligible quantities of starting porphyrin and so the reaction was stopped. The reaction was quenched with 10% HCl (50 cm^3) and the porphyrin extracted with CH$_2$Cl$_2$. The extract was washed with saturated NaHCO$_3$ followed by brine and then dried over MgSO$_4$. The product purified with column chromatography on Si-60 eluting with CH$_2$Cl$_2$ and CH$_3$OH (0 to 3%). The second fraction was collected and the solvent removed to yield the desired product (156 mg, 0.186 mmol, 94%).

^{1}H NMR (400 MHz, CDCl$_3$): δ 2.44 (3 H, s, bpy CH$_3$); 3.90 (2 H, s, CH$_2$ spacer); 7.19 (1 H, d, 4.46 Hz, bpy 5'); 7.50 (1 H, d, 4.80 Hz, bpy 5); 7.70 (1 H, s, bpy 3); 7.77 (9 H, m, *m-/p*-phenyl); 7.88 (2 H, d, 8.02 Hz, *m*-amidophenyl); 8.16 (2 H, d, 8.08 Hz, *o*-amidophenyl); 8.23 (6 H, m, *o*-phenyl); 8.33 (1 H, s, bpy 3'); 8.53 (1 H, s, amide); 8.60 (1 H, d, 4.97 Hz, bpy 6'); 8.78 (1 H, d, 5.14 Hz, bpy 6); 8.86 (8 H, m, β-pyrrole).

ESI-MS: *m/z* = 840.3428 ([M+H$^+$]$^+$, 100%), (M+H$^+$; C$_{57}$H$_{42}$N$_7$O requires 840.3445, difference 1.7 mDa)

7.4.8   5-[4-(4-methylene carboxyamidyl, 4'-methyl-2,2'-bipyridine-) phenyl]-10,15,20-triphenyl porphyrinatozinc(II) (3e)
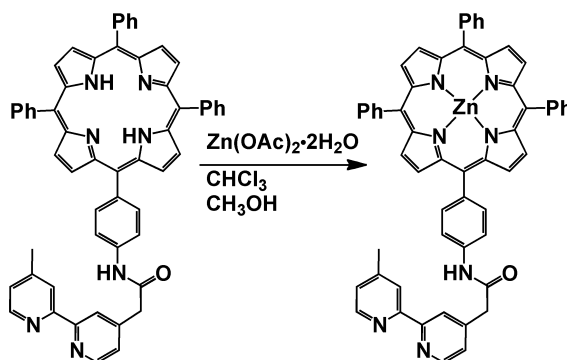
A 100 cm^3 RBF was charged with **3d** (152 mg, 181 μmol), Zn(OAc)$_2$ (179 mg, 815 μmol), CH$_3$OH (5 cm^3) and CHCl$_3$ (25 cm^3). The mixture was heated to reflux for 1 h and the reaction was followed by UV-vis spectroscopy. The reaction mixture was allowed to cool, vacuumed to dryness and re-dissolved in 100 cm^3 CHCl$_2$ and 20 cm^3 CHCl$_3$. This was washed with EDTA solution (2 g in 200 cm^3 10% NaCO$_3$ solution), water (3 x 200 cm^3), dried (MgSO$_4$) and the solvent removed to yield the desired compound (160 mg, 178 μmol, 98%).

^{1}H NMR (400 MHz, THF-d_8): δ 2.49 (3 H, s, bpy CH$_3$); 3.95 (2 H, s, CH$_2$); 7.21 (1 H, d, 4.49 Hz, bpy 5'); 7.55 (1 H, d, 4.08 Hz, bpy 5); 7.78 (9 H, m, *m-/p*-phenyl); 8.09 (2 H, d, 8.43 Hz, *m*-amidophenyl); 8.14 (2 H, d, 8.43 Hz, *o*-amidophenyl); 8.23 (6 H, m, *o*-phenyl); 8.46 (1 H, s, bpy 3'); 8.56 (1 H, d, 4.89 Hz, bpy 6'); 8.67 (1 H, d, 5.03 Hz, bpy 6); 8.68 (1 H , s, bpy 3); 8.86 (6 H, m, β-pyrrole); 8.92 (2 H, d, 4.62 Hz, β-pyrrole); 9.73 (1 H, s, amide)

ESI-MS: *m/z* = 902.2556 ([M+H$^+$]$^+$, 100%), (M+H$^+$ requires 902.2580, difference 2.4 mDa)

7.4.9 5-{4-[Rhenium(I)tricarbonyl(bromide)-4-methyl-2,2′-bipyridine-4′-methylene carboxyamidyl]phenyl}-10,15,20-triphenylporphyrinatozinc(II) (Dyad 3 Br)
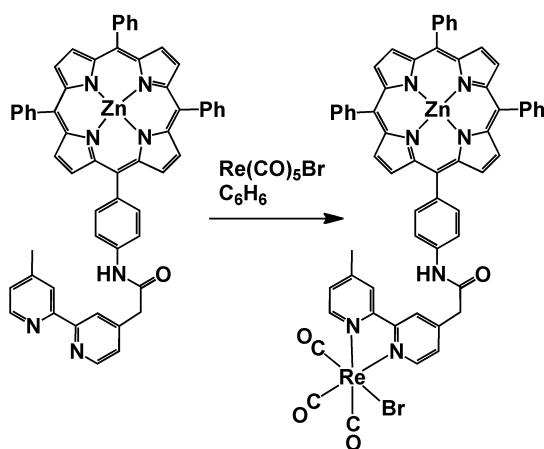
A two-neck 50 cm^3 RBF was fitted with a reflux condenser and gas valve. The setup was flame dried. Under Ar **3e** (200 mg, 221 μmol) was added, followed by Re(CO)$_5$Br (90 mg, 221 μmol). Dry benzene was added (30 cm^3) by syringe. The mixture was heated to 65 ˚C and followed by IR spectroscopy and judged to be complete after 22 h. The reaction mixture was filtered to leave a solid product (263 mg, 210 μmol, 95%).

^{1}H NMR (500 MHz, THF-d_8): δ 2.60 (3 H, s, bpy methyl); 4.09 (2 H, s, methylene); 7.47 (1 H, dd, 0.68 and 5.61 Hz, bpy-5'); 7.73 (10 H, m, *m-, p*-phenyl + bpy-5); 8.05 (2 H, d, 8.61 Hz, bridging phenyl); 8.13 (2 H, d, 8.37 Hz, bridging phenyl); 8.18 (6 H, m, *o*-phenyl); 8.45 (1 H, s, bpy-3'); 8.64 (1 H, d, 0.84 Hz, bpy-3); 8.82 (6 H, m, β-pyrrole); 8.86 (2 H, m, β-pyrrole); 8.90 (1 H, d, 5.69 Hz, bpy-6'); 9.03 (1 H, d, 5.69 Hz, bpy-6); 9.82 (1 H, s, amide)

^{13}C{^{1}H} NMR (100.6 MHz, THF-d_8): δ 21.12 (Bpy CH$_3$); 43.48 (methylene); 117.72 (*m*-amidophenyl); 120.86 (porphyrin meso by amidophenyl); 121.26 (porphyrin meso); 125.05 (Bpy-3'); 125.20 (Bpy-3); 126.96 (*m*-phenyl); 127.88 (*i*-phenyl); 128.48 (Bpy-6'); 128.63 (Bpy-6); 128.81 (Bpy-4); 131.97 (β-pyrrole); 135.13 (*o*-phenyl); 135.47 (*o*-amidophenyl); 139.48 (*i*-amidophenyl); 139.62 (*p*-amidophenyl); 144.31 (*p*-phenyl); 149.60 (Bpy-4'); 150.76 (α-pyrrole); 152.41 (Bpy-5); 153.22 (Bpy-5'); 153.48 (Re carbonyl); 156.41 (Bpy-2); 156.60 (Bpy-2'); 167.22 (amide carbonyl); 198.49 (Re carbonyl)

IR (v/cm^{-1}) (THF) 2019, 1919, 1895 (v(CO)) (ATR) 2021 (CO), 1935 (CO), 1892 (CO), 1668 (C=O), 1622, 1595, 1525 (N-H), 1484, 1441, 1398, 1341, 1241, 1206, 1186, 1070, 993, 828, 797, 756, 717, 703, 686

ESI-MS: *m/z* = 1248.9 ([M+H$^+$]$^+$, 23%), (M+H$^+$; C$_{60}$H$_{40}$N$_7$O$_4$ZnReBr requires 1249.1)

7.4.10 5-{4-[Rhenium(I)tricarbonyl(3-picoline)-4-methyl-2,2′-bipyridine-4′-methylene carboxyamidyl]phenyl}-10,15,20-triphenylporphyrinatozinc(II) Trifluoromethanesulfonate ([Dyad 3 Pic][OTf])
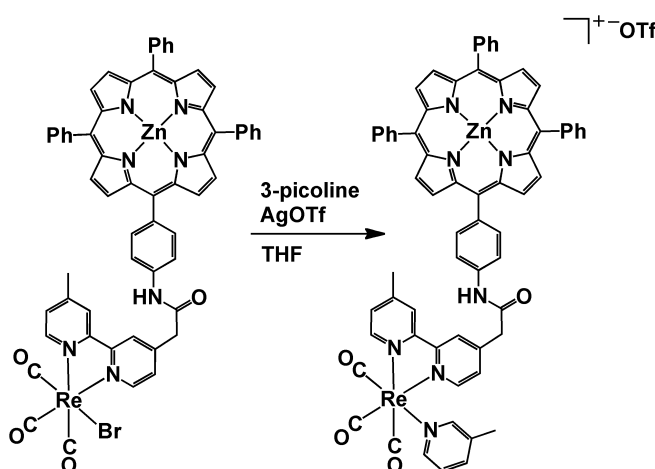
A two-neck 50 cm^3 RBF was fitted with a gas valve and flame dried. It was taken into a glovebox and AgOTf was added (206 mg, 800 μmol). A condenser fitted with a single-neck RBF and gas valve was flame dried, then under Ar the RBF was removed and the condenser and reaction flask were brought together. THF and 3-picoline (1.09 mL, 11.2 mmol) were added and finally **Dyad 3 Br** (200 mg, 160 μmol). The mixture was heated to reflux for 2 h and checked for completion by IR spectroscopy. The mixture was allowed to cool, filtered to remove AgBr and dried under vacuum for 72 h. The oil was redissolved in THF and applied to Sephadex LH20 eluting with THF. The THF was removed and the solid washed with an ethanol/petrol 20/80 mixture. The solid was dried to yield **[Dyad 3 Pic][OTf]** (95 mg, 67.10 μmol, 42%).

^{1}H NMR (400 MHz, THF-d_8): δ 2.26 (3 H, s, picoline methyl); 2.68 (3 H, s, bpy methyl); 4.27 (2 H, s, methylene); 7.31 (1 H, d, 5.73 and 8.08 Hz, pic); 7.71 (1

H, d, 5.91 Hz bpy); 7.74 (1 H, d, 7.88 Hz, pic); 7.79 (9, m, *m-, p-* phenyl); 8.15 (3 H, m, bridging phenyl + bpy); 8.26 (9 H, m, *o*-phenyl + pic); 8.34 (1 H, s, pic); 8.89 (6 H, m, β-pyrrole); 8.95 (2 H, m, β-pyrrole); 9.01 (1 H, s, bpy); 9.17 (1 H, d, 5.60 Hz, bpy); 9.22 (1 H, s, bpy); 9.33 (1 H, d, 5.75 Hz, bpy); 10.44 (1 H, s, amide)

^{13}C{^{1}H} NMR (100.6 MHz, THF-*d$_8$*): δ$_c$ 17.86 (picoline CH$_3$); 21.14 (Bpy CH$_3$); 44.30 (methylene); 117.94 (*m*-amidophenyl); 121.22 (porphyrin meso); 126.93 (*m*-phenyl + Bpy-3); 127.18 (picoline-5); 127.87 (*p*-phenyl); 129.86 (Bpy-5); 130.23 (Bpy-5'); 131.97 (β-pyrrole); 135.20 (*o*-phenyl + *o*-amidophenyl); 138.09 (picoline-3); 139.23 (*i*-amidophenyl); 139.84 (*p*-amidophenyl); 141.13 (picoline-4); 144.41 (*i*-phenyl); 149.78 (picoline-6); 150.76 (α-pyrrole); 151.07 (α-pyrrole); 152.70 (Bpy-4'); 153.22 (Bpy-6); 153.61 (Bpy-6); 155.40 (Bpy-4); 156.73 (Bpy-2); 156.97 (Bpy-2'); 167.22 (amide carbonyl); 192.50 (Re carbonyl); 196.68 (Re carbonyl).

IR (v/cm^{-1}) (CH$_2$Cl$_2$) 2034, 1933, 1924 (v(CO)) (ATR) 2029 (CO), 1912 (CO), 1676 (C=O + N-H), 1597, 1522 (N-H), 1486, 1340, 1280, 1245, 1158, 1068, 1027, 993, 796, 702

ESI-MS: *m/z* = 1265.2453 (M$^+$, 100%, chosen due to poor signal to noise), (M$^+$; C$_{66}$H$_{46}$N$_8$O$_4$ZnRe requires 1265.2476 difference 2.3 mDa)

7.4.11 [Re(Br)(2,2'-bipyridine-4,4'-bis diethylphosphate)(CO)$_3$] (6b)
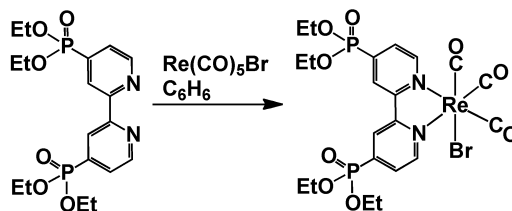
To a flame-dried two neck 50 cm^3 RBF fitted with a reflux condenser was added 2,2'-bipyridine-4,4'-bis diethylphosphate (50 mg, 117 μmol) followed by Re(CO)$_5$Br (47 mg, 117 μmol). The solids were suspended in dry C$_6$H$_6$ (15 cm^3) and the mixture heated to 65 °C. The reaction was followed by IR spectroscopy

showing completion after 19 h. Solvent was removed under reduced pressure.
The product was precipitated as an orange solid from CH_2Cl_2 with hexanes
(84 mg, 108 μmol, 92%).

^{1}H NMR (400 MHz, CDCl$_3$): δ 1.41 (12 H, td, 2.70 and 7.09 Hz, ethyl CH$_3$);
4.26 (8 H, m, ethyl CH$_2$); 7.84 (2 H, qd, 1.09 and 5.41 Hz, Bpy-5); 8.63 (2 H, d,
13.41 Hz, Bpy-3); 9.19 (2 H, t, 4.81 Hz, Bpy-6)

^{13}C{^{1}H} NMR (100.6 MHz, CDCl$_3$): δ 16.58 (CH$_3$); 63.88 (CH$_2$); 125.75 (Bpy-
3); 129.15 (Bpy-5); 140.88 (Bpy-4); 142.75 (Bpy-2); 153.50 (Bpy-6); 155.34 (Re
carbonyl); 196.21 (Re carbonyl)

^{31}P{^{1}H} NMR (109 MHz, CDCl$_3$): δ 11.58

ESI-MS: *m/z* = 798. 9705 ([M+H$^+$]$^+$, 33%), (M+H$^+$; C$_{21}$H$_{27}$BrN$_2$O$_9$P$_2$Re requires
798.9719 difference 1.4 mDa)

IR (ν/cm^{-1}) (CH$_2$Cl$_2$): 2024 (s), 1930 (s), 1901 (s) (ν (CO)). (ATR) 2019 (CO),
1934 (CO), 1907 (CO), 1882 (CO), 1392, 1258 (P=O), 1011 (P-OEt), 975 (P-
OEt), 797

7.4.12 [Re(3-Picoline)(2,2'-bipyridine-4,4'-bis diethyl phosphate)(CO)$_3$](PF$_6$) (6c)
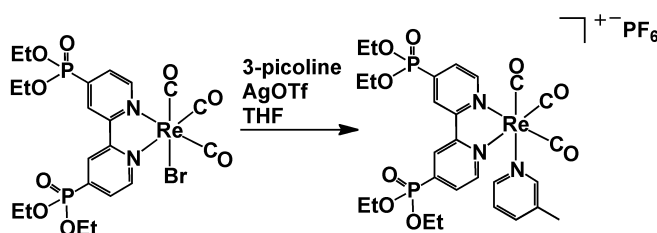
A 250 cm^3 two-neck RBF was fitted with a reflux condenser and a gas valve and
flame dried. Under Ar AgPF$_6$ (430 mg, 1700 μmol) was added followed by THF
(60 cm^3) then 3-picoline (3 cm^3). Finally **6b** (600 mg, 771 μmol) was added and
the solution heated at reflux following by IR spectroscopy, until the reaction was
completed after 19 h. The solution was filtered and evaporated to dryness. The
oil was dried under vacuum overnight and then re-dissolved in CH$_2$Cl$_2$. The

product was precipitated with hexane, collected by filtration and washed exhaustively with hexane. The product was applied to a silica column eluting with EtOAc until picoline no longer eluted and then CH_2Cl_2/CH_3OH 95/5. Picoline remained and so the product was applied to Sephadex LH20 eluting with THF then a second column eluting with CH_3OH. Solvent was removed to yield **6c** (552.5 mg, 590 μmol, 77%).

^{1}H NMR (400 MHz, CDCl$_3$) δ 1.35 (12 H, m, ethyl CH$_3$), 2.25 (3 H, s, picoline CH$_3$), 4.22 (8 H, m, ethyl CH$_2$), 7.35 (1 H, m, picoline-5), 7.60 (1 H, d, 7.81 Hz, picoline-4), 8.00 (1 H, d, 5.47 Hz, picoline-6), 8.10 (1 H, s, picoline-2), 8.14 (2 H, q, 5.48 Hz, Bpy-5), 8.60 (2 H, d, 13.31 Hz, Bpy-3), 9.38 (2 H, t, 4.99 Hz, Bpy-6)

^{13}C{^{1}H} NMR (100.6 MHz, CDCl$_3$): δ 16.31 (ethyl CH$_3$); 18.18 (picoline CH$_3$); 64.16 (CH$_2$); 126.41 (Bpy-3); 126.84 (picoline-5); 131.12 (Bpy-5); 137.74 (picoline-3); 140.74 (picoline-4); 142.34 (Bpy-4); 144.21 (Bpy-2); 148.99 (picoline-6); 151.72 (picoline-2); 154.17 (Bpy-6); 155.21 (Re carbonyl); 190.02 (Re carbonyl), 194.53 (Re carbonyl)

^{31}P NMR (109 MHz, CDCl$_3$): δ 10.59

ESI-MS: m/z = 790.1233 (M$^+$, 59%), (M$^+$; C$_{27}$H$_{33}$N$_3$O$_9$P$_2$Re$^+$ requires 790.1216), difference 1.7 mDa)

IR (v/cm^{-1}) (CH$_2$Cl$_2$): 2036 (s), 1927 (s, broad) (v (CO)). (ATR) 2031 (CO), 1910 (CO), 1396, 1257 (P=O), 1014 (P-OEt), 971 (P-OEt), 833

7.4.13 [Re(3-Picoline)(2,2'-bipyridine-4,4'-bis phosphonic acid)(CO)₃] (6d)
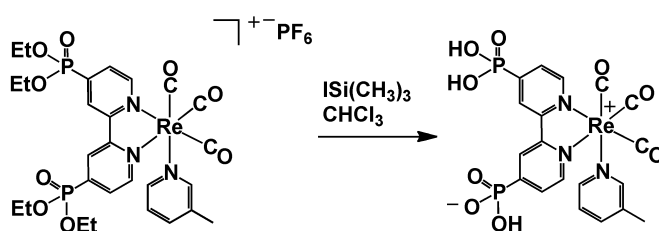
A Schlenk tube was charge with **6c** (179 mg, 191 μmol) and dried under reduced pressure at 40 ˚C overnight. This was then cooled to 0 ˚C. A 1 M solution of $ISi(CH_3)_3$ in $CHCl_3$ was prepared in the glove box, cooled to 0 ˚C and added by cannula (1.09 cm^3, 7.64 mmol of $ISi(CH_3)_3$. The resulting solution was red. The mixture was stirred at 0 ˚C for 5 min and then evapourated to dryness and dried under vacuum for 72 h. The solid was re-dissolved in dry chloroform (1 cm^3) and methanol was added (1 cm^3). The mixture was stirred at 0 ˚C for 10 min and then allowed to warm to RT and stirred for 3 h. The solution was evaporated to dryness and dried under vacuum for 24 h. The solid was precipitated from CH_3OH with Et_2O.

^{1}H NMR (400 MHz, CD$_3$OD) δ 2.22 (3 H, s, picoline CH$_3$); 7.25 (1 H, dd, 5.71 and 8.08 Hz, picoline), 7.75 (1 H, d, 8.04 Hz,picoline), 8.12 (2 H, q, 5.44 Hz, bipyridine), 8.17 (1 H, d, 5.55 Hz, picoline), 8.25 (1 H, s, picoline), 8.77 (2 H, d, 12.70 Hz, bipyridine), 9.44 (2 H, dd, 3.22 and 5.63 Hz, bipyridine)

^{1}H NMR (400 MHz, D$_2$O) δ 2.09 (3 H, s, picoline CH$_3$); 7.09 (1 H, dd, 5.77 and 8.07 Hz, picoline-5); 7.60 (1 H, d, 8.02 Hz, picoline-4); 7.95 (2 H, ddd, 0.77, 5.49 and 11.34 Hz, Bpy-4); 8.02 (1 H, d, 5.49 Hz, picoline-6); 8.14 (1 H, s, picoline-2); 8.59 (2 H, d, 12.51 Hz, Bpy-3); 9.35 (2 H, dd, 3.34 and 5.64 Hz, Bpy-6)

^{13}C{^{1}H} NMR (100.6 MHz, D$_2$O) δ 18.00 (picoline CH$_3$); 125.64 (Bpy-5); 126.46 (picoline-5); 127.55; 129.77 (Bpy-5); 137.93 (picoline-6); 140.97 (picoline-4); 149.58 (picoline-3); 151.17 (Bpy-4 and Bpy-2); 152.66 (picoline-2); 154.25 (Bpy-6); 156.52 (Bpy-4 and Bpy-2)

^{31}P{^{1}H} NMR (109 MHz, CD$_3$OD) δ 6.68

ESI-MS (negative): *m/z* = 676.4 ([M$^+$-2H$^+$]$^-$, 84%), (M$^+$-2H$^+$; C$_{19}$H$_{15}$N$_3$O$_9$P$_2$Re requires 676.0). *m/z* = 583.4 ([M$^+$-2H$^+$-C$_6$H$_7$N]$^-$), (M$^+$-2H$^+$-C$_6$H$_7$N; C$_{13}$H$_8$N$_2$O$_9$P$_2$Re requires 583.93)

IR (v/cm^{-1}) (ATR): 2030 (s), 1908 (s, broad), 1397, 1156 (P=O), 946, 848, 797. (CH$_3$OH): 2037 (s), 1932 (broad) (v (CO))

7.4.14 5-[4-(carboxamidyl methylene diethyl phosphate) phenyl]-10,15,20-triphenyl porphyrin (7a)
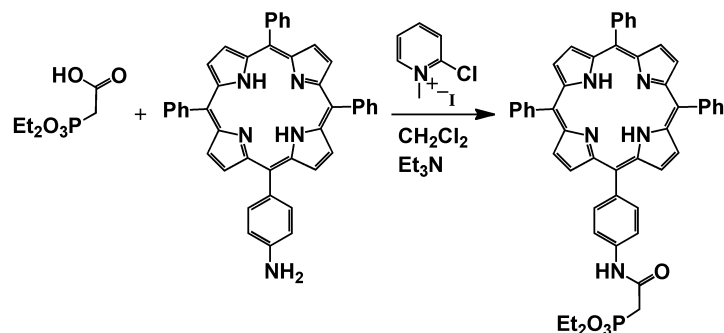
A 25 cm^3 RBF was charged with 5-[4-aminophenyl]-10,15,20-triphenyl porphyrin (50 mg, 79 µmol) and CH$_2$Cl$_2$ (8 cm^3) and cooled to 0 ˚C. A solution of diethyl phosphonoacetic acid (18 mg, 87 µmol) and 2-chloro methyl pyridinium iodide (25 mg, 95 µmol) in CH$_2$Cl$_2$ (8 cm^3) was added, followed by Et$_3$N dropwise. The mixture was stirred at 0 ˚C for 5 min and then allowed to warm to RT. The reaction was followed by TLC (100% ethyl acetate) appearing to reach completion after 0.75 h. The reaction was quenched with 10% HCl solution and the product extracted into CH$_2$Cl$_2$. This was then washed with sat. NaHCO$_3$, followed by brine and then dried over MgSO$_4$. The product was purified by column chromatography on Si-60 eluting with 5% CH$_3$OH in CH$_2$Cl$_2$ yielding the desired product (59 mg, 73 µmol, 92%).

^{1}H NMR (400 MHz, CDCl$_3$): δ -2.79 (2 H, s, pyrrole N-H), 1.46 (6 H, t, 7.09 Hz, CH$_3$), 3.18 (2 H, d, 20.41 Hz, CH$_2$), 4.31 (4 H, m, ethyl CH$_2$), 7.74 (9 H, m, *m*-, *p*- phenyl), 7.94 (2 H, d, 8.49 Hz, *m*-amidophenyl), 8.19 (8 H, m, *o*-phenyl), 8.85 (8 H, m, β-pyrrole), 9.20 (1H, s, amide).

^{31}P{^{1}H} NMR (109 MHz, CDCl$_3$): δ 23.54

ESI-MS: *m/z* = 808.3043 ([M+H$^+$]$^+$, 100%), (M+H$^+$; C$_{50}$H$_{43}$N$_5$O$_4$P requires 808.3047, difference 0.4 mDa)

7.4.15 5-[4-(carboxamidyl methylene diethyl phosphate) phenyl]-10,15,20-triphenyl porphyrinatozinc(II) (7b)
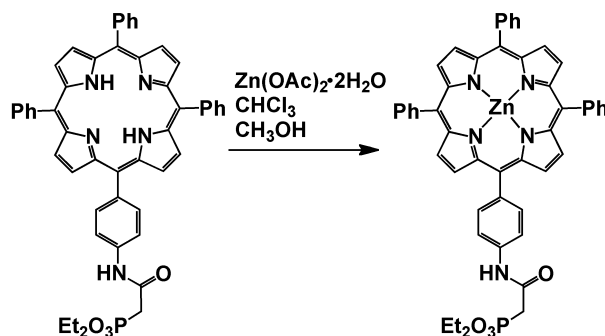
A 25 cm^3 RBF was charged with **7a** (59 mg, 73 μmol), zinc (II) diacetate dihydrate (72 mg, 329 μmol), CHCl$_3$ (9 cm^3) and CH$_3$OH (2 cm^3). The mixture was heated to reflux for 1 h, following by UV vis spectroscopy. The mixture was allowed to cool, diluted with CH$_2$Cl$_2$ (30 cm^3) and washed with EDTA solution (1 g EDTA in 100 cm^3 10% Na$_2$CO$_3$ solution) and then water. The product was dried over MgSO$_4$ and the solvent removed to yield the desired compound (59 mg, 67 μmol, 92%).

^{1}H NMR (400 MHz, CDCl$_3$): δ 1.36 (6 H, t, 7.09 Hz, CH$_3$), 2.66 (2 H, d, 20.31 Hz, CH$_2$), 4.07 (4 H, m, ethyl CH$_2$), 7.60 (2 H, d, 8.42 Hz, *m*-amidophenyl), 7.75 (9 H, m, *m*-, *p*- phenyl), 8.12 (2 H, d, 8.37 Hz, *o*-amidophenyl), 8.21 (6 H, m, *o*-phenyl), 8.80 (1 H, s, amide), 8.94 (8 H, m, β-pyrrole).

^{31}P{^{1}H} NMR (109 MHz, CDCl$_3$): δ 22.68

IR (ν/cm^{-1}) (ATR) 1693, 1664 (C=O), 1597, 1523 (N-H), 1485, 1439, 1400, 1340, 1315, 1237 (P=O), 1204, 1177, 1157, 1066, 1048, 1020 (P-OEt), 993, 797, 750, 719, 702

ESI-MS: *m/z* = 870.2124 ([M+H$^+$]$^+$, 100%), (M+H$^+$; C$_{50}$H$_{41}$N$_5$O$_4$PZn requires 870.2182, difference 5.8 mDa)

7.4.16 5-[4-(carboxamidyl methylene phosphonate triethylammonium) phenyl]-10,15,20-triphenyl porphyrinatozinc(II) (7c)
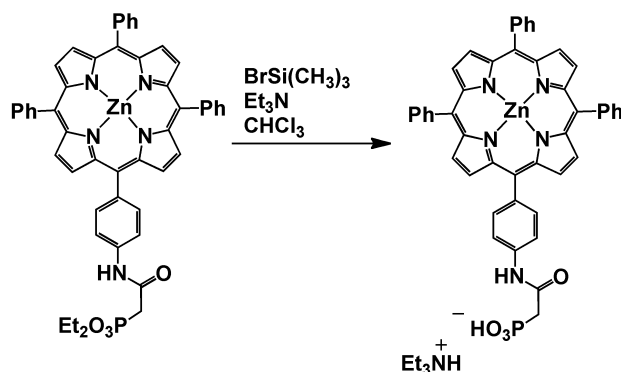
A two-neck 100 cm^3 RBF was fitted with a septum and a condenser and topped with a gas valve. The flask was charged with **7b** (300 mg, 344 μmol) and left under vacuum for 24 h. The setup was purged with Ar and dry CHCl$_3$ (36 cm^3) was added followed by Et$_3$N (957 μL, 5160 μmol). The mixture was brought to reflux and then BrSi(CH$_3$)$_3$ (680 μL, 5160 μmol) was added. The mixture was heated at reflux for 4 h and then allowed to cool. The solution was washed once with water and extracted a little with CH$_2$Cl$_2$, the material that extracted cleanly was collected and fluffy material was discarded. The product was dried under vacuum overnight then re-dissolved in CH$_2$Cl$_2$ and precipitated from hexane, filtered and dried (80 mg, 87.3 μmol, 25%).

^{1}H NMR (400 MHz, CD$_3$OD): δ 1.24 (9 H, t, 7.33 Hz, CH$_3$ of Et$_3$NH), 3.00 (2 H, d, 19.92 Hz, CH$_2$), 3.10 (6 H, q, 7.38 Hz, CH$_2$ of Et$_3$N), 7.78 (9 H, *m-, p-*phenyl), 8.01 (2 H, d, 8.44 Hz, *m*-amidophenyl), 8.15 (2 H, d, 8.34 Hz, *o*-amidophenyl), 8.22 (6 H, m, *o*-phenyl), 8.87 (8 H, m, β-pyrrole)

^{13}C{^{1}H} NMR (100.6 MHz, CD$_3$OD): δ 9.21; 119.07; 121.82; 127.49; 128.41; 132.50; 135.67; 135.86; 139.52; 144.96; 151.40; 151.60

^{31}P{^{1}H} NMR: (109 MHz, CD$_3$OD) δ 14.27

IR (ν/cm^{-1}) (ATR) 1683, 1657 (C=O), 1596, 1523 (N-H), 1483, 1440, 1399, 1338, 1316, 1251 (P=O), 1202, 1178, 1068, 994, 794, 751, 717, 700

ESI-MS: *m/z* = 812.14 (M⁻, 100%), (M⁻; $C_{46}H_{31}N_5O_4PZn^-$ requires 812.14)

Appendix to chapter two
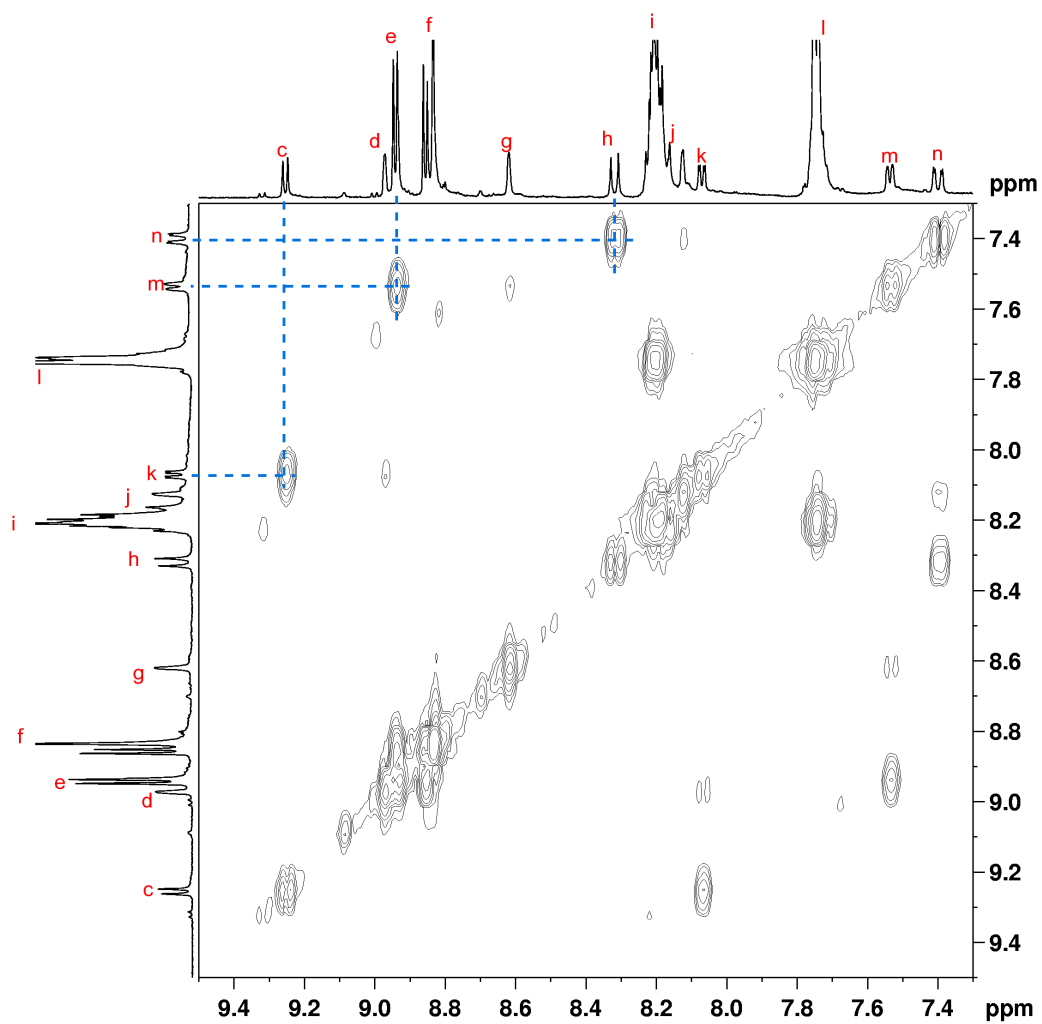
Fig. 184 ^{1}H-^{1}H COSY of **Dyad 2 Br** (THF-d_8 400 MHz).
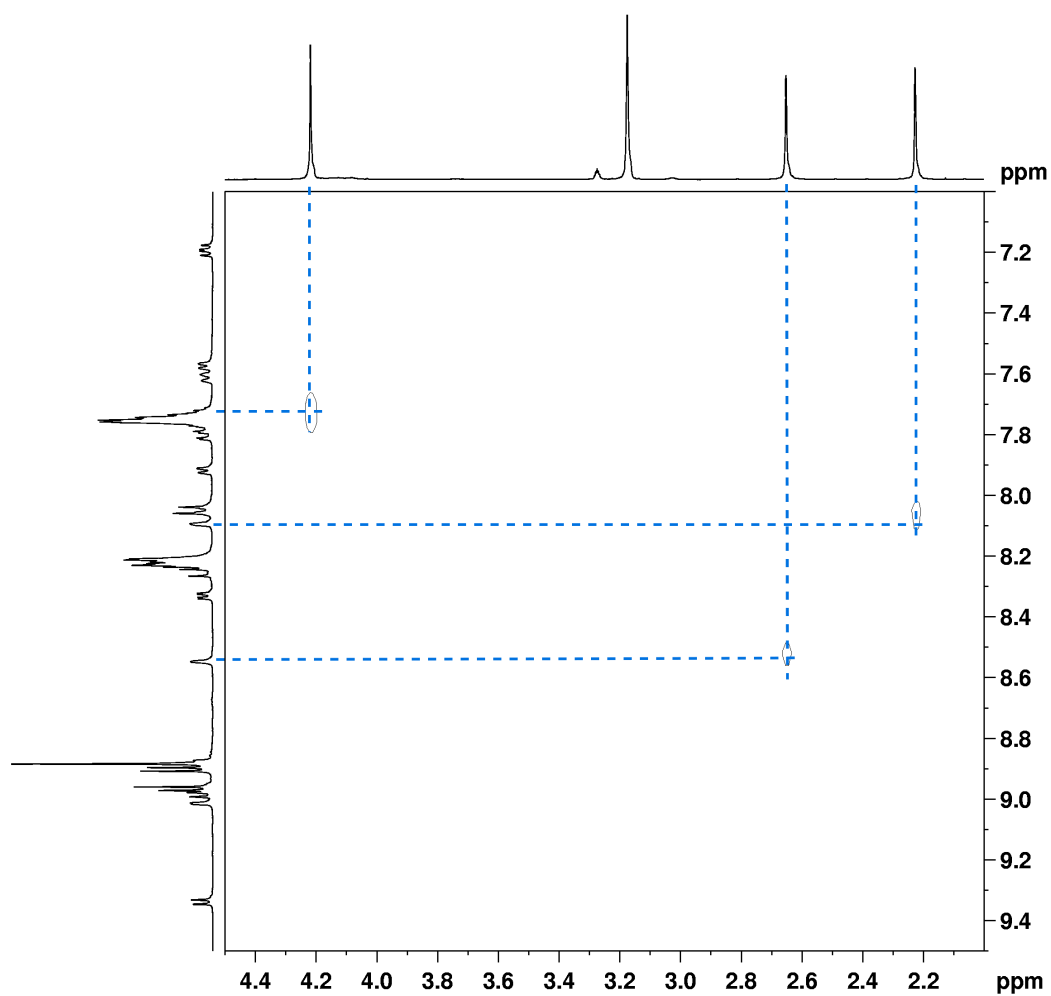
Fig. 185 ^{1}H-^{1}H NOE spectrum of **[Dyad 2 Pic][OTf]** (THF-d_8 400 MHz).
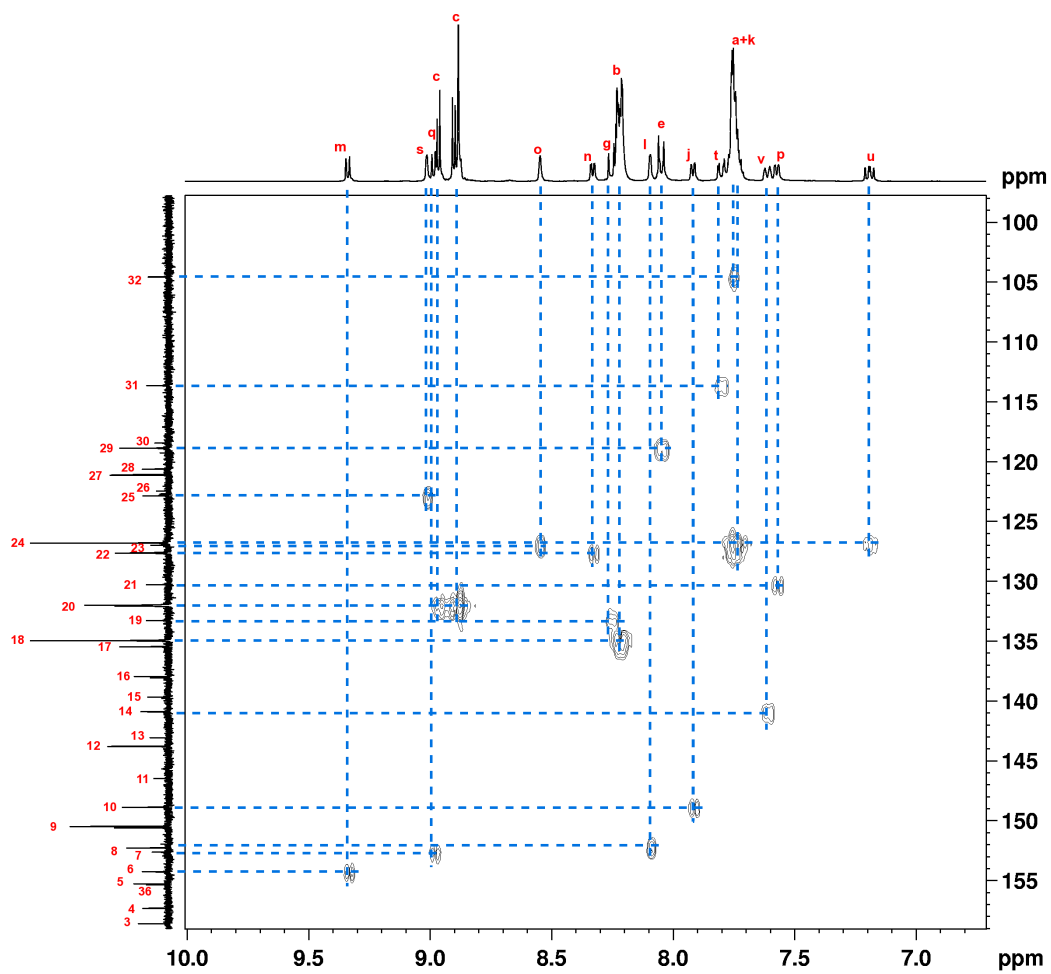
Fig. 186 ^{1}H-^{13}C HMQC spectrum of **[Dyad 2 Pic][OTf]** (THF-d_8 400 MHz).
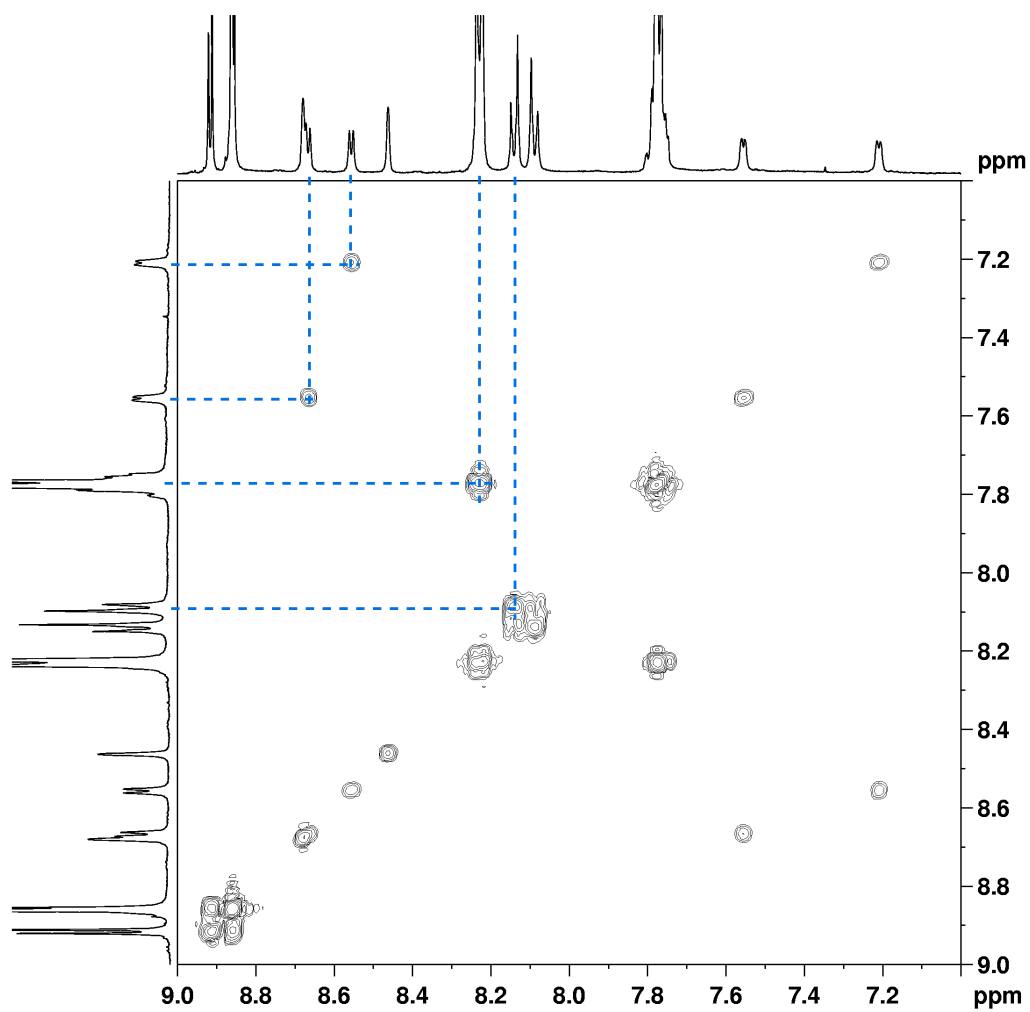
Fig. 187 ^{1}H-^{1}H COSY spectrum of **3e** (CDCl$_3$ 400 MHz).
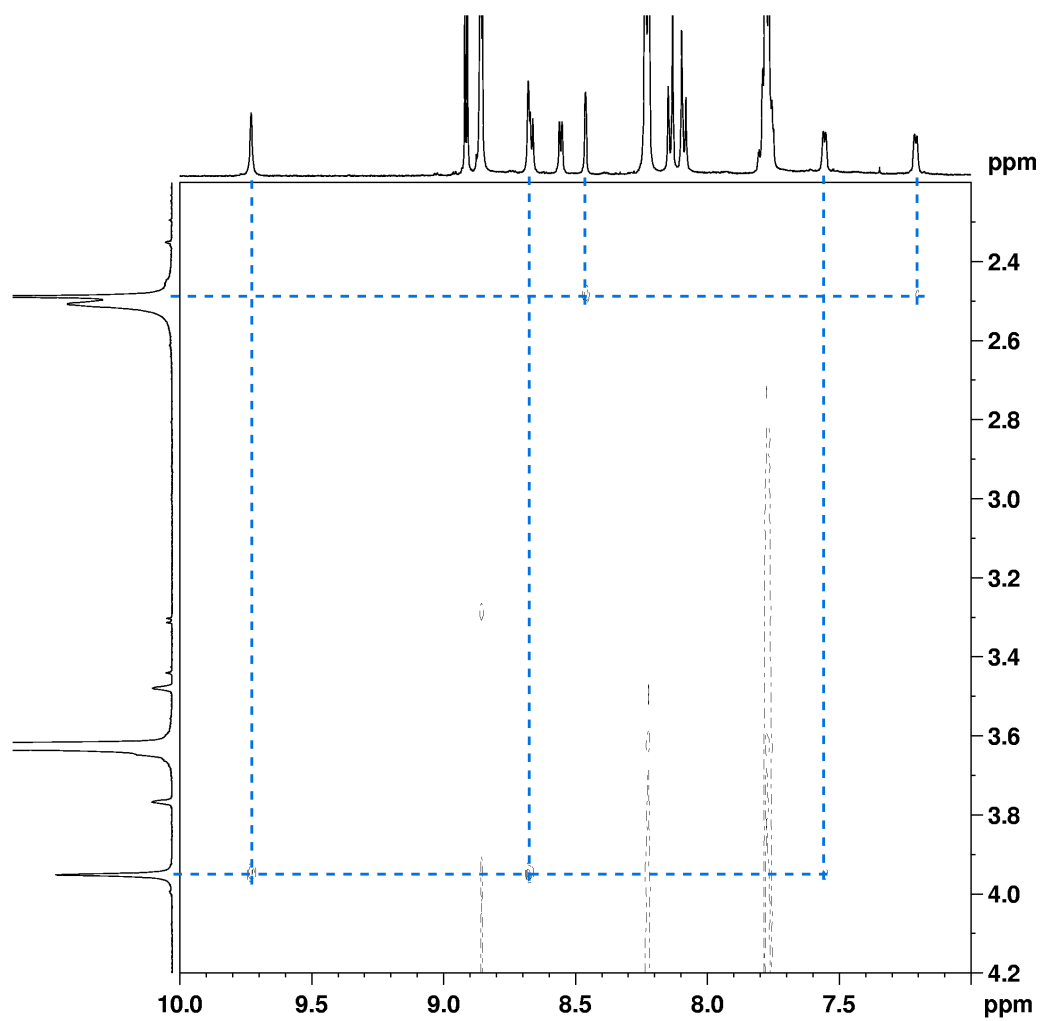
Fig. 188 ^{1}H-^{1}H NOE spectrum of **3e** (CDCl$_3$ 400 MHz).
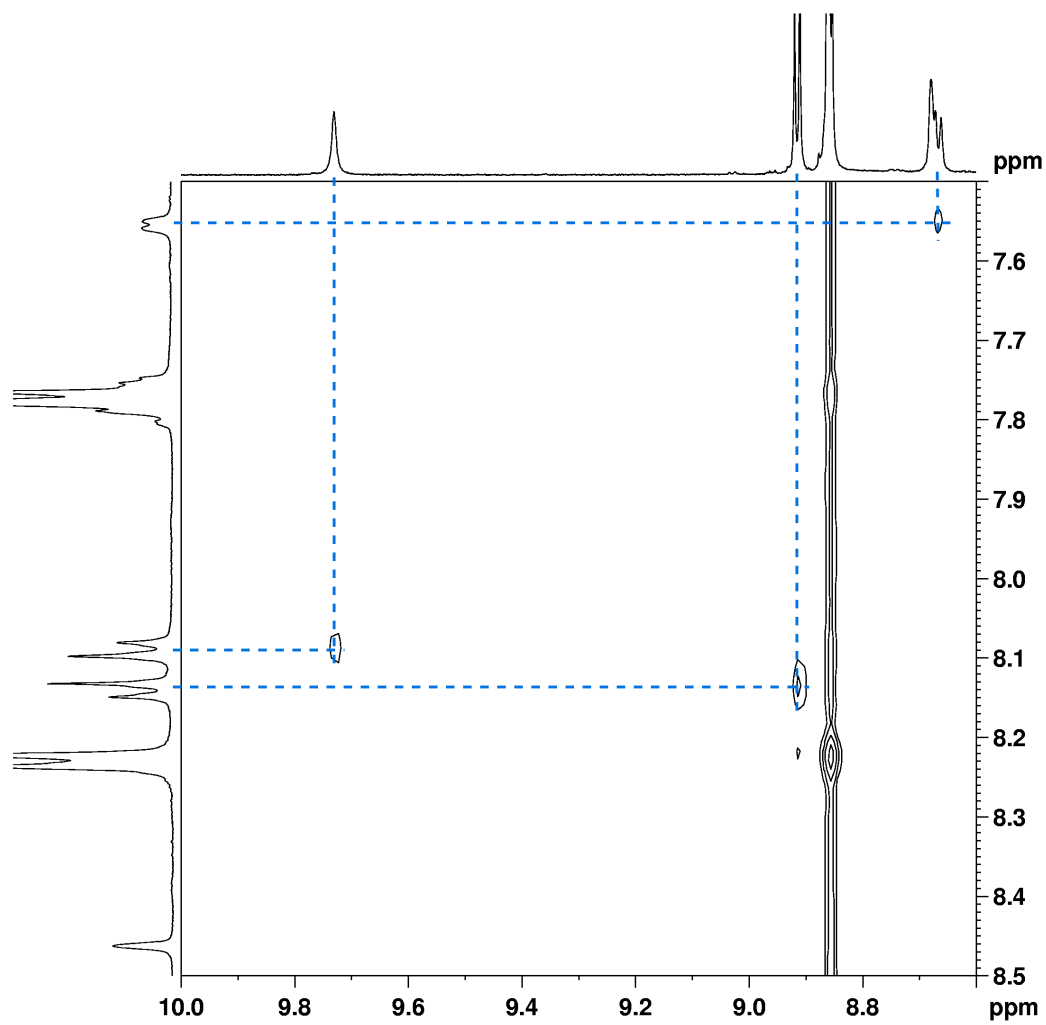
Fig. 189 ^{1}H-^{1}H NOE spectrum of **3e** (CDCl$_3$ 400 MHz).
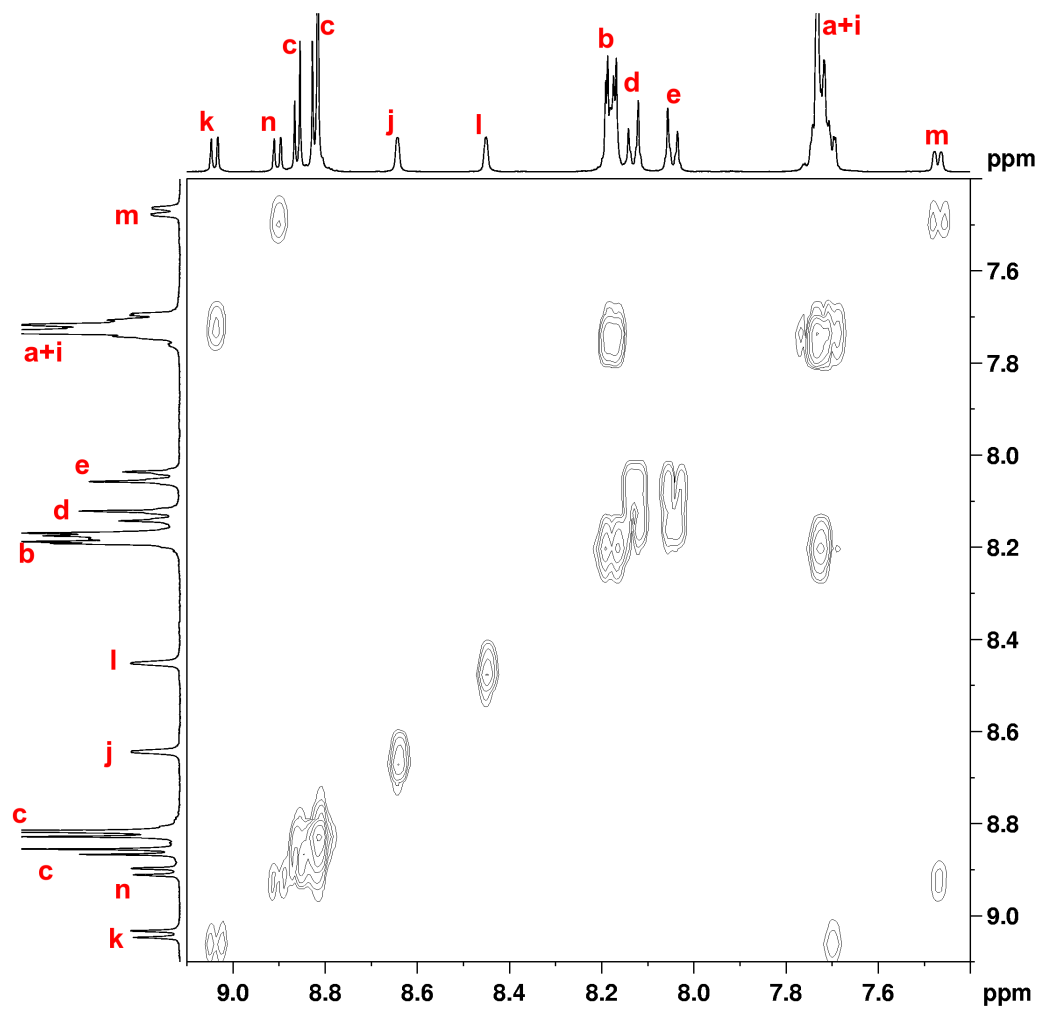
Fig. 190 ^{1}H-^{1}H COSY spectrum of **Dyad 3 Br** (THF-d_8 400 MHz).
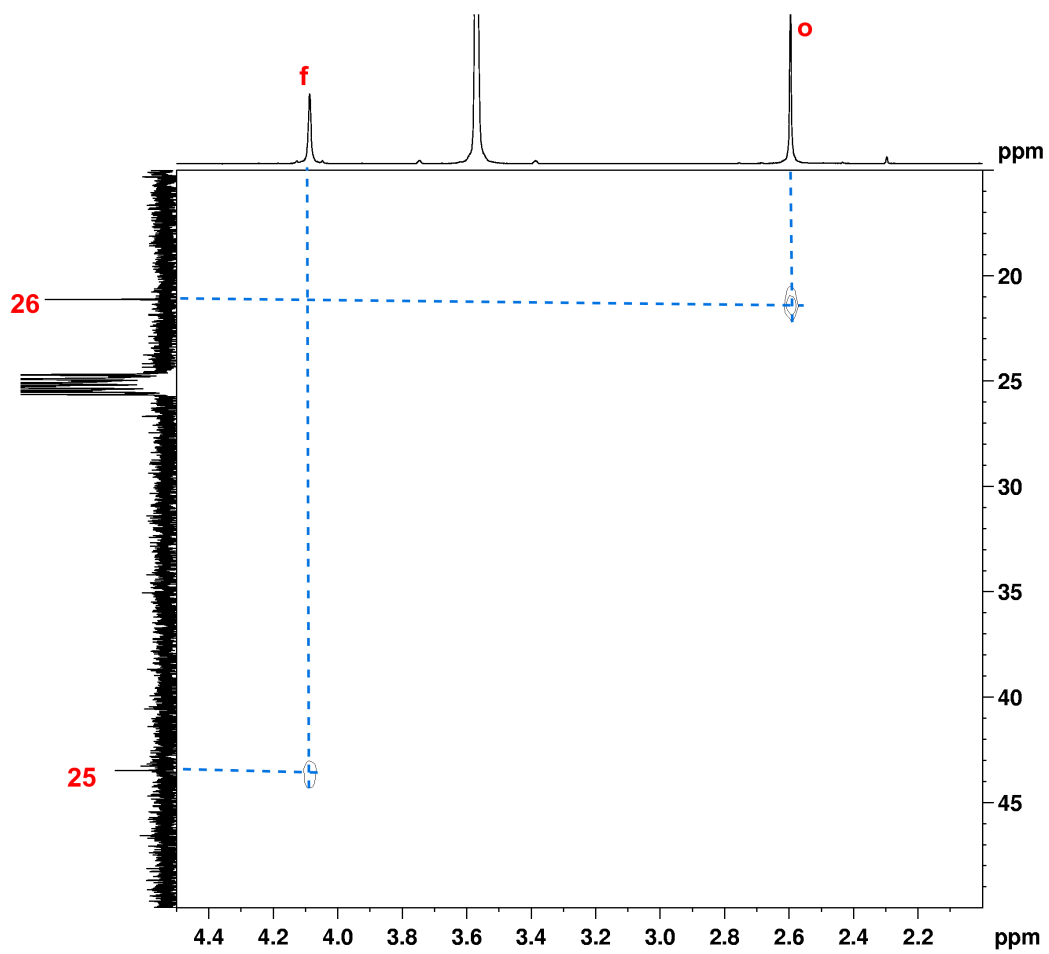
Fig. 191 ^{1}H-^{13}C HMQC of **Dyad 3 Br** (THF-d_8 400 MHz).
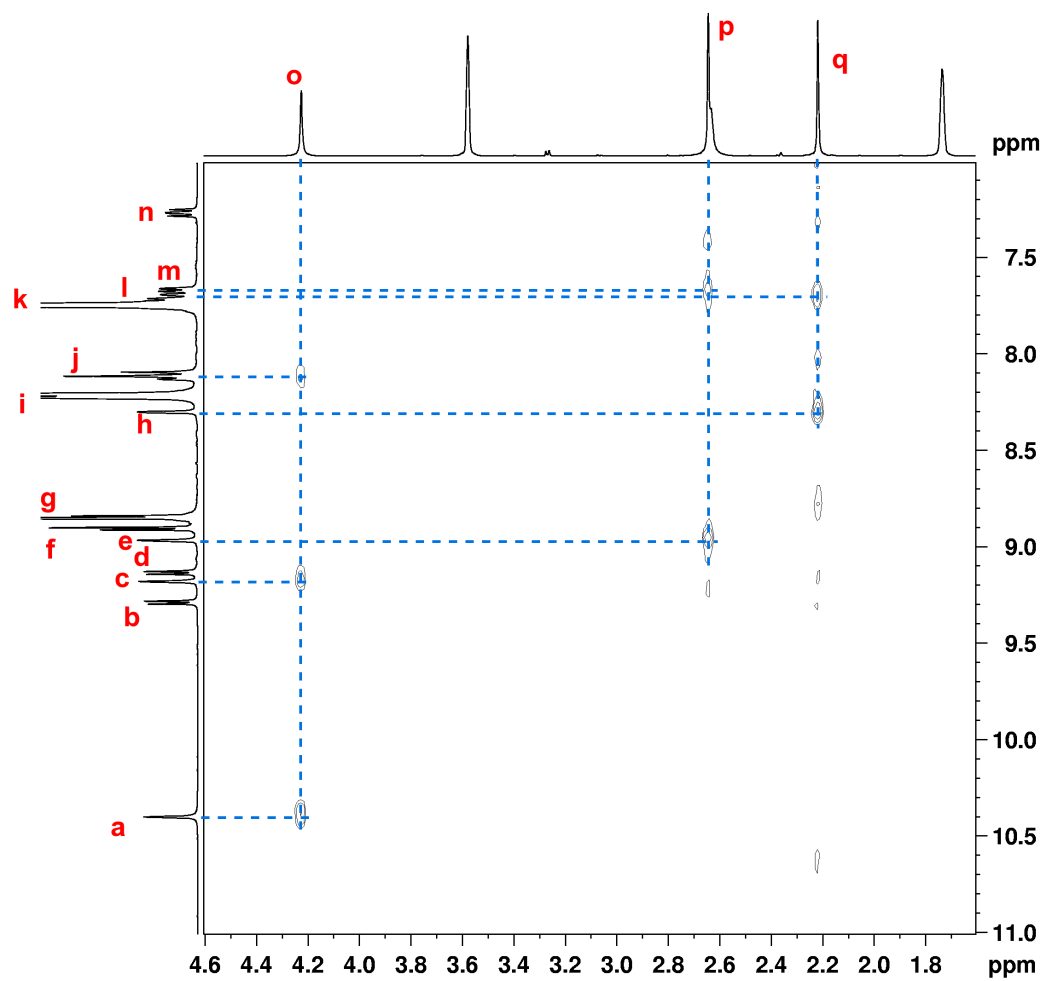
Fig. 192 ^{1}H-^{1}H NOE spectrum of **[Dyad 3 Pic][OTf]** (THF-d_8 400 MHz).
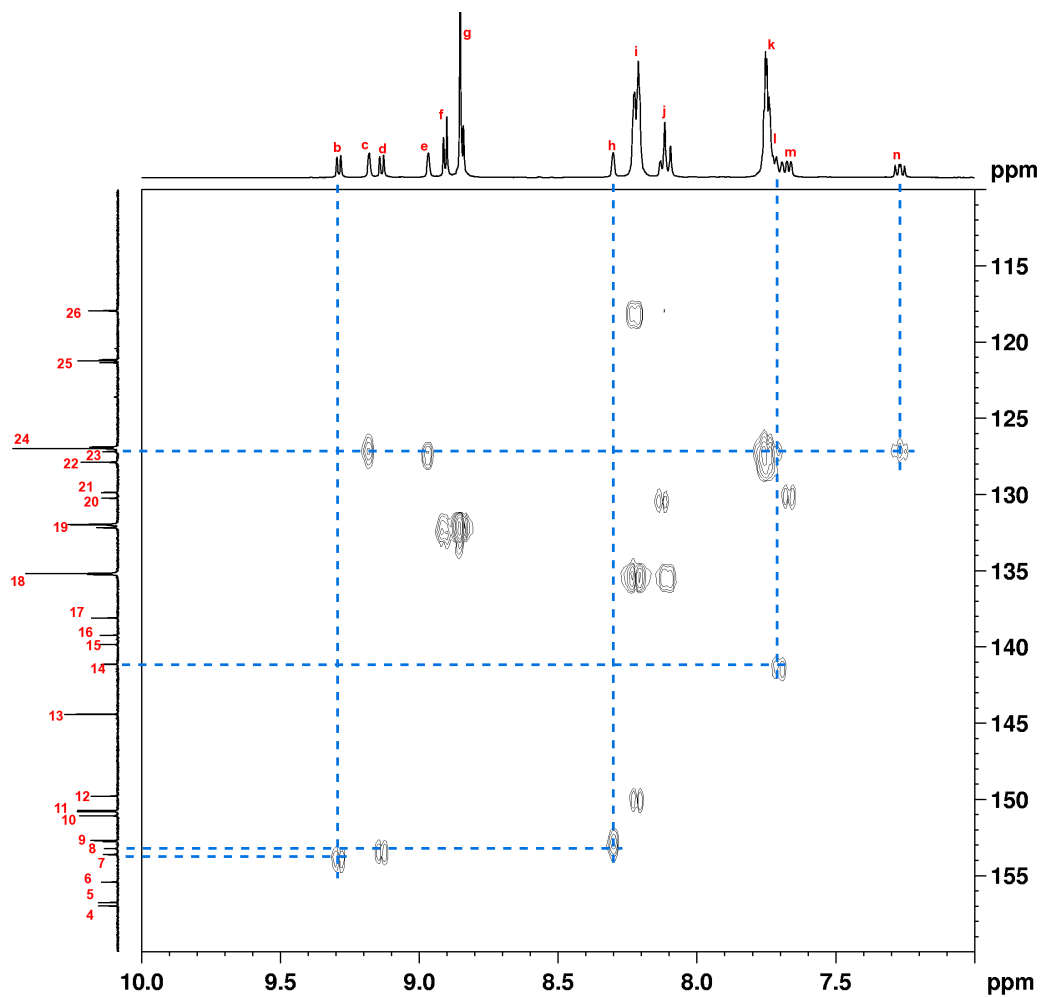
Fig. 193 HMQC spectrum of **[Dyad 3 Pic][OTf]** (THF-d_8 400 MHz).
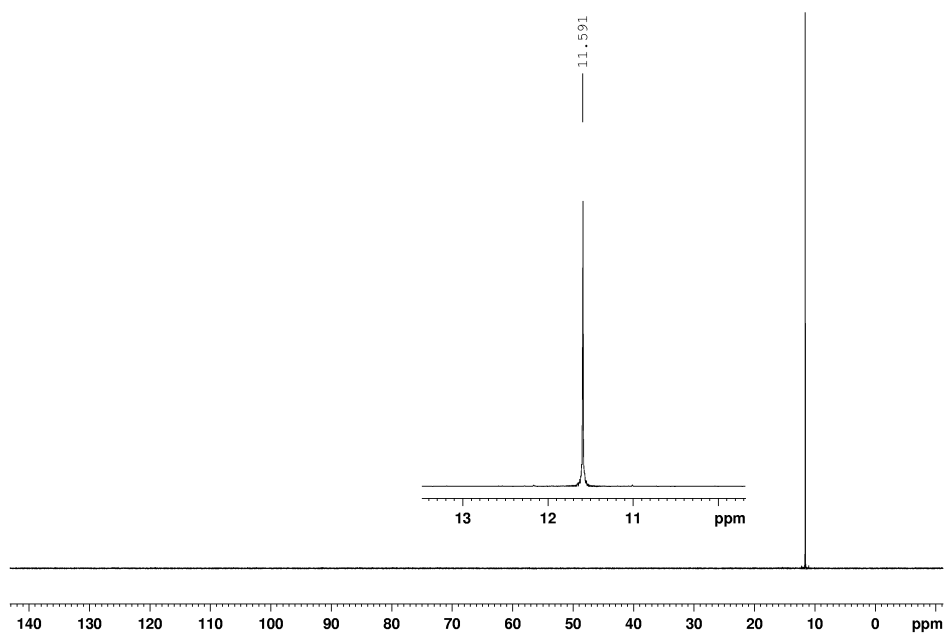
Fig. 194 ^{31}P{^{1}H} NMR spectrum of **6b** (CDCl$_3$, 109 MHz).
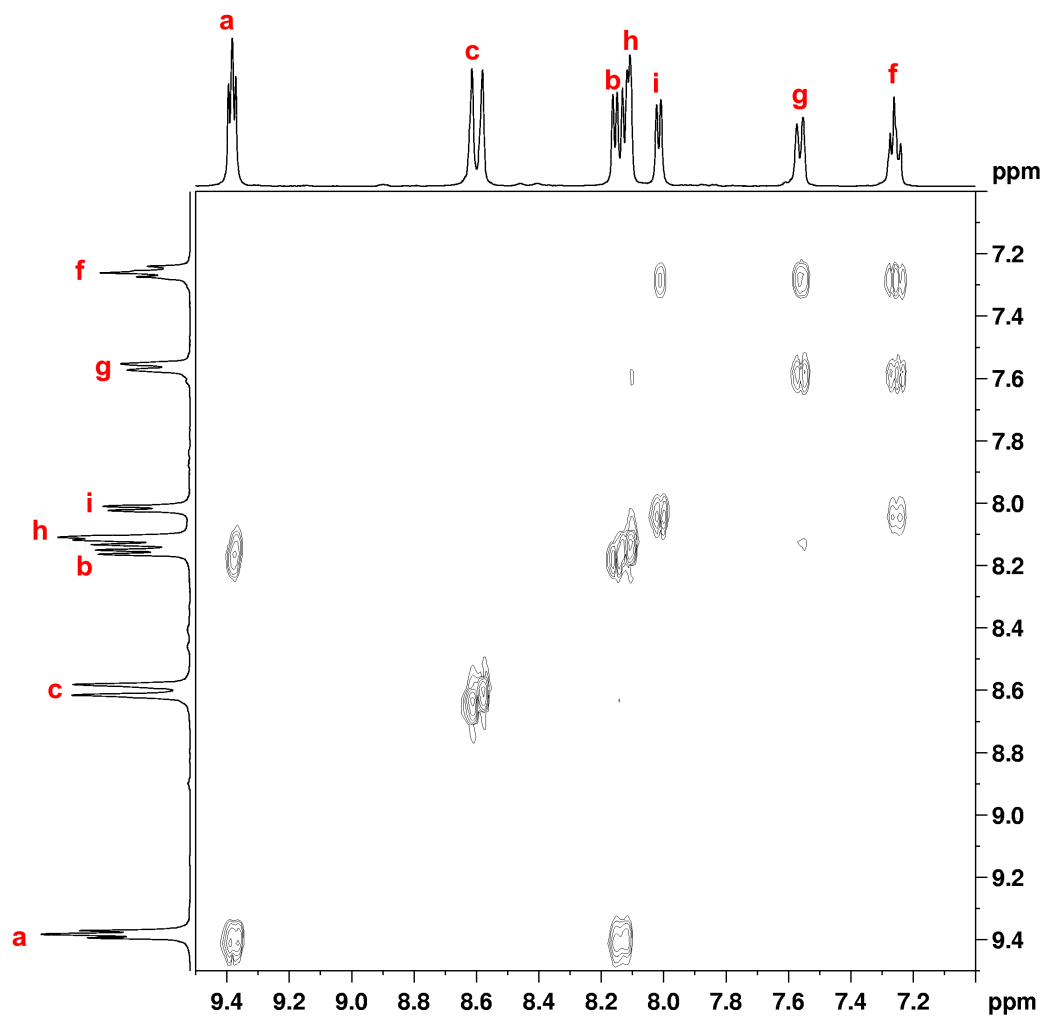
Fig. 195 ¹H-¹H COSY spectrum of **6c** (CDCl₃, 400 MHz).
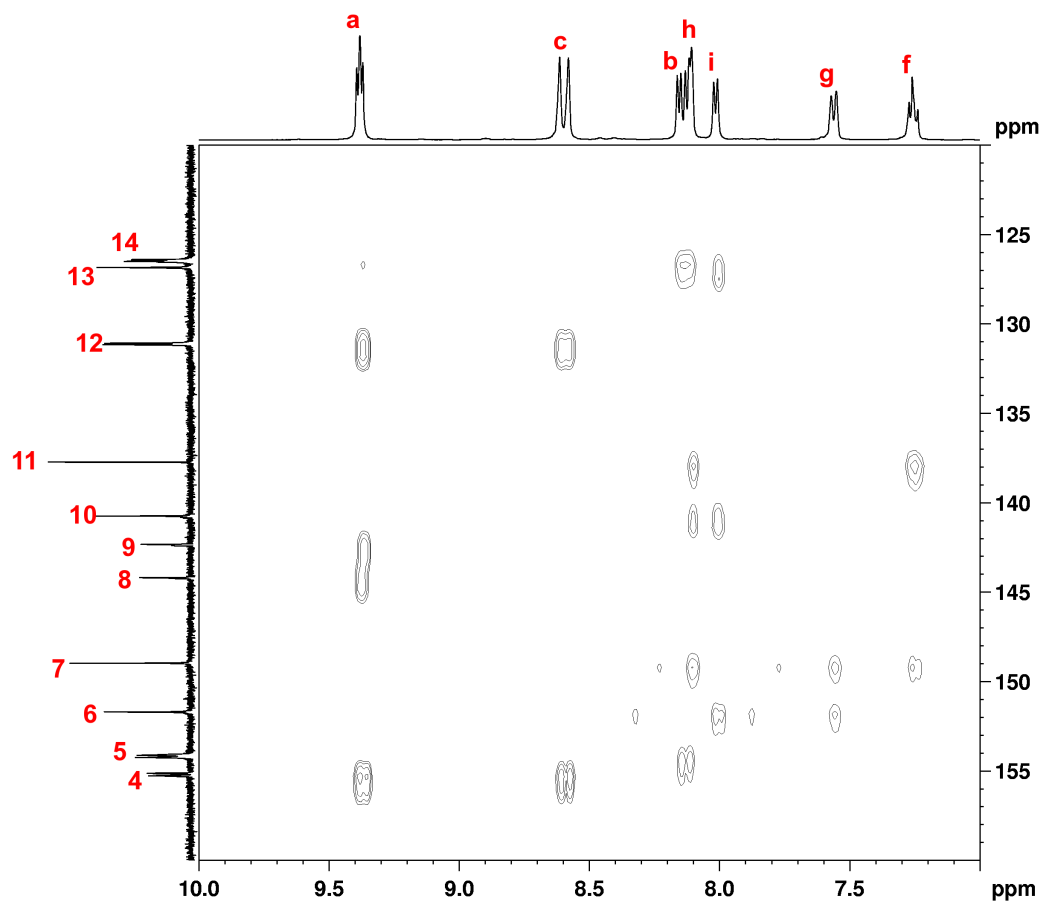
Fig. 196 ^{1}H-^{13}C HMBC spectrum of **6c** (CDCl$_3$, 400 MHz).
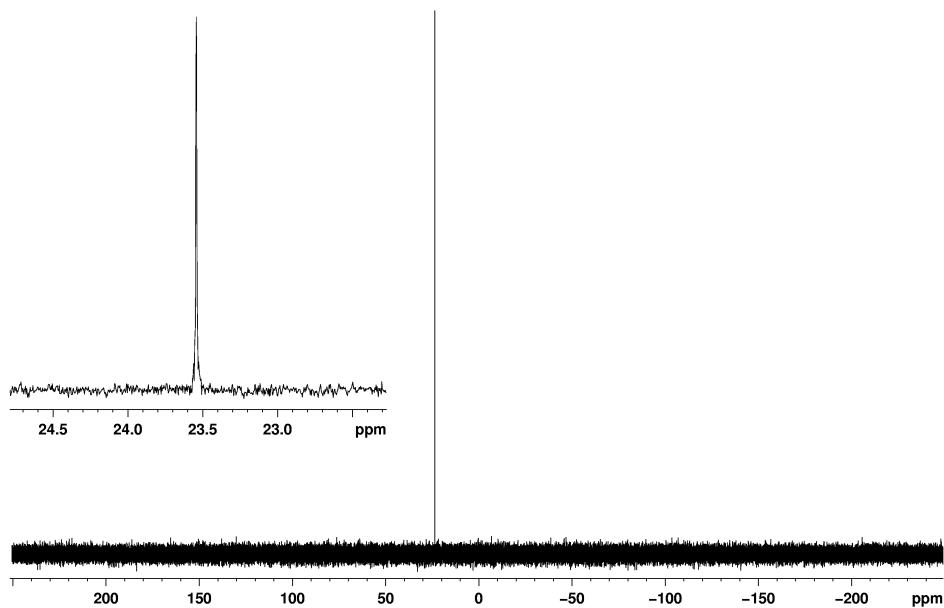
Fig. 197 ^{31}P{^{1}H} NMR spectrum of **7a** (CDCl$_3$, 109 MHz).
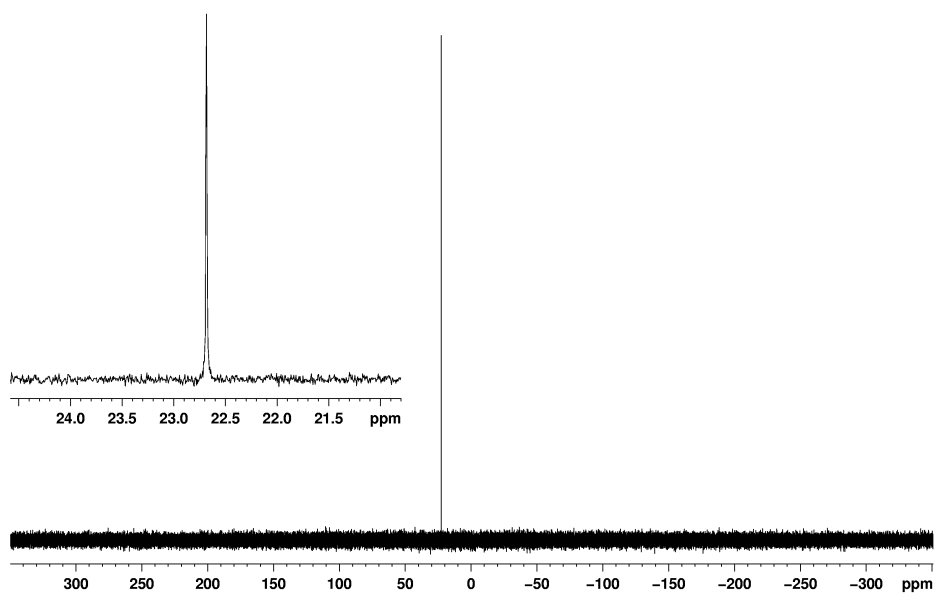
Fig. 198 ^{31}P{^{1}H} NMR spectrum of **7b** (CDCl$_3$, 109 MHz).
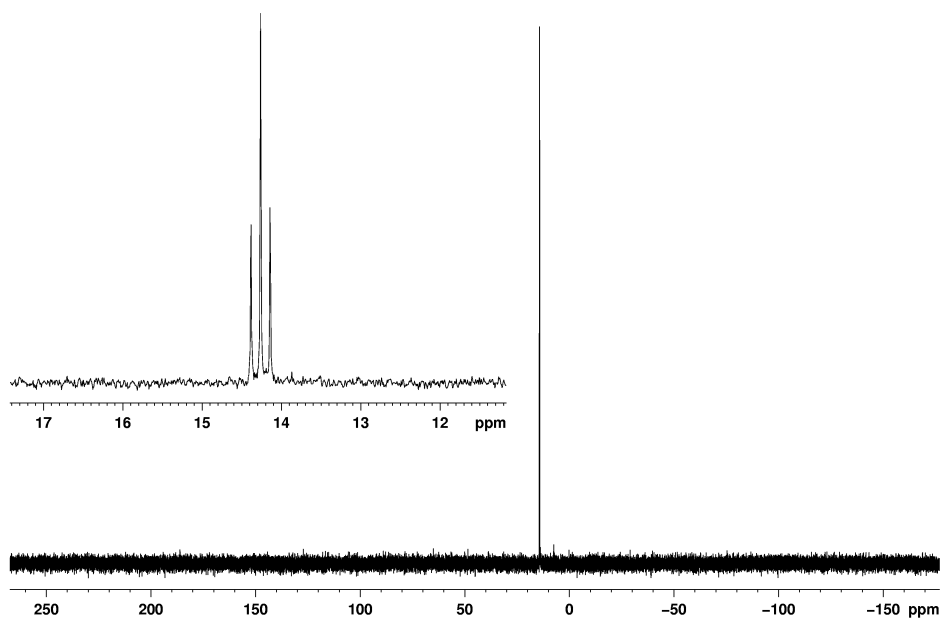
Fig. 199 ^{31}P NMR spectrum of **7c** (CD$_3$OD, 109 MHz).

Abbreviations

acac	2,4-pentanedionate or acetylacetonate
BNAH	1-Benzyl-1,4-dihydronicotinamide
Bpy	Bipyridine
CE	Counter electrode
CV	Cyclic voltammetry
DCC	Dicyclohexyl carbodiimide
DFT	Density functional theory
DMF	Dimethyl formamide
DMSO	Dimethyl sulfoxide
DRUVS	Diffuse reflectance ultra violet visible spectroscopy
EDTA	Ethylenediaminetetraacetic acid
HMPA	Hexamethylphosphoramide
IR	Infra-red
LDA	Lithium diisopropylamide
+/- M	Positive / negative mesomeric effect
Me_2Bpy	Dimethylbipyridine
NADP	Nicotinamide adenine dinucleotide phosphate
OER	One electron reduced
OTf	Trifluoromethanesulfonate anion
Pic	3-Picoline
PMHS	Poly(methylhydrosiloxane)
RBF	Round bottom flask
RE	Reference electrode
RT	Room temperature
TEOA	Triethanolamine
THF	Tetrahydrofuran
TLC	Thin layer chromatography
TMS	Trimethylsilane
TOF	Turnover frequency
TON	Turnover number
TRIR	Time resolved infrared

UV	Ultra violet
UV-Vis	Ultra violet-Visible
WE	Working electrode
ZnTPDHP	Zinc tetraphenyldihydroporphyrin
ZnTPTHP	Zinc tetraphenylisotetrahydroporphyrin
ZnTPP	Zinc tetraphenylporphyrin

Bibliography

1.   C. Song, *Catal. Today*, 2006, **115**, 2-32.
2.   S. C. Roy, O. K. Varghese, M. Paulose and C. A. Grimes, *ACS Nano*, 2010, **4**, 1259-1278.
3.   P. Y. Lipscy, K. E. Kushida and T. N. Incerti, *Environ. Sci. Technol.*, 2013.
4.   N. S. Lewis and D. G. Nocera, *Proc. Natl. Acad. Sci. U. S. A.*, 2006, **103**, 15729-15735.
5.   N. S. Lewis, *Science*, 2007, **315**, 798-801.
6.   J. Barber, *Chem. Soc. Rev.*, 2009, **38**, 185-196.
7.   J.-M. Lehn and R. Ziessel, *Proc. Natl. Acad. Sci. USA*, 1982, **79**, 701-704.
8.   J. Hawecker, J.-M. Lehn and R. Ziessel, *Chem. Commun.*, 1983, 536-538.
9.   E. Fujita, *Coord. Chem. Rev.*, 1999, **185-186**, 373-384.
10.   E. E. Benson, C. P. Kubiak, A. J. Sathrum and J. M. Smieja, *Chem. Soc. Rev.*, 2009, **38**, 89-99.
11.   I. Bhugun, D. Lexa and J.-M. Saveant, *J. Am. Chem. Soc.*, 1996, **118**, 1769-1776.
12.   C. Costentin, S. Drouet, M. Robert and J.-M. Savéant, *Science*, 2012, **338**, 90-94.
13.   B. J. Fisher and R. Eisenberg, *J. Am. Chem. Soc.*, 1980, **102**, 7361-7363.
14.   J. W. Raebiger, J. W. Turner, B. C. Noll, C. J. Curtis, A. Miedaner, B. Cox and D. L. DuBois, *Organometallics*, 2006, **25**, 3345-3351.
15.   R. Angamuthu, P. Byers, M. Lutz, A. L. Spek and E. Bouwman, *Science*, 2010, **327**, 313-315.
16.   J. Hawecker, J. M. Lehn and R. Ziessel, *Helv. Chim. Acta*, 1986, **69**, 1990-2012.
17.   J. M. Smieja and C. P. Kubiak, *Inorg. Chem.*, 2010, **49**, 9283-9289.
18.   B. Kumar, J. M. Smieja and C. P. Kubiak, *J. Phys. Chem. C*, 2010, **114**, 14220-14223.
19.   B. Kumar, J. M. Smieja, A. F. Sasayama and C. P. Kubiak, *Chem. Commun.*, 2012, **48**, 272-274.
20.   J. M. Smieja, M. D. Sampson, K. A. Grice, E. E. Benson, J. D. Froehlich and C. P. Kubiak, *Inorg. Chem.*, 2013, **52**, 2484-2491.
21.   M. Bourrez, F. Molton, S. Chardon-Noblat and A. Deronzier, *Angew. Chem. Int. Ed.*, 2011, **50**, 9903-9906.
22.   Z. Chen, C. Chen, D. R. Weinberg, P. Kang, J. J. Concepcion, D. P. Harrison, M. S. Brookhart and T. J. Meyer, *Chem. Commun.*, 2011, **47**, 12607-12609.
23.   S. Sato, T. Arai, T. Morikawa, K. Uemura, T. M. Suzuki, H. Tanaka and T. Kajino, *J. Am. Chem. Soc.*, 2011, **133**, 15240-15243.
24.   T. Arai, S. Tajima, S. Sato, K. Uemura, T. Morikawa and T. Kajino, *Chem. Commun.*, 2011, **47**, 12664-12666.
25.   G. Seshadri, C. Lin and A. B. Bocarsly, *J. Electroanal. Chem.*, 1994, **372**, 145-150.
26.   E. E. Barton, D. M. Rampulla and A. B. Bocarsly, *J. Am. Chem. Soc.*, 2008, **130**, 6342-6344.

27.   E. Barton Cole, P. S. Lakkaraju, D. M. Rampulla, A. J. Morris, E. Abelev and A. B. Bocarsly, *J. Am. Chem. Soc.*, 2010, **132**, 11539-11551.

28.   B. A. Rosen, A. Salehi-Khojin, M. R. Thorson, W. Zhu, D. T. Whipple, P. J. A. Kenis and R. I. Masel, *Science*, 2011, **334**, 643-644.

29.   O. Ishitani, M. W. George, T. Ibusuki, F. P. A. Johnson, K. Koike, K. Nozaki, C. Pac, J. J. Turner and J. R. Westwell, *Inorg. Chem.*, 1994, **33**, 4712-4717.

30.   H. Hori, O. Ishitani, K. Koike, F. P. A. Johnson and T. Ibusuki, *Energy Convers. Manage.*, 1995, **36**, 621-624.

31.   H. Hori, F. P. A. Johnson, K. Koike, O. Ishitani and T. Ibusuki, *J. Photochem. Photobiol., A*, 1996, **96**, 171-174.

32.   B. Gholamkhass, H. Mametsuka, K. Koike, T. Tanabe, M. Furue and O. Ishitani, *Inorg. Chem.*, 2005, **44**, 2326-2336.

33.   S. Sato, K. Koike, H. Inoue and O. Ishitani, *Photochem. Photobiol. Sci.*, 2007, **6**, 454-461.

34.   J. Agarwal, E. Fujita, H. F. Schaefer and J. T. Muckerman, *J. Am. Chem. Soc.*, 2012, **134**, 5180-5186.

35.   J. Chauvin, F. Lafolet, S. Chardon-Noblat, A. Deronzier, M. Jakonen and M. Haukka, *Chem. Eur. J.*, 2011, **17**, 4313-4322.

36.   Z.-Y. Bian, S.-M. Chi, L. Li and W. Fu, *Dalton Trans.*, 2010, **39**, 7884-7887.

37.   K. Koike, S. Naito, S. Sato, Y. Tamaki and O. Ishitani, *J. Photochem. Photobiol., A*, 2009, **207**, 109-114.

38.   N. Yokoi, Y. Miura, C.-Y. Huang, N. Takatani, H. Inaba, T. Koshiyama, S. Kanamaru, F. Arisaka, Y. Watanabe, S. Kitagawa and T. Ueno, *Chem. Commun.*, 2011, **47**, 2074-2076.

39.   T. Hirose, S. Shigaki, M. Hirose and A. Fushimi, *J. Fluorine Chem.*, 2010, **131**, 915-921.

40.   K. Kiyosawa, N. Shiraishi, T. Shimada, D. Masui, H. Tachibana, S. Takagi, O. Ishitani, D. A. Tryk and H. Inoue, *J. Phys. Chem. C*, 2009, **113**, 11667-11673.

41.   T. Yui, A. Kan, C. Saitoh, K. Koike, T. Ibusuki and O. Ishitani, *ACS Appl. Mater. Interfaces*, 2011, **3**, 2594-2600.

42.   S. Sato, T. Morikawa, S. Saeki, T. Kajino and T. Motohiro, *Angew. Chem. Int. Ed.*, 2010, **49**, 5101-5105.

43.   T. M. Suzuki, H. Tanaka, T. Morikawa, M. Iwaki, S. Sato, S. Saeki, M. Inoue, T. Kajino and T. Motohiro, *Chem. Commun.*, 2011, **47**, 8673-8675.

44.   T. W. Woolerton, S. Sheard, E. Reisner, E. Pierce, S. W. Ragsdale and F. A. Armstrong, *J. Am. Chem. Soc.*, 2010, **132**, 2132-2133.

45.   T. W. Woolerton, S. Sheard, E. Pierce, S. W. Ragsdale and F. A. Armstrong, *Energy Environ. Sci.*, 2011, **4**, 2393-2399.

46.   J.-H. Jeoung and H. Dobbek, *Science*, 2007, **318**, 1461-1464.

47.   Y. S. Chaudhary, T. W. Woolerton, C. S. Allen, J. H. Warner, E. Pierce, S. W. Ragsdale and F. A. Armstrong, *Chem. Commun.*, 2012, **48**, 58-60.

48.   S. Sato, T. Morikawa, T. Kajino and O. Ishitani, *Angew. Chem. Int. Ed.*, 2013, **52**, 988-992.

49.   K. Sekizawa, K. Maeda, K. Domen, K. Koike and O. Ishitani, *J. Am. Chem. Soc.*, 2013, **135**, 4596-4599.

50. F. P. A. Johnson, M. W. George, F. Hartl and J. J. Turner, *Organometallics*, 1996, **15**, 3374-3387.
51. P. Christensen, A. Hamnett, A. V. G. Muir and J. A. Timney, *J. Chem. Soc., Dalton Trans.*, 1992, 1455-1463.
52. T. R. O'Toole, B. P. Sullivan, M. R. M. Bruce, L. D. Margerum, R. W. Murray and T. J. Meyer, *J. Electroanal. Chem. Interfacial Electrochem.*, 1989, **259**, 217-239.
53. K. Koike, H. Hori, M. Ishizuka, J. R. Westwell, K. Takeuchi, T. Ibusuki, K. Enjouji, H. Konno, K. Sakamoto and O. Ishitani, *Organometallics*, 1997, **16**, 5724-5729.
54. H. Takeda, K. Koike, H. Inoue and O. Ishitani, *J. Am. Chem. Soc.*, 2008, **130**, 2023-2031.
55. Y. Hayashi, S. Kita, B. S. Brunschwig and E. Fujita, *J. Am. Chem. Soc.*, 2003, **125**, 11976-11987.
56. K. Shinozaki, Y. Hayashi, B. S. Brunschwig and E. Fujita, *Res. Chem. Intermed.*, 2007, **33**, 27-36.
57. C. D. Windle, M. V. Campian, A.-K. Duhme-Klair, E. A. Gibson, R. N. Perutz and J. Schneider, *Chem. Commun.*, 2012, **48**, 8189-8191.
58. K. A. Grice, N. X. Gu, M. D. Sampson and C. P. Kubiak, *Dalton Trans.*, 2013.
59. E. E. Benson, M. D. Sampson, K. A. Grice, J. M. Smieja, J. D. Froehlich, D. Friebel, J. A. Keith, E. A. Carter, A. Nilsson and C. P. Kubiak, *Angew. Chem. Int. Ed.*, 2013, **52**, 4841-4844.
60. J. M. Smieja, E. E. Benson, B. Kumar, K. A. Grice, C. S. Seu, A. J. M. Miller, J. M. Mayer and C. P. Kubiak, *Proc. Natl. Acad. Sci. U. S. A.*, 2012.
61. E. E. Benson, K. A. Grice, J. M. Smieja and C. P. Kubiak, *Polyhedron*.
62. K. Kalyanasundaram, M. Graetzel and Editors, *Photosensitization and Photocatalysis Using Inorganic and Organometallic Compounds. [In: Catal. Met. Complexes, 1993; 14]*, Kluwer, 1993.
63. R. A. Marcus and N. Sutin, *Biochim. Biophys. Acta, Rev. Bioenerg.*, 1985, **811**, 265-322.
64. P. Atkins and T. Overton, *Shriver and Atkins' Inorganic Chemistry*, OUP Oxford, 2010.
65. M. T. Indelli, F. Scandola, L. Flamigni, J. P. Collin, J. P. Sauvage and A. Sour, *Inorg. Chem.*, 1997, **36**, 4247-4250.
66. A. M. Brun, A. Harriman, V. Heitz and J. P. Sauvage, *J. Am. Chem. Soc.*, 1991, **113**, 8657-8663.
67. C. Monnereau, J. Gomez, E. Blart, F. Odobel, S. Wallin, A. Fallberg and L. Hammarström, *Inorg. Chem.*, 2005, **44**, 4806-4817.
68. D. R. Weinberg, C. J. Gagliardi, J. F. Hull, C. F. Murphy, C. A. Kent, B. C. Westlake, A. Paul, D. H. Ess, D. G. McCafferty and T. J. Meyer, *Chem. Rev.*, 2012, **112**, 4016-4093.
69. S. W. Gersten, G. J. Samuels and T. J. Meyer, *J. Am. Chem. Soc.*, 1982, **104**, 4029-4030.
70. A. A. Pizano, J. L. Yang and D. G. Nocera, *Chem. Sci.*, 2012, **3**, 2457-2461.
71. C. J. Aspley, J. R. Lindsay Smith and R. N. Perutz, *J. Chem. Soc., Dalton Trans.*, 1999, 2269-2272.

72. C. J. Aspley, J. R. Lindsay Smith, R. N. Perutz and D. Pursche, *J. Chem. Soc., Dalton Trans.*, 2002, 170-180.
73. A. Gabrielsson, F. Hartl, H. Zhang, J. R. Lindsay Smith, M. Towrie, A. Vlcek and R. N. Perutz, *J. Am. Chem. Soc.*, 2006, **128**, 4253-4266.
74. A. Gabrielsson, J. R. Lindsay Smith and R. N. Perutz, *Dalton Trans.*, 2008, 4259-4269.
75. J. Schneider, K. Q. Vuong, J. A. Calladine, X.-Z. Sun, A. C. Whitwood, M. W. George and R. N. Perutz, *Inorg. Chem.*, 2011, **50**, 11877-11889.
76. P. Zhang, M. Wang, C. Li, X. Li, J. Dong and L. Sun, *Chem. Commun.*, 2010, **46**, 8806-8808.
77. N. Kaveevivitchai, R. Chitta, R. Zong, M. El Ojaimi and R. P. Thummel, *J. Am. Chem. Soc.*, 2012, **134**, 10721-10724.
78. P. Guillo, O. Hamelin, P. Batat, G. Jonusauskas, N. D. McClenaghan and S. Ménage, *Inorg. Chem.*, 2012, **51**, 2222-2230.
79. O. Hamelin, P. Guillo, F. d. r. Loiseau, M.-F. Boissonnet and S. p. Ménage, *Inorg. Chem.*, 2011, **50**, 7952-7954.
80. H. Cui, M. Hu, H. Wen, G. Chai, C. Ma, H. Chen and C. Chen, *Dalton Trans.*, 2012, **41**, 13899-13907.
81. A. Fihri, V. Artero, M. Razavet, C. Baffert, W. Leibl and M. Fontecave, *Angew. Chem. Int. Ed.*, 2008, **47**, 564-567.
82. A. D. Adler, F. R. Longo, J. D. Finarelli, J. Goldmacher, J. Assour and L. Korsakoff, *J. Org. Chem.*, 1967, **32**, 476-476.
83. R. Luguya, L. Jaquinod, F. R. Fronczek, M. G. H. Vicente and K. M. Smith, *Tetrahedron*, 2004, **60**, 2757-2763.
84. W. J. Kruper, T. A. Chamberlin and M. Kochanny, *J. Org. Chem.*, 1989, **54**, 2753-2756.
85. G. G. Meng, B. R. James and K. A. Skow, *Can. J. Chem.*, 1994, **72**, 1894-1909.
86. J. P. Collman, R. R. Gagne, C. Reed, T. R. Halbert, G. Lang and W. T. Robinson, *J. Am. Chem. Soc.*, 1975, **97**, 1427-1439.
87. C. Aspley, PhD thesis in Chemistry, University of York, York, UK, 2000.
88. E. A. Gibson, PhD thesis in Chemistry, University of York, York, UK, 2006.
89. M. A. McLaughlin and D. M. Barnes, *Tetrahedron Lett.*, 2006, **47**, 9095-9097.
90. K. Kondo, H. Ogawa, H. Yamashita, H. Miyamoto, M. Tanaka, K. Nakaya, K. Kitano, Y. Yamamura, S. Nakamura, T. Onogawa, T. Mori and M. Tominaga, *Biorg. Med. Chem.*, 1999, **7**, 1743-1754.
91. A. Shaginian, L. R. Whitby, S. Hong, I. Hwang, B. Farooqi, M. Searcey, J. Chen, P. K. Vogt and D. L. Boger, *J. Am. Chem. Soc.*, 2009, **131**, 5564-5572.
92. R. J. Rahaim and R. E. Maleczka, *Org. Lett.*, 2005, **7**, 5087-5090.
93. R. J. Rahaim, Jr. and R. E. Maleczka, Jr., *Synthesis*, 2006, 3316-3340.
94. B. P. S. Chauhan, J. S. Rathore and T. Bandoo, *J. Am. Chem. Soc.*, 2004, **126**, 8493-8500.
95. N. J. Lawrence, M. D. Drew and S. M. Bushell, *J. Chem. Soc., Perkin Trans. 1*, 1999, **0**, 3381-3391.
96. A. G. Fang, J. V. Mello and N. S. Finney, *Org. Lett.*, 2003, **5**, 967-970.
97. E. Bald, K. Saigo and T. Mukaiyama, *Chem. Lett.*, 1975, 1163-1166.

98. L. Della Ciana, I. Hamachi and T. J. Meyer, *J. Org. Chem.*, 1989, **54**, 1731-1735.
99. K. Tomioka and K. Koga, *Tetrahedron*, 1988, **44**, 4351-4355.
100. J. M. Khurana, S. Chauhan and G. Bansal, *Monatsh. Chem.*, 2004, **135**, 83-87.
101. G. K. Lahiri, J. S. Summers and A. M. Stolzenberg, *Inorg. Chem.*, 1991, **30**, 5049-5052.
102. V. Penicaud, F. Odobel and B. Bujoli, *Tetrahedron Lett.*, 1998, **39**, 3689-3692.
103. W. Uhlig, *Organometallics*, 1994, **13**, 2843-2848.
104. A. Gabrielsson, PhD thesis in Chemistry, University of York, York, UK, 2002.
105. G. J. Stor, F. Hartl, J. W. M. van Outersterp and D. J. Stufkens, *Organometallics*, 1995, **14**, 1115-1131.
106. G. Hariprasad, S. Dahal and B. G. Maiya, *J. Chem. Soc., Dalton Trans.*, 1996, **0**, 3429-3436.
107. V. V. Pavlishchuk and A. W. Addison, *Inorg. Chim. Acta*, 2000, **298**, 97-102.
108. A. Martinez, MSc dissertation in Chemistry, University of York, York, UK.
109. K. Kalyanasundaram, *Photochemistry of Polypyridine & Porphyrin Complexes*, Acad. Press, 1992.
110. J. Rodriguez, C. Kirmaier and D. Holten, *J. Am. Chem. Soc.*, 1989, **111**, 6500-6506.
111. M. Towrie, D. C. Grills, J. Dyer, J. A. Weinstein, P. Matousek, R. Barton, P. D. Bailey, N. Subramaniam, W. M. Kwok, C. Ma, D. Phillips, A. W. Parker and M. W. George, *Appl. Spectrosc.*, 2003, **57**, 367-380.
112. I. Wender, *Fuel Process. Technol.*, 1996, **48**, 189-297.
113. H. Takeda and O. Ishitani, *Coord. Chem. Rev.*, 2010, **254**, 346-354.
114. H. W. Whitlock and M. Y. Oester, *J. Am. Chem. Soc.*, 1973, **95**, 5738-5741.
115. G. R. Seely and M. Calvin, *J. Chem. Phys.*, 1955, **23**, 1068-1078.
116. L. S. Fox, J. L. Marshall, H. B. Gray and J. R. Winkler, *J. Am. Chem. Soc.*, 1987, **109**, 6901-6902.
117. Y. Harel and J. Manassen, *J. Am. Chem. Soc.*, 1978, **100**, 6228-6234.
118. F. Lakadamyali and E. Reisner, *Chem. Commun.*, **47**, 1695-1697.
119. E. Reisner, D. J. Powell, C. Cavazza, J. C. Fontecilla-Camps and F. A. Armstrong, *J. Am. Chem. Soc.*, 2009, **131**, 18457-18466.
120. F. Lakadamyali, M. Kato, N. M. Muresan and E. Reisner, *Angew. Chem. Int. Ed.*, 2012, **51**, 9381-9384.
121. F. Lakadamyali, A. Reynal, M. Kato, J. R. Durrant and E. Reisner, *Chem. Eur. J.*, 2012, **18**, 15464-15475.
122. W. R. McNamara, R. L. Milot, H. Song, R. C. Snoeberger, V. S. Batista, C. A. Schmuttenmaer, G. W. Brudvig and R. H. Crabtree, *Energy Environ. Sci.*, 2010, **3**, 917-923.
123. K. J. Young, L. A. Martini, R. L. Milot, R. C. Snoeberger Iii, V. S. Batista, C. A. Schmuttenmaer, R. H. Crabtree and G. W. Brudvig, *Coord. Chem. Rev.*, 2012, **256**, 2503-2520.
124. Z. Zhao, H. Liu and S. Chen, *Nanoscale*, 2012, **4**, 7301-7308.

125. E. Bae, W. Choi, J. Park, H. S. Shin, S. B. Kim and J. S. Lee, *J. Phys. Chem. B*, 2004, **108**, 14093-14101.

126. Y. Xu and M. A. A. Schoonen, *Am. Mineral.*, 2000, **85**, 543-556.

127. T. Yoshida, K. Tsutsumida, S. Teratani, K. Yasufuku and M. Kaneko, *Chem. Commun.*, 1993, 631-633.

128. G. Kortüm, W. Braun and G. Herzog, *Angew. Chem. Int. Ed.*, 1963, **2**, 333-341.

129. E.-O. Ganbold, Y. Lee, K. Lee, O. Kwon and S.-W. Joo, *Chem.--Asian J.*, 2010, **5**, 852-858.

130. P. Péchy, T. Renouard, S. M. Zakeeruddin, R. Humphry-Baker, P. Comte, P. Liska, L. Cevey, E. Costa, V. Shklover, L. Spiccia, G. B. Deacon, C. A. Bignozzi and M. Grätzel, *J. Am. Chem. Soc.*, 2001, **123**, 1613-1624.

131. K. Hara, Z.-S. Wang, T. Sato, A. Furube, R. Katoh, H. Sugihara, Y. Dan-oh, C. Kasada, A. Shinpo and S. Suga, *J. Phys. Chem. B*, 2005, **109**, 15476-15482.

132. T. Kitamura, M. Ikeda, K. Shigaki, T. Inoue, N. A. Anderson, X. Ai, T. Lian and S. Yanagida, *Chem. Mater.*, 2004, **16**, 1806-1812.

133. K. D. Dubois, H. He, C. Liu, A. S. Vorushilov and G. Li, *J. Mol. Catal. A: Chem.*, 2012, **363–364**, 208-213.

134. I. Gillaizeau-Gauthier, F. Odobel, M. Alebbi, R. Argazzi, E. Costa, C. A. Bignozzi, P. Qu and G. J. Meyer, *Inorg. Chem.*, 2001, **40**, 6073-6079.

135. H.-P. Lu, C.-Y. Tsai, W.-N. Yen, C.-P. Hsieh, C.-W. Lee, C.-Y. Yeh and E. W.-G. Diau, *J. Phys. Chem. C*, 2009, **113**, 20990-20997.

136. R. Jose, V. Thavasi and S. Ramakrishna, *J. Am. Ceram. Soc.*, 2009, **92**, 289-301.

137. C. Kittel, *Introduction to Solid State Physics*, John Wiley & Sons, 2004.

138. D.-M. Shen, C. Liu and Q.-Y. Chen, *J. Org. Chem.*, 2006, **71**, 6508-6511.

139. D. A. M. Egbe, A. M. Amer and E. Klemm, *Des. Monomers Polym.*, 2001, **4**, 169-175.

140. F. Odobel, F. Suzenet, E. Blart and J.-P. Quintard, *Org. Lett.*, 2000, **2**, 131-133.

141. Y. Y. Enakieva, A. G. Bessmertnykh, Y. G. Gorbunova, C. Stern, Y. Rousselin, A. Y. Tsivadze and R. Guilard, *Org. Lett.*, 2009, **11**, 3842-3845.

142. G. R. Fulmer, A. J. M. Miller, N. H. Sherden, H. E. Gottlieb, A. Nudelman, B. M. Stoltz, J. E. Bercaw and K. I. Goldberg, *Organometallics*, 2010, **29**, 2176-2179.

143. CrysAlisPro, Oxford Diffraction Ltd, Version 1.171.34.40.

144. Empirical absorption correction using spherical harmonics, implemented in SCALE3 ABSPACK scaling algorithm within CrysAlisPro software, Oxford Diffraction Ltd. Version 1.171.34.40.

145. "Olex2" crystallography software, *J. Appl. Crystallogr.*, 2009, **42**, 339-341.

146. "SHELXS-97" - program for structure solution. G. M. Sheldrick, University of Göttingen, Göttingen, Germany, 1997.

147. "SHELXL-97" - program for the refinement of crystal structures., G. M. Sheldrick, University of Göttingen, Göttingen, Germany, 1997.

148. L. Palatinus and G. Chapuis, *J. Appl. Crystallogr.*, 2007, **40**, 786-790.

149.   D. G. McCafferty, B. M. Bishop, C. G. Wall, S. G. Hughes, S. L. Mecklenberg, T. J. Meyer and B. W. Erickson, *Tetrahedron*, 1995, **51**, 1093-1106.
150.   C. Kutal, M. A. Weber, G. Ferraudi and D. Geiger, *Organometallics*, 1985, **4**, 2161-2166.
151.   A. Gabrielsson, F. Hartl, J. R. L. Smith and R. N. Perutz, *Chem. Commun.*, 2002, 950-951.